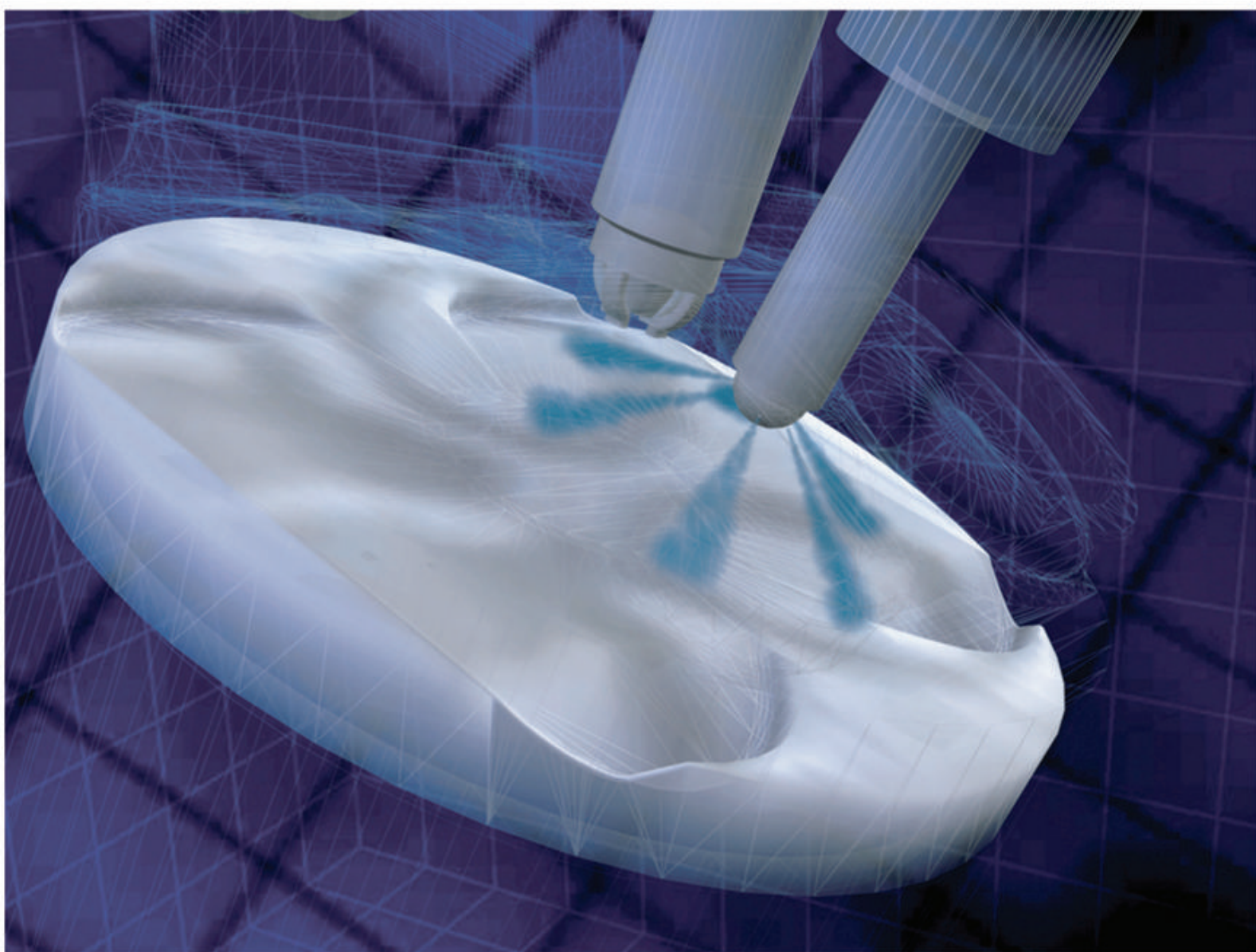Udo Gerke

Numerical Analysis of Mixture Formation and Combustion in a Hydrogen Direct-Injection Internal Combustion Engine

Diss. ETH No. 17477

Numerical Analysis of Mixture Formation and Combustion in a Hydrogen Direct-Injection Internal Combustion Engine

A dissertation submitted to the
SWISS FEDERAL INSTITUTE OF TECHNOLOGY
ZURICH

for the degree of
DOCTOR OF SCIENCE

presented by
UDO GERKE
Dipl.-Ing. Uni. Stuttgart
born February 26th, 1978
citizen of Munich, Germany

accepted on the recommendation of
Prof. Dr. Konstantinos Boulouchos, ETH Zurich, examiner
Prof. Dr. Andreas Wimmer, TU Graz, co-examiner
Prof. Dr. Aldo Steinfeld, ETH Zurich, co-examiner

2007

Preface

The present work was carried out at BMW Group Research and Technology, Munich during my engagement as a doctoral student in the years 2004 to 2007. The work was embedded in the integrated EU-funded research project on hydrogen internal combustion engines, *HyICE*. The aim of this international project was the investigation of hydrogen mixture formation and combustion by means of experimental and numerical analysis with focus on the optimisation of hydrogen IC engines. The experimental investigations include constant volume combustion chambers, optical and thermodynamic research engines as well as multi-cylinder engines. The present work is part of a subproject which involves the adaption and application of 3D-CFD combustion models for hydrogen internal combustion engines.

I would like to express my very special thanks to my Ph.D. adviser Prof. Dr. K. Boulouchos, head of the Laboratory of Aerothermochemistry and Combustion Systems (LAV) at the Swiss Federal Institute of Technology (ETH) Zurich for the excellent supervision, inspiring exchange of views and motivating guidance.

I am particularly grateful to Prof. Dr. R. Freymann, W. Strobl and F. Gerbig from BMW Group Research and Technology for providing the opportunity to arrange this work within the most professional equipped working environment and for their constructive advices.

Furthermore, I wish to thank Prof. Dr. A. Wimmer from Technical University of Graz, Austria and Prof. Dr. A. Steinfeld from ETH Zurich for consenting to be additional examiners.

Among the many colleagues from BMW Group my special thanks go to Dr. A. Obieglo, Dr. M. Hallmannsegger and Dr. J. Ebner for their help and

encouraging discussions. Many thanks also to S. Ellgas, Ch. Fickel, K. Heller, T. Kresse, A. Krohmer and A. Nefischer for their cooperative support.

Regarding the execution of experimental investigations on the thermodynamic and transparent research engine, the assistance of P. Grabner and Dr. W. Kirchweger at Technical University of Graz is much appreciated.

At LAV I wish to thank S. Blatter, P. Obrecht, P. Eberli, A. Schmid and Dr. A. Escher for their assistance during the fixed term project at ETH. There, measurements on hydrogen flame speed were conducted on a single-cylinder compression machine.

As a doctoral student of LAV I was involved in the organisation of several diploma theses in the field of quasi-dimensional simulation of hydrogen engines and hydrogen flame speed measurements. In this respect, I thank M. Hug, M. Atmane, S. Djuranec, P. Rebecchi and K. Steurs for their thoughtful contributions.

Abstract

The present work investigates the mixture formation and combustion process of a direct-injection (DI) hydrogen internal combustion engine by means of three-dimensional numerical simulation. The study specifies details on the validity of turbulence models, combustion models as well as aspects on the definition of hydrogen-air burning velocities with respect to hydrogen IC engine applications. Results of homogeneous, stratified and multi-injection engine operation covering premixed, partially premixed and non-premixed combustion of hydrogen are presented.

Results of the numerical simulations are validated using data of experimental analysis from parallel works [44, 59], employing a one-cylinder research engine and a research engine with optical access. As a fundamental contribution to combustion modelling of hydrogen IC engines, a new correlation for laminar burning velocities of hydrogen-air mixtures at engine-relevant conditions is derived from measurements of premixed outwards propagating flames conducted in a single-cylinder compression machine.

Numerical results of the direct-injection mixture formation give a detailed understanding of the interrelation between injection timing and the degree of mixture homogenisation. A favourable agreement between the computed fuel concentration and results of Planar Laser Induced Fluorescence (PLIF) measurements is reported for various injection timings. Different two-equation turbulence models, a Shear Stress Transport (SST) model and a k-ε model based on Renormalisation Group (RNG) theory as well as a Reynolds Stress Model (RSM) are discussed. The impact of the models on the level of turbulent kinetic energy proves to be of major importance.

State-of-the-art turbulent combustion models on the basis of turbulent flame speed closure (TFC) and on the basis of a flame surface density approach, the Extended Coherent Flame Model (ECFM), are examined. The models are adapted to hydrogen internal combustion engines and are interfaced to the established three-dimensional flow field solver ANSYS CFX within the framework of the international research project *HyICE* [15, 36, 112]. Two different approaches are investigated as input for the laminar burning velocities of hydrogen. Firstly, flame speed data are computed with a kinetic mechanism proposed by Conaire et al. [86]. Secondly, an existing experimentally derived laminar flame speed correlation is extended to rich air/fuel equivalence ratios ($\lambda < 1$) and is compared to measurements conducted within the present work.

In general, the TFC-models show a satisfying agreement for DI operating points compared to experimental data, when mixing computations are conducted with the SST turbulence model. Also, port fuel injection (PFI) operating points demonstrate a good performance with these models, however, the constant model prefactor (multiplier for the closure of turbulent flame speed) has to be defined individually for PFI and DI computations. This effect might be caused by the dissimilar sources of turbulence for the two engine types (PFI and DI) which cannot be adequately predicted by the turbulence models. Combustion computations on the basis of mixture results obtained by the RNG-model generally underrate the level of turbulence intensity for stratified operation points, effecting too weak rates of heat release. The ECFM combustion model shows a satisfying predictability for the PFI case using a constant model prefactor. Computations of DI operating points with this model, however, require a readjustment of the prefactor for each operating point in order to match experimental results.

Regarding turbulent combustion, the hydrogen laminar flame speed is recognised to be the crucial quantity for the employed modelling approaches. Since direct-injection hydrogen engines in the stratified case engender a wide range of equivalence ratios, fundamental data for the laminar flame speed has to be provided as a model input within the entire boundaries of ignition limits. A lack of experimental data of lami-

nar flame speed at engine-relevant conditions (high pressure, high temperature) is noticed. In order to perform a detailed study on hydrogen burning velocities, a single-cylinder compression machine is selected to conduct flame speed measurements of hydrogen-air mixtures at ignition temperatures and pressures up to $T = 700$ K and $p = 45$ bar, considering air/fuel equivalence ratios between $\lambda = 0.4$ and 2.8. Flame front velocities are acquired by means of optical methods using OH-chemiluminescence and thermodynamic, multi-zone evaluation of pressure traces. In comparison to data of laminar flame speed derived from reaction mechanisms and flame speed correlations found in literature, the experimental results show increased burning velocities due to flame front wrinkling caused by hydrodynamic and thermo-diffusive instabilities.

Zusammenfassung

Die vorliegende Arbeit behandelt die numerische Berechnung der Gemischbildung und ottomotorischen Verbrennung von Wasserstoff mit Methoden der reaktiven CFD (Computational Fluid Dynamics). Gegenstand der Untersuchung ist ein Einzylinder-Forschungsmotor, der wahlweise mit Saugrohreinblasung bzw. mit Hochdruck-Direkteinblasung betrieben werden kann. Als Betriebspunkte werden homogene und geschichtete Gemische sowie Mehrfacheinblasung untersucht. Es können somit vorgemischte, teilweise vorgemischte und nicht vorgemischte Verbrennungsmodi dargestellt werden.

Detaillierte CFD-Berechnungen des Einblasevorgangs und der Kraftstoffverteilung zum Zündzeitpunkt werden anhand eines Einzylinder-Transparentmotors validiert [59]. Die Verifikation von Berechnungen des Brennstoffumsatzes erfolgt mittels Indizierdaten eines thermodynamischen Forschungsmotors [44].

Mit Bezug auf die Hochdruck-Direkteinblasung stellt neben der Düsengeometrie der Einblasezeitpunkt eine wesentliche Einflussgröße auf die Form der Gemischbildung dar. CFD-Berechnungen der inneren Gemischbildung liefern detaillierte Erkenntnisse über den Zusammenhang zwischen Einblasezeitpunkt und dem Grad der Gemischhomogenisierung. Für verschiedene Einblasezeitpunkte ist eine gute Übereinstimmung der berechneten Kraftstoffverteilung mit optischen Lichtschnitt-Aufnahmen (PLIF) des Transparentmotors nachgewiesen worden.

Als Turbulenzmodelle werden ein Shear Stress Transport (SST) Modell und ein k-ε Modell auf Basis eines Renormalisierungs-Ansatzes (RNG) eingesetzt und mit Ergebnissen eines Reynolds Stress Modells (RSM) verglichen. Die Turbulenzmodelle zeigen deutliche Unterschiede in der durch die

Wasserstoff-Einblasung generierten turbulenten kinetischen Energie, während der Einfluss verschiedener Turbulenzmodelle auf die Vorausberechnung der Gemischverteilung weniger stark ausgeprägt ist.

Zur Berechnung der Kraftstoffumsetzung werden unterschiedliche turbulente Verbrennungsmodelle auf Basis eines turbulenten Flammgeschwindigkeits-Modells (Turbulent Flame Speed Closure, TFC) und eines Flammenoberflächendichte-Ansatzes (Extended Coherent Flame Model, ECFM) untersucht. Die Modelle sind im Rahmen des internationalen EU-Förderprojektes *HyICE* an die spezifischen Eigenschaften der Wasserstoff-Verbrennung angepasst und in den CFD-code ANSYS CFX implementiert worden [15, 36, 112].

Zur Definition laminarer Wasserstoff-Flammgeschwindigkeiten werden zwei unterschiedliche Ansätze verfolgt. Einerseits werden theoretische Werte für Flammgeschwindigkeiten auf der Basis eines detaillierten Reaktionsmechanismus berechnet. Diese Methode liefert Flammgeschwindigkeiten einer stabilen laminaren Verbrennung. Andererseits wird als Eingabegröße für die Verbrennungsmodelle eine Flammgeschwindigkeits-Korrelation auf Basis experimenteller Daten verwendet. Im Gegensatz zu theoretischen Werten berücksichtigt diese Methode den Einfluss von Flammfrontinstabilitäten auf die effektive Brenngeschwindigkeit.

Berechnungen unterschiedlicher Betriebspunkte mit innerer Gemischbildung (DI) zeigen für die TFC-Verbrennungsmodelle in Kombination mit dem SST-Turbulenzmodell eine zufriedenstellende Übereinstimmung mit experimentellen Daten. Betriebspunkte mit äusserer Gemischbildung (AGB) werden von den Modellen ebenfalls gut wiedergegeben, jedoch ist eine Übertragbarkeit der Modellkonstanten (Multiplikatoren zur Schließung des Terms der turbulenten Flammgeschwindigkeit) zwischen den AGB- und DI-Berechnungen nicht gegeben. Verbrennungsberechnungen auf Basis des RNG-Turbulenzmodells unterschätzen das Niveau der Turbulenzintensität für Direkteinblasung mit sehr späten Einblasezeiten. Als Konsequenz sind die Brennverläufe der CFD-Berechnungen mit diesem Turbulenzmodell im Vergleich zu Ergebnissen der Brennverlaufsanalyse stark verlangsamt.

Das ECFM-Verbrennungsmodell zeigt zufriedenstellende Resultate für Betriebspunkte mit äußerer Gemischbildung. Verbrennungsberechnungen mit innerer Gemischbildung erfordern jedoch eine Anpassung der Modellkonstanten an experimentelle Daten für jeden einzelnen Betriebspunkt, wodurch die Allgemeingültigkeit dieses Ansatzes stärker limitiert ist als für Berechnungen mit dem TFC-Modell.

In Bezug auf die Berechnung der Kraftstoffumsetzung erweist sich die laminare Flammgeschwindigkeit als eine der kritischen Einflussgrößen der turbulenten Verbrennungsmodelle. Aufgrund des weiten Bereiches der lokalen Luft/Kraftstoff-Verhältnisse bei innerer Gemischbildung müssen Werte der laminaren Brenngeschwindigkeit innerhalb der gesamten Zündgrenzen bekannt sein. Ein fundamentaler Beitrag zur Bestimmung dieser Größen wird durch detaillierte Untersuchungen laminarer Flammgeschwindigkeiten in einem Einhubtriebwerk erbracht. Die betrachteten Luft-/Kraftstoff-Verhältnisse, Zünddrücke und Temperaturen liegen in einem Bereich von $0{,}4 \leq \lambda \leq 2{,}8$, $p = 5$ bar bis 45 bar und $T = 350$ K bis 700 K und stellen eine wesentliche Erweiterung von bisher in der Literatur verfügbaren experimentellen Daten dar. Eine Bestimmung des Flammradius erfolgt sowohl durch optische Messmethoden (OH-Chemilumineszenz) als auch durch thermodynamische Analyse des indizierten Druckverlaufes. Die abgeleiteten laminaren Brenngeschwindigkeiten werden durch einen Vergleich mit Werten einer reaktionskinetischen Berechnung plausibilisiert.

Contents

Contents

List of Figures

List of Tables

Nomenclature

Symbols

a	m^2/s	Thermal diffusivity
b	m	Cylinder bore
c	-	Reaction progress variable
d	m	Diameter
e	J/kg	Internal energy
f	Hz	Frequency
h	J/kg	Enthalpy
h	m	Height
k	m^2/s^2	Turbulent kinetic energy
l	m	Piston lift
l	m	Length
l_t	m	Turbulent length scale
m	kg	Mass
$\dot{m}$	g/s	Mass flow
n	1/min	Engine speed
n	-	Wavenumber
p	bar	Pressure
r	m	Radius
s_L	m/s	Laminar flame speed
t	s	Time
u	m/s	Velocity
u'	m/s	Velocity fluctuations
u_l	m/s	Stable laminar burning velocity
u_n	m/s	Unstable laminar burning velocity
v_g	m/s	Gas expansion velocity
z	-	Mixture fraction variable
z''	-	Mixture fraction variance

Symbols (continued)

A	m^2	Area
A	-	Zimont model coefficient
C	-	Bradley model coefficient
C_i	-	Turbulence model coefficient
$\mathcal{D}$	-	Destruction term of ECFM model
D	m^2/s	Diffusion coefficient
F	-	Burning velocity enhancement factor
H	J/kg	Total enthalpy
L_b	m	Markstein Length
P	W	Power
P	-	Probability density function
$\mathcal{P}_i$	-	Source term of ECFM model
Q	W	Integral heat release
R	J/molK	Ideal gas constant
S	m/s	Stable laminar flame front velocity
S_n	m/s	Unstable laminar flame front velocity
T	K	Temperature
U_t	m/s	Turbulent flame speed
V_{ki}	m^2/s	Diffusion of species k in direction i
V	m^3	Volume
W	kg/mol	Molecular weight
X_i	-	Volume fraction of species i
Y_i	-	Mass fraction of species i
Z_T	-	Tracer variable

Greek Symbols

α	-	ECFM model coefficient
α	1/s	Flame stretch rate
α	-	Temperature exponent of flame speed correlation
β	-	ECFM model coefficient
β	-	Pressure exponent of flame speed correlation
γ	-	Ratio between unburned and burned densities
γ	-	Residual gas factor of flame speed correlation
δ_l	m	Laminar flame thickness
δ_{ij}	-	Kronecker symbol
ϵ	-	Compression ratio
ε	m^2/s^3	Turbulent eddy dissipation
η	-	Efficiency
η	m	Kolmogorov length scale

Greek Symbols (continued)

κ_{exp}	-	Expansion coefficient
κ_t	1/s	Turbulent strain rate
λ	-	Air/fuel equivalence ratio ($\lambda = \frac{(m_{air}/m_{fuel})_{actual}}{(m_{air}/m_{fuel})_{stoic}} = 1/\phi$)
λ	m	Wavelength
λ_u	W/(mK)	Thermal conductivity
μ_t	Ns/m^2	Turbulent dynamic viscosity
ν_t	m^2/s	Turbulent kinematic viscosity
ρ	kg/m^3	Density
σ_i	-	Turbulence model coefficient
Σ	m^2/m^3	Flame surface density
φ	° CA	Crank angle
ϕ	-	Fuel/air equivalence ratio ($= 1/\lambda$)
Φ_{ij}	-	Pressure-strain correlation
$\dot{\omega}$	kg m^3/s	Reaction rate

Subscripts

0	Reference condition
1	First injection
2	Second injection
a	Axial
b	Burned
cr	Critical
d	Deficient
e	Excessive
eff	Effective
ff	Flame front
i, j, k	Index
i	Indicated
k	Turbulent kinetic energy
r	Radial
s	Sensible
$stoic$	Stoichiometric
th	Thermal
u	Unburned
EGR	Exhaust gas
F	Fuel
O	Oxygen

Characteristic Numbers

Da	Damköhler number
Ka	Karlovitz number
Le	Lewis number
Ma	Markstein number
Pe	Peclet number
Re	Reynolds number
Sc_Σ	Flame surface turbulent Schmidt number
Sc_t	Turbulent Schmidt number
Ze	Zeldovich number

Abbreviations

$AGTDC$	After Gas Exchange Top Dead Centre
$AITDC$	After Ignition Top Dead Centre
BDC	Bottom Dead Centre
$BGTDC$	Before Gas Exchange Top Dead Centre
$BITDC$	Before Ignition Top Dead Centre
CA	Crank Angle
CCD	Charge Coupled Device
CFD	Computational Fluid Dynamics
DI	Direct-Injection
$DOHC$	Double Overhead Camshaft
$ECFM$	Extended Coherent Flame Model
IC	Internal Combustion
$IMEP$	Indicated Mean Effective Pressure
PFI	Port Fuel Injection
$RANS$	Reynolds Approximated Navier-Stokes
RMS	Root Mean Square
RNG	Renormalisation Group
RSM	Reynolds Stress Model
SOI	Start of Injection
SST	Shear Stress Transport
TDC	Top Dead Centre
TEA	Triethylamine
TFC	Turbulent Flame Speed Closure

Chapter 1

Introduction

The current chapter gives an overview on hydrogen fuel properties, mixture formation strategies for hydrogen internal combustion engines and reviews former and recent activities on hydrogen engine research. The main part of the present work – combustion modelling of hydrogen engines – is introduced by a summary on the state-of-the-art with regard to the application of three-dimensional numerical simulation of hydrogen engines and hydrogen turbulent combustion modelling.

1.1 Hydrogen as a Fuel for Internal Combustion Engines

A finite nature of fossil fuel resources and the necessity to reduce greenhouse gas emissions require to investigate other energy carriers than the today established hydrocarbon fuels, gasoline and diesel. Internationally, hydrogen is considered to be a promising secondary energy carrier as a long-term solution. Governments of the U.S., of Japan and of the European Union initiated several strategies on hydrogen research, focussing on the automotive sector, e.g. the U.S. Hydrogen Posture Plan [85], the Japan Hydrogen and Fuel Cell Demonstration Project [56] and the European Hydrogen and Fuel Cell Technology Platform [81]. The common aim of all of these programs is to establish equal-zero emission and high efficient propulsion technologies based on a hydrogen infrastructure.

Most of the programs concentrate on fuel cell technology. Hydrogen internal combustion engines, however, are considered as able to possibly close the gap between a carbon-based and a hydrogen-based economy [80]. Being part of future vehicle propulsion systems, hydrogen internal combustion engines have the potential of an improved operation concerning power, efficiency and emissions compared to conventionally fuelled engines, even with regard to the demands of sustainable mobility [42].

Although the suitability of hydrogen as a widespread used secondary energy carrier is still being discussed, there are contrary environmental concerns regarding the impact of molecular hydrogen gas leakage on the chemistry of ozone depletion and perturbations of the climate system [104, 109]. Regarding a net-weight reduction of greenhouse gas emissions, the technology used for production of hydrogen is decisive. Beside the commonly aspired method of hydrogen production from renewable resources, different potential production pathways exist which, for instance, are based on nuclear or fossil sources. An outline of the accumulated greenhouse gas emissions depending on the selected pathway may be found in Well-to-Wheels analyses, e.g. the recently published report of the European Union [84].

Automotive applications need a lightweight and cost efficient storage system for hydrogen vehicles. Generally, the mileage is a key issue of nowadays techniques. Compressed gas in high-pressure vessels and cryogenic storage systems are field-tested while solid storage in organic compounds is still being researched. International research and development efforts are undertaken in order to reduce weight and cost of hydrogen storage systems, e.g. the integrated EU research project *StorHy* [82].

1.1.1   Combustion Characteristics of Hydrogen

Focussing on the development of an engine combustion process, hydrogen has unique combustion characteristics to achieve highly efficient and virtually zero emission combustion. The wide-flammability limits, the fast fuel conversion, the reliable ignition behaviour and the carbon-free combustion make hydrogen an ideal fuel for internal combustion engine applications.

Property	Unit	Hydrogen	Methane	Gasoline
Lower heating value	MJ/kg	120.0	50.0	45.0
Stoichiometric air fraction	kg_{air}/kg_{fuel}	34.3	17.2	14.7
Rich λ flammability limit[1,2]	-	0.2	0.7	0.4
Lean λ flammability limit[1,2]	-	10.0	2.1	1.4
Laminar flame speed [1,2,3]	m/s	2	0.4	0.4-0.8
Adiabatic flame temperature [2,3]	K	2390	2225	2275
Auto-ignition temperature[3]	K	858	813	~ 500
Minimum ignition energy[2,3,4]	mJ	0.02	0.29	0.24
Density [4]	g/l	0.09	0.72	730-780
Boiling temperature [5]	°C	-253	-162	25-215

[1] 1 bar, 300 K   [2] air   [3] $\lambda = 1$ [4] 1.013 bar, 273 K   [5] 1.013 bar

Table 1.1: Properties of hydrogen and hydrocarbon fuels, modified from [32, 45, 111].

Compared to hydrocarbon fuels, the flammability of hydrogen/air mixtures ranges between air/fuel equivalence ratios of $\lambda = 0.14$ and 10.5 while those of gasoline and methane are restricted to $0.4 \leq \lambda \leq 1.4$ and $0.7 \leq \lambda \leq 2.1$, respectively. Consequently, quality controlled engine operation in a homogeneous spark-ignited mode is feasible for a wide range of loads using hydrogen. Engine efficiency increases remarkably by de-throttling and lean operation at low engine loads. Homogeneous operation with $\lambda > 2$ reduces combustion temperatures below the formation temperature of thermal nitric oxides, resulting in virtually zero combustion emissions.

Further to the flammability limits, the laminar burning velocities of hydrogen remarkably differ from those of hydrocarbon fuels. Taking atmospheric conditions ($p = 1.013$ bar, $T = 293.15$ K) as reference, the laminar flame speed of stoichiometric hydrogen-air mixtures ($u_l = 2.65$ m/s to 3.25 m/s) is about seven times higher than the laminar flame speed of gasoline and methane ($u_l = 0.37$ m/s to 0.45 m/s). Even at lean conditions the flame speed is high enough to prevent efficiency losses caused by delayed combustion. In case of high-pressure hydrogen direct-injection an additional gain of the effective burning velocity due to an increased turbulence level can be obtained.

The easy ignitability of hydrogen-air mixtures shows a considerable reduction of cycle-to-cycle variation coefficients compared to gasoline engines enabling efficiency-optimised spark-timing settings.

The stoichiometric air requirement of hydrogen ($L_{stoic} = 34.3$ kg/kg) is slightly more than twice above that of gasoline fuels. The ratio of the lower heating caloric values of the two fuels, however, exceeds this value extensively. Assuming air-aspirating engines with equal charge, the mixture caloric value of the hydrogen engine will theoretically exceed the level of the gasoline type by 17 %. This outlines the benefit of direct-injection engines where the negative influence of air displacement effects, commonly known also from port fuel injection gas engines, is eliminated. The most important thermophysical properties of hydrogen are summarised and compared to properties of conventional hydrocarbon fuels in Table 1.1.

1.1.2 Mixture Formation Strategies for Hydrogen Engines

1.1.2.1 External Mixture Formation

Port fuel injection (PFI) describes a continuous or sequential injection of hydrogen into the intake duct where major parts of the mixture preparation are located outside the combustion chamber. Traditionally, hydrogen internal combustion engines have been realised by means of naturally aspirated premixed combustion systems using PFI. Phenomena, however, such as pre-ignition, knock and air-displacement effect of hydrogen engender low power output and low volumetric efficiency as well as instable engine performance accompanied by these engine concepts [116]. The disadvantages given by hydrogen port fuel injection engines may be overcome employing combustion engines with advanced hydrogen injection techniques, such as cryogenic port fuel injection. Using this technique, gaseous hydrogen is carried from a cryogenic storage system in isolated pipes to the intake duct where the mixing process with the aspirated air induces an increase of the mixture density through cooling. In stoichiometric operation with hydrogen, injection temperatures of $T = 45$ K and mixture temperatures of $T = 205$ K may be achieved which results in a theoretical increase of volumetric power density by about 40 % compared to ambient hydrogen port fuel injection. An additional positive effect of the cryogenic mixture formation is the significant reduction of combustion anomalies compared to ambient port fuel injection. Early investiga-

tions on cryogenic mixture formation beginning in the late 1970's have been conducted by a Japanese research group [37]. Recent investigations are performed at BMW Group Research and Technology [49]. For further details reference is made to work on cryogenic hydrogen engines, conducted in parallel in an associated research project [32, 45].

1.1.2.2   Internal Mixture Formation

The rapid progress in fuel direct-injection (DI) technology within the last decades also proved to be advantageous for hydrogen internal combustion engines. Similar to today's conventionally fuelled engines, modern injection technology facilitates direct-injection operation which dramatically increases the potential for engine design. State-of-the-art DI technology allows specific combustion characteristics to be arranged in hydrogen engines, e.g. fuel stratification and multiple injections of determined amounts of fuel. Depending on the injection strategy, the mixture formation of hydrogen high-pressure direct-injection engines is not restricted to premixed combustion as in PFI engines, but allows a combination of premixed, partially premixed and non-premixed diffusion-controlled flames. Phenomena such as pre-ignition and backfiring, generally known as disadvantages of PFI hydrogen engines, may be avoided by the use of hydrogen direct-injection.

While hydrogen cryogenic port fuel injection exploits the density increase of the aspirated hydrogen-air mixture via cooling, direct-injection avoids air displacement effects and thus results in increased charge load. The volumetric power density for direct-injection is enlarged by about 40 % compared to ambient hydrogen external mixture formation.

An important attribute that characterises different direct-injection modes is the level of hydrogen pressure supply. Variations of injection timings – as investigated in the present work – require a fuel mass flow which is almost independent from the counter pressure in the cylinder. This is only the case for high pressure direct-injection, when the ratio between injection pressure and counter pressure exceeds a critical ratio ($p_{H_2} \geq 150$ bar). Other hydrogen DI strategies where the hydrogen supply pressure is re-

markably lower and injection is limited to an early stage of the compression stroke are characterised as homogeneous modes.

Regarding fuel-mixture preparation, hydrogen high pressure direct-injection allows a variety of operation strategies. Air/fuel stratification as well as multiple injections of fuel are possible. This additional degree of freedom encourages hydrogen direct-injection as a suitable method for a selective arrangement of combustion based on the injection strategy. The injection timing directly influences the fuel-mixture preparation. Accordingly, the start of injection (SOI) is the most representative parameter for hydrogen DI. Different combustion modes have to be distinguished, depending on start, duration and quantity of fuel injections.

On the subject of single injection events, a premixed combustion regime, comparable to PFI, is present when fuel injection takes place at the beginning of the compression stroke, e.g. $SOI = -120°$ CA (with respect to top dead centre, TDC). In this case, large timeframes for the fuel/air mixture preparation are available. A partially premixed combustion mode may be obtained when timeframes for the fuel/air mixture preparation decrease, e.g. when the injection event occurs close to the end of the compression stroke (e.g. $SOI = -25°$ CA). The mixing timeframes and thus the degree of air/fuel stratification are directly related to SOI. The injection ends prior to spark ignition and, consequently, the combustion proceeds in a propagation-flame manner comparable to gasoline engines.

Operation with multiple injection events requires a distinction whether secondary injection takes place prior to or after ignition timing. The former type is referred to as propagation-flame combustion mode described above for single injection. In this mode, several injections may be used to improve either mixture homogenisation or stratification. Latter types result in a diffusion-flame combustion mode which is caused by fuel injection into the flame front of a previously generated spark ignited propagation flame. This mode, referred to as combustion control, is comparable to a combined gasoline/diesel engine type process (non-premixed, diffusion flame mode), accomplished by various discrete injection events [42]. The different portions of injected fuel may be expressed in terms of individual values of fuel/air equivalence ratio, e.g. ϕ_1 and ϕ_2 belong to the first

and second injection event. The global fuel/air equivalence ratio is then given by $\phi = \phi_1 + \phi_2$ $(1/\lambda = 1/\lambda_1 + 1/\lambda_2)$.

In addition to the increase in specific volumetric efficiency, high-pressure DI hydrogen combustion systems offer potential benefits regarding an increase in fuel efficiency due to reduced compression work. In stratified operation, a significant reduction of thermal nitric oxides emissions can be reported where combustion locally proceeds in rich zones. Several additional methods, such as water injection [98] and exhaust gas recirculation [48], in order to prevent combustion anomalies and to reduce nitric oxide emissions have been investigated, but are not further discussed here.

1.2 Review of Research Activities

Research on hydrogen combustion engines has a long tradition. Because of its special combustion characteristics hydrogen has always been of greatest interest as a fuel in the area of combustion engine research. First publications found on hydrogen internal combustion engines date back to the twenties of the last century, where Ricardo [101] investigated the effect of equivalence ratio on knock-limited engine operation. The suitability of quality controlled engine operation due to the wide flammability range of hydrogen was already pointed out. Abnormal combustion phenomena – such as pre-ignition and backfiring – led to the assumption that hydrogen was inapplicable for most uses. Erren and Oehmichen [33, 89] published results of several engines operated with low-pressure direct cylinder injection of hydrogen. Using cylinder injection of hydrogen, an improvement of the mixture formation process was achieved and combustion anomalies were reduced.

Substantial progresses in the development of hydrogen internal combustion engines after World War II were not noticed until the early seventies of the last century. Then, in 1973 – after the oil embargo – expectations about energy supply changed dramatically, resulting in the energy crisis. Consequently, intense programs on the investigation of alternative fuels,

in particular hydrogen, were launched within the following decades by industrial and public funds in Europe, the U.S. and Japan [35, 37, 90, 123]. A remarkably enhanced level of hydrogen engine technology was reached at this point, covering direct-injection, surface ignition, exhaust gas recirculation and supercharging.

Among many investigations performed within the last decade, a sequence of dissertation theses published at Technical University of Munich and University of Stuttgart are to be mentioned. Studies are conducted on the field of experimental hydrogen engine analysis [24, 29, 55, 97, 103, 117] and basic research is performed on combustion properties of hydrogen, related to engine operation [30, 62, 96].

A comprehensive survey on hydrogen research activities over the past decades may also be found in the reports of Homan [52], Das [28] and in the review published by White et al. [116].

The latest international consortium on hydrogen internal combustion engine research is the EU-funded project *HyICE*. With the objective of developing a new generation of clean and fuel-economic hydrogen car and bus engines, a cooperation between academic institutions, research centres and industry was formed in 2004 [1]. Recently launched hydrogen internal combustion engine vehicles are, e.g. series-production passenger cars of BMW Hydrogen 7-Series [42], city-busses provided by MAN Nutzfahrzeuge Group [99] and lightweight shuttle busses presented by Ford Motor Company [122]. Details on the engine designs of these vehicles may be found in the overview on hydrogen engine technology given below (Section 1.2.1). The state-of-the-art with regard to simulation and computation of hydrogen combustion engines, with special emphasis on turbulent combustion modelling of hydrogen, is separately discussed in Section 1.2.2.

1.2.1   State-of-the-Art: Hydrogen Engine Technology

Important individual studies on hydrogen fuelled engines and injection technology, not directly related to one of the research activities listed below, may be found in literature. Investigations with optical measurement techniques reported by Blotevogel et al. [18, 64], studies on hydrogen en-

riched gases reported by Conte [27] and developments of components for hydrogen injection reported by Koch et al. [61] and Bartunek et al. [12] should also be mentioned.

1.2.1.1　BMW Group, Germany

Already in 1978 BMW started to research on hydrogen engines and presented several prototype vehicles within the following years. Actually, a naturally aspirated 6 litre 12-cylinder engine driving the BMW Hydrogen 7-Series is equipped with sequential external mixture formation. The dual-fuel engine is supplied with a three-way-catalyst reducing nitric oxides in stoichiometric operation. Leaner-than-stoichiometric operation is limited to loads which result in combustion temperatures below the formation temperatures of nitric oxides. Due to the air-displacement effect the overall power output of this engine is limited to $P = 161$ kW. In a modified mono-fuel version of this engine, employed in the hydrogen record car H2R, the power output is increased to $P = 210$ kW.

Further to the hydrogen engine series development research, efforts are undertaken to improve the combustion process by means of alternative mixture formation strategies, e.g. cryogenic port fuel injection, high-pressure direct-injection and supercharged spark ignited hydrogen engines [16]. Investigations are carried out on a one-cylinder research engine with a typical displacement of $V = 0.5$ litre and a bore of $b = 84$ mm. Adjustable compression ratios range between $\epsilon = 9$ and 13.5.[1] Cryogenic port fuel injection reduces combustion anomalies and engine performance is significantly increased [49]. Regarding direct-injection, homogeneous and stratified mixture formation as well as multiple injections are investigated. A gain in specific engine power density is reported up to $P \approx 100$ kW per litre displacement. The indicated engine efficiency is increased up to $\eta_i \gtrsim 42$ %. A survey of the capabilities of hydrogen engines on the basis of the corresponding research results is given in the report of Gerbig et al. [38] and Grabner et al. [44]. Efforts regarding numerical simulation of hydrogen mixture formation and combustion are undertaken for both PFI and DI engines [32, 39, 40, 45].

---

[1]The specified research engine is used for experimental analysis of the present work. A detailed description on the engine parameters is given in Section 2.1.

1.2.1.2   MAN Nutzfahrzeuge Group, Germany

Hydrogen fuelled four-stroke spark-ignition engines are investigated as propulsion systems for city busses by MAN Nutzfahrzeuge Group. A large-displacement 6-cylinder in-line engine with a bore of $b = 128$ mm and an overall displacement of approximately $V = 12.8$ litre is equipped with a turbocharger. The target power output at lean operation ($\lambda \geq 2$) and an engine speed of $n = 2000$ rpm is $P = 200$ kW. The compression ratio is $\epsilon = 11$. A homogeneous mixture formation is achieved by low pressure direct-injection with start of injection at the beginning of compression stroke. The engine is designed to conform to emission standards (EU 5) without aftertreatment [99].

1.2.1.3   Ford Motor Company, USA

At Ford Motor Company, a 6.8 litre V-10-cylinder engine is used for propulsion of a series of lightweight shuttle busses. The engine is equipped with a twin screw compressor resulting in a maximum power output of $P = 175$ kW at $n = 4000$ rpm. Mixture preparation is accomplished by sequential port fuel injection. The engine is operated at homogenous mixtures in lean mode without aftertreatment [122]. Additionally, investigations on small-scale passenger car engines are conducted in the Ford Scientific Research Laboratories and at University of California at Riverside. Detailed studies on engine operating strategies of a hydrogen port fuel injection 2-litre 4-cylinder hydrogen engine are performed with respect to an increase of engine efficiency and reduction of nitric oxide emissions using exhaust gas recirculation [48, 107].

1.2.1.4   Technical University of Graz, Austria

In addition to fundamental research on thermodynamic single-cylinder engines, investigations are carried out on an engine that features optical access through a quartz-glass liner and a window in the piston. Applying the method of Planar Laser Induced Fluorescence (PLIF), the hydrogen/air mixture formation process and the propagation of the flame front during

combustion can be measured. Investigations on hydrogen injection strategy and injector nozzle-geometry are performed for both port fuel and direct-injection mixture formation [59,60]. The optical results are used for a further development of the hydrogen combustion process and also act as basis for the verification of CFD-simulations within the present work (see Section 6.1). Dissertation theses on hydrogen direct-injection engines have been published at TU Graz within the last years with focus on experimental investigations of injection strategies [113] and optical analysis [59]. Numerical analysis is performed in terms of engine cycle simulations in order to perform global prediction of heat release [118]. Detailed three-dimensional computations of the mixture formation and combustion [63, 73, 74] are performed on the commercial CFD solver FLUENT. Regarding combustion modelling, a turbulent flame speed closure approach is applied.

1.2.1.5 Argonne and Sandia National Laboratories, USA

At Argonne National Laboratories several experimental studies on hydrogen engines are conducted in close collaboration with Ford Motor Company. The influence of injection timing as well as different nozzle geometries of direct-injection engines are analysed [114] by means of OH-chemiluminescence through UV-endoscopic investigations. Benefit of the endoscopic technique is that two-dimensional results are provided while the engine operation range is not restricted by pressure limitations. Details regarding inhomogeneities of the engine combustion process can be recognised. It is observed that for significantly lean air/fuel equivalence ratios ($\lambda > 2$) the OH-intensity is too weak to be detected by the endoscope.

At Sandia National Laboratories investigations on a transparent hydrogen research engine are performed in order to analyse the influence of injection variations on the mixture formation process. Prior to combustion, the mixture distribution is visualised by means of Planar Laser Induced Fluorescence (PLIF), using acetone as a tracer. During combustion, OH-chemiluminescence is employed to evaluate the mixture distribution. The results confirm that the pressure and timing of injection as well as the noz-

zle geometry and location of the injector are important parameters for the mixing process [116].

1.2.1.6   University of Ghent, Belgium

Investigations at University of Ghent cover experimental operation and analytic research of hydrogen internal combustion engines. Examinations on external mixture formation are conducted on a 7.4 litre V-8-cylinder engine with a compression ratio of $\epsilon = 8.5$ and a Cooperative Fuel Research (CFR) engine with adjustable compression ratio. Variations on injection timing, injector inlet geometries and spark timing are studied [111]. The experimental results are used in order to validate engine cycle simulations. Essential work is provided in the determination of hydrogen laminar burning velocities by combustion bomb measurements, as further described in Section 5.2.4.

1.2.1.7   Hydrogen Research Institute, Canada

The Canadian Hydrogen Research Institute focuses on investigations regarding storage, safety and the use of hydrogen, e.g. fuel cells and hydrogen internal combustion engine applications. Regarding internal combustion engines, measurements of converted commercial car engines are conducted with attention on injection systems, combustion anomalies, fuel-efficiency and exhaust emissions [2].

1.2.2   State-of-the-Art: Hydrogen Turbulent Combustion Modelling

Numerical analysis of turbulent reactive flows is employed and developed in many fields of conventionally fuelled internal combustion engine applications. On the subject of gasoline and diesel engines, modelling of two phase flows and turbulent spray combustion are the main fields of activity, e.g. the investigations of [26, 47, 91, 120]. The present work outlines recent hydrogen engine simulation activities and hydrogen combustion

modelling. Investigations focussing entirely on fundamental combustion properties of hydrogen, e.g. the laminar flame speed, are discussed in detail in Chapter 5. A survey on elemental methods of turbulent combustion modelling is given in the compendium of Poinsot & Veynante [94].

Several investigations on hydrogen engine simulation not related to the research activities listed below may be found in literature: Liu [69] reported on studies of the capability of commercial CFD codes to compute supersonic hydrogen injection. Simulations of the mixture formation with different injector nozzles are performed on a simplified engine geometry. A sensitivity study on various combustion models, provided in the CFD Code FIRE, is performed on the basis of academic test cases. Errico et al. [34] conduct simulations of heat release predictions of a PFI hydrogen engine using a fractal-based model in engine-cycle-simulations.

1.2.2.1 University of Armed Forces Munich, Germany

Within the *HyICE* research project a contribution to a model on the basis of a turbulent flame speed closure is performed, initially proposed for premixed gas combustion by Zimont and Lipatnikov [124]. The investigated combustion model combines a reaction progress description with an empirical approach for the burning velocity and is linked to a flamelet library. The correlation for the turbulent flame speed includes the laminar flame speed, which is generally related to premixed combustion. Referring to direct-injection hydrogen engines, an extension for diffusion and partially premixed flames is presented where pressure and temperature dependent flammability limits are considered by introducing a presumed probability density function for the mixture fraction dependence of the laminar flame speed. In order to represent unsteady conditions during combustion in reciprocating engines, the model is enhanced to account for variable enthalpy and pressure. The modifications are validated by experimental measurements of a non-premixed hydrogen jet flame [112]. In the present work, parts of the model are evaluated for hydrogen direct-injection applications (see Chapter 7). Details on the theory of the model are given in Section 4.3.1.

1.2.2.2   Institut Francais du Petrole (IFP), France

Combustion models for three-dimensional simulation of spark ignition combustion engines are developed and applied. Recent investigations concern computation of partially premixed turbulent combustion of highly stratified gasoline engines. A flame surface density approach is augmented by a variance/scalar dissipation model in combination with a presumed probability density function to account for stratification effects. The model, also referred to as Extended Coherent Flame Model (ECFM), is validated by experimental measurements on a single cylinder research engine [26]. Concerning hydrogen engine applications, the existing ECFM model is adapted to hydrogen combustion. The improvements include the addition of laminar propagation and preferential diffusion effects in the production of the flame surface density, considering stretch effects on the laminar flame speed and the addition of a model for the flame thickness calculation [15]. Modifications, accounting for hydrogen specific combustion, are adapted to the model within the framework of the associated international research project *HyICE* and are available within the present work. Details on the theory of the model are defined in Section 4.4. An evaluation of the model and a comparison to results of alternative modelling approaches is given in Chapter 7.

1.2.2.3   Los Alamos National Laboratories, USA

Beginning in the late 1950's fundamental contributions on CFD-methods have been made at Los Alamos National Laboratories. Since the 1980's early investigations on the modelling of chemically reactive flows in combustion engines have been carried out developing the three-dimensional flow solver KIVA [10]. In the mid 1990's first investigations on the simulation of hydrogen-fuelled engines are reported by Johnson et al. [54]. Three-dimensional computations of the gas exchange and the subsequent compression and combustion of hydrogen are conducted on simplified hexahedral meshes (approximately 40.000 cells) of a single-cylinder research engine geometry. The necessity of modelling the intake flow on the prediction of combustion rate and nitric oxides emissions is demonstrated

by a comparison with computations of compression and combustion of a quiescent hydrogen-air mixture. Regarding combustion modelling, a reactive kinetic model is applied. Hydrogen oxidation is described by a single forward kinetic equation with Arrhenius temperature dependence. The effect of turbulence on combustion is computed by using a mixing controlled model on the basis of the proposals made by Magnussen and Hjertager [70]. Values for hydrogen laminar flame speed are obtained by an adjustment of parameters in the single step oxidation kinetics in order to reproduce flame speed data proposed by detailed chemical mechanism.

Currently, numerical studies on Large Eddy Simulation (LES) of hydrogen mixture formation and combustion are performed at Sandia National Laboratories [88]. A tabulated combustion closure based on a Linear Eddy Model is applied, which solves one-dimensional reaction-diffusion equation over entire length scales of turbulence and chemistry and may predict local extinction and re-ignition behaviour. The scheme proposed by Conaire et al. [86] – also employed in the present work – is taken as a detailed hydrogen-air kinetics mechanism. Ongoing investigations focus on the computation of an optical research engine including the prediction of pollutant formation.

1.2.2.4 University of Leeds, GB

Investigations on premixed turbulent flames are performed to obtain models for correlating turbulent burning velocities to laminar flame speed, turbulent quantities and physical-chemical quantities. Corresponding correlations may be used for turbulent flame speed closure of premixed CFD combustion models, e.g. the equation proposed by Bradley et al. [22] which is also investigated within the present work (see Section 4.3.2 for a description of the model and Chapter 7 for computational results). Being part of the investigated combustion models, fundamental studies on laminar burning velocities are conducted. Using spherical explosion bomb measurement techniques, flame speeds of hydrogen-air-mixtures for stoichiometric and leaner-than-stoichiometric values of equivalence ratio are obtained at pressures up to $p = 10$ bar [23]. Procedures, based on flame

instability theory, in order to derive corresponding laminar burning velocities are examined and measured values are compared with results of detailed chemical schemes. Correlations on laminar burning velocities at elevated pressure conditions are presented in the work of Verhelst [111], cf. Section 5.2.4.

1.3   Motivation and Objectives of the Present Work

Hydrogen DI engines offer a wide range of options for combustion design, such as fuel stratification and multiple injections. Previous experimental studies show a substantial potential of hydrogen direct-injection engines as virtually zero emission and highly efficient combustion systems for automotive propulsion systems [16, 38, 44, 113]. The complexity of hydrogen direct-injection operation, however, requires a fundamental knowledge about the in-cylinder processes. An analysis of global data may promote an overall understanding of hydrogen DI combustion. It is obvious, however, that information on local fuel preparation and conversion is of main importance for the optimisation of the process. For this reason, methods of computational reactive fluid mechanics are consulted. A view inside the phenomena of a hydrogen engine may be acquired by the application of advanced development methods such as optical experimental methods and numerical analysis in terms of three-dimensional Computational Fluid Dynamics (CFD). Optical experimental methods on hydrogen engines are investigated by means of Planar Laser Induced Fluorescence (PLIF) in different works [17, 18, 59, 60, 64] and are already developed to a level that they can be productively used in engine research. Regarding three-dimensional numerical simulation of hydrogen engines, most former studies only affect issues on preparation of the cold mixture while the prediction of heat release, especially for direct-injection, is still an open subject [32, 45, 63, 74].

One objective of the present work is to obtain a deepened understanding of mixture formation and energy conversion by the application of three-dimensional numerical simulation. The goal is also to establish a basis for recommendations regarding an optimisation of the combustion concept.

A challenge of combustion engine simulation is the suitability of the numerical models to predict heat release for a wide operation range. While considerable research efforts are undertaken on the development of combustion models and mixing models for conventional gasoline and diesel engines [26, 47, 91], corresponding models for hydrogen engines have not yet been comprehensively investigated [45, 69, 74]. Consequently, as a second objective of the present work, different types of turbulence models and newly developed combustion models are examined in single-cylinder engine simulations in order to estimate the suitability of a predictive computation of the hydrogen-air mixing and combustion process of premixed, partially premixed and non-premixed combustion modes that occur in hydrogen direct-injection engines. The applied CFD code is a modified version of the three-dimensional flow solver ANSYS CFX [36], based on combustion models developed within the framework of the European Research Project *HyICE* [15, 112]. Numerical results are validated by means of experimental data of optical and thermodynamic research engines. To evaluate the influence of laminar flame speed on the effective burning velocity, results of in-cylinder combustion with different assumptions for the laminar flame speed are compared.

The third objective of the present work – as a contribution to the development of hydrogen engine combustion models – focuses on the evaluation of hydrogen burning velocities at engine-relevant conditions. Fundamental data on laminar hydrogen flame speed are the key input parameter of the investigated combustion models. Corresponding experimental values at engine-relevant conditions are only partially available in literature. As a consequence, experimental investigations on premixed hydrogen flames are conducted on a single-cylinder compression machine. Optical and thermodynamic measurements of the flame speed provide a database of laminar burning velocities to be used for hydrogen engine applications.

Chapter 2

Subject of Investigation

2.1 Description of Hydrogen Research Engines

The present study employs two types of hydrogen research engines for CFD validation purposes: A thermodynamic research engine for the measurement of global data and a transparent research engine for optical measurements of hydrogen concentration. The specifications of both engines and a definition of engine operating points are presented in the following.

2.1.1 Thermodynamic Research Engine

Measurements of indicated traces and exhaust gas analysis are conducted on a hydrogen direct-injection research engine test bed [43, 113]. The intention of the analysis is to produce experimental data for a validation of simulation results.

2.1.1.1 Engine Specifications

Subject of investigation is a 4-valve spark-ignition single-cylinder research engine with $V = 0.5$ litre displacement, $b = 84$ mm bore and $l = 90$ mm stroke. The compression ratio may be adjusted in the range between $\epsilon = 9.0$ and 13.5. In-cylinder pressure is limited to $p = 150$ bar. Maximum engine speed is $n = 7000$ rpm. In aspirated direct-injection mode an increase in full load IMEP of 45 % with respect to ambient port fuel injec-
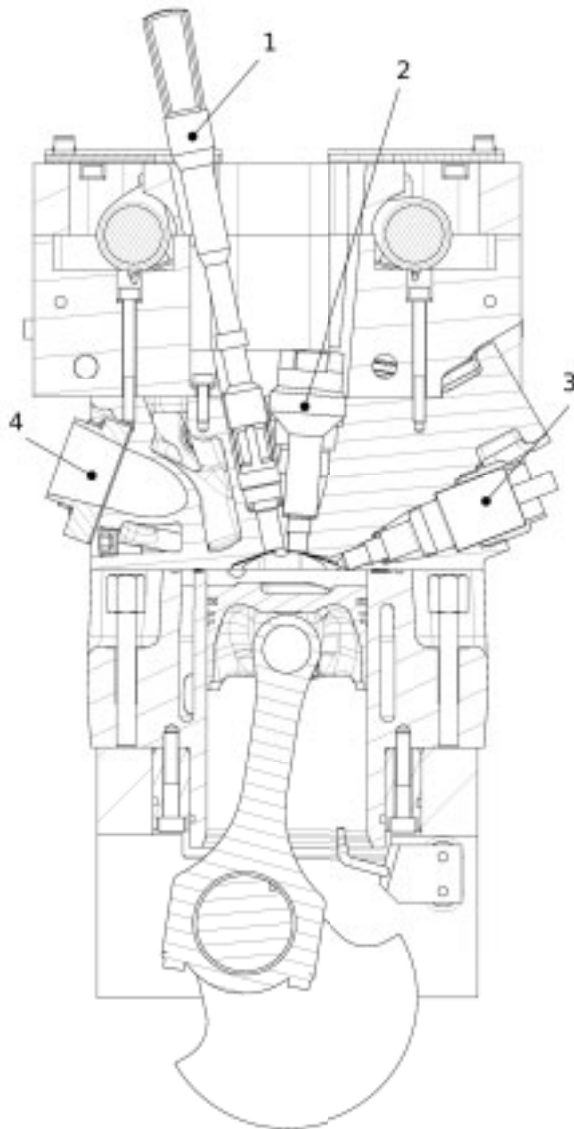
Research engine specifications:

Engine type	Single-cylinder,
	4-stroke,
	Water cooled,
	Spark ignited
Bore / Stroke	84 mm / 90 mm
Displacement	498.8 cm^3
Compression	$9.0 \leq \epsilon \leq 13.5$
Max. speed	7000 rpm
Cylinder pressure	150 bar, max
Valve train	4 valves, DOHC
	Toothed belt
	Hydraulic tappets
	Bi-Vanos
Valve timing	
Std. spread	110° CA / 110° CA
Inlet	34 BGTDC / 126 BITDC
Exhaust	106 AITDC / 14 AGTDC
Valve lift max.	
Inlet	9.7 mm
Exhaust	9.7 mm
Lubrication	Dry sump
Cylinder liner	Wet
Mass comp.	First order

1: Spark plug

2: Central injector dummy

3: Lateral injector

4: Exhaust duct

Figure 2.1: Single-cylinder thermodynamic research engine employed for CFD valida-
tion purposes in a cross sectional view and engine specifications.

tion is observed. Additionally, the range of maximum engine efficiency
($\eta_i \geq 42\,\%$) is significantly increased in comparison to PFI. In supercharged
operation, a maximum specific power density near $P = 100$ kW per litre
displacement at stoichiometric conditions and $n = 5000$ rpm is demon-
strated [44].

Concerning hydrogen injection, a configuration with a piezo activated high-
pressure gas injector in a lateral position is examined. The injector nozzle
geometry features eight holes with a diameter of $d = 0.4$ mm each, result-

ing in a geometric flow area of $A = 1 \text{ mm}^2$. The supply pressure of hydrogen is $p = 150$ bar which allows shortened injection duration due to the increased density of high pressure gas and permits wide limits of injection timing, e.g. injection into the compressed charge at the end of compression stroke. The maximum steady hydrogen mass flow is $\dot{m} = 6.5$ g/s. An alternative configuration where the injector is positioned centrally inside the cylinder head is investigated in attendant studies [43, 59, 73, 102], but is not considered within the present work. The spark plug is located in the centre of the combustion chamber. Information on engine specifications and a cross sectional view of the engine is given in Figure 2.1.

2.1.1.2   Thermodynamic Engine Operating Points for CFD Validation

The measurements performed on the thermodynamic research engine are intended to validate heat release predictions of the investigated combustion models. Operating points are defined for various levels of equivalence ratio and degrees of mixture homogenisation, covering premixed, partially premixed and non-premixed combustion modes. Injection timings are varied for stoichiometric operation in three steps, namely $SOI = -120°$, $-60°$ and $-25°$ CA resulting in homogenous, stratified and highly stratified air-fuel mixtures. Corresponding local values of equivalence ratio in the stratified case extend to the ignition limits. Homogeneous leaner-than-stoichiometric operation is realised with direct-injection at $SOI = -120°$ CA and global air/fuel equivalence ratios of $\lambda = 2.4$. Since direct-injection significantly influences the level of turbulence kinetic energy, additional operation points for premixed mixtures in PFI mode are arranged, where turbulence is largely determined by the gas exchange process, i.e. intake-generated turbulence. Non-homogeneous combustion is analysed by means of multi-injections, where in a second injection fuel is directly supplied into the flame front. Corresponding parameters of the operating points are summarised in Table 2.1, labelled as D1 to D5 and P1 to P3 for the direct-injection and port fuel injection engine, respectively. Experimental and numerical results are compared in Chapter 7.

Thermodynamic engine operating points:

No.	Inj.	Mixture type	λ_{global}	Inj. start	Inj. duration	Spark timing	IMEP
			-	° CA	° CA	° CA	bar
D1	DI	Homogeneous	1.0	-120	30	4.0	11.86
D2	DI	Stratified	1.0	-60	30	3.5	11.86
D3	DI	Highly stratified	1.0	-25	30	5.0	11.08
D4	DI	Homogeneous	2.4	-120	15	-11.0	5.91
D5	DI	Multi-Injection	1.0	-120 / -5*	15 / 17.5*	-13.0	10.00
P1	PFI	Homogeneous	1.0	340	68	-2.7	9.22
P2	PFI	Homogeneous	1.2	340	62	-2.0	8.05
P3	PFI	Homogeneous	1.8	340	46	-11.8	6.01

* value of first/second injection.

Table 2.1: Operating points of the thermodynamic research engine to be used for validation of three-dimensional computations of heat release. The investigated engine speed is $n = 2000$ rpm and the compression ratio is $\epsilon = 10.5$ for all measurements. Values of CA are given with respect to TDC.

2.1.2   Transparent Research Engine

While the thermodynamic research engine provides measurement of temporal evolution of cylinder pressure and exhaust gas analysis, optical measurements are carried out on a transparent version of the research engine that allows optical access to the combustion chamber. Experimental results on the basis of Planar Laser Induced Fluorescence (PLIF) are used within the present work to validate the highly turbulent mixing process computed with CFD, e.g. to verify the influence of different turbulence models on mixture formation by comparison of computed hydrogen concentrations to values obtained from optical experiments.

2.1.2.1   Engine Specifications

The engine is equipped with a quartz glass cylinder liner of $h = 44$ mm height located below the cylinder head and an additional quartz glass window embedded in the piston. The glass cylinder is shaped in line with the contour of the cylinder head dome in order to achieve a maximum side visibility of the area around the spark plug and the injector nozzle. An optimized illumination of the combustion chamber is obtained by splitting the laser beam into two single beams passing separately through the glass ring and the piston-window. A vertical light sheet is produced
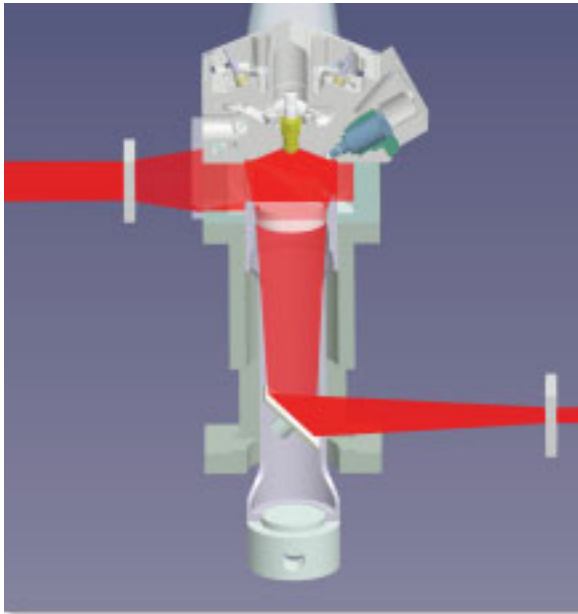
Transparent engine specifications:	
Engine type	Single-cylinder, 4-stroke, Spark ignited
Bore / Stroke	86 mm / 86 mm
Displacement	499.6 cm^3
Compression ratio	$\epsilon = 9.1$
Max. speed	2000 rpm
Cylinder pressure	60 bar, max.
Glass liner height	44 mm
Fuel tracer	Triethylamine (TEA) 200 ppm
LIF Laser System	KrF-Excimer laser, 248 nm
Camera System	LaVision Imager 3s CCD

Figure 2.2: Specifications of transparent research engine and engine model with laser beams passing through the glass ring and the piston window separately. Results of PLIF measurements are used for validation of CFD calculations.

which incorporates the cylinder axis and is positioned perpendicular to the crankshaft. The illuminated plane includes the lateral injector position and the location of the spark plug, cf. Figure 2.2. Using the glass window as optical access of the CCD camera, the visualisation of a horizontal light-section below the cylinder head gasket is possible.

To assure compatibility of results between both types of engines, the transparent research engine features approximately the same geometric properties as the thermodynamic research engine. As restriction, the engine speed of the transparent engine is limited to $n = 2000$ rpm, the compression ratio is $\epsilon = 9.1$ and the maximum in-cylinder pressure is $p = 60$ bar. The geometrical properties of the optical and thermodynamic research engine are comparatively identical.

To visualise hydrogen distribution during the mixture formation process, a tracer substance has to be admixed to the fuel. Hydrogen applications require particular transport properties of the tracer so that demixing may be avoided. Following the considerations of Blotevogel et al. [17], Triethylamine (TEA) is chosen as a suitable tracer substance. The tracer can be

Transparent engine operating points:

No.	Inj.	Mixture type	λ_{global}	Inj. start	Inj. duration	Spark timing	IMEP
			-	° CA	° CA	° CA	bar
O1	DI	Homogeneous	2.4	-120	20	-7.0	4.5
O2	DI	Stratified	2.4	-45	20	-7.0	4.0

Table 2.2: Operating points of the transparent research engine to be used for valida-
tion of three-dimensional computations of mixture formation. The investi-
gated engine speed is $n = 2000$ rpm and the compression ratio is $\epsilon = 9.1$
for all measurements. Values of CA are given with respect to TDC.

excited by laser light at a wavelength of $\lambda = 248$ nm using a Krypton-
Fluoride (KrF) excimer laser. The fluorescence signal of the tracer is rec-
orded with a CCD-camera allowing a quantitative determination of hydro-
gen concentration. Regarding the visualisation of the combustion process
either excitation of OH-radicals or tracer-measurements are employed.

With regard to the first method, the passing flame front is detected by
OH-fluorescence. Concerning the latter method, the unburned zone is vi-
sualized by tracer-fluorescence while in the burned zone the tracer is con-
sumed by the flame and thus becomes invisible. Experiments are aver-
aged over 50 cycles for comparison with CFD-results in terms of Reynolds
Approximated Navier-Stokes (RANS). Due to thermal restrictions the en-
gine is limited to about 200 cycles in fired mode. The optical experimental
investigations are performed in an associated work [59, 60] where a de-
tailed description of the applied PLIF measurement technique is noted.

2.1.2.2   Transparent Engine Operating Points for CFD Validation

As a reference for validation of CFD results a homogeneous and a stratified
operating point is defined: Firstly, a homogeneous mixture where the start
of injection is located right after intake valve closing (early injection) and
secondly, a stratified mixture where injection starts close to TDC (late in-
jection). Corresponding engine parameters are listed in Table 2.2 labelled
as operating points O1 and O2. CFD simulations of homogeneous and
stratified mixture types will be conducted and set side by side with the op-
tical results, including the evaluation of different turbulence models. The
comparison is being discussed in Section 6.1. Although flame propagation

measurements are conducted on the transparent engine, it is discerned that a validation of computed heat release on the thermodynamic engine is preferred because boundary conditions are more stable (e.g. lower blow-by rates, no cycle restrictions by thermal limitations, wall temperatures).

2.2   Thermodynamic Research Engine Measurements

In order to improve the understanding of the investigated engine's operating behaviour, the performed experimental measurements are outlined. As described in Section 1.1.2, high-pressure hydrogen DI offers a wide range of possible operating strategies. The injection strategy has the main impact on local hydrogen distribution, insofar as the degree of air/fuel stratification is strictly related to the start of injection (*SOI*).

The influence of a variation of injection timing on engine performance is investigated for a wide range of equivalence ratios, as defined in Table 2.1. The impact of different *SOI* on nitric oxides (NO) formation, amount of unburned hydrogen and indicated efficiency is discussed in the following.

2.2.1   Nitric Oxides Formation

A very sensitive criterion regarding an assessment of the degree of local mixture stratification is the amount of raw nitric oxides emissions. Since this quantity is easy to determine by measurements, it is predestined as an index for the homogeneity of the mixture. During hydrogen combustion thermal nitric oxides are formed by thermal dissociation and oxidation of nitrogen when a critical formation temperature is reached. The formation process corresponds to the analogy known as Zeldovich mechanism.

Considering a perfectly stirred hydrogen-air mixture, above a certain air/fuel equivalence ratio ($\lambda_{NO,limit} \approx 2$), no nitric oxides are formed, since combustion temperature is below the nitric oxides formation temperature ($T \approx 1800$ K). With respect to values of air/fuel equivalence ratio below $\lambda_{NO,limit}$, nitric oxides increase while reaching a maximum at
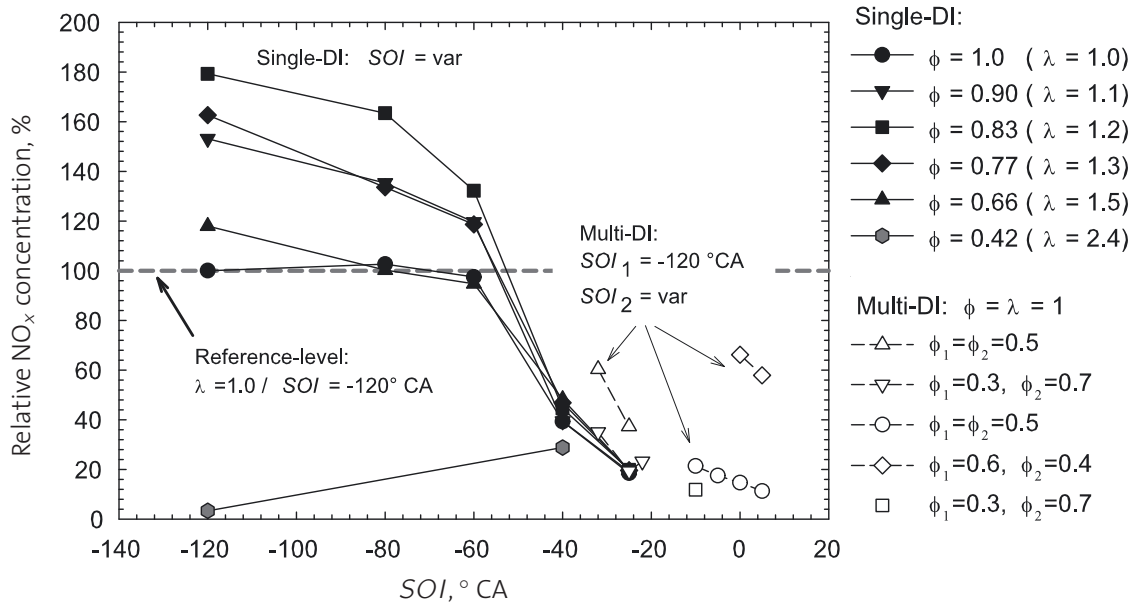
Figure 2.3: Measured concentrations of nitric oxide as a function of *SOI* in direct-injection operation at $n = 2000$ rpm. Closed symbols: Operating points with single injection. Open symbols: Multi-injection points ($SOI_1 = -120°$ CA, SOI_2: x-axis).

$\lambda_{NO,max} \approx 1.2$. Air/fuel equivalence ratios below $\lambda_{NO,max}$ cause reduction of nitric oxides due to reduction of the limiting reactant oxygen. The exact value of $\lambda_{NO,limit}$ in IC engines is affected mainly by the compression ratio, the spark timing, charge load and local inhomogeneity of the mixture.

Measurements on the research engine of dry exhaust gas nitric oxides are depicted as a function of injection timing for varying loads in Figure 2.3. A comparison is given for both single injection and multiple injection events. Spark ignition timing is set to optimal mean effective pressure for each operation point.

Regarding single injection, a significant decrease in NO_x-concentrations between $\lambda = 1$ and 1.5 ($\phi = 1$ and 0.66) is observed when the start of injection is relocated towards TDC, while for $\lambda = 2.4$ ($\phi = 0.42$) the concentration increases. For global values of $\lambda \leq 1.5$ ($\phi \geq 0.66$) this effect may be explained by the fact that due to shortened mixing timescales stratification occurs where parts of the fuel are burned as a rich mixture and nitric oxides production is reduced due to the lack of oxygen. The remaining fuel is burned as a lean mixture below the nitric oxides formation temperature. Depending on the degree of stratification, the overall amount of nitric oxides accordingly drops below the level of those for the homogeneous case

with corresponding global equivalence ratio. Operating points with global values of $\lambda > 1.5$ ($\phi < 0.66$) show an increase of nitric oxides for cumulative stratification compared to the homogeneous case. Here, stratification causes a shift of local air/fuel equivalence ratio λ from lean towards stoichiometric values, resulting in combustion temperatures above the nitric oxides formation temperature. With respect to engine injection strategies, stratification may be useful to lower NO_x-concentrations for global values of $\lambda \leq 1.5$ ($\phi \geq 0.66$), whereas for leaner mixtures the most suitable homogenisation should be acquired.

With respect to global stoichiometric operation, by using multiple injection even lower levels of NO_x-concentrations may be reached, depending on the location of the first and second injection event and the ratio of fuel proportioning of each injection. The different portions of injected fuel are expressed in terms of individual values of fuel/air equivalence ratio, e.g. ϕ_1 and ϕ_2 belong to the first and second injection event. The global fuel/air equivalence ratio $\phi = 1/\lambda$ is then given by $\phi = \phi_1 + \phi_2$. The mass of injected fuel may be split in three different types of proportioning: Fuel/air equivalence ratios of $\phi_1 = \phi_2$, $\phi_1 > \phi_2$ and $\phi_1 < \phi_2$. The lower the value of ϕ_1, the leaner is the premixed part of combustion. Consequently, the amount of NO_x produced by premixed combustion is reduced. Regarding $\phi_1 < 0.5$ ($\lambda_1 > 2.0$), NO_x formation generated by premixed combustion may almost be neglected in conjunction with a second injection. It may be derived from the measured NO_x-concentration that engine operation with secondary injection before spark ignition – due to the premixed part of the first injection event – always results in minor stratification compared to an equivalent single injection operation. Secondary injection after spark ignition includes substantial amounts of non-premixed combustion and shows the slightest NO_x-concentration of all injection strategies investigated.

2.2.2 Unburned Hydrogen in the Exhaust

Another criterion for the assessment of the mixture quality is the amount of unburned hydrogen which is measured in the exhaust gas. According
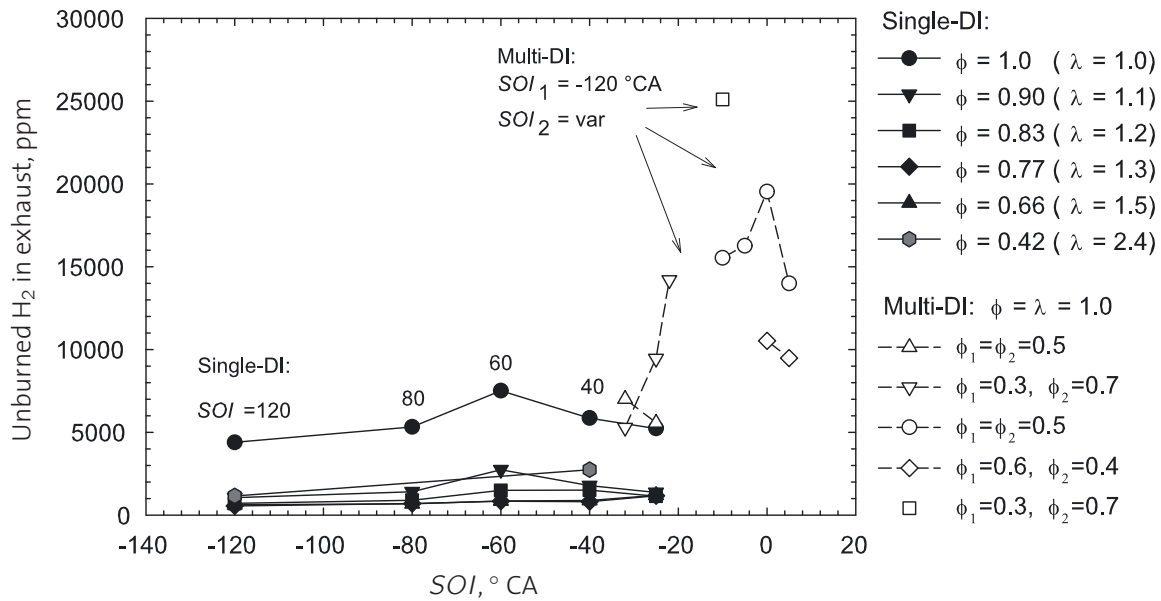
Figure 2.4: Measured concentrations of unburned hydrogen as a function of *SOI* in direct-injection operation at $n = 2000$ rpm. Closed symbols: Operating points with single injection. Open symbols: Multi-injection points ($SOI_1 = -120°$ CA, SOI_2: x-axis).

to Figure 2.4, the amount of unburned hydrogen gradually increases with delayed *SOI*. At $SOI = -60°$ CA the level is locally inflated which demonstrates the poor mixture preparation of this configuration. In multi injection mode generally the highest levels of unburned hydrogen are measured, where approximately 2.5 % of the fuel remains unburned.

2.2.3   Indicated Efficiency

The dependence of indicated efficiency on injection timing is displayed in Figure 2.5. Results for air/fuel equivalence ratios from $\lambda = 1.0$ to 2.4 are compared at $n = 2000$ rpm. The indicated efficiency increases for higher values of global air/fuel equivalence ratio λ due to an increased expansion stroke work for leaner mixtures. With respect to stoichiometric operation, the influence of injection timing demonstrates a trend of increasing efficiency for delayed injection timings from $SOI = -120°$ towards $-60°$ CA and a decrease in efficiency for later *SOI*. Two contrary effects are the determining factors for this behaviour: First, a reduction in compression work increases the efficiency for delayed injection timings; second, locally premixed fuel-rich zones are generated which cause a reduction of the
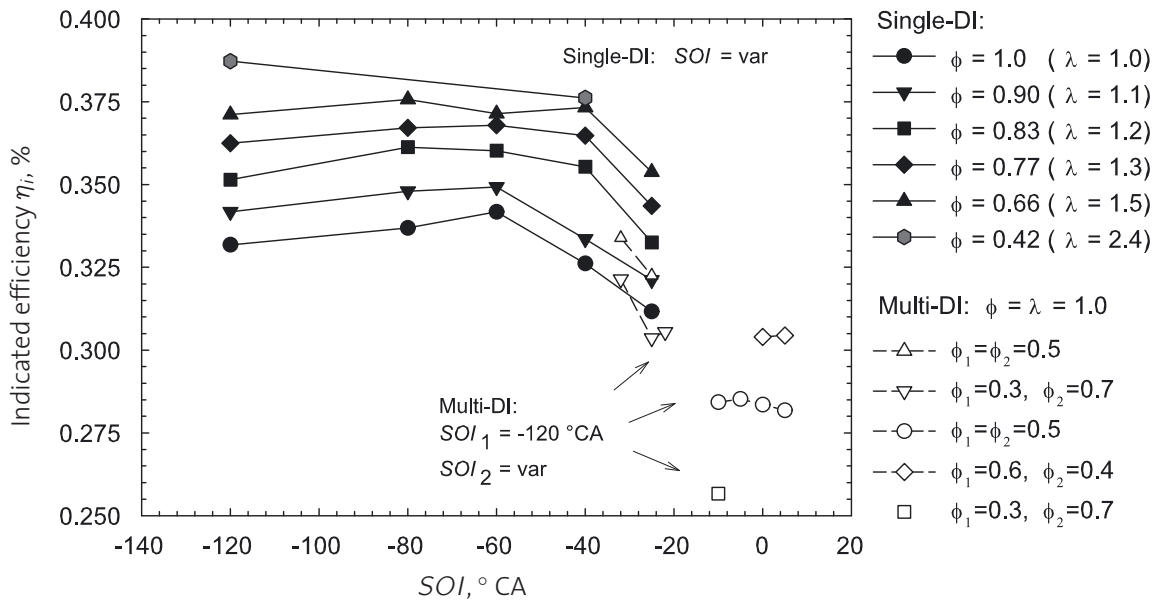
Figure 2.5: Measured indicated efficiency as a function of *SOI* in direct-injection operation at $n = 2000$ rpm. Closed symbols: Operating points with single injection. Open symbols: Multi-injection points ($SOI_1 = -120°$ CA, SOI_2: x-axis).
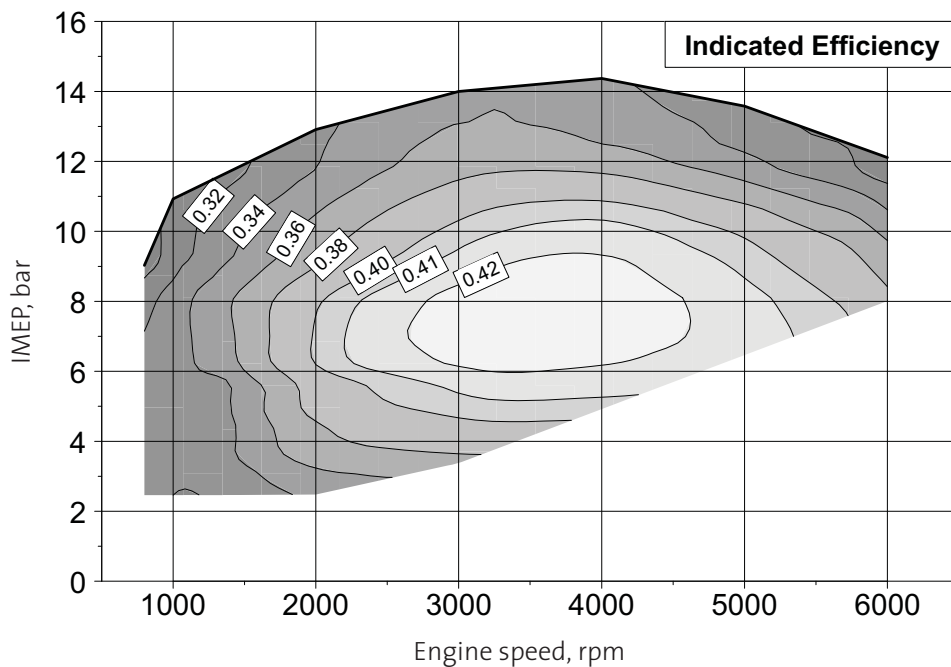
Figure 2.6: Measured map of indicated efficiency in direct-injection operation with $SOI = -120°$ CA, compression ratio of $\epsilon = 10.5$ and $n = 2000\ rpm$, modified from [44]. Measurements at low engine loads and high engine speeds are not available.

fuel conversion rate. Delayed injection timings with $SOI = -25°$ CA and multi injection operating points show the lowest efficiency due to diffusion type flames which significantly increase the burning duration. In Figure 2.6 the map of indicated efficiency is illustrated for the entire operation range of the research engine with $SOI = -120°$ CA. The maximum value derived from pressure traces is $\eta_i = 42\,\%$ being reached within a range of IMEP from $p = 6$ bar ($\lambda = 2.4$) to 10 bar ($\lambda = 1.7$) and engine speeds of $n = 3000$ rpm to 4000 rpm.

Chapter 3

Computational Model

Fluid dynamics of internal combustion engines have to be considered as unsteady, compressible, highly turbulent and reactive multiple species flows. In order to describe temporal and spatial evolution of density, temperature, velocity and mass fractions of the reacting species, three-dimensional computations are conducted. The employed CFD code ANSYS CFX [78] describes the physical problem in terms of mass-weighted averaged balance equations for reacting flows, based on the usual Navier-Stokes equations for the non-reacting case. In the following, the set of governing equations is presented (Section 3.1) and approaches for modelling of the unclosed quantities and wall treatment are introduced (Section 3.2). Section 3.3 discusses initial and boundary conditions used in the model and Section 3.4 describes the unstructured numerical grid employed for computations. The chapter closes with Section 3.5 where the applied discretisation schemes are explained.

3.1 Conservation Equations for Reacting Flows

The conservation equations for reacting flows differ from usual Navier-Stokes equations for the non-reacting case insofar as a reacting mixture, for example, a gas of multiple species, is non-isothermal and that these species may react chemically. Therefore, an additional modelling of the reaction rate is necessary. Further, in a multiple species mixture of gases, unequal heat and species diffusivity and unequal viscosity have to be con-

sidered, cf. Poinsot & Veynante [94]. Especially for a high diffusible gas like hydrogen which mixes faster with air at the molecular level than conventional fuels, the question arises whether preferential diffusion of hydrogen should be introduced into the CFD model for hydrogen/air mixture formation simulation. Colin [25] carried out a study to preferential diffusion modelling for RANS mixture formation simulations in hydrogen combustion engines. He concluded that for relatively high turbulent Reynolds numbers ($Re_t \gg 1$), as occur in internal combustion engines, preferential diffusion effects can be neglected in comparison to turbulent fluxes. Regarding mean species diffusion fluxes, turbulent diffusion largely exceeds molecular diffusion, so that preferential diffusion effects do not have to be taken into account in the current investigation of mixture formation.

3.1.1   Navier-Stokes Equations

Based on the Eulerian approach, the conservation equations may be derived[1] by differential balancing of a stationary fluid element with a given volume V. For N species in the reacting mixture with mass fractions Y_k ($k = 1$ to N), the total mass of gas m, the density $\rho = m/V$, the three-dimensional velocity field u_i and the enthalpy h are taken as primitive variables. The Navier-Stokes equations, representing the conservation of continuity (3.1) and momentum (3.2) could be then written as

$$\frac{\partial \rho}{\partial t} + \frac{\partial}{\partial x_i}(\rho u_i) = 0 \,, \tag{3.1}$$

$$\frac{\partial \rho u_j}{\partial t} + \frac{\partial}{\partial x_i}\rho u_i u_j = -\frac{\partial p}{\partial x_j} + \frac{\partial \tau_{ij}}{\partial x_i} + \rho g \,. \tag{3.2}$$

Here, the terms on the left describe temporal variation and convective transport due to the local velocity field u_i. The terms on the right of the momentum equation account for pressure gradients ($\partial p/\partial x_j$), buoyancy effects (ρg) and molecular momentum transport due to the viscous tensor

$$\tau_{ij} = -2/3\mu\frac{\partial u_k}{\partial x_k}\delta_{ij} + \mu(\frac{\partial u_i}{\partial x_j} + \frac{\partial u_j}{\partial x_i}) \tag{3.3}$$

---

[1]The presented description of equations relies on detailed derivation of governing equations by Poinsot & Veynante [94] and Munson et al. [76].

where μ is the dynamic viscosity and the Kronecker symbol $\delta_{ij} = 1$ if $i = j$ and $\delta_{ij} = 0$ if $i \neq j$. Compared to non reacting flows, the above presented total mass conservation equation as well as the equation of momentum remain unchanged for reacting flows.

3.1.2 Species Transport and Energy Equation

The set of governing equations is being completed by transport equations for $k = 1, N$ species (Eqn. 3.4) and the energy equation (Eqn. 3.6). The species transport equation may be written in general form as

$$\frac{\partial}{\partial t}\rho Y_k + \frac{\partial}{\partial x_i}\rho u_i Y_k = -\frac{\partial}{\partial x_i}(\rho V_{k,i} Y_k) + \dot{\omega}_k. \tag{3.4}$$

Here, $V_{k,i}$ is the i-component of the diffusion velocity of species k and $\dot{\omega}_k$ is the reaction rate of each species with

$$\sum_{k=1}^{N} Y_k V_{k,i} = 0 \quad \text{and} \quad \sum_{k=1}^{N} \dot{\omega}_k = 0. \tag{3.5}$$

The energy equation in terms of the total non-chemical enthalpy H may be written as

$$\frac{\partial \rho H}{\partial t} + \frac{\partial}{\partial x_i}(\rho u_i H) = \frac{\partial p}{\partial t} - \frac{\partial q_i}{\partial x_i} + \frac{\partial}{\partial x_j}(\tau_{ij} u_i) + \dot{\omega}_T + \dot{\omega}_S \tag{3.6}$$

where $\dot{\omega}_T = -\sum_{k=1}^{N} \Delta h_{f,k}^0 Y_k \dot{\omega}_k$ is the heat release due to combustion and $\dot{\omega}_S$ is an additional heat source term, e.g. due to heat release of an electric spark. The energy flux q_i includes a heat diffusion term expressed by Fourier's Law ($\lambda \partial T/\partial x_i$) and a term accounting for diffusion of species with different enthalpies h_k and may be written as

$$q_i = -\lambda \frac{\partial T}{\partial x_i} + \rho \sum_{k=1}^{N} h_k Y_k V_{k,i}. \tag{3.7}$$

The enthalpy h_k of each species of the mixture is defined as the sum of

sensible and chemical enthalpy as

$$h_k = h_{sk} + \Delta h^0_{f,k} = \int_{T_0}^{T} c_{pk} dT + \Delta h^0_{f,k} \tag{3.8}$$

where $\Delta h^0_{f,k}$ is the formation enthalpy needed to form $m = 1$ kg of species k at the reference temperature T_0. The sensible enthalpy h_{sk} of each species is zero at a reference temperature T_0 and with a heat capacity at constant pressure of

$$c_p = \sum_{k=1}^{N} c_{pk} Y_k, \tag{3.9}$$

the enthalpy of the entire mixture becomes

$$h = \underbrace{\int_{T_0}^{T} c_p dT}_{sensible} + \underbrace{\sum_{k=1}^{N} \Delta h^0_{f,k} Y_k}_{chemical}. \tag{3.10}$$

In the CFD code the total non-chemical enthalpy H is used as energy form which is given in terms of the specific sensible enthalpy h_s and the kinetic energy equation $u_i u_i / 2$ as

$$H = h_s + \frac{1}{2} u_i u_i. \tag{3.11}$$

The energy e is correlated to the enthalpy h by definition as

$$e = h - p/\rho \tag{3.12}$$

and so does the sensible energy which satisfies

$$e_{sk} = h_{sk} - p_k/\rho_k. \tag{3.13}$$

With an ideal gas constant $R = 8.314 J/(molK)$ and the density ρ and the molecular weight of the mixture W given as

$$\rho = \sum_{k=1}^{N} \rho_k \quad \text{and} \quad \frac{1}{W} = \sum_{k=1}^{N} \frac{Y_k}{W_k} \tag{3.14}$$

the equation of state is

$$p = \rho \frac{R}{W} T.$$ (3.15)

The balance equations for continuity (3.1), momentum (3.2), species (3.4) and energy (3.6) can now be closed with the algebraic thermodynamic equations, the equation of state (3.15) and the constitutive relationships (3.10).

3.2 Turbulence Modelling and Wall Treatment

The instantaneous balance equations (3.1), (3.2), (3.4) and (3.6) have to be averaged in order to achieve balance equations of mean quantities to be used in RANS (Reynolds Approximated Navier-Stokes) simulation. As a result of the averaging approach, the Reynolds stresses $\overline{\rho u_i'' u_j''}$ are produced in the momentum equations. These unclosed turbulence quantities have to be closed using turbulence models.

The present investigation employs two different approaches for a closure of the Reynolds stresses: Firstly, two-equation k-ε turbulence models based on eddy viscosity hypothesis, e.g. the RNG k-ε model and the Shear Stress Transport (SST) model. Secondly, the so-called Reynolds Stress Model (RSM) which is a higher order modelling approach, where transport equations for all components of the Reynolds stresses and dissipation rate are derived and solved. The CFD analysis performed discusses the influence of the turbulence models on mixture formation, turbulent kinetic energy and heat release. Computational results of mixture and combustion simulations are verified in Chapters 6 and 7 against experimental data.

Instead of turbulence modelling in terms of RANS, computation may be performed in terms of Large Eddy Simulation (LES). In this method, the largest structures of the flow field are explicitly computed and only smallest eddies are modelled. Consequently, a higher predictability of turbulent quantities is reported for this approach. Due to the increased numerical expense compared to RANS, this modelling technique is not investigated in the present work. Investigations on internal combustion engine fluid

dynamics employing LES are currently researched in the EU funded project *LESSCO2* [83].

3.2.1 Eddy Viscosity Turbulence Models

In eddy viscosity turbulence models, the turbulent Reynolds stresses of the averaged momentum equation are modelled using the turbulence viscosity assumption proposed by Boussinesq [95]. In this assumption, Reynolds stresses are related to the mean velocity gradients and turbulent viscosity by the gradient diffusion hypothesis. The viscous tensor expression (3.3) for Newtonian fluids is used resulting in

$$\overline{\rho u_i'' u_j''} = -\mu_t \left(\frac{\partial \tilde{u}_i}{\partial x_j} + \frac{\partial \tilde{u}_j}{\partial x_i} - \frac{2}{3} \delta_{ij} \frac{\partial \tilde{u}_k}{\partial x_k} \right) + \frac{2}{3} \overline{\rho} k. \tag{3.16}$$

Here, k is the turbulent kinetic energy expressing the variance of fluctuations in velocity and μ_t is the turbulent dynamic viscosity expressed as

$$k = \frac{1}{2} \sum_{k=1}^{3} \widetilde{u_k'' u_k''} \quad \text{and} \quad \mu_t = \overline{\rho} C_\mu \frac{k^2}{\varepsilon}, \tag{3.17}$$

with C_μ as a model constant and ε as the turbulent eddy dissipation.

3.2.1.1 The Standard k-ε Model

Applying the standard k-ε model for the closure of the turbulent kinetic energy k and the dissipation rate ε, two balance equations have to be solved:

$$\frac{\partial}{\partial t}(\overline{\rho} k) + \frac{\partial}{\partial x_i}(\overline{\rho} \tilde{u}_i k) = \frac{\partial}{\partial x_i} \left[\left(\mu + \frac{\mu_t}{\sigma_k} \right) \frac{\partial k}{\partial x_i} \right] + P_k - \overline{\rho} \varepsilon, \tag{3.18}$$

$$\frac{\partial}{\partial t}(\overline{\rho} \varepsilon) + \frac{\partial}{\partial x_i}(\overline{\rho} \tilde{u}_i \varepsilon) = \frac{\partial}{\partial x_i} \left[\left(\mu + \frac{\mu_t}{\sigma_\varepsilon} \right) \frac{\partial \varepsilon}{\partial x_i} \right] + \frac{\varepsilon}{k}(C_{\varepsilon 1} P_k - C_{\varepsilon 2} \overline{\rho} \varepsilon) \tag{3.19}$$

where P_k is the source term of turbulent kinetic energy

$$P_k = -\overline{\rho}\widetilde{u_i'' u_j''}\frac{\partial \tilde{u}_i}{\partial x_j} \tag{3.20}$$

with the Reynolds stresses modelled according to expression (3.16) and $C_{\varepsilon 1}$, $C_{\varepsilon 2}$, σ_k and σ_ε are model constants.

Finally, the solution of the transport equations (Eqn. 3.18) and (Eqn. 3.19) provides values for the turbulent kinetic energy k and the dissipation rate ε which are used to calculate the Reynolds stresses. Turbulent length scales may be estimated from the two properties k and ε, representing the turbulence field. The model constants in the Equations (3.17) to (3.19) used for the standard k-ε model are listed in App. A.

3.2.1.2 The RNG k-ε Model

The RNG k-ε model – a derivative of the standard k-ε model – is suggested by Yakhot & Orszag [121] on the basis of Renormalisation Group (RNG) analysis of the Navier-Stokes equations and is available in the standard ANSYS CFX solver [77]. In previous studies on engine CFD calculations, a capable prediction of the large-scale structures is reported for the RNG-model [46]. In hydrogen DI engines large-scale structures are generated by the hydrogen jet during injection. Therefore, the model might be favourable for the computation of hydrogen direct-injection mixture formation.

In comparison to the standard k-ε approach, the model constants in Equations (3.17) to (3.19) are changed and an analytic function for the definition of constant $C_{\varepsilon 1}$ is specified. The model constants are listed in App. A.

3.2.1.3 The Shear Stress Transport Model

The Shear Stress Transport (SST) model is a two-equation turbulence modelling approach that combines two sub-models, the standard k-ε and the turbulence/frequency k-ω approach [72].

The k-ω model is solved at the wall and the k-ε model in the outer part of the flow. The two sub-models are combined by a blending function that ensures a smooth transition between the two approaches. The model is formed by a transformation of the k-ε description to a k-ω description and an addition of the two approaches. The corresponding modified k and ω equations result in

$$\frac{\partial}{\partial t}(\overline{\rho}k) + \frac{\partial}{\partial x_i}(\overline{\rho}\tilde{u}_i k) = \frac{\partial}{\partial x_i}\left[\left(\mu + \frac{\mu_t}{\sigma_k}\right)\frac{\partial k}{\partial x_i}\right] + P_k - C_k\overline{\rho}k\omega, \qquad (3.21)$$

$$\frac{\partial}{\partial t}(\overline{\rho}\omega) + \frac{\partial}{\partial x_i}(\overline{\rho}\tilde{u}_i \omega) = \frac{\partial}{\partial x_i}\left[\left(\mu + \frac{\mu_t}{\sigma_{\omega_1}}\right)\frac{\partial \omega}{\partial x_i}\right] + (1 - F_1)2\overline{\rho}\frac{1}{\sigma_{\omega_2}\omega}\frac{\partial k}{\partial x_i}\frac{\partial \omega}{\partial x_i}$$

$$+ C_{\omega 1}\frac{\omega}{k}P_k - C_{\omega 2}\overline{\rho}\omega^2 \qquad (3.22)$$

where C_i and σ_i are specific model constants which are derived by linear blending of the constants of the k-ε and k-ω model using the hyperbolic tangent blending function F_1. The explicit model constants are listed in App. A.

In order to suppress the over-accentuation of the eddy viscosity, the expression for the turbulent dynamic viscosity, $\mu_t = \overline{\rho}\frac{k}{\omega}$, is limited by functions based on the wall distance.

The SST model is identical to the k-ε model for free shear flows. The approach provides higher accuracy for boundary layer effects than the standard k-ε model. In comparison to other available industrial two-equation models, the SST model achieves reasonable computational costs. Details on the model are given in the publication of Menter [72].

3.2.2　The Reynolds Stress Turbulence Model

The Reynolds stress turbulence model (RSM) solves single transport equations for the Reynolds stresses $\overline{\rho}\widetilde{u_i'' u_j''}$ and consequently is a more sophisticated approach than the eddy viscosity models. The RSM model applied within the present work is suggested by Speziale et al. [105] and uses a second-order description for the pressure-strain correlation of the transport equations in the Reynolds stresses. The model is available in the stan-

dard ANSYS CFX solver with an isotropic formulation of the diffusion coefficients where the equations for the transport of the Reynolds stresses are given by

$$\frac{\partial}{\partial t}(\overline{\rho}\widetilde{u_i''u_j''}) + \frac{\partial}{\partial x_k}(\widetilde{u}_k\overline{\rho}\widetilde{u_i''u_j''}) = \frac{\partial}{\partial x_k}\left[\left(\mu + \frac{2}{3}C_s\overline{\rho}\frac{k^2}{\varepsilon}\right)\frac{\partial\widetilde{u_i''u_j''}}{\partial x_k}\right] + P_{ij} + \Phi_{ij} - \frac{2}{3}\delta_{ij}\overline{\rho}\varepsilon$$

(3.23)

where C_s is a constant, Φ_{ij} is the pressure-strain correlation and the production term P_{ij} is expressed as

$$P_{ij} = -\overline{\rho}\widetilde{u_j''u_i''}\frac{\partial\widetilde{u}_j}{\partial x_i} - \overline{\rho}\widetilde{u_i''u_j''}\frac{\partial\widetilde{u}_i}{\partial x_j} .$$

(3.24)

The dissipation of turbulence is modelled with a transport equation for the dissipation rate that is equal to Equation (3.19) used in the standard k-ε model. The model constants applied with the RSM approach are summarised in App. A. There, also the coefficients of the pressure-strain correlation are noted [78].

Results of in-cylinder mixture formation calculations with this type of model show an improved correlation with experimental results compared to computations with two-equation turbulence models (Chapter 6). Numerical costs of the RSM approach are increased due to the solution of additional transport equations by a factor above 2, limiting the everyday applicability of this approach.

3.3 Initial and Boundary Conditions

The CFD computations consider gas exchange of the exhaust and intake stroke, hydrogen injection during the compression stroke and the combustion/expansion phase. Initial and boundary conditions of the computational model are derived from experimental results of engine measurements as well as from one-dimensional engine cycle process simulations using the program code GT-POWER [3].

The domain is initialised with burned gas mixture at the beginning of the exhaust stroke. Unsteady pressure and temperature boundary conditions are defined at the intake and exhaust port received from one-dimensional engine cycle simulations.

Wall boundary conditions are derived from one-dimensional engine cycle simulations applying a simplified finite element model in order to estimate the mean wall-temperatures of the in-cylinder geometry.

Inlet boundary conditions for the hydrogen injection are defined at the blind hole of the injector. The hydrogen injection profile is determined as mass flow inlet boundary condition derived from injector needle lift measurements and from values of the averaged mean mass flow. With the assumption of proportionality between needle lift and mass flow, a profile is derived from the start of injection (*SOI*) and from the end of injection. The measured absolute value of the injected fuel mass is used to specify a representative trapezoid profile which is finally used as boundary condition for the hydrogen mass flow in the CFD computations. Measurements of hydrogen injection temperature at the blind hole are not conducted. The hydrogen is assumed to be heated up to the level of the coolant temperature within the cylinder head, since the injector is entirely enclosed by the cylinder head geometry and the engine is operated in steady state.

3.4   Computational Mesh

The physical domain of the engine is discretised with an unstructured tetrahedral grid and prismatic layers at the wall boundary using the mesh generator ICEM CFD [4]. Due to the lateral, symmetric position of the hydrogen injector and the unthrottled, swirl-free charge cycle, a symmetrical flow field is assumed. This assumption allows the computational domain to be modelled as one half of the physical domain. The vertical plane through the injector's central axis is defined as a symmetry plane. With regard to a simplification of the model, the fire land at the piston is not considered. The optical access requires a slight modification of the cylinder head geometry. Consequently, two different computational meshes are

prepared for the thermodynamic research engine and the transparent research engine (see Section 2.1). The methods of grid generation, however, are identical.

All-in-one meshing procedures for internal combustion engine applications are not provided in the ANSYS CFX environment. Therefore, the motion of the mesh is arranged in terms of grid deformation. The movement of the piston and the valves is specified by crank angle based functions. The displacement of the mesh in the remaining volume of the domain is calculated by solving a displacement diffusion equation in the ANSYS CFX code. In order to control the local deformation of the mesh, a scalar variable for the mesh stiffness is introduced which acts as diffusivity in the mesh displacement equation. Global remeshing of the physical domain is required. The piston and valve movement involves extreme deformations and consequently inaccurate conditions of the tetrahedral elements occur. At the end of each deformation procedure, the results are interpolated to an updated mesh and the deformation is continued.

To reduce the size of the model, three distinct phases are defined within a single engine cycle. The computational mesh is reduced to the required geometrical elements: The gas exchange phase, the hydrogen injection phase and the compression/expansion stroke. The global size of tetrahedral elements in the domain is $h = 3\,\text{mm}$ and is locally refined near valves, injector nozzle, spark plug and walls. The boundary layer of the grid is modelled with four prismatic layers of $h = 0.05\,\text{mm}$ to $0.2\,\text{mm}$ height.

3.4.1 Gas Exchange Phase

The domain for the computation of the gas exchange includes parts of the intake and exhaust duct with approximately $l = 250\,\text{mm}$ and $180\,\text{mm}$ length, respectively. Boundary conditions at the domain limits are obtained from engine cycle calculations using a one-dimensional model. The duct is modelled with tetrahedral elements of $h = 5\,\text{mm}$ size. The size of tetrahedral elements is refined near the valves to $h = 2\,\text{mm}$ and near the valve seats to $h = 0.1\,\text{mm}$. Cross-sectional views through the computational domains of the intake and overlap phase are depicted in App. C. Sep-

$\varphi = -40° \, CA$
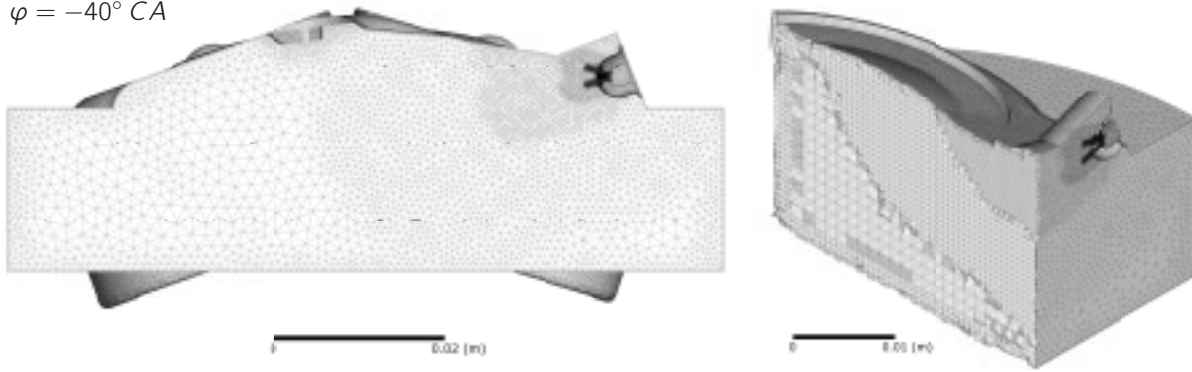
(a) Side view of computational mesh with hydrogen injector.   (b) Isometric view: Zones of refined grid at injection area.

Figure 3.1: Computational mesh of the thermodynamic research engine for the hydrogen injection phase. From the injector wall to the inner flow field the size of tetrahedral elements is incrementally increased within four zones from 0.05 to 0.25, 0.5 and 1 mm. The global element size is 3 mm.

arate meshes exist for the intake, the exhaust and the overlap phase. The overall size of the computational mesh in the gas exchange phase varies between 2 and 3 million elements.

3.4.2   Hydrogen Injection Phase

Considering the computation of the supersonic hydrogen jet and high velocity gradients at the hydrogen inflow, the resolution of the numerical grid around the injector nozzle is refined systematically. The resolution in the area of the injector's holes is refined to an element size of $h = 0.05$ mm (16 elements per pipe). From the injector wall to the in-cylinder flow the size of tetrahedral elements is incrementally increased within four zones from $h = 0.05$ to 0.25 mm, 0.5 mm and 1 mm, as depicted in Figure 3.1. Hydrogen injection starts after intake valve closes. Consequently, the intake and exhaust duct and the valve motion are not modelled during injection. Despite these restrictions, the highly refined grid at the injector nozzle causes a total size of the computational mesh of 3 to 4.5 million elements. A sensitivity analysis regarding the influence of the grid resolution on computational results shows a sufficient discretisation of the proposed mesh.

3.4.3   Compression and Expansion Stroke

The compression and the expansion stroke require less numerical resolution, since no hydrogen injection occurs. The size of tetrahedral elements in the combustion chamber is $h = 3$ mm and the elements are refined to $h = 1$ mm in the region of the spark during the combustion phase. The overall number of elements within the domain varies between 0.25 and 0.75 million elements depending on the piston lift. The computational domain of the combustion phase is depicted in App. C.

3.5   Numerical Settings

The governing equations are discretised by a scheme based on First Order Upwind Differencing where a Numerical Advection Correction of second order is applied by an adaptive blending function [78]. Regarding the convergence of the solution an accuracy for the root-mean-square residual of $RMS = 10^{-4}$ is defined.

Transient terms are generally solved by a Second Order Backward Euler scheme except for the continuity equation and the species transport equations. The approximation of these equations is limited to first order accuracy caused by mass conservation issues which arise for second order transient schemes in combination with grid deformation.

The width of time steps is adjusted for each of the different engine phases. In the gas exchange phase and in the compression phase the time step is defined as $\Delta\varphi = 0.5°$ CA. The combustion phase is conducted with a smaller time step of $\Delta\varphi = 0.1°$ CA due to high flame propagation velocities. The width of time steps in the hydrogen injection phase is even reduced to $\Delta\varphi = 0.025°$ CA in order to resolve supersonic velocity fields.

The ANSYS CFX code employs a coupled solver using a fully implicit discretisation of the equations. The hydrodynamic equations are solved as a single system. Consequently, relatively robust solutions are obtained for the convergence.

Chapter 4

Turbulent Combustion Modelling

This chapter addresses turbulent combustion modelling techniques applied for the computation of hydrogen engines. To classify the different combustion modes appearing in hydrogen engines, combustion regimes are compared to conventionally fuelled engines. Moreover, a detailed explanation of the employed turbulent combustion models is submitted. A non-premixed laminar Flamelet Concept is used to model the interaction of chemistry with turbulence. Two individual approaches with regard to the description of premixed combustion are discussed using hydrogen specific adaptations: The Zimont model and the Bradley model – both an approach for closure of turbulent flame speed; and the Extended Coherent Flame Model (ECFM) – a flame surface density approach. The premixed combustion models are coupled to the Flamelet Concept and tracer for fuel, oxygen and exhaust gas are introduced to consider the computation of partially premixed flames. The modifications of the code ANSYS CFX have been arranged within the framework of European research project *HyICE* by Bender et al. [36].

4.1   Classification of Hydrogen Engine Combustion Regimes

In order to classify turbulent premixed combustion in hydrogen engines we resort to established combustion diagrams, as proposed by Borghi [19].

Three non-dimensional numbers are generally used for the characterisation of the different regimes: The turbulent Reynolds number ($Re_t = Da^2Ka^2$), with the Damköhler number Da – comparing turbulent τ_t and chemical time scales τ_c, and the Karlovitz number Ka – comparing the chemical time scale with the Kolmogorov time τ_k. The turbulent premixed combustion of classical piston engines at large turbulent Reynolds and Damköhler numbers is characterised by $1 < u'/s_L < 10$ (u': turbulent velocity, s_L: laminar flame speed) and $10 < l_t/\delta < 100$ (l_t: integral scale, δ: flame front thickness), located in the flamelet regime. Because of the larger laminar flame speed of hydrogen, smaller u'/s_L-ratios have to be expected for hydrogen engines in comparison to hydrocarbon fuelled engines.

Concerning conventional internal combustion engines, two different combustion modes can be clearly distinguished: A premixed combustion mode with propagation flame combustion in port injected spark ignited gasoline engines, and a non-premixed, mixing controlled combustion mode – also known as diffusion flame combustion in diesel engines. In gasoline spark ignited engines the combustion chamber is filled with a premixed charge of fuel and air where a flame initialised by spark ignition propagates through the chamber until the fresh charge is completely consumed. Direct injected spark ignited gasoline engines with large-scale fuel stratification extend the premixed mode to partially premixed propagation flame combustion. Diesel combustion is initialized by auto-ignition of a small premixed portion of air and fuel, followed by mixing controlled combustion of a thin reaction zone that separates air and the injected fuel. Regarding non-premixed combustion, interaction of chemistry with turbulence is characterised by large Damköhler numbers Da. In the context of high turbulent Reynolds numbers, Re_t, combustion occurs in the flamelet regime, where the flame is treated as an ensemble of laminar thin flame elements (flamelets) embedded into the flow field.

With respect to hydrogen fuelled direct-injection IC engines, premixed and partially premixed propagation flame combustion as well as non-premixed mixing controlled diffusion flame combustion exist. In detail, the combustion modes are strictly related to the timing of fuel injection. A premixed

fuel/air mixture at ignition timing is assumed for early injection timings. Fuel/air stratification increases for late injection timings, leading to a partially premixed regime. Both cases result in a propagation flame combustion mode, comparable to those of gasoline engines. In a third case combustion proceeds simultaneously through propagation flame and diffusion flame. Here, a second injection supplies fuel immediately into the flame that was previously generated by spark ignition from the fuel/air mixture of a first injection. This mode, called combustion control, is comparable to a combined gasoline/diesel engine type process. Combustion control can be realised with a various number of discrete injections or a single injection with variable injection characteristics.

In the present investigation of hydrogen direct-injection engines, a partially premixed combustion model is examined that covers both propagation flame and diffusion flame combustion modes.

4.2 The Laminar Flamelet Model

In the present computations a Flamelet Concept proposed by Peters [79, 92] is used to model the interaction of chemistry with turbulence. The approach is originally used for non-premixed flames and is modified to account for premixed and partially-premixed flames by coupling with a reaction progress description (cf. Sections 4.3 and 4.4).

Precalculated information of laminar model flames is stored in a library, assuming fast chemistry, unity Lewis number for all species and combustion modes within the flamelet regime. Introducing the mixture fraction $\tilde{z}$ as a scalar variable for the description of the mean mixture composition, the transport equations for each species may be substituted by conservation equations for the mean Favre averaged mixture fraction $\tilde{z}$ and its variance $\widetilde{z''^2}$. The principal of this approach is to combine the laminar chemistry of the flamelet assumption with a statistical method in order to describe the fluctuating turbulent flow field and to reduce chemistry to a one-dimensional problem in mixture fraction space. The mixture fraction z is based on the atomic elements and is linked to species mass fractions

as

$$z = \frac{\frac{1}{2M_H}(Z_H - Z_{H,o}) + \frac{1}{M_O}(Z_{O,o} - Z_O)}{\frac{1}{2M_H}(Z_{H,f} - Z_{H,o}) + \frac{1}{M_O}(Z_{O,o} - Z_{O,f})} \tag{4.1}$$

where Z_j is the mass fraction of a chemical element j as the sum of all elementary mass fractions with

$$Z_j = \sum_{j=1}^{n} \frac{M_j}{M_i} Y_i \tag{4.2}$$

and Y_i is the mass fraction of species i and M the molecular mass. The indices o and f indicate the mass fraction of a chemical element in the oxidizer and fuel stream, respectively.

According to [78], the transport equations for $\tilde{z}$ and $\widetilde{z''^2}$ may be written as

$$\frac{\partial \bar{\rho}\tilde{z}}{\partial t} + \frac{\partial}{\partial x_i}(\bar{\rho}\tilde{u}_i\tilde{z}) = \frac{\partial}{\partial x_i}\left(\frac{\mu_t}{Sc_{tz}}\frac{\partial \tilde{z}}{\partial x_i}\right) \tag{4.3}$$

and

$$\frac{\partial \bar{\rho}\widetilde{z''^2}}{\partial t} + \frac{\partial}{\partial x_i}(\bar{\rho}\tilde{u}_i\widetilde{z''^2}) = \frac{\partial}{\partial x_i}\left(\frac{\mu_t}{Sc_{tz''}}\frac{\partial \widetilde{z''^2}}{\partial x_i}\right) + 2\frac{\mu_t}{Sc_{tz}}\frac{\partial \tilde{z}}{\partial x_i}\frac{\partial \tilde{z}}{\partial x_i} - \bar{\rho}\widetilde{\chi} \tag{4.4}$$

where the turbulent viscosity is μ_t and Sc_t is the turbulent Schmidt number as a model constant with $Sc_{tz} = Sc_{tz''} = 0.9$. The mean scalar dissipation rate $\widetilde{\chi}$ in the dissipation source term of the $\widetilde{z''^2}$ equation is modelled using an empirical relation

$$\widetilde{\chi} = C_\chi \frac{\varepsilon}{k}\widetilde{z''^2} , \tag{4.5}$$

with $C_\chi = 2.0$ as a model coefficient.

Values for the mean species mass fractions of the fluid and the mean temperature are directly obtained from the flamelet library as a function of $\tilde{z}$, $\widetilde{z''^2}$ and $\widetilde{\chi}$. Integration over the probability density function $P(z)$ results in

$$\widetilde{Y}_i = \int_0^1 Y_i(z, \widetilde{\chi})P(z)\partial z \tag{4.6}$$

and

$$\widetilde{T} = \int\limits_0^1 T(z, \widetilde{\chi}) P(z) \partial z \,. \tag{4.7}$$

Using Equations (4.6) and (4.7) the determination of $\widetilde{Y_i}$ and $\widetilde{T}$ is reduced to the determination of the probability density function P of the mixture fraction z. Transport equations for species mass fractions and temperature are not required any more, also mean reaction rates $\bar{\dot{\omega}}_k$ are not modelled. Balance equations are computed only for the flow variables, i.e. mean density $\bar{\rho}$ and mean velocities $\tilde{u}_i$ and the mixture fraction $\tilde{z}$ as well as the mixture fraction variance $\widetilde{z''^2}$.

To avoid extremely large computational efforts, the present work applies a β-function as a presumed probability density function $P(z)$ [78]. Depending on the mean mixture fraction $\tilde{z}$ and its variance $\widetilde{z''^2}$,

$$P(z) = \frac{\Gamma(a+b)}{\Gamma(a)\Gamma(b)} z^{a-1}(1-z)^{b-1} \,, \tag{4.8}$$

whereas the parameters a and b and the Γ function are defined as

$$a = \tilde{z}\left[\frac{\tilde{z}(1-\tilde{z})}{\widetilde{z''^2}} - 1\right], \quad b = \frac{a}{\tilde{z}} - a \quad \text{and} \quad \Gamma(x) = \int\limits_0^{+\infty} e^{-t} t^{x-1} dt \,. \tag{4.9}$$

The mixture fraction approach is completed with a model for the description of exhaust gas recirculation developed by Bender et al. [14]. As additional variables a fuel tracer $Z_{T,F}$, an oxygen tracer $Z_{T,O}$ and a tracer for the mass fraction of exhaust gas $Z_{T,EGR}$ are introduced. Assuming a stoichiometric composition of the exhaust gas mass fraction, an additional transport equation for the fuel tracer is solved according to Equation (4.4)

$$\frac{\partial \bar{\rho} Z_{T,F}}{\partial t} + \frac{\partial}{\partial x_i}(\bar{\rho} \tilde{u}_i Z_{T,F}) = \frac{\partial}{\partial x_i}\left(\frac{\mu_t}{Sc_{tz}}\frac{\partial Z_{T,F}}{\partial x_i}\right) \,. \tag{4.10}$$

Values for the oxygen tracer and the tracer for the mass fraction of ex-

haust gas are obtained from algebraic relations:

$$Z_{T,O} = 1 - \frac{\partial \tilde{z}}{\partial z_{st}} + \frac{\partial(1 - z_{st})}{\partial z_{st}} Z_{T,F} \quad \text{and} \quad Z_{T,EGR} = 1 - Z_{T,F} - Z_{T,O}. \quad (4.11)$$

To consider variable enthalpy and pressure during combustion, flamelet libraries are generated for various pressure and temperature levels and are merged to a single library by means of linear interpolation. The accuracy of the library depends on the number of sampling points n_p and n_T defined for pressure and temperature. The sensitivity of major and minor combustion products on the number of sampling points is analysed in Section 7.1.

4.3   Turbulent Flame Speed Closure Approach

The flamelet model, as described in Section 4.2, is coupled with a Turbulent Flame Speed Closure approach for the description of the progress of the global reaction. The resulting model accounts for combined premixed and partially premixed combustion.

A scalar variable for the averaged reaction progress $\tilde{c}$ is introduced, dividing the flow regime into a non-reacted and reacted region where pure fresh gas and fully reacted gas are considered as $\tilde{c} = 0$ and $\tilde{c} = 1$, respectively. Under the assumption of high turbulence and fast chemistry, compared to the integral turbulent timescales of the flow ($Da \gg 1$), a bimodal distribution of $\tilde{c}$ is justified for piston engine applications.

A single transport equation for the Favre averaged progress variable $\tilde{c}$ is solved

$$\frac{\partial}{\partial t}(\bar{\rho}\tilde{c}) + \frac{\partial}{\partial x_i}(\bar{\rho}\tilde{u}_i\tilde{c}) = \frac{\partial}{\partial x_i}\left(\frac{\mu_t}{Sc_t}\frac{\partial \tilde{c}}{\partial x_i}\right) + \overline{\dot{\omega}}_c + \overline{\dot{\omega}}_k \quad (4.12)$$

describing the progress of the global reaction, with μ_t as the turbulent viscosity. Equation (4.12) does not contain a term for molecular diffusion. The diffusive exchange of species and energy is contained in the source term $\overline{\dot{\omega}}_c$ which may be closed by the turbulent flame speed according to Bradley et al. [22]

$$\overline{\dot{\omega}}_c = \rho_u U_t |\nabla \tilde{c}| \quad (4.13)$$

where the turbulent flame speed U_t – representing the turbulent burning velocity of the propagating flame front – is a new model quantity used for closure of the equations that can either be measured directly in experiments or can be modelled. The approaches listed in Sections 4.3.1 and 4.3.2 are used to make the closure complete. The source term $\bar{\omega}_k$ is part of the ignition model and accounts for the growth of the flame kernel during an initial phase of combustion.

With the averaged reaction progress variable $\tilde{c}$ from 0 (unburned) to 1 (burned), describing the probability whether the fluid's reaction proceeded, the mean species mass fraction of the fluid $\widetilde{Y}_i$ is computed in terms of the fresh and burned values

$$\widetilde{Y}_i = (1 - \tilde{c})\widetilde{Y}_{i,fresh} + \tilde{c}\widetilde{Y}_{i,burned} \,. \tag{4.14}$$

The composition of the burned gas $\widetilde{Y}_{i,burned}$ is provided by the flamelet library from Equation (4.6). As proposed by [14], the composition of the fresh gas is expressed as

$$\widetilde{Y}_{i,fresh} = \hat{c}^{fr}\widetilde{Y}_{i,flm} + (1 - \hat{c}^{fr})\widetilde{Y}_{i,mix} \tag{4.15}$$

where $\widetilde{Y}_{i,flm}$ is the composition of recirculated products provided by flamelet libraries and $\widetilde{Y}_{i,mix}$ is the composition of the unreacted fuel and oxidizer mixture. $\hat{c}^{fr}$ is the fraction of product gases within the unburned mixture with

$$\hat{c}^{fr} = Z_{T,EGR} \max \left[z_{st}/\tilde{z}, (1 - z_{st})/(1 - \tilde{z}) \right]. \tag{4.16}$$

4.3.1 The Zimont Model

A correlation proposed by Zimont & Lipatnikov [124–127] is investigated as one possible approach for the closure of the turbulent flame speed U_t in Equation (4.13). The correlation is determined from theoretical considerations and expresses the turbulent combustion velocity as a function of the physico-chemical properties of the combustible mixture and turbulence parameters as

$$U_t = A u'^{3/4} s_L^{1/2} a^{-1/4} l_t^{1/4} \tag{4.17}$$

where l_t is the turbulent integral length scale , a the thermal diffusivity of the unburned mixture and s_L is the laminar flame speed – representing values of laminar burning velocities. The dimensionless leading factor A is determined by experimental evaluation and is an exclusive empirical constant.

The remaining factors of correlation (4.17) are basing on dimensionless analysis and phenomenological assumptions, as described in detail in [127] and summarised in the following:

According to the Kolmogorov methodology for a flamelet sheet wrinkled by turbulence, the turbulent combustion velocity U_t is given by the product of the propagation velocity of the thickened flame front U_{nt} multiplied by the instantaneous flame sheet area for the unit of cross sectional area A/A_0[1]

$$U_t = U_{nt}\overline{A/A_0} \tag{4.18}$$

where the local propagation velocity itself and the instantaneous flame sheet area A/A_0 can be expressed as

$$U_{nt} \cong u'Da^{-1/2} \quad and \quad \overline{A/A_0} \cong Da^{3/4} , \tag{4.19}$$

describing an increase of the local propagation velocity with decreasing Damköhler numbers Da and an increase in thickness of the flamelet with a reduction of Da. Combined with a stretching factor concerning the reduction of the flame velocity due to large strain rate, the final expression for U_t resulting from Equations (4.18) and (4.19) is given by

$$U_t \cong u'Da^{1/4} \tag{4.20}$$

where the correlation for U_t as stated in Equation (4.17) can be derived from. The model is completed with expressions for the integral velocity fluctuations, the integral turbulent length scale and the Kolmogorov length scale

$$u' = \sqrt{\frac{2}{3}k} , \quad l_t = k^{3/2}/\varepsilon \quad and \quad \eta = \nu^{3/4}/\varepsilon^{1/4} . \tag{4.21}$$

---

[1]A/A_0 is the ratio between the area of a flame surface element and its projection normal to the averaged propagation direction. U_{nt} includes small-scale turbulent structures, only. U_t also includes wrinkling of large-scale turbulent vortices.

The value of the laminar flame speed s_L proved to be of fundamental influence on the correlated turbulent flame speed U_t. Chapter 5 discusses the question regarding a definition of hydrogen laminar burning velocities for a wide range of equivalence ratio which finally is used as an input in Equation (4.17). The model coefficient A, as an empirical constant, is adjusted in order to fit experimental results within the present work, cf. Chapter 7.

The correlation for U_t as presented in Equation (4.17) does not consider adequately effects of laminar flame propagation at some limits, e.g. for $u' \to 0$ the prediction is $U_t \to 0$ which is not the case for hydrogen combustion. Consequently, the model is adapted in order to limit the effective turbulent flame speed below the laminar burning velocity according to

$$U_{eff} = max(U_t, s_L) \qquad (4.22)$$

where U_{eff} instead of U_t is used as an effective value in Equation (4.13).

The Zimont model provides an efficient approach for turbulent premixed gaseous combustion at high turbulent Reynolds numbers. Only one transport equation has to be solved in addition to the non-reacting flow case. The theoretical expression for turbulent combustion velocity (4.17) includes information about the speed, thickness and critical gradient of the laminar flame as well as turbulent length scale and fluctuation intensity. Thus, the model accounts for phenomena as thickening, wrinkling of flame front and straining by the turbulent velocity field. Non-equal diffusivity effects on the production of turbulent flame speed are not explicitly considered in the model. These effects, however, should be partially integrated in the laminar flame speed and the thermal conductivity of the unburned mixture which are strongly affected by equivalence ratio variations.

4.3.2 The Bradley Model

A correlation proposed by Bradley et al. [22] is alternatively investigated as closure of the turbulent flame speed. The correlation is based on measurements of premixed turbulent burning velocities conducted in combustion bombs. Bradley et al. suggested a power function of the products

of Karlovitz stretch factor and Lewis number ($KaLe$) as an approximation of the linearly increasing parts of the curves U_t/s_L vs. u'/s_L. The resulting correlation for the turbulent burning velocity in the case of fully developed flames reads

$$U_t/u' = 0.88(KaLe)^{-0.3} . \qquad (4.23)$$

The dimensionless Karlovitz stretch factor Ka as a ratio of chemical to eddy lifetimes may be defined as

$$Ka = 0.157(u'/s_L)^2 Re_t^{-0.5} \qquad (4.24)$$

where $Re_t = u'l_t/\nu$ is the turbulent Reynolds number and the constant of 0.157 results from the relation between turbulent Taylor microscale λ' and turbulent integral length scale l_t according to [6].

Finally, the combination of Equations (4.23) and (4.24) leads to an expression where the turbulent burning velocity is given by

$$U_t = CLe^{-0.3}u'^{0.55}s_L^{0.6}l_t^{0.15}\nu^{-0.15} \qquad (4.25)$$

where again l_t is the turbulent integral length scale, ν is the kinematic viscosity and s_L is the laminar flame speed – representing values of laminar burning velocities. The parameter C is a model coefficient which may be computed in terms of the factors in Equations (4.23) and (4.24) as

$$C = 0.88(0.157)^{-0.3} = 1.5336. \qquad (4.26)$$

In contrast to the before mentioned closure of Zimont & Lipatnikov, defined in Equation (4.17), the approach of Bradley et al. accounts at least in a simplified way for diffusional-thermal effects by considering the Lewis number (Le) of the mixture. Bradley et al. assumes a Lewis number based on a simplified reaction of fuel and oxygen molecules. Accordingly, the value given for Le in Equation (4.25) represents the Lewis number of the deficient reactant Le_d, e.g. for lean mixtures $Le_d = Le_{H_2}$. The Lewis number Le_i is defined as

$$Le_i = \frac{\lambda}{\rho D_{i-N_2} c_p} \qquad (4.27)$$

where λ is the thermal conductivity, c_p the specific heat and ρ the density of the mixture. Assuming diffusion in a binary mixture, D_{i-N_2} is the diffusion coefficient of the ith species in a mixture with nitrogen. Values for $D_{H_2-N_2}$ and $D_{O_2-N_2}$ are obtained from equations proposed by Hirschfelder et al. [51] for the approximation of diffusion coefficients.

Regarding the application of the model on hydrogen direct-injection IC engines, lean and rich zones occur during mixing. Consequently, the proposed definition of $Le = Le_d$ will result in a step-function near stoichiometry.

In order to improve the Lewis number description in the applied model, a function for the effective Lewis number is specified, according to Lipatnikov & Chomiak [68]

$$Le_{eff} = 1 + \frac{(Le_e - 1) + (Le_d - 1)(1 + Ze(\phi^\star - 1))}{2 + Ze(\phi^\star - 1)} \tag{4.28}$$

where $\phi^\star = max(\phi, 1/\phi)$ depending on the fuel/air equivalence ratio ϕ and Le_d (Le_e) is the Lewis number of the deficient (excessive) reactant. The Zeldovich number Ze is defined as

$$Ze = \frac{T_a}{T_b}\frac{\gamma - 1}{\gamma} \tag{4.29}$$

where the ratio between unburned and burned densities is given by $\gamma = \rho_u/\rho_b$ and for the activation temperature of hydrogen $T_a = 13000$ K is assumed [57]. Finally, the definition for the effective Lewis number 4.28 is used instead of the Lewis number of the deficient reactant as an input in Equation (4.25).

As specified for the Zimont model in Equation (4.22), the Bradley model considers laminar flame propagation by limiting the turbulent flame speed below its laminar value.

Regarding the definition of hydrogen laminar burning velocities, the same correlations as applied to the Zimont model are investigated. The model coefficient C is adjusted in order to fit experimental results of the thermodynamic research engine. Computational results are presented in Chapter 7.

4.4   Flame Surface Density Approach

In analogy to the procedure formulated in Section 4.3 for the Turbulent Flame Speed Closure approach, the Flamelet Model is coupled with a Flame Surface Density approach for the description of the progress of the global reaction. The resulting model includes in a combined way premixed and partially premixed combustion.

The model is based on a geometrical analysis for reaction rate closure, where the flame front is considered as an infinitely thin surface evolving in the turbulent flow field separating fresh and burned gases. The concept is a description of the specific fuel consumption in terms of the product of the flame surface density and the local consumption speed, as proposed for the Coherent Flame Model (CFM) [20, 93]. The present approach relies on general developments of the CFM by Colin et al. [26] and hydrogen specific adaptations by Benkenida et al. [15] resulting in an improved version of the model, the Extended Coherent Flame Model (ECFM). The hydrogen specific adaptations include laminar propagation effects in the transport equation on the flame surface density, stretch effects on laminar flame speed and instability effects related to low Lewis number of hydrogen flames.

4.4.1   The Extended Coherent Flame Model

In the flame surface density approach the mean reaction rate for a closure of Equation (4.12) is estimated in terms of flame surface area as

$$\overline{\dot{\omega}_c} = \bar{\rho}_u s_L \Sigma \tag{4.30}$$

where ρ_u is the density of the unburned mixture, s_L is the laminar flame speed and Σ is the flame surface density (available flame area per unit volume) measuring the flame front convolutions. In this approach complex chemistry and turbulence are decoupled. Chemistry is integrated in the Flamelet Model described in Section 4.2. A transport equation for the

flame surface density is derived which in its closed form reads as

$$\frac{\partial \Sigma}{\partial t} + \frac{\partial \tilde{u}_i \Sigma}{\partial x_i} = \frac{\partial}{\partial x_i} \left(\frac{\nu_t}{Sc_\Sigma} \frac{\partial \Sigma}{\partial x_i} \right) + \mathcal{P}_1 + \mathcal{P}_2 + \mathcal{P}_3 + \mathcal{P}_4 - \mathcal{D} \, . \qquad (4.31)$$

The terms on the left of Equation (4.31) correspond to unsteady effects and flame surface convection by the flow field, respectively. On the right side a diffusive term with the flame surface turbulent Schmidt number Sc_Σ and the turbulent kinematic viscosity ν_t as well as source ($\mathcal{P}_i$) and consumption ($\mathcal{D}$) terms are considered.

Literature provides various models expressing the source and consumption terms to complete the closure of Equation (4.31). The approach used in the present work is based on formulations proposed by Benkenida et al. [15], where hydrogen specific effects of laminar flame propagation are considered. The additional source and consumption terms are defined as follows:

$$\mathcal{P}_1 = \alpha \kappa_t \Sigma \, , \qquad (4.32)$$

as a flame surface production term due to strain rate effects induced by turbulent stretch where α is an adjustable model constant and κ_t the turbulent strain rate.

$$\mathcal{P}_2 = \frac{2}{3} \frac{\partial \tilde{u}_i}{\partial x_i} \Sigma \, , \qquad (4.33)$$

as a flame surface production term due to strain rate effects induced by mean flow.

$$\mathcal{P}_3 = \frac{2}{3} \frac{\bar{\rho}_u}{\bar{\rho}_b} s_L \frac{1 - \bar{c}}{\bar{c}} \left(\Sigma - |\nabla \tilde{c}| \right) \Sigma \, , \qquad (4.34)$$

as a flame surface production term due to effects of flame thermal expansion and curvature, where s_L is the laminar flame speed, $\bar{c}$ is the volume fraction of the burned gas and $\bar{\rho}_u$ and $\bar{\rho}_b$ is the density of the unburned and burned gas, respectively.

$$\mathcal{P}_4 = \frac{\partial}{\partial x_i} \left(\frac{\bar{\rho}_u}{\bar{\rho}} s_L \frac{1}{|\nabla \tilde{c}|} \frac{\partial \tilde{c}}{\partial x_i} \Sigma \right) \, , \qquad (4.35)$$

as an additional source term to account for laminar flame propagation effects of hydrogen.

The destruction term describing the consumption of the flame surface limits the transport equation to predict an infinite growth of the flame surface density with

$$\mathcal{D} = \beta s_L \frac{(\Sigma - |\nabla \tilde{c}|)\, \Sigma}{1 - \bar{c}} \, , \tag{4.36}$$

and $\beta = 1$ as a constant model parameter.

The volume fraction of the burned gas is computed in terms of the mean reaction progress

$$\bar{c} = \frac{\tilde{c} \rho_u}{\tilde{c} \rho_u + (1 - \tilde{c}) \rho_b} \, . \tag{4.37}$$

Possible numerical problems with the ECFM model can emerge in case the value of the laminar flame speed is locally equal zero within the domain, e.g. in highly stratified mixtures. As the laminar flame speed is not considered, initial low levels of flame surface density caused by numerical disturbances may be amplified by the production terms $\mathcal{P}_1$ and $\mathcal{P}_2$. The destruction term $\mathcal{D}$, however, will not be effective, since it includes the laminar flame speed as a factor. An unphysical infinite production of flame surface density may be the result.

In order to increase the robustness of the ECFM model, Bender et al. [14] introduced numerical modifications which disable the production terms $\mathcal{P}_1$ and $\mathcal{P}_2$ (Equations 4.32 and 4.33) below a certain level of laminar flame speed defined as $s_{L,limit} = 0.01$ m/s. The destruction term $\mathcal{D}$ (Equation 4.36) is modified insofar as for the value of laminar flame speed a lower limit is introduced, also defined as $s_{L,limit} = 0.01$ m/s. Additionally, to prevent division by zero, the dominators in the terms $\mathcal{D}$ and $\mathcal{P}_3$ – which depend on the reaction progress – are limited by very small numbers, specified as 10^{-4}.

The ECFM approach is coupled to the Flamelet concept by Equation (4.14) as specified for the TFC approach in Section 4.3. Regarding the definition of the laminar flame speed s_L, the same correlations as applied for the TFC approach are investigated. To calibrate the model to experimental data, the model constant α in the surface production term is adjusted (cf. Chapter 7 for calculation results).

4.4.2 Modelling of Turbulent Strain Rate

The source term for flame surface production given by Equation (4.32) includes a factor for the turbulent strain rate κ_t which has to be modelled separately. In the ECFM model a proposal of Meneveau [71] is implemented, also known as Intermittent Turbulence Net Flame Stretch Model (ITNFS) where κ_t is expressed as

$$\kappa_t = \Gamma_K \left(\frac{u'}{s_L}, \frac{l_t}{\delta_l} \right) \frac{\varepsilon}{k} \, , \tag{4.38}$$

with Γ_K as an efficiency coefficient[2] which is a function of the laminar flame speed s_L and the laminar flame thickness δ_l. The value of δ_l is computed with the correlation proposed by Blint

$$\delta_l = \kappa \left(2 \frac{D_{th}}{s_L} \right) \tag{4.39}$$

where the coefficient κ is unity for hydrocarbon fuels. With respect to hydrogen applications, an expression for κ defined by Benkenida et al. [15] on the basis of detailed kinetics computations is used, according to

$$\kappa = \alpha_0 f(\phi) g(T_u) h(p) \tag{4.40}$$

where $f(\phi)$, $g(T_u)$ and $h(p)$ are polynomials expressing the dependence on the equivalence ratio, the fresh gas temperature and the pressure, as listed in App. A.2. The value of the coefficient varies between $\kappa = 2.0$ and 7.0 for fuel/air equivalence ratio in the range of $\lambda = 0.8$ to 2.0 and consequently differs obviously from the value proposed for hydrocarbon fuels.

---

[2]A detailed description on the evolution of the efficiency coefficient is presented in [94].

4.5   Ignition Model

A simplified approach is applied in order to model ignition by the spark plug during the initial phase of combustion. Assuming that the flame kernel is smaller than the smallest turbulence eddies, the initial flame propagation is considered as a laminar flame not influenced by turbulence. According to Bender et al. [14], a radius for the flame kernel $r_k(t)$ as a function of the time t is defined by the equation

$$r_k(t) = s_L(t - t_{start})\frac{T_b}{T_u} + r_0 \tag{4.41}$$

where r_0 is the initial flame radius, T_b and T_u are the burned and unburned gas temperatures, respectively. According to a sensitivity analysis of the flame propagation to the initial conditions of the flame kernel, the maximum radius of the flame kernel is defined as $r_{k,max} = 4$ mm, describing a transition volume where the ignition phase is closed.

During ignition, the reaction progress is calculated as the ratio of the burned mass to the total mass within the transition volume and an additional source term

$$\overline{\dot{\omega}}_k = \rho_u s_L |\nabla \tilde{c}| \tag{4.42}$$

is added to the $\tilde{c}$-transport Equation (4.12).

Chapter 5

Hydrogen Burning Velocities

An elementary understanding of burning velocities – as the most significant characteristics of a combustible mixture – is of crucial importance for the computation of fuel conversion in IC engines. The employed combustion models yield effective, turbulent flame speeds on the basis of physico-chemical and turbulent quantities and require values of the laminar flame speed as a model input. The determination of laminar flame speed of hydrogen/air mixtures at engine-like conditions is discussed in the present chapter. To provide an insight into the complexity of hydrogen laminar flames at elevated pressures, Section 5.1 describes basic considerations regarding a characterisation of different flame speed types, the sensitivity of hydrogen laminar flame speed and instability effects. A review of hydrogen flame speed investigations is described in Section 5.2, focussing on engine-relevant measurements of spherical premixed hydrogen flames at elevated pressure levels. To improve the understanding on hydrogen laminar flame speed, the database found in literature is extended by computations and measurements presented in Sections 5.3 and 5.4. The computations provide burning velocities of laminar, smooth flames and are based on a detailed chemical kinetic model of one-dimensional flames. The measurements provide burning velocities of laminar wrinkled flames and include instability effects which arise at elevated pressure levels but are not covered by the kinetic model. As experimental setup, a single-cylinder compression machine is employed using OH-chemiluminescence for optical evaluation of the flame front and pressure measurements for zero-dimensional analysis. Finally, a correlation is derived and compared to existing works in Section 5.5.

5.1 Basic Considerations

Before focussing on hydrogen flame speeds at engine-relevant conditions, basic phenomena of spherical expanding hydrogen flames are considered, such as the influence of equivalence ratio, temperature and pressure on the laminar flame speed (Section 5.1.2). Regarding the sensitivity on pressure, hydrogen flames also show cellular instability for thermo-diffusive stable flames (rich mixtures) at higher pressure levels. To define the flame speed magnitude it is crucial whether the accelerating impact of instabilities is taken into consideration. The different effects of flame instabilities on the cellularity of expanding spherical flames is well researched and will be described in Section 5.1.3. Due to effects, such as instability, stretch and thermal expansion, different types of flame speed and burning velocities may be identified as specified in the following.

5.1.1 Flame Propagation Relations

Regarding the characterisation of spherical expanding laminar flames, two categories of velocities have to be distinguished: First, the velocities of the laminar flame front which describe the propagation in a fixed reference spatial frame. Second, corresponding burning velocities which differ from the flame front velocity by the amount of the burned gases expansion velocity. Finally, an effective turbulent flame speed may be defined which includes an enhancement of the laminar flame speed due to turbulent quantities.

5.1.1.1 Laminar Flame Front Velocities S_n and S

With respect to spherical expanding flames, the stretched flame front velocity S_n is determined by the time derivative of the flame radius r according to

$$S_n = \frac{dr}{dt} \tag{5.1}$$

where r may be specified by optical measurements or indirectly by means of zero-dimensional pressure analysis. Depending on the size of the flame radius, S_n includes effects of stretch and in case of cellularity also instability effects. The stretch-free flame front velocity S can be expressed by linear regression in terms of a Markstein length L_b and the stretch rate α according to

$$S = L_b \alpha + S_n \quad \text{and} \quad \alpha = \frac{2}{r}\frac{dr}{dt}. \tag{5.2}$$

Methods with regard to cellular instable flames may be employed for a derivation of instability corrected flame speeds, e.g. the linear stability analysis proposed by Addabbo et al. [8] and Bradley et al. [23] yielding stable flame front velocities from originally unstable flames.

5.1.1.2 Laminar Burning Velocities u_n and u_l

The amount of the burned gases expansion velocity v_g may be subtracted from the laminar flame front velocities S_n and S yielding laminar burning velocities u_n and u_l, respectively. Alternatively, the gas expansion effect may be taken into account using an expression based on the expansion ratio of densities of the unburned and burned gas ρ_u/ρ_b where

$$u_n = S_n - v_g = \frac{S_n}{\kappa_{exp}}, \qquad u_l = S - v_g = \frac{S}{\kappa_{exp}} \tag{5.3}$$

and

$$\kappa_{exp} = \frac{\rho_u/\rho_b}{((\rho_u/\rho_b) - 1)\, x_b + 1} \tag{5.4}$$

is the expansion coefficient according to [50] with x_b representing the burned mass fraction at a specific time.

The stretch-free stable laminar burning velocity u_l is a fundamental combustion characteristic and depends only on pressure, temperature and the mixture composition. Effects of instability and stretch are not included in u_l, since this value is assigned to the stretch-free stable flame front velocity S. On the contrary, the burning velocity u_n includes stretch effects and is unstable by nature and depends consequently on the history of the flame.

In fact, stretch-free stable laminar hydrogen burning velocities u_l at engine-like conditions may be only obtained by theoretical approaches. With respect to experimental investigations, instability effects at elevated pressures cannot be suppressed without inert gas dilution of hydrogen-air mixtures. Regarding investigations within the present work, computations of one-dimensional flames using a detailed chemical kinetic model yield values of stable burning velocities u_l, while measurements on the Single Cylinder Compression Machine provide unstable burning velocities u_n. Corresponding burning velocities are compiled into laminar flame speed correlations in Section 5.5 to be used as input for the employed turbulent combustion modelling approaches.

5.1.1.3 Turbulent Flame Speed U_t

The turbulent flame speed U_t is calculated by means of turbulent combustion models, presented in Equations (4.17) and (4.25), describing the enhancement of the laminar flame speed caused by turbulent quantities. U_t is the effective burning velocity of the mean propagation front, expressed in the CFD calculations as the gradient between burned and unburned regions of the mean reaction progress $\tilde{c}$.

5.1.2 Sensitivity on Thermochemical Conditions of the Mixture

Due to the wide ignition limits, the computation of lean or highly stratified hydrogen engines require flame speed data for a broad range of equivalence ratios. First, the dependency of hydrogen laminar burning velocity on equivalence ratio is analysed, considering ambient conditions where already numerous experimental investigations on hydrogen flames have been undertaken. Concerning an estimation of the influence of temperature and pressure on the value of laminar flame speed, this is the most challenging task for IC engine applications, since varying conditions of the unburned gas temperature and pressure arise, exceeding levels of $T = 600$ K and $p = 20$ bar during combustion by far.
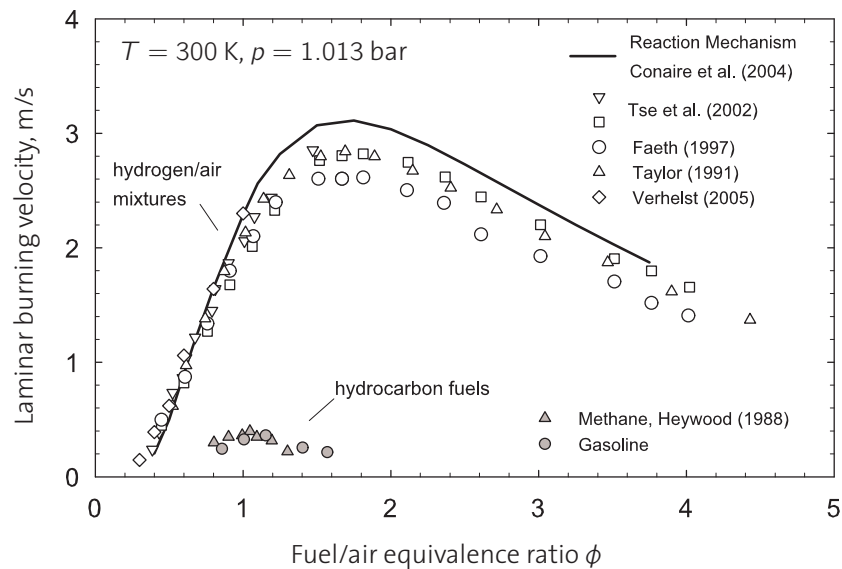
Figure 5.1: Hydrogen laminar burning velocities u_l as function of $\phi = 1/\lambda$ at ambient conditions ($T = 300$ K, $p = 1.013$ bar). Experimental values [11, 108, 110, 111] are represented as symbols, computational results (cf. Section 5.3) are displayed as line. For comparison to hydrocarbon fuel, laminar burning velocities of methane and gasoline are presented [50].

5.1.2.1 Dependency on Equivalence Ratio

In order to demonstrate the dependency of flame speed on the equivalence ratio, hydrogen planar laminar burning velocities u_l are analysed at ambient conditions, as depicted in Figure 5.1. Values of u_l are given as a function of the fuel/air equivalence ratio ϕ (= $1/\lambda$). Experimental data, proposed by several authors, are compared with those predicted by calculations using a detailed chemical kinetic model based on the reaction mechanism presented by Conaire et al. [86] (see Section 5.3). The different experimental results show a similar behaviour in the interval of $0.4 \leq \phi \leq 4.0$. The peak laminar burning velocity is slightly located in the rich regime at $\phi = 1.5$ to 1.7 with values ranging between $u_l = 2.6$ m/s and 2.8 m/s. Burning velocities of rich and lean mixtures decrease almost in a linear behaviour towards the extinction limits that are located at $\phi = 10.0$ and 0.1 for the rich and lean regime. Compared to experimental results, the computational results predict a moderately intensified gradient angle in the lean regime and the values of maximum flame speed are slightly overestimated. The differentiation to hydrocarbon fuels shows that the laminar burning velocities of stoichiometric hydrogen/air

mixtures are increased by a multiple of the value given by gasoline and methane, for instance. Moreover, the elementary distinction of hydrogen ignition limits compared to hydrocarbon fuels has to be mentioned.

Measurements at ambient conditions may be taken as a basis for a definition of a laminar flame speed correlation. Nevertheless, a detailed study of laminar flames at elevated pressure and temperature levels is necessary for a correct prediction of burning velocities at engine-like conditions. Coherent experimental data found in literature are discussed in Section 5.2.

5.1.2.2   Dependency on Temperature and Pressure

The evolution of laminar burning velocities on variation of temperature and pressure is depicted in Figure 5.2 for stoichiometric hydrogen/air mixtures starting at ambient conditions. Again, experimental data of laminar burning velocities are compared to theoretical values obtained by kinetic schemes. While the influence of temperature on the reaction kinetics and consequently on the tendency of flame speed is obvious, different assumptions concerning the dependency of flame speed evolution with regard to pressure are reported. The data proposed by Iijima & Takeno [53] as well as by Verhelst [111] predict an enlargement of laminar burning velocity for increasing temperature and pressure. The values predicted by reaction mechanism calculations confirm the growth of burning velocities for increasing temperatures, although diminishing values for elevated pressures are obtained. The discrepancy may be anticipated by the fact that different kind of flame speed types are observed: Unstable cellular flames are investigated in the experiments where instability effects lead to an increase of flame speed at elevated pressure levels. Contrarily, computations with the kinetic scheme do not show this effect since cellular instability is not considered in the chemical kinetic model.

Theoretically, an increase in pressure has a decelerating effect on the laminar burning velocity of smooth stable flames. Consistent experimental results at elevated pressure levels are reported by Tse et al. [110] using helium diluted mixtures in order to suppress instabilities (cf. Section 5.2.3). In fact, instabilities arise at increasing pressure and result in wrinkling
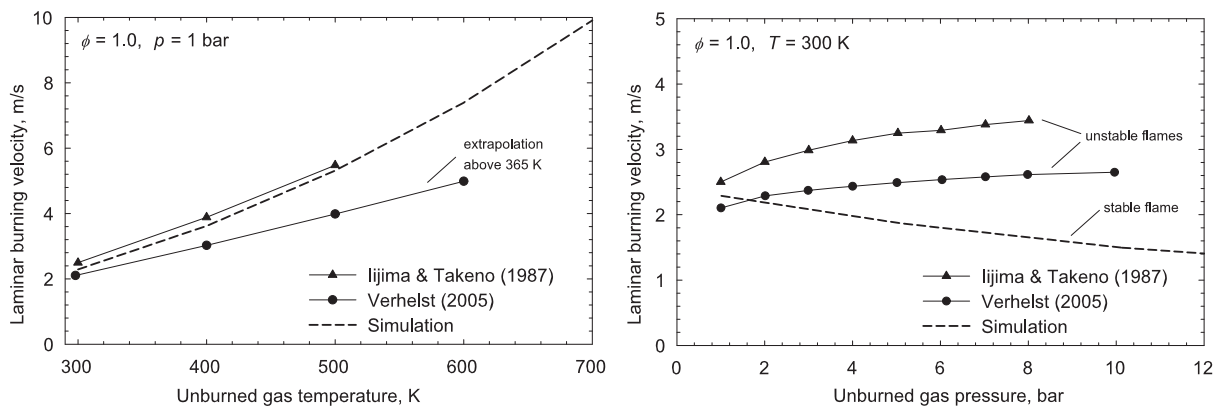
Figure 5.2: Influence of temperature (left) and pressure (right) conditions of the unburned gas on the value of the hydrogen laminar burning velocity. Experimental data of Iijima & Takeno [53] and Verhelst [111] derived by $dr(t)/dt$ are compared with calculations based on the kinetic scheme proposed by Conaire et al. [86].

and in an acceleration of the flame front. Since the laminar burning velocity is used as an input for the employed turbulent combustion model the question arises whether the input value should include flame instability effects. With regard to hydrogen IC engine combustion, the ratio of turbulent to laminar flame speed is far below the ratio of hydrocarbon fuels. At increasing pressure the onset of instability is shifted towards extremely small flame radii r where the influence of turbulence is not yet established. Consequently, the increase of flame velocity due to instabilities may not be neglected. Further considerations regarding the effect of instabilities are noted in the following.

5.1.3 Flame Instabilities of Premixed Hydrogen Combustion

Two basic modes of instabilities may be classified for spherical expanding flames: Thermodiffusive instabilities, as a consequence of unequal diffusivities of the reactants and heat, and hydrodynamic instabilities caused by the discontinuity of unburned and burned gas density. Diffusion and hydrodynamic effects on the stability of laminar hydrogen flames are well examined, cf. the review of Law [66] and former works of Bechtold & Matalon [13]. Due to the relevance of these effects on high-pressure hydrogen laminar flames, a brief description of the instability mechanisms is given below. Additional instability effects arising from buoyancy (Rayleigh-Taylor

instability), pulsating instabilities and strong pressure oscillations, which may wrinkle the flame front, are of minor importance for the investigations and hence are not addressed here.

5.1.3.1　Thermodiffusive Instabilities

Thermodiffusive instabilities result from the competing effects of heat conduction from the flame front and reactant diffusion towards the flame front. With reference to the Lewis number Le of the mixture, cell formation establishes when Le is less than unity (when the mass diffusivity of the limiting reactant is sufficiently larger than the thermal diffusivity of the mixture). Hydrogen flames of lean mixtures are correspondingly characterised by $Le < 1$ and are unstable to thermodiffusive perturbations, while rich mixtures with $Le > 1$ are stable with respect to the thermodiffusive mechanism.

5.1.3.2　Hydrodynamic Instabilities

Flame instability is also generated by the density jump across the flame, specified as hydrodynamic instability or Darrieus-Landau instability. According to this mechanism, hydrodynamic disturbances caused by thermal expansion interact with the expanding flame front. The effect of hydrodynamic instability is omnipresent during all stages of flame propagation, disregarding the Lewis number of the mixture. Hydrodynamic instabilities, however, will not necessarily lead to flame cellularity as long as stabilising effects, such as curvature of sufficiently thick flames and thermodiffusive stabilisation (effect of $Le > 1$), are high enough to prevent the flame front from wrinkling. In spherical expanding flames, the flame thickness and correspondingly the curvature effect is directly related to pressure. While at low pressure environments curvature is strong enough to prevent the formation of cellular structures, the flame becomes thinner and the stabilising effect of curvature diminishes at increasing pressure. Above a critical pressure level, even flames of rich hydrogen mixtures ($Le > 1$) show cellular structures, since the stabilising effects of curvature

and thermo-diffusivity are too weak to suppress perturbations generated by hydrodynamic instabilities.

With reference to hydrogen engine applications, pressure levels are typically located above the level where hydrodynamic instabilities develop. Consequently, the propagating flames are hydrodynamically unstable by nature. Regarding the modelling procedure of the combustion process, the question arises whether coinciding effects of both turbulence and flame front wrinkling by means of instability have to be considered. The influence of instability on burning velocities is further discussed in Section 5.4.

5.2 Review of Flame Speed Measurements

In general, combustion characteristics of hydrogen/air mixtures are well researched. Regarding burning velocities, however, most experiments published in literature are limited to atmospheric conditions, while only few investigations exist which consider hydrogen flame speeds at pressure and temperature levels that are related to IC engine applications. With respect to flame speed measurements of spherical expanding premixed hydrogen flames at pressure levels above $p = 5$ bar, experimental investigations are reported by Milton & Keck, Iijima & Takeno, and – most relevant for the present work – by research groups at Princeton University and at University of Leeds.

5.2.1 Investigations of Milton & Keck

Milton & Keck [75] conducted measurements of premixed hydrogen/air mixtures limited to stoichiometric equivalence ratio and initial pressure and temperature conditions of $p = 1.013$ bar and $T = 298$ K, using a combustion bomb technique. Laminar burning velocities are derived from zero-dimensional analysis of the pressure history. At initial conditions values of $u_l = 2.3$ m/s are reported which agree to the results shown in Figure 5.1. Values derived at higher pressure and temperature levels (up to $p = 7$ bar and $T = 512$ K) depend on the history of the flame (e.g. growth

period) and are influenced by cellularity effects. Thus, the obtained data are less reliable with respect to stable laminar burning velocities.

5.2.2　Investigations of Iijima & Takeno

In a similar way, Iijima & Takeno [53] employed combustion bomb pressure measurements of hydrogen-air mixtures with air/fuel equivalence ratios in the range between $0.25 \leq \lambda \leq 2$. Temperature and pressure conditions of the unburned gas vary from $T = 291$ K to 500 K, and from $p = 1$ bar to 25 bar. A correlation for laminar burning velocities is derived which is valid within the range specified above. The data are related to cellular unstable laminar flames according to the increase of flame speed at elevated pressure levels as discussed in Figure 5.2. Regarding the influence of temperature on the laminar flame speed, a similar behaviour as predicted by the detailed chemical kinetic model is observed in the figure. Considering atmospheric temperature and pressure conditions, the maximum flame speed is found in the rich regime, near a air/fuel equivalence ratio of $\lambda = 0.6$. At these conditions the experiments reveal good compliance with results of other authors, cf. Figure 5.1. In the experiments flame stretch and instability effects are not taken into consideration.

5.2.3　Investigations of C. K. Law et al.

Recently, at Princeton University comprehensive studies on hydrogen laminar burning velocities and instability effects have been accomplished, using pure hydrogen/air mixtures and diluted blends.

Experimental studies on constant-pressure, spherical expanding hydrogen flames have been conducted by C. K. Law et al. [66, 67, 110] using an apparatus similar to a combustion bomb. Unstretched laminar burning velocities of pure hydrogen/air mixtures are derived from optical measurements of $dr(t)/dt$ for air/fuel equivalence ratios in the range of $0.25 \leq \lambda \leq 2$ and initial ambient temperature and pressure conditions. The results show good compliance with computations and data presented by other authors, cf. Figure 5.1. Increasing cellular flames are reported at elevated

pressure levels due to hydrodynamic instability for pure hydrogen/air mixtures. In order to suppress instability effects, helium is used as a diluent for hydrogen-oxygen-nitrogen mixtures with initial pressure and temperature conditions of $p = 3$ bar to 60.8 bar and $T = 298$ K. The experiments with dilution provide data of non-cellular stable flames. From the acquired smooth flame burning velocity, data for the stretch-free laminar flame are derived.

Concerning pressure dependency of the burning velocity, a decreasing trend for the flame speed of the helium diluted hydrogen mixtures is found for increasing initial pressure levels. The results comply well with computations based on the detailed chemical kinetic model (cf. Section 5.3). This trend is contrary to the experimental results obtained from non-diluted high-pressure flames, where an increase of burning velocity at elevated pressure has been observed. Supposing that dilution with inert gas does not affect the reaction kinetics of hydrogen oxidation, the diluted flame is more likely to reflect the situation that is assumed to be valid for smooth, stable laminar flames. Following the considerations of Section 5.1.3, the diluted smooth laminar flame is not affected by cellular instability effects which cause the burning velocity of the non-diluted wrinkled flame to increase at elevated pressure levels due to cellularity.

5.2.4   Investigations of Verhelst and Bradley et al.

With respect to laminar hydrogen flames, recent investigations at University of Leeds have been conducted by Verhelst [111] and Bradley et al. [23] using a hydrogen/air spherical explosion bomb.

5.2.4.1   Experimental Investigations

Verhelst [111] carried out experimental studies in order to determine laminar flame speed at engine-like conditions. The undertaken experiments involve hydrogen/air mixtures with air/fuel equivalence ratios in the lean regime for $1 \leq \lambda \leq 3.3$. Initial temperature and pressure conditions of the unburned gas mixture vary in the range between $T = 300$ K to 365 K

and $p = 1$ bar to 10 bar. Laminar burning velocities are derived by means of optical analysis of the flame front using Schlieren technique. Flames at sufficiently small flame radii ($r = 10$ mm) are recorded in order to limit the acceleration due to instability effects. Linear regression for correction of stretch effects is applied to measurements of low initial pressure conditions ($p < 5$ bar). Laminar burning velocities at ambient conditions show considerable compliance with data found in literature, cf. Figure 5.1. Cellularity is reported for high-pressure flames with $p > 5$ bar due to flame instabilities. As a result, an acceleration of the stretched unstable laminar burning velocities at elevated pressure conditions is found for air/fuel equivalence ratios of $\lambda \leq 2.4$ and a slight decrease for values of λ above. A correlation for the laminar burning velocity of cellular flames is derived upon the basis of the measurements, valid in the above mentioned range. The use of corresponding data for hydrogen direct-injection engines, however, is limited due to the narrow validity range of λ which does not cover rich mixtures for $\lambda < 1$. Since the rich equivalence range is the most important part for stratified engine operation and multi-injection, the correlation will not suffice for modelling of hydrogen direct-injection engines. Consequently, an extended version of the correlation is proposed within the present work, where the validity range is enlarged to the rich regime on the basis of computational results (see Section 5.5.2).

5.2.4.2   Instability Correction of Burning Velocities

Bradley et al. [23] considered hydrodynamic and thermodiffusive instability effects of premixed hydrogen flames, using linear stability theory of Bechtold & Matalon [13, 21]. An instability correction of laminar burning velocities, obtained by the above mentioned experimental investigations, is conducted for flames up to $p = 10$ bar. At increasing pressure, the onset of instability is shifted to very small flame radii ($r < 1$ mm) so that no stable regime could be measured. While the laminar burning velocity of the unstable flame accelerates at increasing pressure levels, the instability-corrected value shows a decelerating effect. This trend correlates to computational results obtained from kinetic schemes. Altogether, the approach substantiates the role of flame front instabilities on the ac-

celeration of laminar hydrogen flames and estimates the magnitude of instability effects. However, with respect to IC engine combustion modelling, the validity of imaginary, artificial values of smooth laminar burning velocities as input for combustion models is questionable.

# 5.3 Computations with Detailed Chemical Kinetic Model

Further to experimental investigations, computations on the basis of reaction mechanisms may be employed in order to determine fundamental values of laminar flame speed. As discussed above, hydrogen flames at elevated pressures engender flame front instabilities and cellular wrinkling resulting in an acceleration of the flame during experiments. The information on flame speed received from measurements is consequently related to unstable cellular flames, while simulations with kinetic schemes provide details of smooth laminar flames without disturbing influence of flame front instabilities. In a differentiation with experimental results these values may be used for a quantification of the acceleration caused by instability effects. The employed kinetic mechanism is compared to experimental data found in literature and flame speed simulations of hydrogen/air mixtures at engine-relevant conditions are conducted. Finally, laminar flame speed correlations are derived from the computational results in order to be used for CFD calculations.

5.3.1 Validation by Experimental Data

Hydrogen laminar burning velocities are calculated with a chemical model of a one-dimensional adiabatic planar premixed flame, using the program package CHEMKIN 4.0, Kee et al. [58]. A detailed kinetic scheme with 10 species and 19 reactions proposed by Conaire et al. [86] is taken as a reaction mechanism. A list of the considered reactions is presented in App. D. According to [86], the kinetic scheme is validated by a quantity of experimental data covering a temperature range from $T = 298$ K to 2700 K,
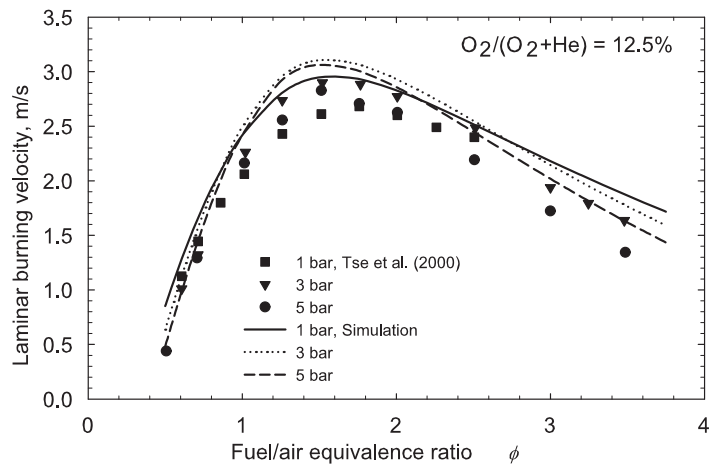
(a) Dependency on $\phi = 1/\lambda$ at $T = 298$ K, $p = 1$ to 5 bar.
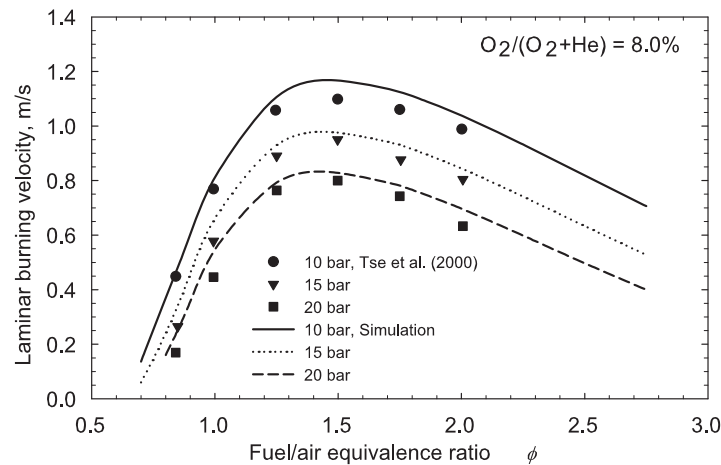
(b) Dependency on $\phi = 1/\lambda$ at $T = 298$ K, $p = 10$ to 20 bar.
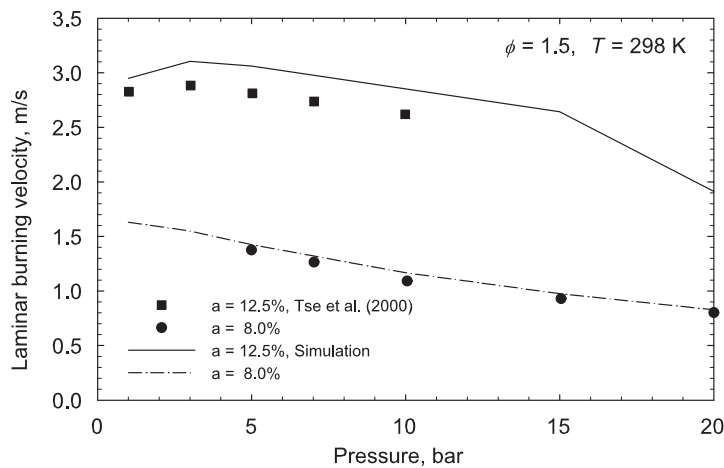
(c) Dependency on pressure at $\phi = 1/\lambda = 1.5$ and $T = 298$ K.

Figure 5.3: Comparison of reaction mechanism calculations with burning velocities of helium diluted flames obtained from Tse et al. [110]. The dilution is increased at the higher pressures to suppress instabilities. The kinetic scheme proposed by Conaire et al. [86] is employed in the simulations.

pressures from $p = 1$ bar to 87 bar, and air/fuel equivalence ratios in the range of $0.2 \leq \lambda \leq 5.0$. Consequently, the mechanism is considered to be valid at conditions relevant for IC engines.

A validation of the flame speed simulations is obtained by comparison of computational results with experimental data. Adequate measurements found in literature are the investigations of Tse et al. [110]. Measurements of hydrogen/air flames are available at atmospheric conditions, while flame speed analysis at elevated pressure levels are diluted with helium in order to minimise instability and formation of flame cells. Burning velocities of helium-diluted flames are computed for additional comparison with these experiments. Third-body efficiency factors of argon are used instead of helium for the termolecular reactions in the kinetic mechanism. This assumption may be justified since both inert gases show equal kinetic parameters.

With respect to non-diluted flames at atmospheric conditions, a comparison of the obtained numerical data presents satisfying agreement with experimental data from literature, cf. Figure 5.1. In the rich regime, however, flame speed is slightly overestimated by the computations.

Regarding flame speeds at elevated pressures, the kinetic mechanism calculations show a satisfying representation of the experimental measurements for a broad range of pressure and equivalence ratio variations, as demonstrated in Figure 5.3. Flame speed values of the calculations overestimate the experimental results slightly. At elevated pressure levels, the trend of decelerating laminar flame speed with increasing pressure seems to be appropriately described by the reaction mechanism.

5.3.2 Laminar Flame Speed at Engine-Relevant Conditions

Laminar burning velocities at engine-relevant conditions are computed as an input for subsequent CFD calculations using the kinetic scheme of Conaire et al. [86]. However, the validity of this approach is limited since instability effects – which have a relatively strong influence on combustion at low turbulence, high pressure conditions – are not considered by the kinetic scheme. In comparison to experimentally derived values of
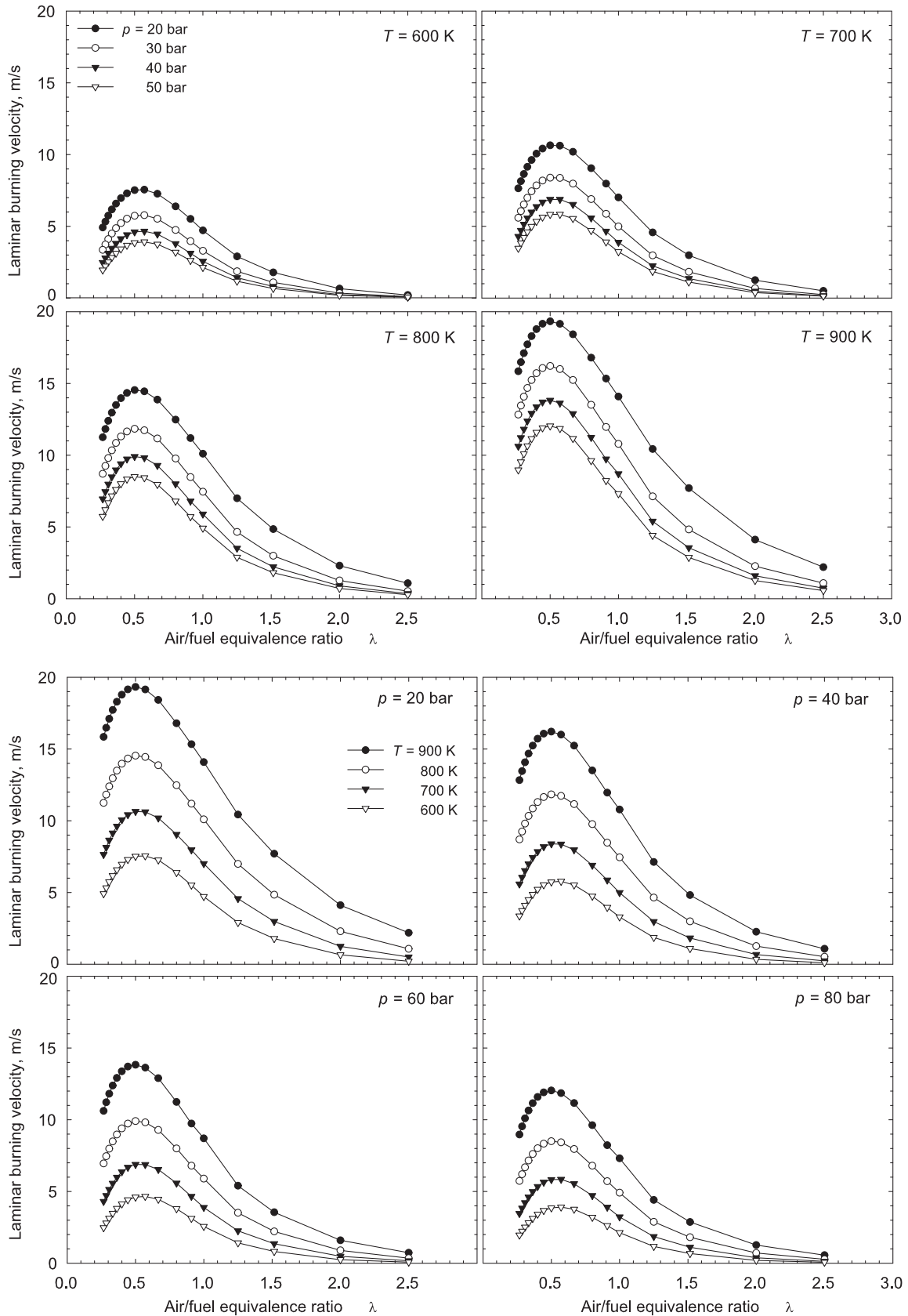
Figure 5.4: Laminar burning velocities predicted by computations with the kinetic scheme of Conaire et al. [86]. Data represent theoretical values of smooth stable flames where acceleration of the flame due to instability effects is not considered.

laminar flame speed, the computations underestimate flame velocities at elevated pressure levels.

Unburned temperature and pressure conditions are varied in the range from $T = 300$ K to 900 K and $p = 1$ bar to 80 bar. Air/fuel equivalence ratios are considered in the range from $\lambda = 0.3$ to 2.5. The λ-limits are defined by convergence issues of the numerical scheme. Robust solutions could not be found outside these limits.

The computed data predict an acceleration of the flame due to temperature increase and a deceleration of the flame caused by an increase of pressure, while the impact of pressure is below the impact of temperature. The peak flame speed over the entire regime is located at rich equivalence ratios, near $\lambda = 0.6$. Figure 5.4 shows computed laminar flame speed as a function of air/fuel equivalence ratio λ for most engine-relevant values of temperature ($T > 600$ K) and pressure ($p > 20$ bar).

5.4 Measurements on ETH-LAV Compression Machine

The necessity for experimental investigations on hydrogen laminar burning velocities arose from CFD simulations, employing laminar flame speed correlations on the basis of kinetic schemes and suggestions found in literature (cf. Section 5.5). As a consequence to the sparse extent of basic experimental investigations on hydrogen flame speed measurements at engine-like conditions, measurements on a single-cylinder compression machine are conducted at LAV, ETH Zurich within the present work, supported by associated master theses [100,106].

5.4.1 Investigated Conditions

The investigation focuses on engine-relevant combustion of hydrogen/air mixtures at high-pressure environments. Variations of the air/fuel equivalence ratio are performed in the range between $\lambda = 0.4$ and 2.8. The ig-

(a) *T*-*p* dependency.   (b) *T*-λ dependency.   (c) *p*-λ dependency.
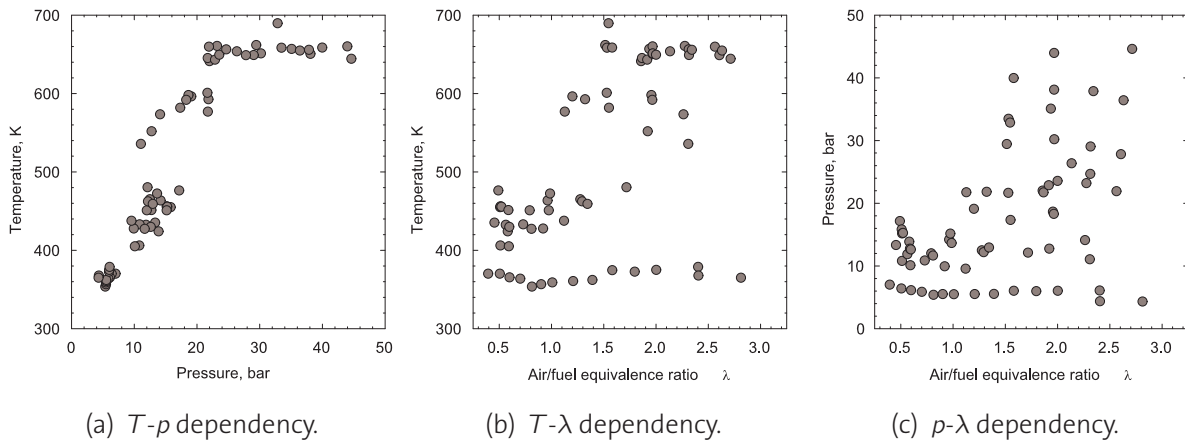
Figure 5.5: Ignition conditions of operating points investigated in the single-cylinder compression machine listed by air/fuel equivalence ratio λ, temperature and pressure.

nition temperatures and pressures vary from $T = 350$ K to 700 K and from $p = 5$ bar to 45 bar. An overview on the investigated operation points is given in Figure 5.5. Flame propagation speeds are determined by an optical analysis where the OH-chemiluminescence in the reaction zone is detected with a high-speed camera. Additionally, a zero-dimensional analysis of pressure traces is employed.

The purpose of the measurements is to define burning velocities under realistic conditions, including a possible increase of flame speed due to hydrodynamic instability effects which are not covered by one-dimensional simulations using detailed kinetic schemes. Regarding hydrogen IC engine combustion, instability effects might interfere with flame front wrinkling caused by turbulence.

5.4.2   Experimental Setup

A single-cylinder compression machine, basically designed for investigation of auto ignition combustion [31], is adapted to spark ignition of premixed hydrogen/air mixtures in order to examine high pressure, high temperature spherically expanding flames. The device is characterised by a large flexibility regarding initial conditions and compression ratio and is capable to withstand in-cylinder pressures up to $p = 200$ bar. The piston movement of the compression machine is caused by hydraulic and pneu-

Specifications of ETH-LAV Compression Machine:

Stroke	mm	120-250	Driving pressure	bar	15-50
Bore	mm	84	Cylinder charge pressure	bar	1.1-3
Compression Ratio	-	11-21	Max. combustion pressure	bar	200
Equivalent engine speed	rpm	1500-3000	Hydrogen supply pressure	bar	50

1: Cylinder head
2: Pressure sensor
3: Hydrogen injector
4: Spark plug
5: Liner
6: Piston
7: Glass window
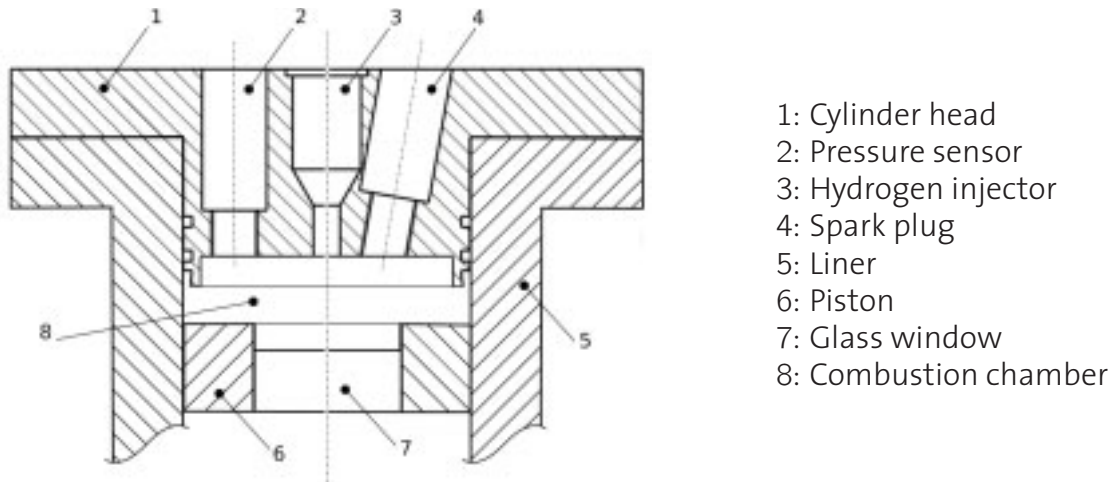8: Combustion chamber

Figure 5.6: Specifications of the single-cylinder compression machine and cross sectional view with description of the components.

matic forces. The machine operates on a single compression and expansion stroke followed by an oscillation of the free moving piston. The compression ratio is adjusted by setting of the driving pressure and cylinder charge pressure, influencing the acceleration of the piston and the load.

The combustion chamber is axially symmetric with a plain cylinder head. A bar of $w = 4$ mm width and $h = 9$ mm height is kept at the rim of the cylinder in order to avoid collision with the piston. The piston has a cylindrical cavity of 17 mm depth and 45 mm in diameter and is equipped with a quartz window of the same size enabling optical access to the combustion chamber. The spark plug is positioned with an offset of 16.6 mm to the central vertical axis and is declined by 10° in order to increase the visible range of the passing flame front through the piston window.

Images of the OH-chemiluminescence of the combustion process are recorded with a high-speed CCD camera (La-Vision Ultra Speed Star 5) using a frequency of $f = 10$ kHz and a resolution of 512×512 pixel. An image intensifier module (La-Vision IRO) is used to amplify the light intensity of the OH-signal released during combustion. The amplification is adjusted in correlation to the measured level of air/fuel equivalence ratio λ. The

system is capable of detecting OH-signals even of very lean mixtures (up to $\lambda = 3.0$) where the intensity of chemiluminescence is known to be particular weak. To protect the phosphor screen of the intensifier module at high gain levels, a lens aperture of 10 mm diameter is used to mask the spark location where an excessive OH-signal is produced during ignition.

A piezo-actuated standard gasoline injector with a cone nozzle is used for fuel injection. Hydrogen is supplied from a small reservoir with an initial pressure limited to $p = 50$ bar in order to prevent gas leakage at the injector nozzle. The injected hydrogen mass is determined by pressure measurements in the reservoir using a piezoresistive pressure sensor (Kistler 4045A100). To maximise the decrease in pressure and consequently increase the accuracy of the measurements, the size of the hydrogen reservoir is sufficiently small ($V = 18.75$ cm^3). Hydrogen is injected into the cylinder with a time advance of $\Delta t \approx 3$ s prior to start of compression in order to provide a sufficient homogenisation of the mixture. The air mass is specified by temperature and pressure measurement of the charge at bottom dead centre for a determination of fuel/air equivalence ratio. Main specifications of the compression machine are summarised in the table given in Figure 5.6.

5.4.3   Estimation of Mixture Homogenisation and Turbulence Intensity

CFD simulations of the injection and compression process are conducted to estimate the mixture homogenisation and turbulence intensity at ignition timing. The objective is to obtain high levels of fuel homogeneity and lowest levels of turbulence velocity fluctuations for the investigation of laminar flames. Three different operating points, $\lambda = 0.5$, 1.0 and 2.0 are numerically examined. To reduce computational costs, a rotation-symmetric grid is applied as CFD model disregarding the geometry of the spark plug.

The evolution of mean radial and axial velocities of the cold gas is illustrated in Figure 5.7 (a). During compression the axial velocity in the combustion chamber reaches maximum mean values of $u_a = 3.5$ m/s while
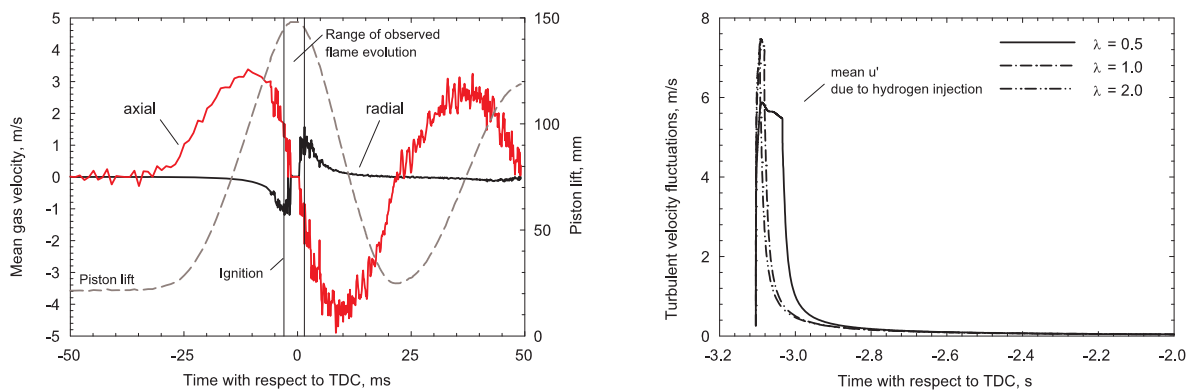
(a) Mean axial and radial gas velocities of the cold mixture ($\lambda = 1.0$).

(b) Mean values of u' during injection.

Figure 5.7: Computed mean axial and radial gas velocities of the cold mixture and turbulent velocity fluctuations u' in the compression machine during hydrogen injection.
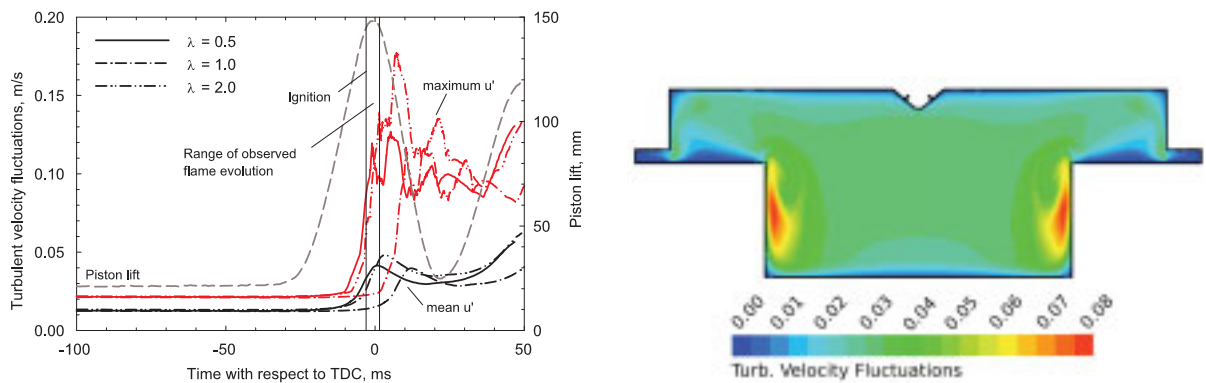
(a) Mean and maximum values of u' in m/s.

(b) Allocation of u' in m/s at ignition timing ($\sim$TDC).

Figure 5.8: Computed turbulent velocity fluctuations u' in the compression machine for start of injection at $\Delta t = 3.1$ s prior to compression.
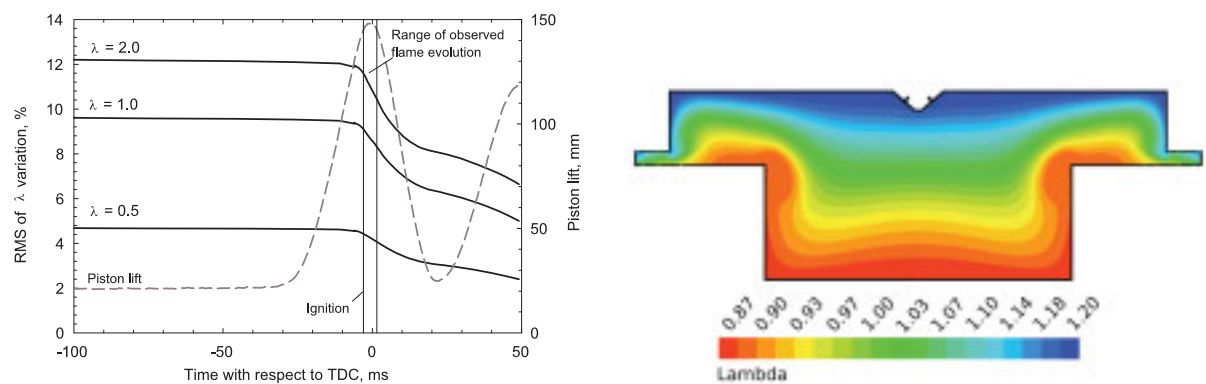
(a) Root mean square of variations of λ.

(b) Spatial distribution of air/fuel equivalence ratio λ at ignition timing ($\sim$TDC).

Figure 5.9: Computed distribution of local air/fuel equivalence ratio λ in the compression machine for start of injection at $\Delta t = 3.1$ s prior to compression.

the maximum radial component is about $u_r = 1$ m/s. In order to avoid influence of the cold gas motion on the propagation of the flame, measurements have to be conducted close to TDC where both axial and radial velocity components are virtually zero.

Figure 5.7 (b) depicts mean turbulent velocity fluctuations with start of hydrogen injection approximately 3 s prior to compression. Employing a sufficient time delay between the end of injection and the start of compression, the turbulence kinetic energy of the hydrogen jet is completely dissipated. As depicted in Figure 5.8 (a), the turbulence velocity fluctuations at the onset of flame propagation are merely caused by compression of the mixture. Maximum values range at a level of $u' = 0.1$ m/s to 0.15 m/s near TDC. In Figure 5.8 (b) turbulence velocity fluctuations are shown in a cross-sectional view at ignition timing. The mean values in the centre of the combustion chamber range at a level of $u' = 0.03$ m/s to 0.05 m/s. Consequently, with respect to the high values of laminar burning velocities expected for hydrogen flames, the existing turbulence in the cold mixture may be expected to be of inferior influence on the flame speed.

Regarding fuel homogenisation, it is found that rich mixtures show lower fluctuations in equivalence ratio than stoichiometric or lean mixtures. This effect is caused by an enlargement of injection time frames for rich mixtures resulting in an extension of the turbulence level during injection. Mixing is entirely driven by turbulence. Accordingly, those operating points with a higher amount of turbulence during injection lead to improved mixture homogenisation. Values of the averaged root mean square (RMS) calculated for the variance between local and global air/fuel equivalence ratios λ are given in Figure 5.9 (a). The comparison of different operating points shows that with respect to TDC, the RMS of the mixture variance is below 5 % for rich mixtures ($\lambda = 0.5$) and slightly exceeds 10 % for lean mixtures ($\lambda = 2$).

The field of local air/fuel equivalence ratio λ within the vertical symmetry plane of the domain is depicted in Figure 5.9 (b) for a stoichiometric mixture. Relevant zones for the optical measurements are placed in the centre of the combustion chamber and show local air/fuel equivalence ratios which are sufficiently close to the nominal value of $\lambda = 1.0$. Rich and

lean regions are located close to the walls of the domain. Consequently, the entire minimum and maximum values of air/fuel equivalence ratio, predicted by CFD, range between $\lambda = 0.87$ and 1.20. The deviations from the nominal value of λ, however, do not affect the present measurements significantly, since the corresponding leaner and richer regions are mostly placed outside the observed flame radii ($r = 10$ mm to 40 mm).

5.4.4 Measuring Methods

Propagation velocities of the flame front are derived by evaluation of high-speed OH-chemiluminescence measurements and by thermodynamic analysis of pressure traces. Two independent measurement techniques are employed in order to verify the plausibility of the results. Measurements of each operating point are iterated six times for averaging. The pressure in the combustion chamber is recorded with a piezoelectric pressure transducer (Kistler 7061B). The corresponding temperatures of the burned and unburned gas zones are calculated by zero-dimensional models.

5.4.4.1 Optical Analysis of OH-Chemiluminescence

Illustrations of the OH-chemiluminescence of representative laminar and moderate turbulent hydrogen flames are given in Figures 5.10 and 5.11. Images of each single combustion event are recorded by a high-speed camera with a frequency of $f = 10$ kHz. Averaging of the images is not applied. The flame kernel, located at the spark, is masked for protection of the sensitive amplification system. The measurement is conducted close to TDC to avoid influence of the gas motion on the flame front velocity. The upper half of the presented flame propagation is located outside the window area due to an asymmetric position of the spark plug and is hence not visible in the images.

Measurements depicted in Figure 5.10 show that a delay between the injection and the start of compression is introduced to provoke a dissipation of the turbulent kinetic energy of the hydrogen jet. The turbulent velocity fluctuations at ignition timing decay with increasing latency after the end
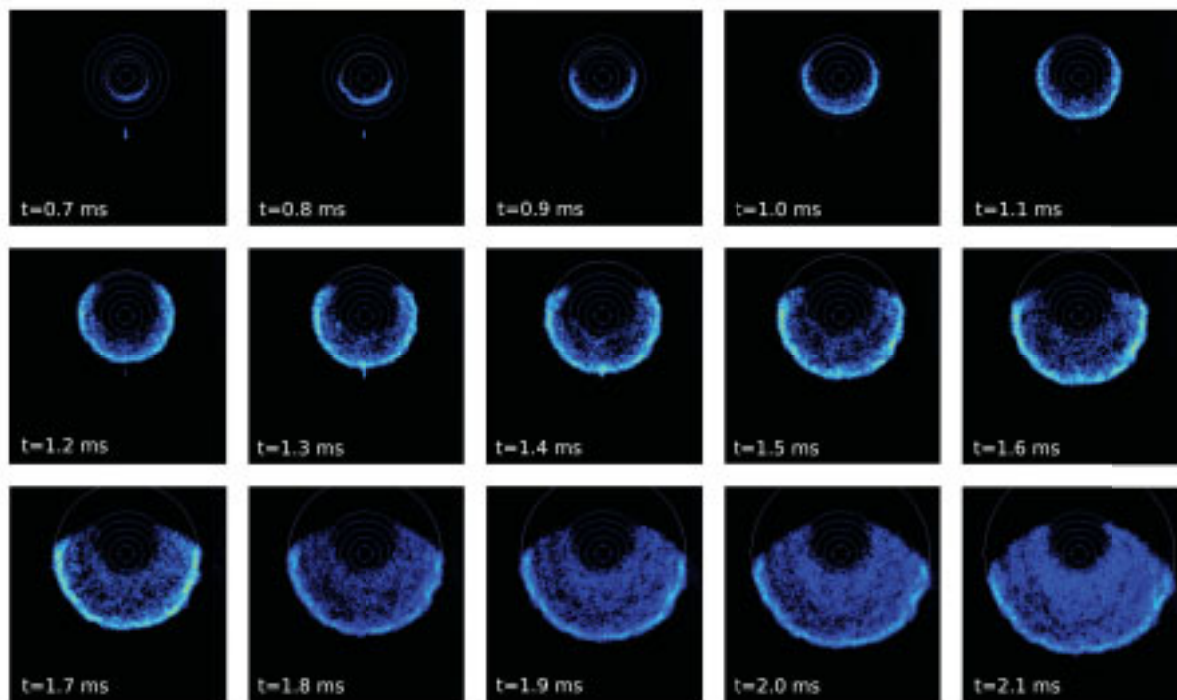
Figure 5.10: OH-chemiluminescence of a laminar hydrogen flame, as used for derivation of laminar burning velocities ($\lambda = 1.6$, $p_{ign} = 13$ bar, $T_{ign} = 600$ K). Compression starts with a delay of 3 seconds after hydrogen injection in order to provide low turbulence intensity and high degree of homogenisation. Scale: The diagonal of each frame is $l = 88.3$ mm.
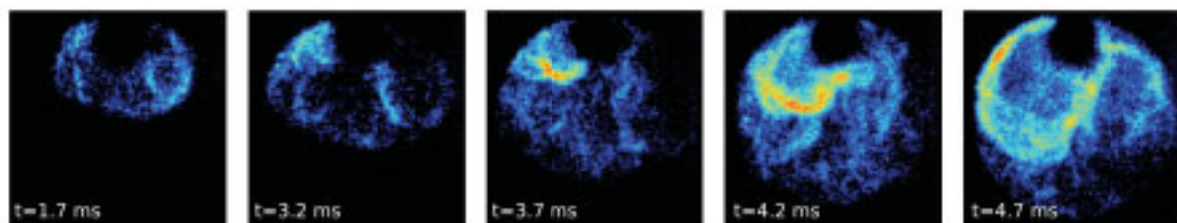
Figure 5.11: OH-chemiluminescence of a moderately turbulent hydrogen flame ($\lambda = 2.4$, $p_{ign} = 11$ bar, $T_{ign} = 600$ K). Compression starts synchronically with hydrogen injection. Turbulence intensity is increased and inhomogeneities within the mixture occur. Corresponding flame types are not employed for derivation of burning velocities. Scale: The diagonal of each frame is $l = 88.3$ mm.

of injection. Consequently, the flame develops in a quasi turbulence-free environment and is referred to as laminar. The spherical growth of the flame and the uniform intensity of the OH-signal in the burned zone accentuate the low turbulence intensity and the high degree of homogenisation of the mixture. Assumptions are confirmed by results of CFD calculations which show negligible turbulent intensities and sufficient mixture homogenisation, as discussed before.

(a) Optical analysis.

(b) Thermodynamic analysis.
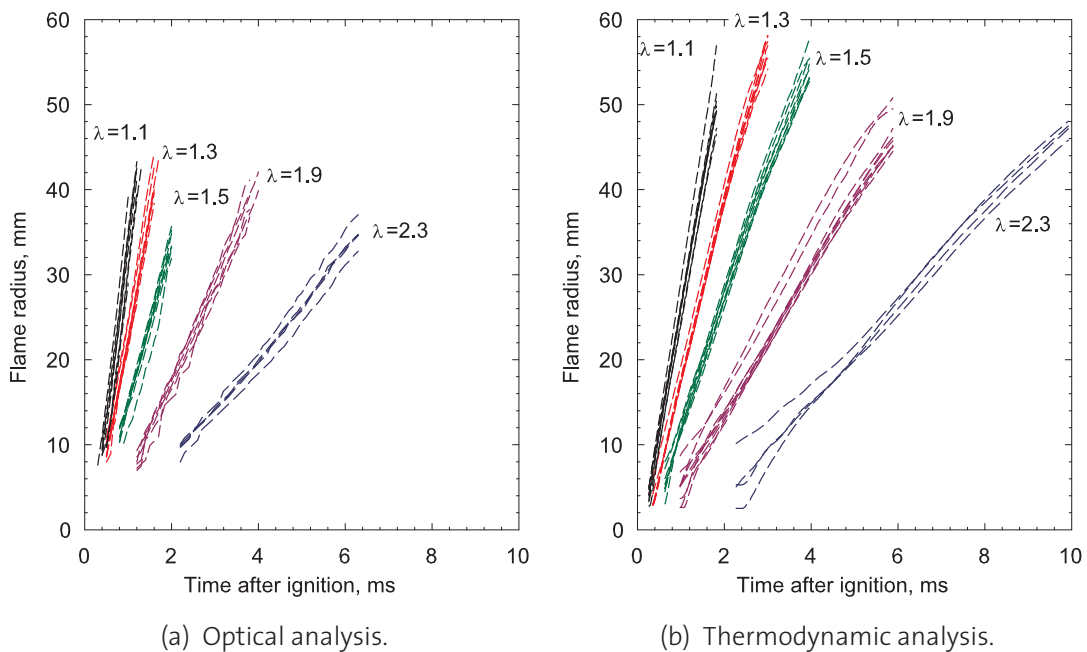
Figure 5.12: Flame front radius as a function of time for various values of air/fuel equivalence ratio λ. Conditions at ignition timing vary in the range of $p_{ign} = 21$ bar to 23 bar, $T_{ign} = 575$ K to 660 K.

Contrarily, hydrogen is injected during the beginning of the compression phase for measurements depicted in Figure 5.11. The time scales are too short for a dissipation of the turbulence energy generated by injection. Correspondingly, the optical analysis shows an unstructured flame front with varying intensities of the OH-signal, suggesting a moderately turbulent flame and mixture inhomogeneities. This type of flame propagation is only examined for a comparison to the homogeneous laminar case. Values of burning velocities are not derived.

The radii r_f of the expanding flame are determined by analysis of OH-chemiluminescence photographs. The values of r_f are a linear function of time. Measurements with approximately equal ignition conditions ($p_{ign} = 21$ bar to 23 bar, $T_{ign} = 575$ K to 660 K) are grouped in Figure 5.12 for various equivalence ratios and compared to results of thermodynamic analysis. The intense influence of mixture stoichiometry on the propagation speed of the flame front is demonstrated. The measurements are averaged for each of the series. The corresponding stretched flame front velocity S_n is obtained by derivation of the averaged flame radius r_f according to Equation (5.1).

5.4.4.2   Thermodynamic Analysis of Pressure Traces

An engine cycle simulation program, WEG [87], which is especially designed for calculation of heat release in the single-cylinder compression machine, is employed for thermodynamic analysis of the measured pressure traces. A spherical growth of the flame front is assumed, and the volume of the burned zone $V_b = f(r_f, z)$, and the flame surface $A_f = f(r_f, z)$ are calculated by means of the flame radius r_f and the piston position z using a three-dimensional model of the combustion chamber. Similar to the optical approach, the acquired flame radius is used for a derivation of the stretched flame front velocity S_n according to Equation (5.1).

Figure 5.13 (a) shows a correlation between values of S_n derived by the optical and the thermodynamic approach. The bisector in the graph describes the line of identical solutions. Points situated above this line denote higher flame front velocities received from optical measurements in comparison to results of the thermodynamic analysis. With respect to flame front velocities from $S_n = 10$ m/s to 15 m/s, both methods give quite identical results. With respect to higher absolute values of S_n, the optical approach slightly overrates the velocities. In Figure 5.13 (b) results are plotted as a function of air/fuel equivalence ratio λ at varying temperature and pressure conditions. Although both approaches of evaluating flame front velocities S_n are fundamentally independent, a satisfying compliance between the results can be observed.

5.4.5   Determination of Laminar Burning Velocities

The flame front velocities S_n derived by the optical approach and by thermodynamic analysis differ from the burning velocity u_n by the unburned gas expansion velocity v_g. The expansion factor κ_{exp} (Equation 5.4) is used for the conversion between S_n and u_n. Values for the burning velocities u_n of the stretched unstable flame are derived, describing the rate at which the fresh mixture is being consumed by the flame front. Figures 5.13 (c-d) show a comparison of results obtained by the optical and thermodynamic analysis. Corresponding values for the expansion factor are given in Fig-
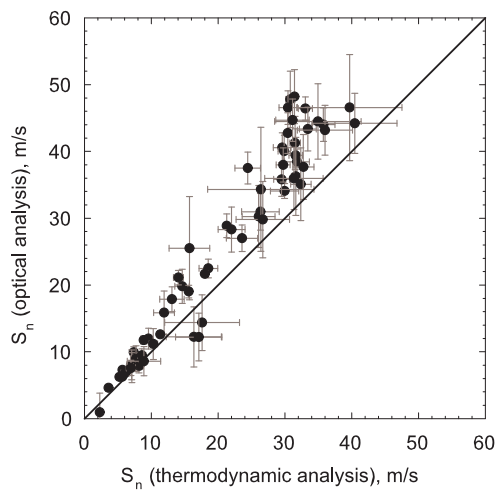
(a) Comparison of S_n predicted by optical and thermodynamic analysis.
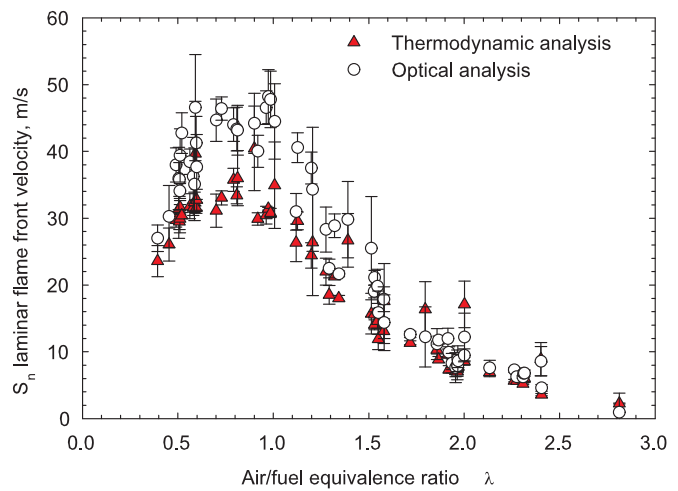
(b) S_n versus air/fuel equivalence ratio λ at varying temperature and pressure conditions.
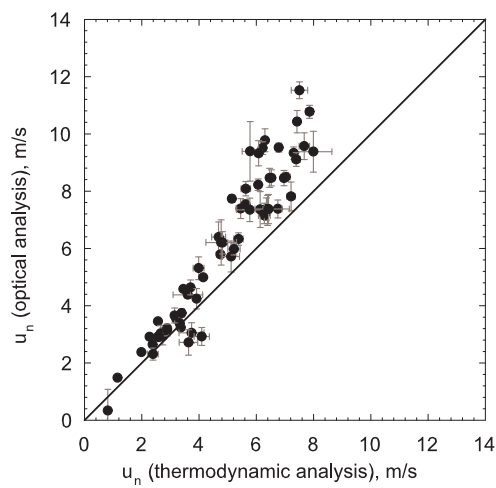
(c) Comparison of u_n predicted by optical and thermodynamic analysis.
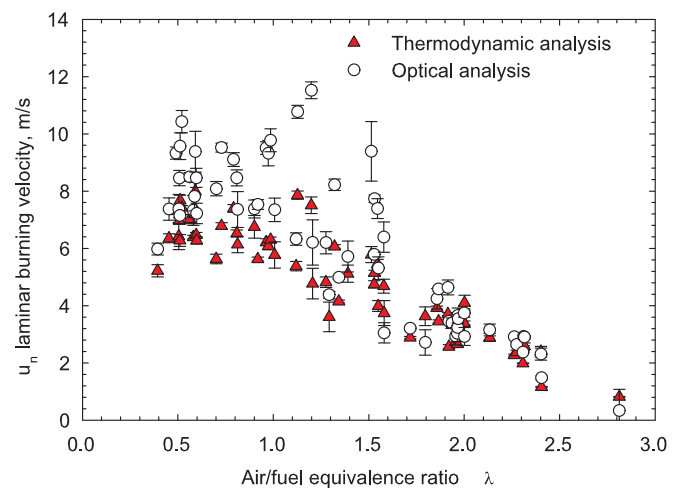
(d) u_n versus air/fuel equivalence ratio λ at varying temperature and pressure conditions.
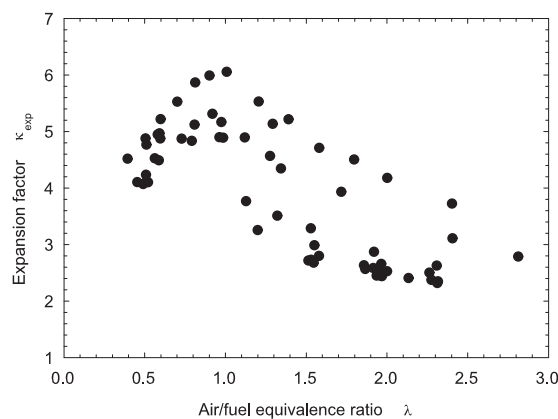
(e) Expansion factor computed by Equation (5.4) for all T,p-combinations.

Figure 5.13: Laminar flame front velocities S_n (a,b) and laminar burning velocities u_n (c,d) obtained by experimental investigations. The expansion factor κ_{exp} (e) is used for the conversion between S_n and u_n.

ure 5.13 (e). Similar to the findings regarding flame front velocities, burning velocities of lean mixtures show a satisfying agreement between the two approaches, whereas discrepancies appear for air/fuel equivalence ratios $\lambda < 1.5$. Again, the values of the optical analysis are slightly higher than the thermodynamic results. Uncertainties in the determination of the flame front radius may be caused by the OH-threshold of the chemiluminescence method which – in contrast to the Schlieren method – provides limited accuracy regarding the identification of the frontier between the burned and unburned zone.

Stretch effects and flame instabilities are important for the derivation of burning velocities. The stretched flame front velocity S_n is connected to its stretch-free value S by a term containing the Markstein length L_b and the stretch rate α (Equation 5.2). The flame is always positively stretched ($L_b < 0$) in the present measurements. The weight of this effect, however, decays with increasing flame radii and relatively large flame balls in the range from $r = 10$ mm to 40 mm are currently investigated. Consequently, small values of strain rate ($\alpha < 5000$ s^{-1}) are obtained where the accelerating influence of flame instabilities far exceeds the increase of laminar flame speed due to stretch (cf. Figure 5.15).

5.4.6   Comparison of Unstable and Stable Flames

A remarkable influence on the value of burning velocities emerges from thermodiffusive and hydrodynamic instabilities leading to an acceleration of the flame front. The instabilities arise from Lewis number and high-pressure effects and are present at engine-like conditions. Measurements of burning velocities include instability effects. Correspondingly, the results obtained differ to predictions of kinetic models which give theoretical flame speed values of smooth stable flames. Experimental data and reaction mechanism calculations are compared to evaluate the magnitude of instabilities. Additionally, an instability analysis is applied for a correction of measured unstable burning velocities.
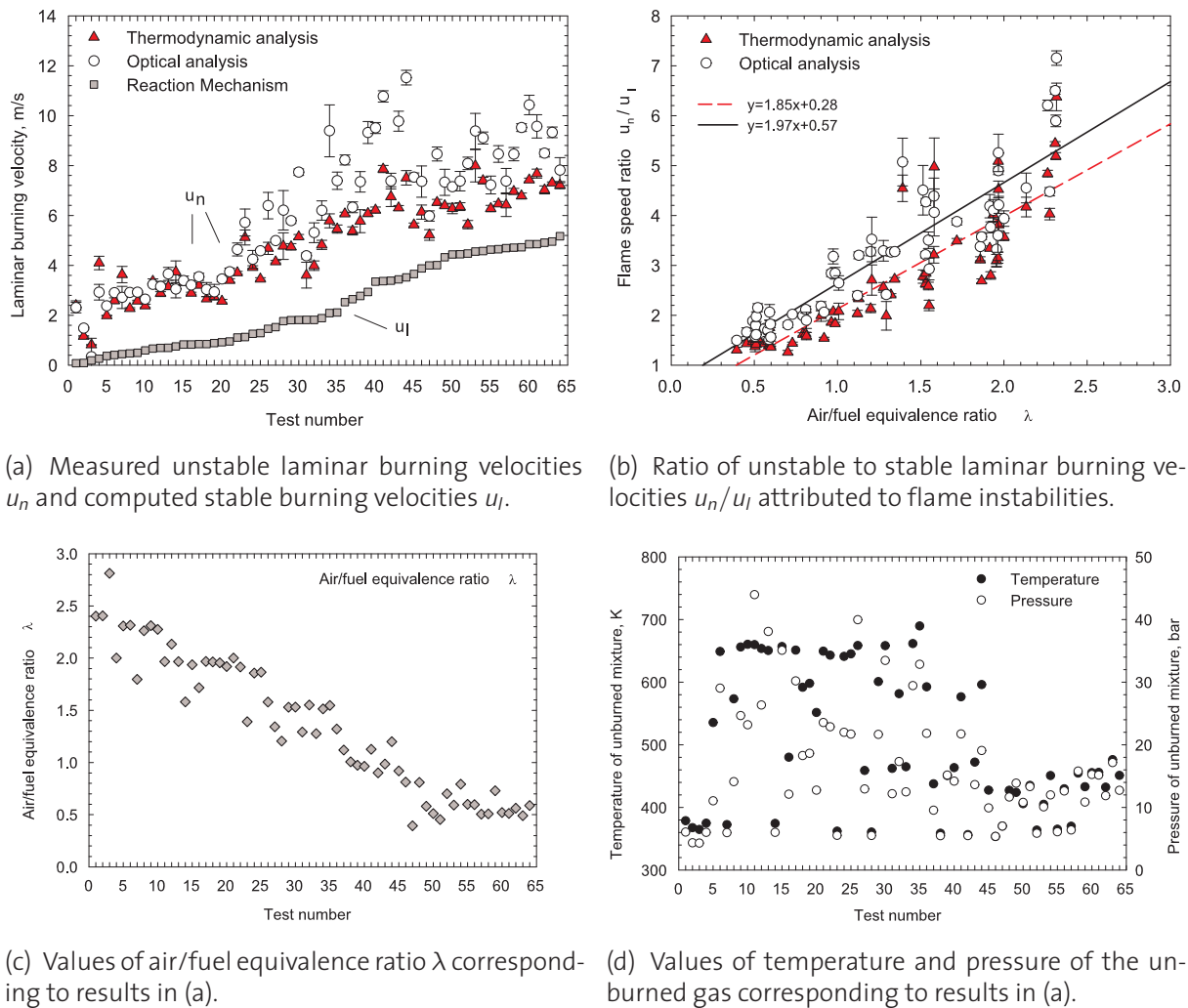
(a) Measured unstable laminar burning velocities u_n and computed stable burning velocities u_l.

(b) Ratio of unstable to stable laminar burning velocities u_n/u_l attributed to flame instabilities.

(c) Values of air/fuel equivalence ratio λ corresponding to results in (a).

(d) Values of temperature and pressure of the unburned gas corresponding to results in (a).

Figure 5.14: Comparison of unstable laminar burning velocities u_n derived from flame speed measurements (thermodynamic and optical analysis) and stable results u_l predicted by reaction mechanism computations employing the kinetic scheme of Conaire et al. [86].

5.4.6.1 Estimation of the Magnitude of Instability

Figure 5.14 (a) shows a comparison of laminar burning velocities of optical and thermodynamic analysis and data obtained from reaction mechanism computations. Burning velocities are set by test numbers for various equivalence ratios, unburned temperature and pressure conditions. Generally, laminar burning velocities determined within the present investigations are of higher magnitude than values given by the kinetic scheme.

The relative gradient of the measured slope, however, corresponds satisfyingly to all cases. A direct differentiation of the burning velocities is not

justified due to the different types of flame speeds of the individual measurements and correlations, e.g. the measured data include instability effects that are not covered by the mechanism.

As a rough estimation of the magnitude of instability, the enhancement of flame speed caused by instability effects is classified as the ratio between the laminar burning velocities u_n and u_l of unstable and stable flames. Values for u_n are received from thermodynamic analysis and optical measurements; values for u_l are employed from results predicted by reaction mechanism computations, using the scheme of Conaire et al. [86].

Figure 5.14 (b) depicts the ratio u_n/u_l as a function of air/fuel equivalence ratio λ. Rich mixtures indicate the lowest values of $u_n/u_l < 2$. The ratio increases almost linearly towards leaner mixtures, reaching values of about $u_n/u_l = 4$ at $\lambda = 2.0$. Results are quite similar for optical and thermodynamic measurements. Assuming that stretch effects are negligible in the measurements – due to the large flame radius – the increase of burning velocity is mostly dominated by instability effects. The positive gradient of the ratio u_n/u_l for increasing values of λ may be explained by intensified thermodiffusive perturbations for lean mixtures due to $Le < 1$.

5.4.6.2 Correction of Flame Front Instabilities

As depicted in Figure 5.14, the level of flame velocities identified within the present measurements is considerably located above the values given by reaction mechanism calculations. The discrepancy may be explained by the different nature of flames where measurements represent unstable flames and kinetic models represent stable flames. As discussed before, hydrogen flames at high-pressure environments are affected by instability effects which cause cellularity and increase of the flame front velocity.

A method proposed by Bradley et al. [21] is applied for a correction of flame front instability effects. The approach is based on linear stability theory, supposing an onset of instability for Peclet numbers above a critical value Pe_{cl}, given by the critical flame radius r_{cr} according

$$Pe = \frac{r_{cr}}{\delta_l} \tag{5.5}$$

where $\delta_l = \nu/u_l$ is the laminar flame thickness determined by computations with a kinetic scheme.

The instability is assumed to be limited by an upper and lower wavenumber $n_u = f(Pe)$ and $n_l = f(Pe)$ defining a peninsula of instability as a function of Pe. The flame is entirely stable with respect to all wavenumbers n for Peclet numbers below Pe_{cl}. Following Al-Shahrany et al. [9], a burning velocity enhancement factor F is defined at each Peclet number as

$$F = \left(\frac{S_n}{S}\right)_{Pe} = \left(\frac{n_u}{n_l}\right)^{1/3}_{Pe}. \qquad (5.6)$$

The factor expresses the ratio of flame front velocity enhancement by instabilities compared to the laminar flame front velocity. The approach is based on the assumption that the ratio of burning velocities with and without instabilities is equal to that of the surface areas. Values for the upper wavenumber n_u and the lower wavenumber n_l are calculated with the theory of Bechtold & Matalon [13]. Correspondingly, instability corrected flame speeds $S = S_n/F$ are derived at each Peclet number, using measurements of unstable propagation speed $S_n = dr/dt$. An instability correction is applied in order to give an explanation for the discrepancy observed between measurements and reaction mechanism computations.

Figure 5.15 shows values of flame front velocities as a function of flame stretch α. Smaller values of α correspond to larger flame radii. An infinitely large flame radius is reached for $\alpha = 0$, representing stretch-free flame front velocities. The closed symbols depict flame speeds S_n obtained by thermodynamic analysis of measurements. While S_n follows a linear behaviour for $\alpha > \alpha_{cr}$, a rapid increase of flame speed is noted at α_{cr}, depicting the onset of instability. Applying the described method for a correction of instability effects, stable flame front velocities (S, open symbols) are derived from unstable values (S_n, closed symbols). A critical flame radius of $r_{cr} = 5.4$ mm is determined for stoichiometric mixtures with initial unburned conditions of $p = 13.6$ bar, $T = 472$ K. Fuel-rich flames ($\lambda = 0.6$) demonstrate more stable critical flame radii ($r_{cr} = 6$ mm) whereas the instability occurs already at $r_{cr} = 2.7$ mm considering fuel-lean flames ($\lambda = 1.5$). The corrected values show a remarkable reduction in the flame
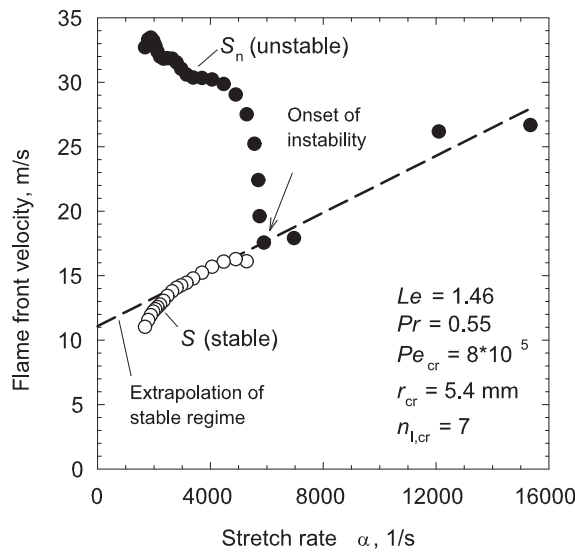
(a) Stoichiometric: $\lambda = 1.0$, $p = 13.6$ bar, $T = 472$ K.
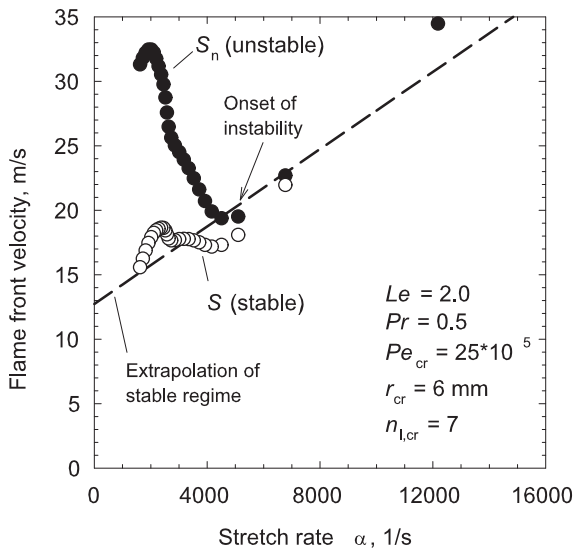
(b) Fuel-rich: $\lambda = 0.6$, $p = 11.9$ bar, $T = 432$ K.   (c) Fuel-lean: $\lambda = 1.5$, $p = 29.4$ bar, $T = 662$ K.
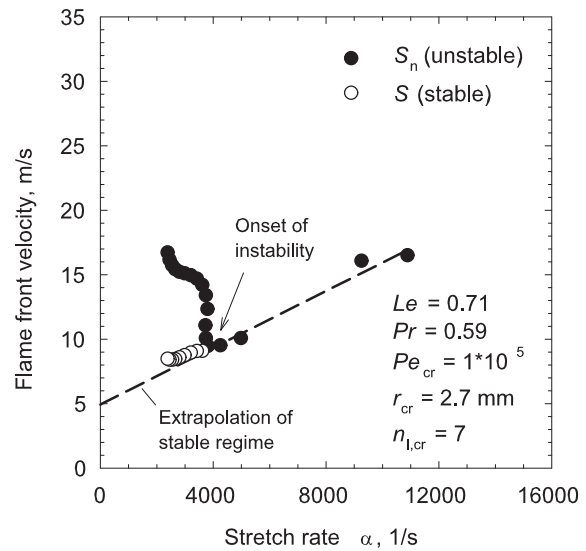
Figure 5.15: Flame front velocity $S_n = dr/dt$ as a function of stretch rate $\alpha = \frac{2}{r}S$. Comparison of measured unstable flame front velocities (S_n, closed symbols) and corrected, stable values derived by linear stability theory (S, open symbols).

front velocity and are in good agreement with an extrapolation of values measured prior to the onset of instability ($r < r_{cr}$), cf. the dashed line in Figures 5.15 (a)-(c). The gradient of this line, being negative in the present case, specifies the Markstein length L_b according to Equation (5.2). The theoretical stretch free, stable laminar flame speed is indicated by the extrapolated value of this line towards $\alpha = 0$. The level of corresponding values shows to be comparable to results predicted by kinetic computa-

tions with the employed reaction mechanism, considering the influence of the gas expansion coefficient κ.

Objective of the explained approach is to contribute to discussions concerning the disagreement noticed between measurements and reaction mechanism calculations. The investigations lead to the conclusion that laminar flame speeds at the investigated high-pressure conditions are unstable by nature. Consequently, a correction of measured data will yield imaginary values of stable flame speeds which cannot be reproduced by experiments. Since the significance of this procedure is questionable with respect to IC engine applications, non-corrected values of flame speed – directly obtained from experimental results – are employed for the derivation of burning velocities.

5.5 Derivation of Laminar Flame Speed Correlations

Laminar burning velocities are summarised in an expression which may be used as an input for turbulent combustion models. The analytical expression in the form of

$$s_L = s_{L0}(\phi) \left(\frac{T_u}{T_0} \right)^{\alpha} \left(\frac{p}{p_0} \right)^{\beta} (1 - \gamma X_{EGR}) , \qquad (5.7)$$

as proposed by Milton & Keck [75] is used. Depending on the type of investigated laminar flame speed, s_{L0} describes values of laminar burning velocities u_l (for stable flames) or u_n (for unstable flames) as a function of the equivalence ratio at the reference condition specified by T_0 and p_0. The flame speed s_L of a mixture conditioned with the unburned temperature T_u and the pressure p may then be obtained in terms of the temperature exponent α and the pressure exponent β. The coefficient γ accounts for a change in flame speed due to variation of the mass fraction of the residual gases X_{EGR}. The correlations provide values of s_L which are taken as an input for the turbulent combustion models specified in Sections 4.3 and 4.4.

5.5.1   Reaction Mechanism Correlation

Employing flame speed data of the kinetic computations presented in Section 5.3, two different strategies are followed. On the one hand, the computational results are directly used to derive a correlation, representing stable laminar flames. On the other hand, these results provide a basis for an extension of the validity range of existing experimental correlations, as described in Section 5.5.2.

A polynomial fit of order 6 is used to reproduce the computed data in the interval between $0.2 \leq \phi \leq 3.75$. Values of the polynomial prefactors a_0 to a_6 are adjusted to results of the reaction mechanism computations at $T_0 = 500$ K and $p_0 = 20$ bar in order to obtain a valid expression for s_{L0}.

The influence of temperature on the laminar burning velocity is determined by a logarithmic approach

$$ln\left(\frac{s_L}{s_{L0}}\right) = \alpha \cdot ln\left(\frac{T_u}{T_0}\right) , \tag{5.8}$$

at the constant pressure p_0 where α is a function of ϕ. Accordingly, the pressure exponent β is specified at the constant temperature T_0. Values for α range between 2.2 and 5.7 describing an increase of flame speed with rising temperature, and values for the pressure exponent range between $\beta = -0.5$ and -0.8 describing a moderate decrease in flame speed with rising pressure, cf. Figure 5.19.

The validity domain of the correlation based on reaction mechanism computations is $0.4 \leq \phi \leq 3.75$, $1 \leq p \leq 80$ bar and $300 \leq T_u \leq 900$ K. Beyond this range, the flame speed is linearly extrapolated to the extension limits. The correlation, referred to as Reaction Mechanism Correlation, is listed in App. B.2.

5.5.2   Extension of Leeds Database

Verhelst [111] presented a laminar flame speed correlation which is derived from measurements in the Leeds combustion bomb and is valid for
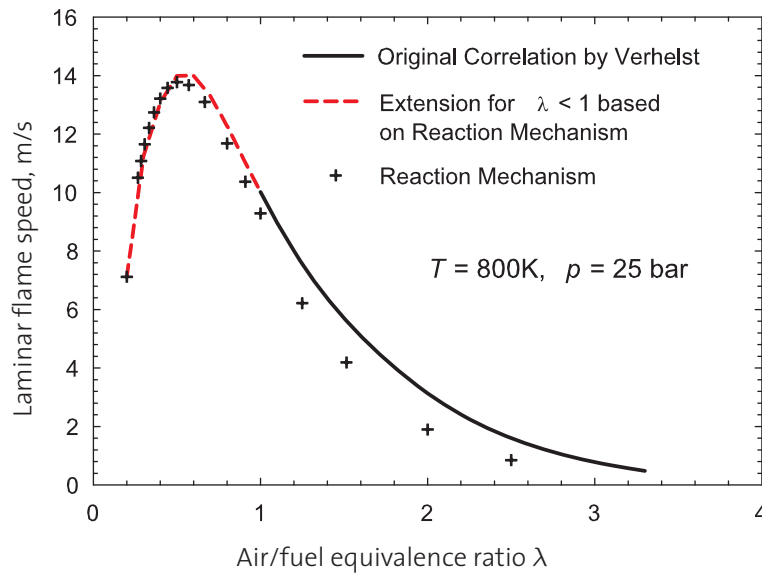
Figure 5.16: Extension of flame speed correlation proposed by Verhelst [111] using results of reaction mechanism computations with the kinetic scheme of Conaire et al. [86].

air/fuel equivalence ratios of $\lambda \geq 1.0$. With respect to the wide range of equivalence ratios present in DI hydrogen engines, the fundamental flame speed s_{L0} of this correlation is extended to the rich regime using results of reaction mechanism calculations. At basic conditions, p_0 and T_0, the values of s_{L0} for $\lambda < 1.0$ correspond to results predicted by the kinetic scheme, whereas for $\lambda \geq 1.0$ the original correlation is adopted, cf. Figure 5.16.

Regarding the influence of temperature and pressure on the flame speed, the expressions for the exponents α and β determined by experimental measurements in the Leeds combustion bomb remain unchanged. Correspondingly, a uniform increase in flame speed by rise of temperature is assumed over the entire regime of ϕ, expressed by $\alpha = 1.232$. For rising pressure levels and fuel/air equivalence ratios of $\phi \geq 0.42$ an increase in flame speed is supposed ($0 \leq \beta \leq 0.2$), while for $\phi < 0.42$ the value of flame speed decreases ($-0.26 \leq \beta < 0$), cf. Figure 5.19.

The validity domain of the correlation based on experimental results is limited by $0.3 \leq \phi \leq 1.0$, $1 \leq p \leq 10$ bar, $300 \leq T_u \leq 430$ K and $0 \leq X_{EGR} \leq 0.3$. For values of $1 < \phi \leq 3.75$, the correlation is based on results of computations with the kinetic scheme of Conaire et al. [86]. An extrapolation outside these limits yields reasonable physical results, how-

ever data are not verified yet in any experiment. A description of the correlation, referred to as Extended Leeds Database, is presented in App. B.3.

5.5.3   ETH-LAV Experimental Correlation (2007)

A preliminary correlation for laminar unstable hydrogen flame speed which is valid at engine-relevant conditions is derived from the measurements presented in Section 5.4 using data provided by thermodynamic analysis.[1] This preliminary correlation uses the same functional form as the existing expression described in Equation 5.7 where s_{L0} is the flame speed at basic conditions. A polynomial function of 6th order is used for a description of s_{L0} within the range of $0.4 < \phi < 2.5$. The temperature and pressure exponents α and β are defined as linear functions of equivalence ratio. The flame speed is linearly extrapolated for $\phi > 2.5$. The correlation, referred to as ETH-LAV Experimental Correlation, is listed in App. B.1. A more generic form of flame speed correlation, also including results of the optical analysis, is taken into consideration within a subsequent publication of the present work.

Since the measured data are not systematically arranged by temperature and pressure, an evolutionary algorithm is used for the determination of the correlation coefficients [106]. Target for the computations with the algorithm is the minimisation of the deviation between original values of the measurements and data provided by the correlation. A comparison between laminar burning velocities predicted by the correlation and experimental data of thermodynamic analysis is given in Figure 5.17. The correlation shows a good agreement with experimental data, despite the fact that most of the measurements are slightly underestimated. Results are repeated as a function of air/fuel equivalence ratio, pressure and temperature. A satisfying sensitivity of the correlation with respect to these quantities is noticed. Overall, the root mean square deviation between correlation and experimental results is 11.05 %.

---

[1]This correlation is based on experimental investigations conducted within the last part of the present work. Due to a restricted time schedule, additional CFD computations using this correlation are not conducted. In order to give an estimation of the results, the value Hf laminar burning velocities is postprocessed and compared with the different correlations on the basis of temperature and pressure traces for each of the computed operating points. Corresponding results are depicted in Section 7.3.1.
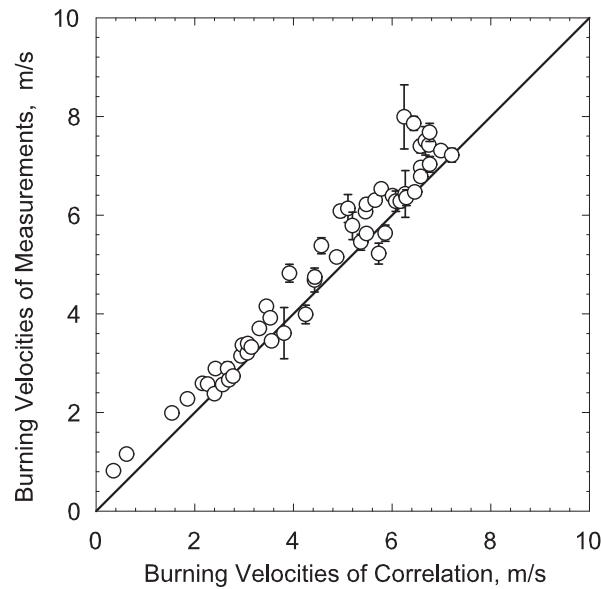
Figure 5.17: Comparison of correlated laminar burning velocities to results directly obtained from thermodynamic analysis of measurements.

Regarding the definition of the correlation exponents, the influence of temperature on flame speed is almost constant with respect to air/fuel equivalence ratio λ. The mean value of the temperature exponent is $\bar{\alpha} = 2.0$. A moderately decelerating influence of the pressure exponent β is predicted for mixtures with $\lambda \leq 2.5$. Fuel-rich mixtures are characterised by a small negative value of $\beta = -0.2$ with a direction towards zero for increasing values of λ, cf. Figure 5.19.

The validity domain of the correlation based on experimental results of the present work is $0.4 \leq \phi \leq 2.5$, $10 \leq p \leq 45$ bar and $350 \leq T_u \leq 800$ K. An extrapolation beyond these limits yields reasonable physical results, although these data are not verified.

5.5.4 Comparison of Correlations

The flame speed correlations presented above are based on independent types of laminar burning velocities and are fundamentally different. The ETH-LAV Experimental Correlation depends merely on flame speed derived from experimental investigations of high pressure flames and displays values of unstable laminar burning velocities u_n. The Reaction Mechanism Correlation is derived from a kinetic scheme which does not consider flame

front instabilities and predicts stable burning velocities u_l. Burning velocities of the Extended Leeds Database display unstable values of u_n; the significance of the results, however, is limited due to the small pressure and temperature range ($p \leq 10$ bar, $T_u \leq 430$ K) investigated. Additionally, results of this correlation for the rich regime are only a rough estimation, since the extension for $\lambda < 1.0$ is based on computational data.

Figure 5.18 gives a comparison between the correlations at engine-relevant temperature and pressure levels. Generally, the results show a maximum near $\lambda = 0.6$ with declining values of laminar flame speed towards the rich and lean regime. The gradient of the burning velocities with respect to varying values of equivalence ratio is comparable for all three correlations. A vertical offset between the different approaches is, however, observed. At unburned mixture conditions of $T = 600$ K and $p = 20$ bar (Figure 5.18 a), values of laminar burning velocities predicted by the ETH-LAV Experimental Correlation are close to the results of the Extended Leeds Database. Laminar burning velocities of stable flames predicted by the Reaction Mechanism Correlation result in lower values, as discussed in Section 5.4.6. At increased pressure levels ($T = 600$ K and $p = 40$ bar) comparable values of laminar burning velocities for the LAV-ETH Experimental Correlation and the Extended Leeds Database are shown with respect to air/fuel equivalence ratios $\lambda \geq 1.0$. As a result of the positive pressure exponent β, the magnitude of burning velocities for $\lambda < 1.0$ is remarkably increased for the Extended Leeds Database. At increased temperature levels ($T = 800$ K and $p = 20$ bar, Figure 5.18 b), similar results as those for the Reaction Mechanism Correlation are obtained. Here, the weakness of the Extended Leeds Database for extrapolations beyond the experimental validity range becomes obvious. Measured burning velocities at these conditions should be significantly increased compared to results of reaction mechanism computations due to the influence of flame front instabilities. This is not the case for the predicted values. The burning velocities obtained from the ETH-LAV Experimental Correlation, however, result in increased values of u_n. Due to the positive pressure exponent of the Extended Leeds Database there is a satisfying correspondence with results of the LAV-ETH Experimental Correlation at increased pressure levels ($T = 800$ K and $p = 40$ bar).

(a) Laminar burning velocities at $T = 600$ K, $p = 20$ bar to 40 bar.

(b) Laminar burning velocities at $T = 800$ K, $p = 20$ bar to 40 bar.
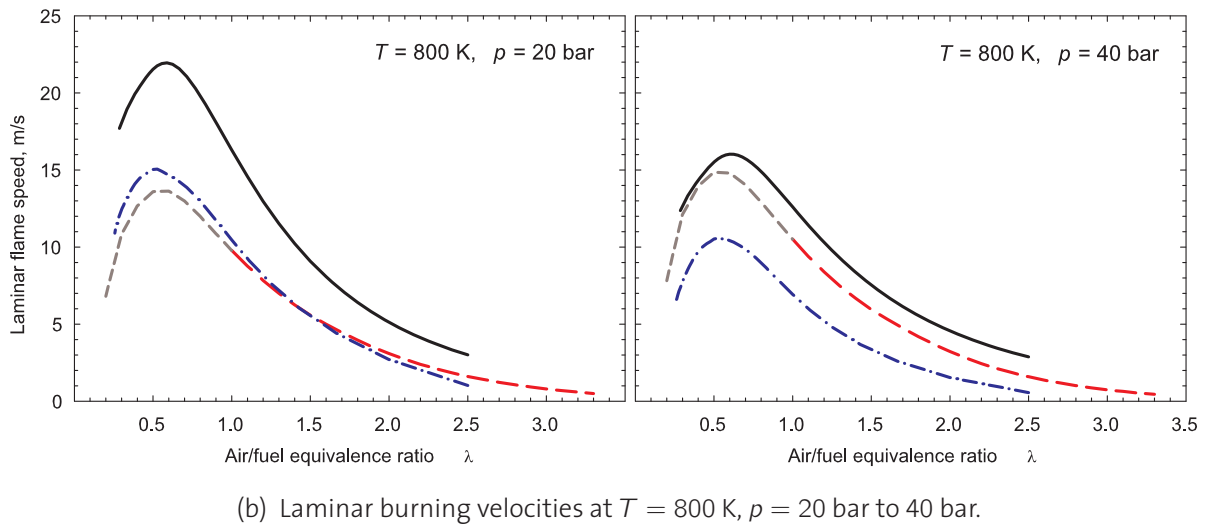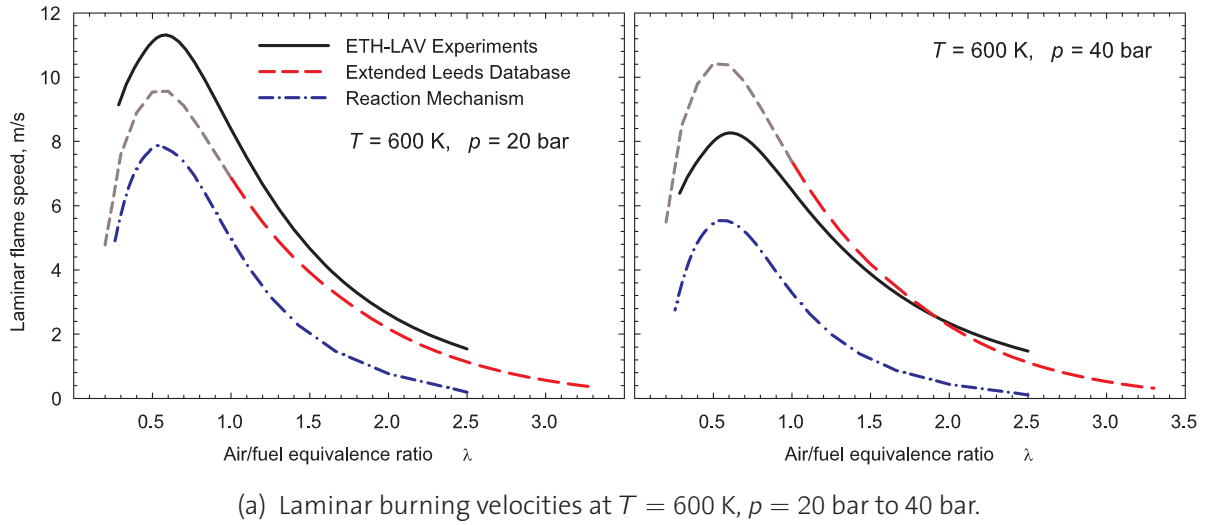
Figure 5.18: Laminar burning velocities of different flame speed correlations as a function of air/fuel equivalence ratio λ.

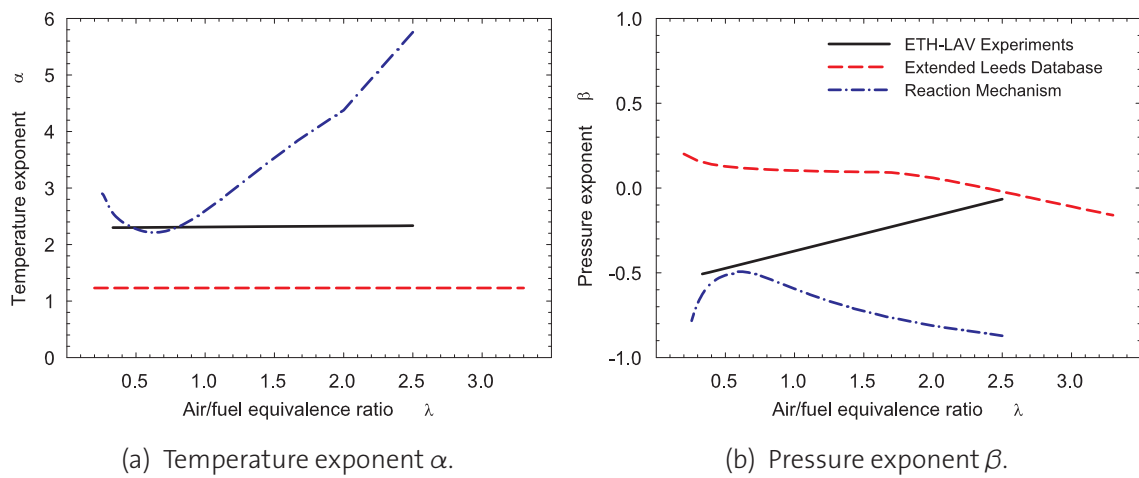(a) Temperature exponent α.

(b) Pressure exponent β.

Figure 5.19: Temperature and pressure exponents of flame speed correlations presented in Fig. 5.18 as a function of air/fuel equivalence ratio λ.

The sensitivity of the correlations with regard to pressure and temperature variations may be analysed by means of the temperature and pressure exponents α and β as displayed in Figure 5.19. Values of α are positive for all three correlations, whereas the values of β have opposite signs. The Extended Leeds Database comprehends a relatively low value for the temperature exponent ($\alpha \approx 1.2$), resulting in a smaller growth of the flame speed with increasing temperature. The value of β is positive for this correlation if $\lambda < 2.4$. The ETH-LAV Experimental Correlation and the Reaction Mechanism Correlation assume larger temperature exponents $\alpha \geq 2$ and mainly negative pressure exponents β. In the rich regime a negative value of $\beta \approx -0.5$ is obtained for both correlations. With increasing air/fuel equivalence ratio λ the pressure exponent moves towards positive values for the ETH-LAV Experimental Correlation and further declines for the Reaction Mechanism Correlation. The evolution of β towards positive values demonstrated for the ETH-LAV Experimental Correlation may be justified by an increase of instability for intensified lean mixtures due to $Le < 1$. The Reaction Mechanism Correlation does not show this effect because laminar stable flames are considered. This is not apparent for the Extended Leeds Database since not high enough pressure levels ($p < 10$ bar) have been examined for the determination of the pressure exponent.

In Figure 5.20, laminar burning velocities at rich, stoichiometric and lean conditions ($\lambda = 0.5$, 1.0 and 2.0) are displayed for temperatures and pressures in the range between $500 \leq T_u \leq 900$ K and $20 \leq p \leq 70$ bar. The gradient of iso-contours demonstrates the sensitivity of the correlations with respect to pressure. The ETH-LAV Experimental Correlation and the Reaction Mechanism Correlation show decreasing burning velocities for increasing pressure, indicated by a negative value of the pressure exponent β. The Extended Leeds Database shows a contrary effect with increasing burning velocities for elevated pressure levels. Regarding the temperature influence of the Reaction Mechanism Correlation, it can be noted that the high values of α at lean mixtures are of marginal influence due to general low values of burning velocities.
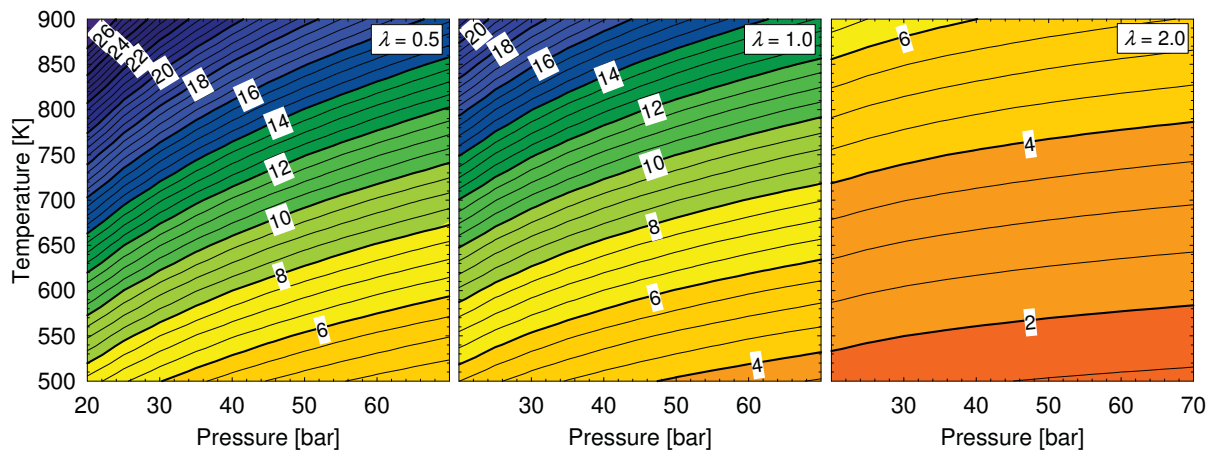
(a) **ETH-LAV Experiments**: Burning velocities in m/s corresponding to unstable laminar flames.
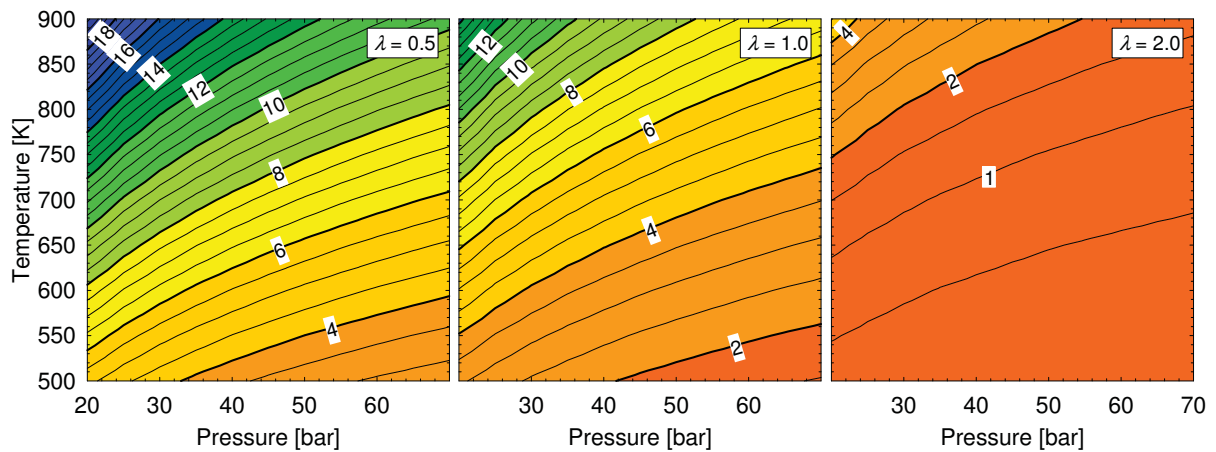
(b) **Reaction Mechanism**: Burning velocities in m/s corresponding to stable laminar flames.
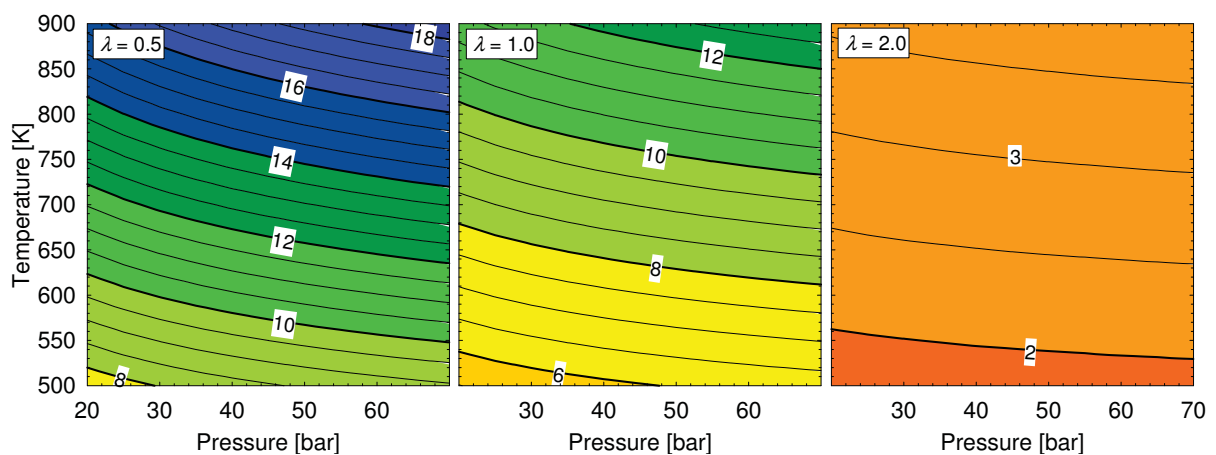
(c) **Extended Leeds Database**: Burning velocities in m/s corresponding to unstable laminar flames.

Figure 5.20: Laminar burning velocities as a function of unburned temperature and pressure, computed with flame speed correlations presented in Section 5.5 and in App. B.

5.6   Summary of Results

A fundamental contribution with respect to the determination of engine-relevant laminar hydrogen burning velocities is presented. Investigations include theoretical and experimental analysis of hydrogen flames of fuel-rich, stoichiometric and fuel-lean hydrogen/air mixtures. Computations employ a kinetic scheme of a recently published reaction mechanism [86] and are compared to experimental data. An experimental method is established to measure high-pressure high-temperature laminar flames at engine-like conditions in a single-cylinder compression machine by means of OH-chemiluminescence and zero-dimensional analysis of pressure traces. The question is addressed whether flame instability effects at high-pressure conditions influence the propagation speed of the flame front which might be relevant for IC engine applications. A comparison of results shows that flame speed measurements at high-pressure conditions demonstrate an accelerating effect of flame front instabilities on the value of laminar hydrogen burning velocity. Computations with a chemical model of a one-dimensional premixed flame are not able to reproduce this effect. Approaches of linear stability theory are applied in order to estimate the magnitude of instability effects. The mean ratio between unstable and stable laminar flame speeds observed in measurements is determined to $u_n/u_l \approx 2$ for stoichiometric mixtures. The ratio linearly increases towards lean air/fuel equivalence ratios λ.

The presented data may be used as input for CFD combustion models. Consequently, laminar flame speed correlations of stable and unstable flames are derived from computational and experimental results. With respect to variations of air/fuel equivalence ratio λ, the different correlations behave similar. Maximum flame speeds are slightly located in the rich regime. Due to instability effects, however, burning velocities of unstable flames (measurements) are substantial higher than those of stable flames (computations). The offset increases towards lean air/fuel equivalence ratios.

Chapter 6

Simulation of Mixture Formation

The present chapter depicts results of hydrogen mixture formation simulations conducted for the engine operating points specified in Chapter 2. A validation of hydrogen injection simulations is performed in Section 6.1, using Planar Laser Induced Fluorescence (PLIF) of the transparent research engine provided by [59]. Turbulent velocity fluctuations predicted by the applied turbulence models which are significant for the subsequent combustion simulations are compared in Section 6.1.2. A variation of injection timing and the impact on the achieved mixture distribution and turbulent velocity fluctuations are analysed in Section 6.2. The results are summarised and discussed in Section 6.3.

The gas exchange is computed with CFD using transient pressure and temperature states from one-dimensional engine cycle calculations as boundary conditions at the intake and exhaust port. As initial state of the exhaust cycle a homogeneous burned mixture is assumed. Camshaft timing is adjusted to minimise the level of residual gases in the cylinder charge. According to the CFD simulations, the residual gas content for stoichiometric mixtures is $Y_{EGR} \approx 2\,\%$.

6.1 Transparent Engine Mixture Formation

CFD simulations of the operating points defined in Section 2.1.2 are differentiated to PLIF measurements acquired in the transparent research engine. The objective is to compare computed and measured local mix-

ture concentrations within the vertical symmetry plane of the combustion chamber for discrete crank angles in order to verify the accuracy of the model.

Although information regarding turbulent velocity fluctuations is not acquired by the experiments, the computations are accomplished using alternate turbulence models, as explained in Section 3.2. Hydrogen mixture formation inside the combustion chamber of an engine is dominated by turbulence. Even for a highly molecular diffusive gas as hydrogen, time scales are too short that diffusion effects may significantly influence mixing. Turbulence controls the penetration of the hydrogen jet and affects the local mixture concentration. Consequently, the suitability of each turbulence model with respect to mixture formation simulations may be evaluated by a comparison of local mixture concentrations. In the following, results of early and late injection timings are validated, representing homogeneous and stratified mixtures.

6.1.1 Validation of Hydrogen Injection by LIF Measurements

6.1.1.1 Operating Point O1: $\lambda = 2.4$, $SOI = -120°$ CA

Figure 6.1 shows computations of an early hydrogen injection with $SOI = -120°$ CA (operating point O1) employing the SST, the RNG k-ε and the RSM turbulence model. The results are compared to experimental PLIF measurements in terms of hydrogen concentration. Regions leaner than $\lambda \geq 10$ are emphasised in blue, fuel-rich regions below $\lambda \leq 0.1$ are emphasised in red. The global equivalence ratio is $\lambda_{global} = 2.4$ and the engine speed is $n = 2000$ rpm, cf. operating point O1 in Table 2.2. In this configuration nearly the complete time of the compression stroke is available for the mixing process where the hydrogen jet propagates in a cylindrical path along the walls through the combustion chamber. The injection is hardly affected by the motion of the charge cycle since the engine is operated without swirl motion. The final mixture obtained at the end of the compression stroke shows partially homogenisation of hydrogen and air. Regarding the quality of the calculations, a generally satisfying compli-

Figure 6.1: Operating point O1: Hydrogen mixture formation simulations with different turbulence models (SST, k-ε RNG, RSM) in comparison to PLIF measurements. Blue regions specify equivalence ratio $\lambda \geq 10$, red regions $\lambda \leq 0.1$. Crank angle is given with respect to TDC ($SOI = -120°$ CA, $\lambda_{global} = 2.4$, $n = 2000$ rpm).

SST model k-ε RNG model   RSM model   PLIF measurements
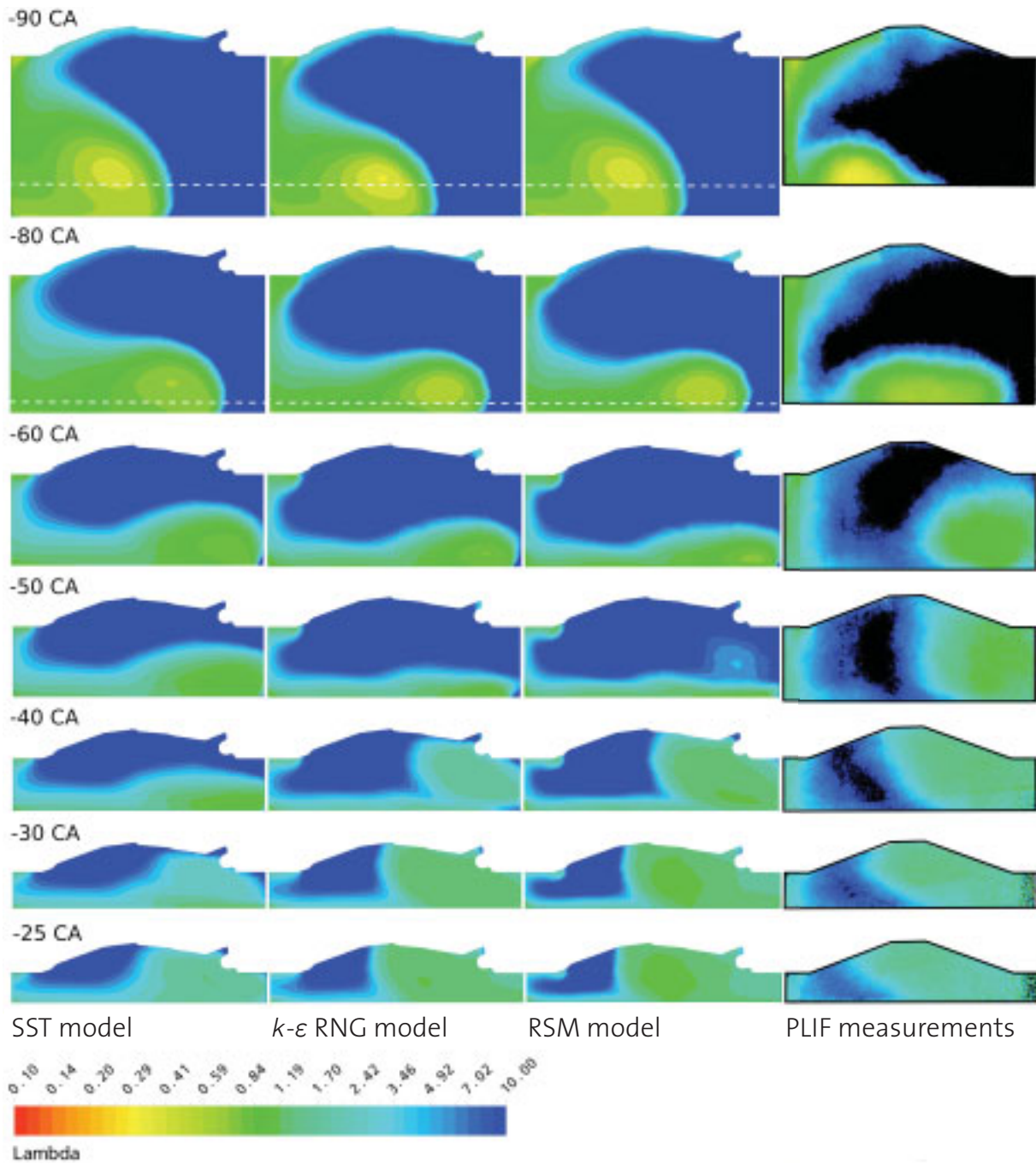
Variation of colour scale:

SST model k-ε RNG model   RSM model   PLIF measurements

Figure 6.1 continued.

ance of the numerical results with experimental measurements is noted in the context of RANS simulation.

At early stages of hydrogen mixture formation no significant difference of the mixture-distribution obtained from the individual turbulence models is observed from $\varphi = -120°$ CA to $-80°$ CA. The penetration depth of the hydrogen jet as well as the local equivalence ratio calculated by CFD gives an appropriate description of the mixture formation.

With reference to crank angle from $\varphi = -60°$ CA towards TDC, perceptible discrepancies between computational and experimental results emerge. Compared to results of the experimental analysis, the computed hydrogen jet propagation is decelerated for all three turbulence models. The experiment shows a faster detach of the hydrogen jet from the piston which is not predicted by the computational results. The hydrogen concentration computed with the RNG k-ε model and the RSM model is higher on the injection-side of the domain. This is caused by flow perpendicular to the displayed symmetry plane from $\varphi = -50°$ CA to $-40°$ CA. Finally, the results obtained with these two models at $\varphi = -25°$ CA correspond appropriately to the hydrogen distribution given by the PLIF measurements.

Due to the solution of additional transport equations, the numerical effort for calculations with the RSM model is more than twice as high compared to the two-equation models. Furthermore, numerical instabilities have to be managed. Consequently, to achieve applications of lower numerical expense, the RNG k-ε model should be employed prior to the RSM approach. The fact that different hydrogen mixture concentrations are generated by the three turbulence models, applying one and the same numerical grid, shows that the influence of artificial viscosity of the grid is of less weight than the influence of the turbulence models on turbulent viscosity.

The results obtained with the SST model underestimate the intensity of hydrogen concentration in the upper centre of the domain. It is supposed that turbulent kinetic energy is overrated in the SST model, as deduced from a comparison of turbulent velocity fluctuations of all three turbulence models in Section 6.1.2. There, additional information on the hydrogen distribution is given and the hydrogen volume fractions, obtained from computations with the discussed turbulence models, are displayed as a function of the equivalence ratio λ in Figure 6.4.
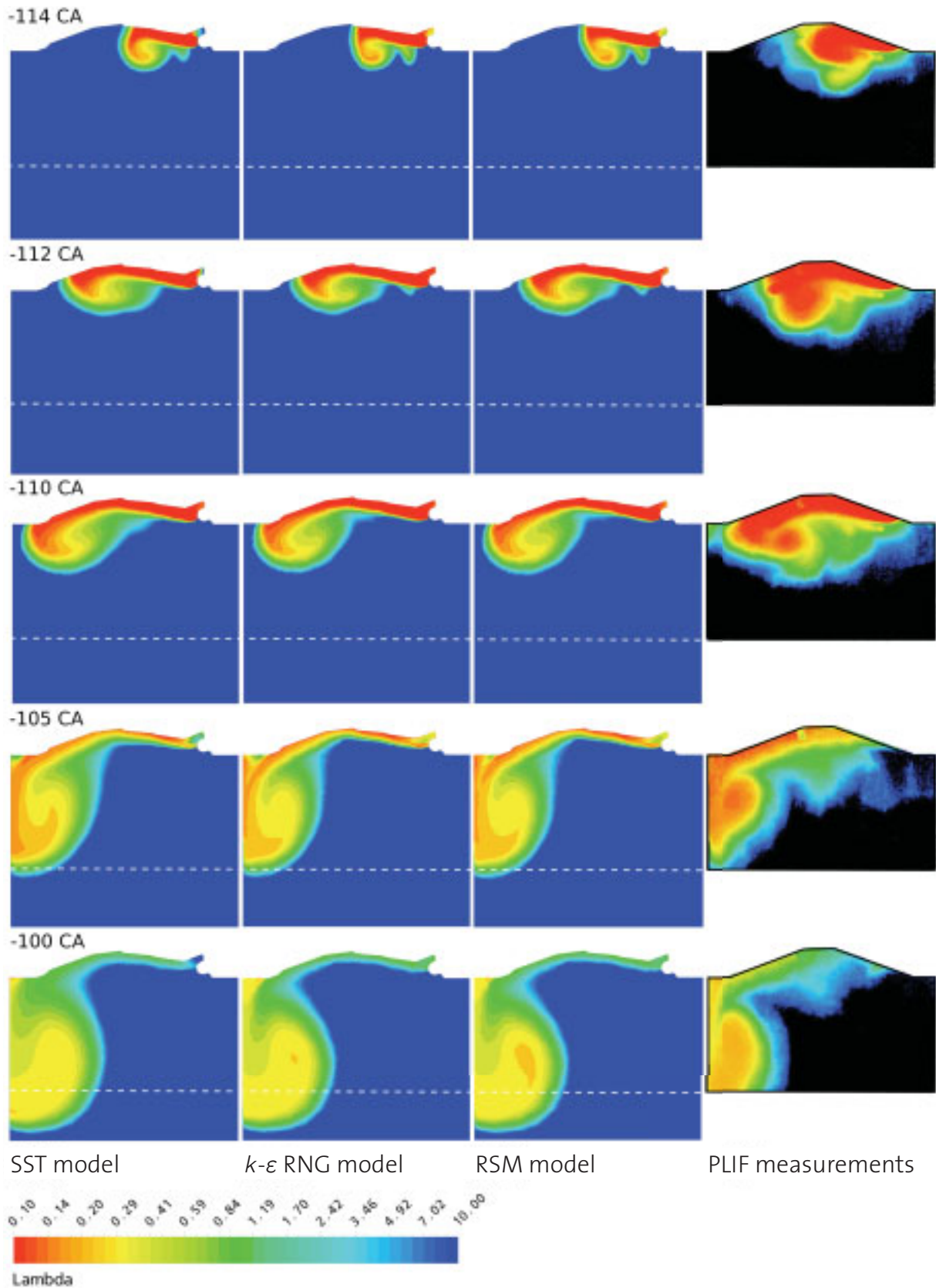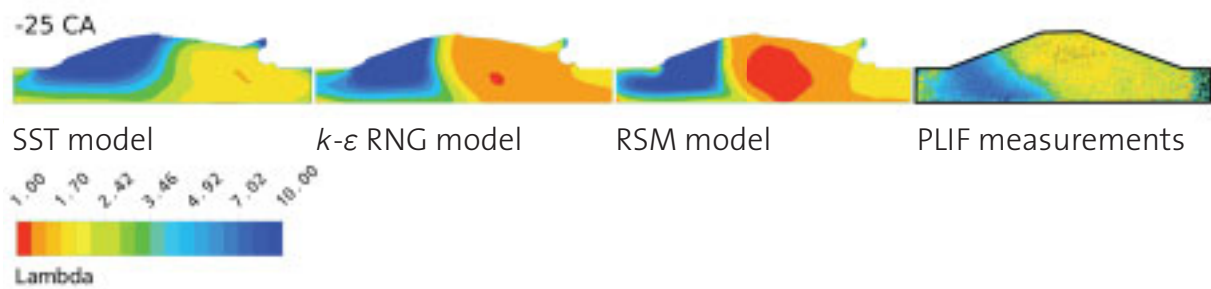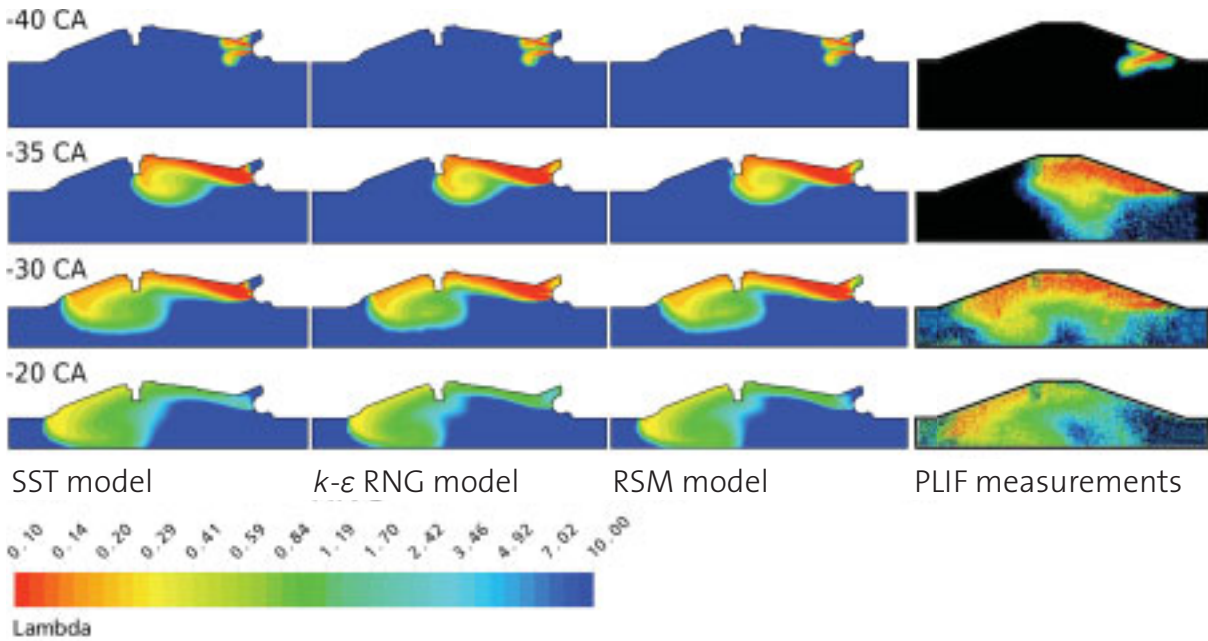
Figure 6.2: Operating point O2: Hydrogen mixture formation simulations with different turbulence models (SST, k-ε RNG, RSM) in comparison to PLIF measurements. Blue regions specify equivalence ratio $\lambda \geq 10$, red regions show $\lambda \leq 0.1$. Crank angle is given with respect to TDC ($SOI = -45°$ CA, $\lambda_{global} = 2.4$, $n = 2000$ rpm).

6.1.1.2   Operating Point O2: $\lambda = 2.4$, $SOI = -45°$ CA

As to CFD simulation of late injection, the hydrogen mixture formation is of crucial importance for the subsequent fuel conversion. Consequently, numerical analysis of the combustion process can only be as accurate as the computation of the mixture distribution. To validate the CFD model, a comparison between simulations and experimental PLIF measurements is given in Figure 6.2 for the late injection case with $\lambda = 2.4$ and $SOI = -45°$ CA (operating point O2). Due to the delayed timing of the injection at the end of the compression stroke, a stratified charge is obtained where fuel-rich regions ($\lambda < 1.0$) and regions of pure air are present.

In contrast to the early injection case discussed above, the mixture distribution for late injection is virtually not affected by the type of turbulence model. Simulations conducted with the SST, the RNG and the RSM turbulence approach show similar results with respect to the allocation of hydrogen concentration within the interval from $\varphi = -40°$ CA to $-20°$ CA. The penetration depth of the hydrogen jet and the location of fuel-rich regions predicted by the CFD model are in satisfying agreement with the op-

tical measurements. The main difference between the results obtained by both methods is that a scattering of hydrogen intensity along the main hydrogen jet is shown in the experiments which is not described by numerical computations. Consequently, the fuel-lean region at the injection-side of the domain in Figure 6.2 is more explicitly developed by the simulations.

Despite the very similar solutions of mixture distribution obtained by the three turbulence models, the intensity of turbulent kinetic energy induced by the hydrogen jet is varying between the different simulation results. Corresponding turbulent quantities and hydrogen volume fractions are analysed in Section 6.1.2.

6.1.2 Mixture and Turbulence Kinetic Energy Spatial Distribution

The evolution of mean turbulence levels is displayed as a function of crank angle in Figure 6.3 for computations of the early (O1) and the late injection (O2). The turbulence intensity, being the most determining value for combustion modelling, is specified in terms of turbulent velocity fluctuations $u' = \sqrt{\frac{2}{3}k}$. Moreover, the turbulence dissipation rate ε and the turbulence frequency ε/k employing the turbulence kinetic energy k is provided.

With respect to turbulent velocity fluctuations, the SST approach predicts significantly higher levels of u' during injection than the other models. The maximum mean velocity fluctuation for the SST model is $\overline{u'}_{max} \approx 12$m/s with injection timings of $SOI = -120°$ CA and $\overline{u'}_{max} \approx 8$ m/s with $SOI = -45°$ CA. The levels given by the RNG and the RSM approach are below $\overline{u'}_{max} = 3$m/s for both cases. In case of early injection timings – after the end of injection and during compression – the velocity fluctuations decrease for the SST model and slightly increase for the RNG model. Comparable levels of $\overline{u'} \approx 3$ m/s are reached near TDC for both model types. In case of injection timings close to the end of the compression stroke, the difference in u' between the models becomes effective since ignition timing follows shortly after end of injection. The RSM model predicts mean velocity fluctuations on the level of the RNG results, although the inten-
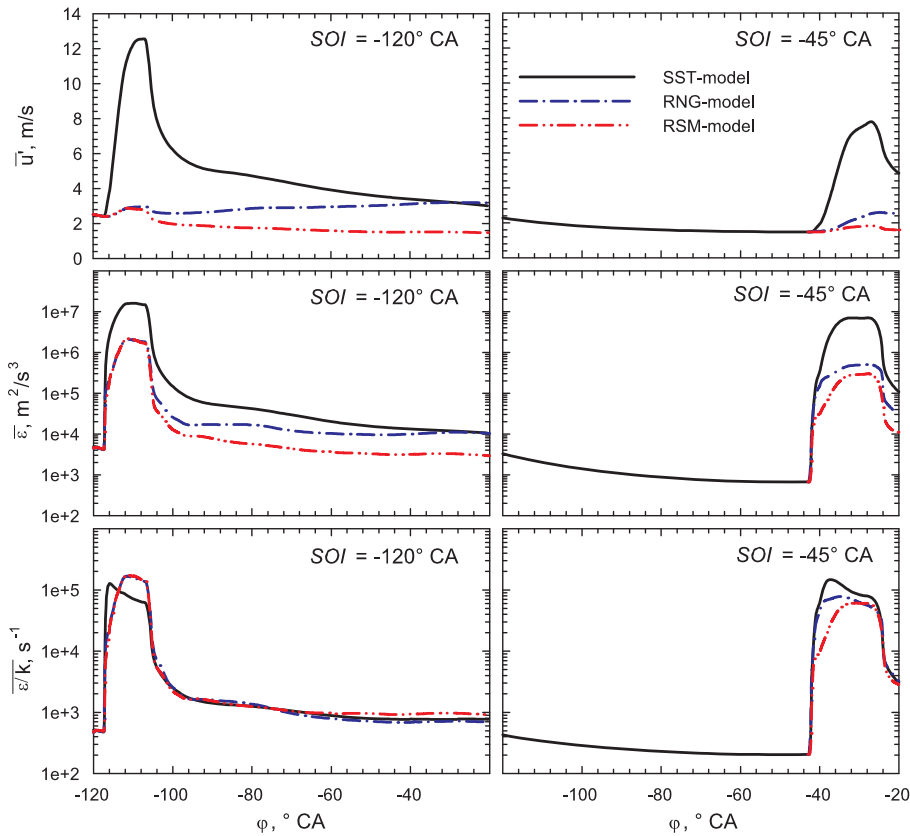
Figure 6.3: Comparison of mean turbulent quantities for computations with different turbulence models: $SOI = -120°$ CA (left); $SOI = -45°$ CA (right); $\lambda_{global} = 2.4$, $n = 2000$ rpm.

sity decreases additionally during the compression phase. Regarding simulations of the $SOI = -45°$ CA case, the results obtained from the SST model at start of injection are considered as initial conditions for the computations with the RNG and RSM model for a better comparison of the approaches.

Although the values of ε slightly differ between the models, the comparison of the ratio ε/k shows only minor differences. This emphasises the equal influence of the turbulence dissipation rate for all three models. A further analysis of the turbulence models is demonstrated in the following, focussing on the local allocation of mixture and turbulence.

6.1.2.1   Operating Point O1: $\lambda = 2.4$, $SOI = -120°$ CA

Regarding simulations with $SOI = -120°$ CA, Figure 6.4 depicts the volume fraction levels of fuel/air equivalence ratio ϕ, turbulence velocity fluc-

tuations u' and turbulence eddy dissipation ε obtained from a spatial analysis of the entire domain for the employed turbulence approaches at crank angle of $\varphi = -80°$ CA, $-50°$ CA and $-25°$ CA. A comparison of the spatial fuel-allocation within the entire domain shows only slight influence of the different turbulence models on the equivalence ratio. The initially wide range of equivalence ratio, present at $\varphi = -80°$ CA, homogenises during the compression phase. At $\varphi = -50°$ CA where in Figure 6.1 definite discrepancies between the SST, RNG and RSM calculations are expressed in a cross-sectional view, the spatial description reveals quite comparable global hydrogen allocations for all three turbulence models. At $\varphi = -25°$ CA, despite the homogenisation process, the results still show a certain rate of inhomogeneity, including regions with fuel/air equivalence ratio located outside the ignition limits $\phi < 0.1$. The objective to obtain the quality of a well homogenised mixture is, however, not obtained using early injection timings due to the small amount of fuel injected and the therefrom resulting lower levels of turbulence intensity.

Regarding the allocation of turbulent quantities, at $\varphi = -80°$ CA, a strong impact of the hydrogen jet on turbulent velocity fluctuations is demonstrated for computations with the SST model, while the RSM model is hardly affected by the injection and predicts a rather homogeneous turbulence distribution. The results obtained with the RNG model are somewhere located between the results of the other models. During the injection phase, maximum values of turbulent velocity fluctuations are $u'_{max} = 12.5$ m/s, 6.5 m/s and 5.0 m/s for the SST, RNG and RSM model. During the compression phase, the characteristics of the turbulence velocity fluctuations of the SST and RNG model converge, resulting in a comparable turbulence field with $u'_{max} = 5.0$ m/s at $\varphi = -25°$ CA.

The excessive production of turbulent kinetic energy during injection predicted by the SST model in comparison to the RNG model and the RSM model is underlined by the results. The impact on turbulent viscosity leads possibly to a bad accuracy for swirling flows computed with the SST model. Accordingly, the turbulent viscosity of the swirl-like hydrogen flow is increased, resulting in the discrepancies between computations and optical measurements which do not occur in simulations using the RNG and
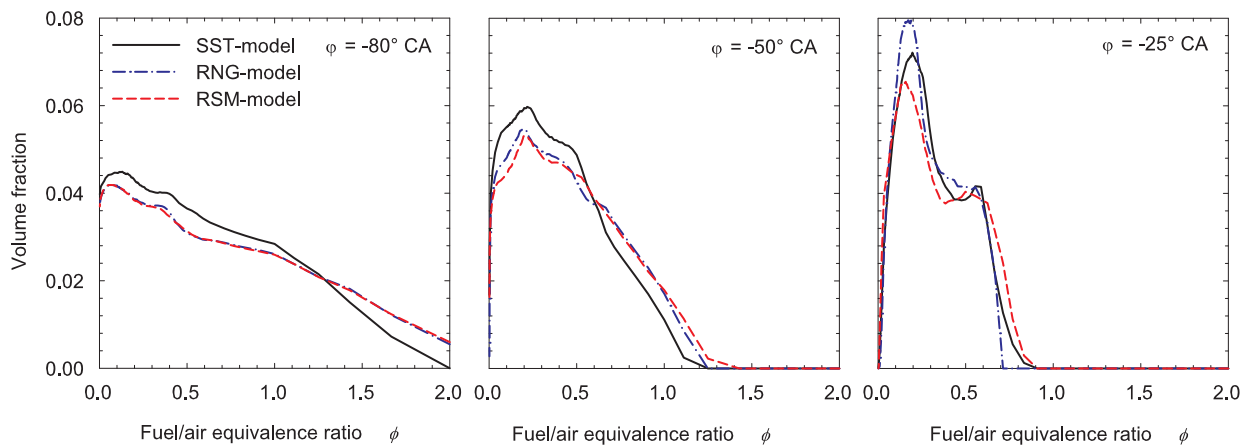
(a) Fuel/air equivalence ratio ϕ.
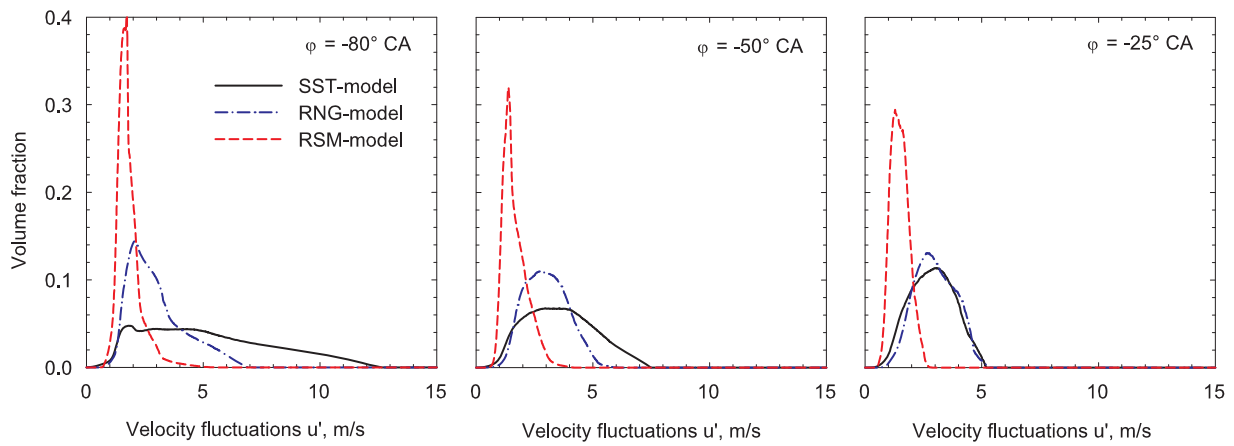
(b) Turbulent velocity fluctuations u'.
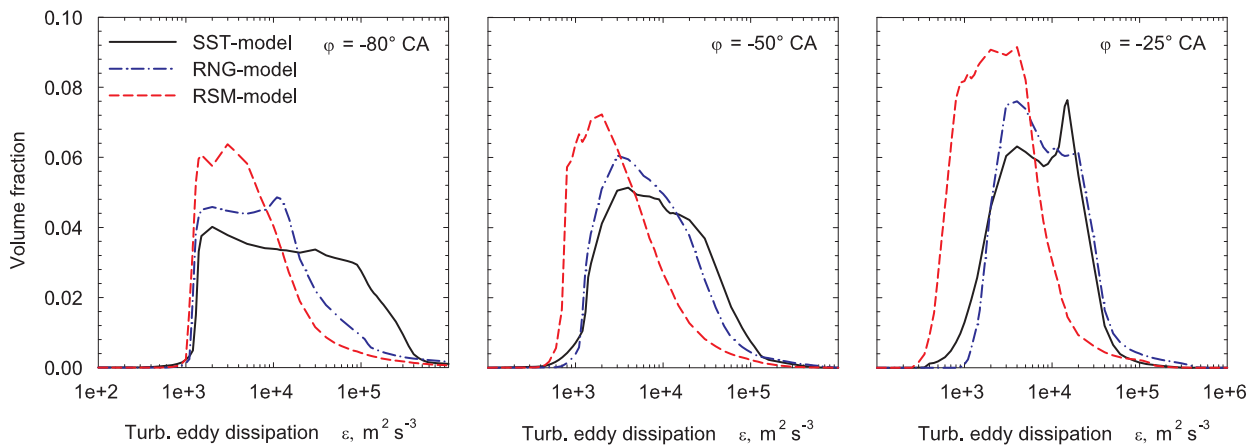
(c) Turbulent eddy dissipation ε.

Figure 6.4: Volume shares of fuel/air equivalence ratio ϕ and turbulent quantities for computations with different turbulence models at $\varphi = -80°$ CA, $-50°$ CA and $-25°$ CA. (**Operating point O1:** $SOI = -120°$ CA, $\lambda_{global} = 2.4$, $n = 2000$ rpm).

(a) Fuel/air equivalence ratio ϕ.

(b) Turbulent velocity fluctuations u'.
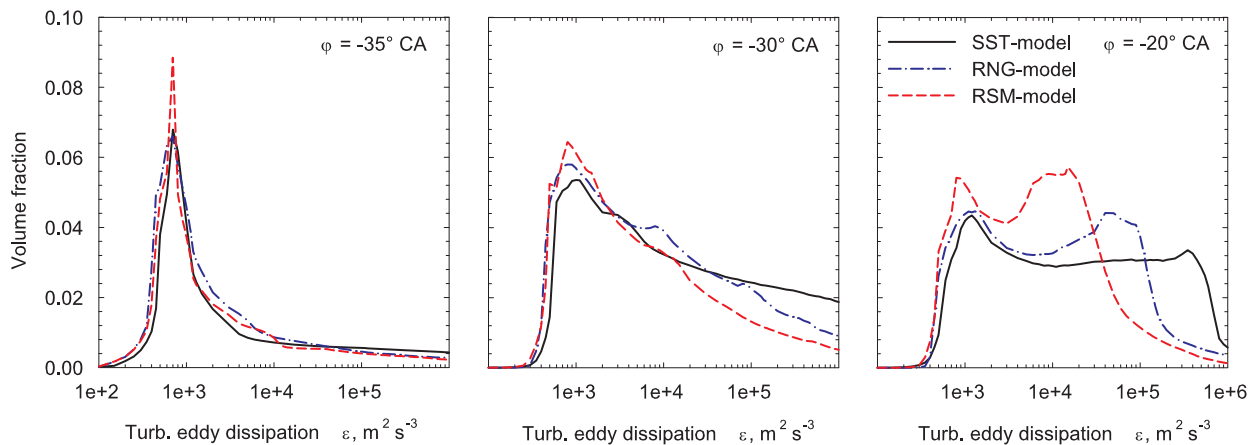
(c) Turbulent eddy dissipation ε.

Figure 6.5: Volume shares of fuel/air equivalence ratio ϕ and turbulent quantities for computations with different turbulence models at $\varphi = -35°$ CA, $-30°$ CA and $-20°$ CA. (**Operating point O2:** $SOI = -45°$ CA, $\lambda_{global} = 2.4$, $n = 2000$ rpm).
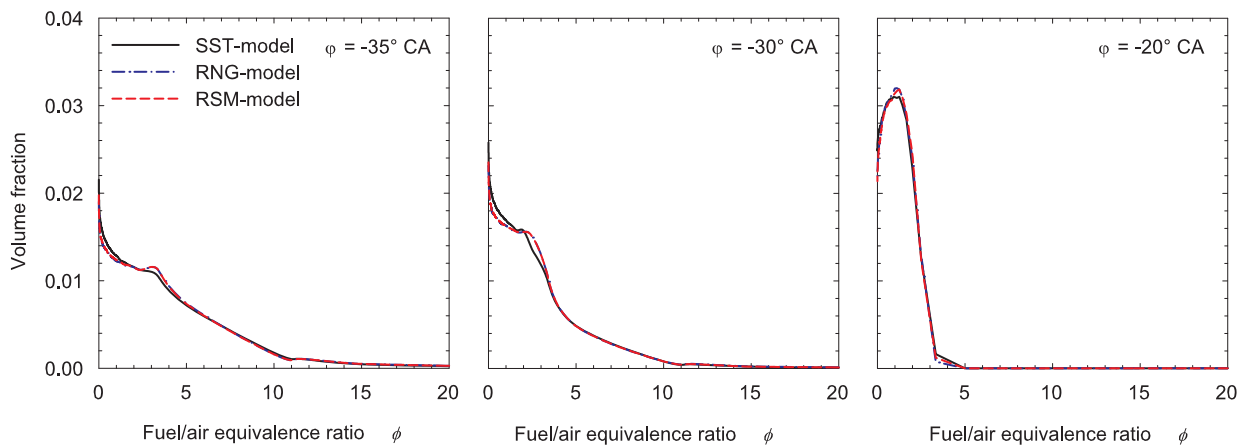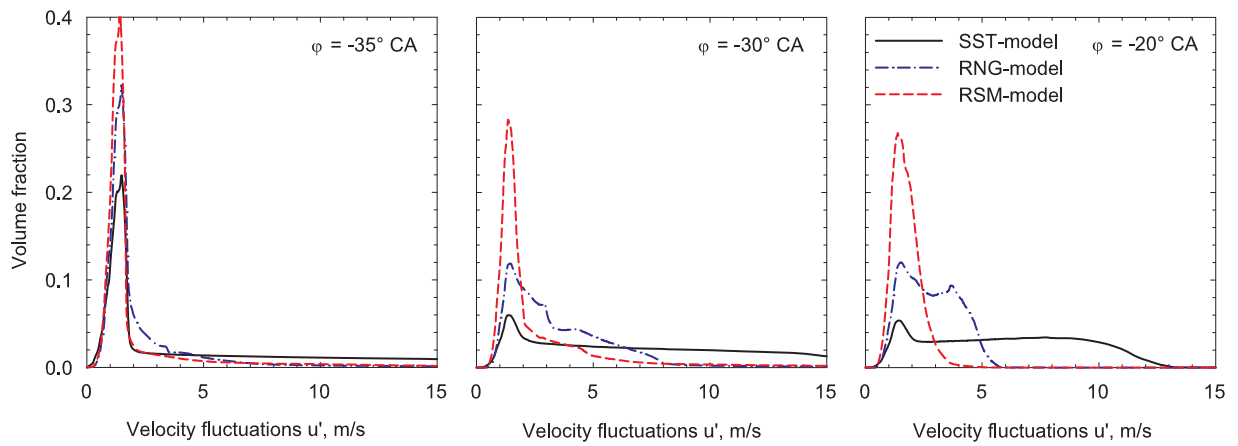
RSM models (cf. Figure 6.1). Generally, the prediction of turbulent viscosity might be enhanced for the RNG model, since the model parameters C_i are arranged to improve swirling and tumbling flows.

In contrast to the two-equation models discussed before, the results computed with the RSM model show a different behaviour. Maximum turbulent velocity fluctuations vary only in the range between $u'_{max} = 3$ m/s and 4 m/s. The impact of hydrogen injection on turbulence is low and the significance of the results is therefore questionable. Allocation of turbulence eddy dissipation is given as additional information. The level of ε is quite identical for the SST and RNG approach despite the different turbulence model constants $C_{\varepsilon 1/2}$. The RSM calculations give lower values. The ratio between ε and k, not depicted here, differs only slightly between all three types of turbulence models.

6.1.2.2 Operating Point O2: $\lambda = 2.4$, $SOI = -45°$ CA

Information on the spatial fuel and turbulence distribution corresponding to computations of the late injection operating point O2 are depicted in Figure 6.5 for crank angle of $\varphi = -35°$ CA, $-30°$ CA and $-20°$ CA.

In comparison to the early injection results depicted before, the late injection case shows significant volume shares of pure air and fuel-rich regions within the range from $0 < \phi < 4.5$ prior to ignition timing. Consequently, this mode may be referred to as stratified operation.

While the discrepancy between the results of the investigated turbulence models is negligible with respect to volume shares of equivalence ratio, fundamental dissimilarities between the models are observed regarding the allocation and level of turbulent velocity fluctuations. Concerning mean values of turbulent quantities defined in Figure 6.3, different maximum values of turbulent velocity fluctuations are predicted by the models at $\varphi = -20°$ CA, with $u'_{max} = 12.5$ m/s, 5.5 m/s and 3.5 m/s for the SST, RNG and RSM model. The SST model shows large variations of values for u', whereas the RSM model identifies more homogeneous, decreased levels of velocity fluctuations. The RNG approach is located somewhere between the results of the other models.

6.2   Thermodynamic Engine Mixture Formation

The suitability of the CFD model to compute hydrogen mixture formation has been validated by means of LIF measurements in Section 6.1, using the transparent research engine. Due to load limitations of this engine, the single cylinder thermodynamic research engine is employed for heat release simulations. Corresponding mixture formation computations are presented in the following as a basis for subsequent combustion simulations.

The investigated operating points D1 to D4 cover global stoichiometric and lean equivalence ratios as well as homogeneous and stratified mixtures. The application of the SST and RNG approach results in reasonable computational costs. Due to an increase of numerical effort by a factor of 2-3, the RSM model is not followed.

In Figure 6.6 a comparison of mean values of turbulent velocity fluctuations $\overline{u'}$ and turbulent eddy dissipation $\overline{\varepsilon}$ is given for various injection timings. The results resemble the findings observed for the transparent research engine. The turbulence levels are increased during the injection phase, whereas levels predicted by the RNG approach are far below those of the SST model. With regard to $SOI = -120°$ CA, maximum mean turbulent velocity fluctuations during injection are $\overline{u'} = 15.0$ m/s for the SST model and $\overline{u'} = 3.5$ m/s for the RNG model. Concerning the SST computations, the turbulence intensity decreases substantially after end of injection and is gradually reduced towards TDC, whereas an increase of u' in the compression phase can be noted for the RNG model. Finally, similar levels of mean values of u' are reached at ignition timing, independent from the global value of equivalence ratio. It is assumed that the increase in u' towards TDC, predicted by the RNG computations, is generated by the squish gaps during compression. In contrast to the SST model, the turbulence intensity due to injection is very low for the RNG approach. A similar interrelation is observed for $SOI = -60°$ CA, although – due to higher counter pressure – mean peak values of u' are reduced during injection. Again at TDC for the SST and RNG approach, similar levels of turbulent velocity fluctuations are obtained. With SOI towards top dead centre, higher values of u' are reached at ignition timing, since the global level of
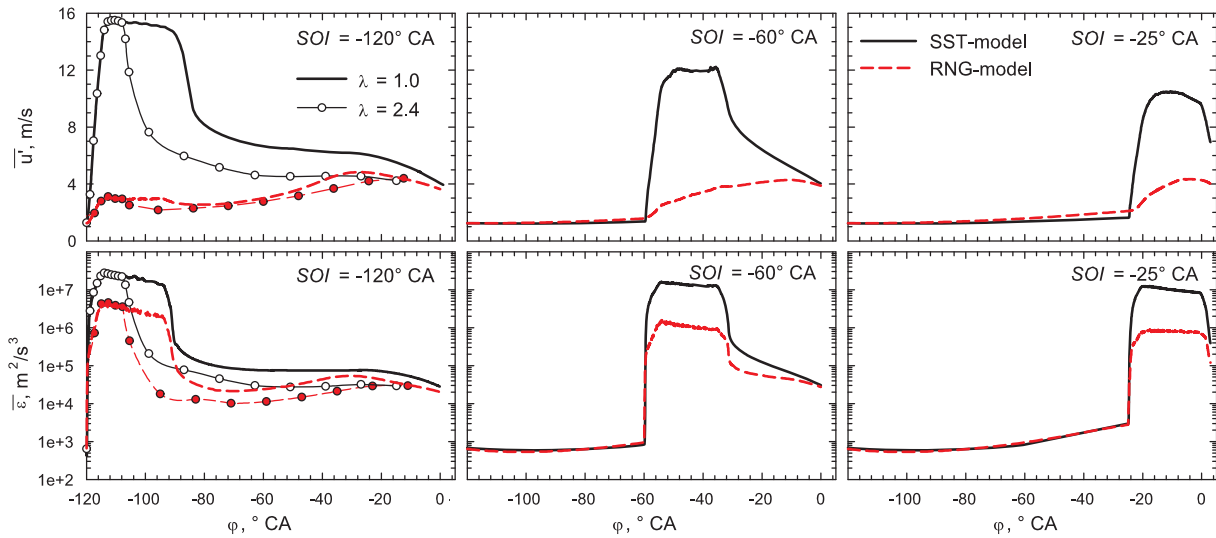
Figure 6.6: Comparison of mean values of turbulent velocity fluctuations $\overline{u'}$ and turbulent eddy dissipation $\overline{\varepsilon}$ for operating points D1 to D4 computed with SST and RNG turbulence models.

turbulence intensity is dominated by the injection phase. Consequently, the levels predicted by the SST and the RNG approach differ remarkably. Comparable results are found for the mean turbulent eddy dissipation. These values are generally increased for the SST model in comparison to the RNG solutions.

6.2.1   Operating Point D1: $\lambda = 1.0$, $SOI = -120°$ CA

Information on the spatial allocation of fuel/air equivalence ratio ϕ and turbulent quantities is given in Figure 6.7 (a) for a stoichiometric operating point with $SOI = -120°$ CA. Results are depicted at $\varphi = -80°$ CA, $-40°$ CA and at TDC. The initially wide range of equivalence ratio, which is present right after injection ($\varphi = -80°$ CA), is gradually homogenised towards TDC. Here, the equivalence ratio volume fraction peak at $\phi = 1.0$ demonstrates for both turbulence models only small deviations from the global value of equivalence ratio within the domain.

Regarding turbulent velocity fluctuations, the results at $\varphi = -80°$ CA emphasise the impact of injection on turbulence using the SST model where local values up to $u'_{max} = 15$ m/s are reached. Contrarily, the RNG model predicts values of u'_{max} reduced by a factor of 3. The discrepancy between the turbulence models vanishes towards TDC where only small deviations in the distribution of turbulent velocity fluctuations are observed.

In Figure 6.9 (a) the local air/fuel equivalence ratio λ and turbulence velocity fluctuations u' at ignition timing are displayed in a vertical and horizontal cut of the combustion chamber for computations with the SST model. The results show a well homogenised mixture in the centre of the domain with lean zones at the cylinder wall. Highest levels of turbulent velocity fluctuations are located in the centre of the domain. Computations obtained by the RNG model differ only slightly from the SST results.

6.2.2 Operating Point D2: $\lambda = 1.0$, $SOI = -60°$ CA

With respect to moderately delayed injection timings ($SOI = -60°$ CA), as depicted in Figure 6.7 (b), no relevant discrepancy between the mixture distribution of the SST and RNG computations is observed. At TDC the inhomogeneity of the mixture is significantly increased compared to results with $SOI = -120°$ CA, so that small regions of fuel-rich zones and unmixed regions exist. Turbulent velocity fluctuations show increased values of u' for the SST computations in comparison to the RNG approach. Towards TDC turbulent kinetic energy dissipates, resulting in a quite similar spatial distribution of u' for the SST and the RNG case.

Figure 6.9 (b) illustrates the local air/fuel equivalence ratio λ and turbulence velocity fluctuations u' at ignition timing acquired with the SST model. Unmixed regions are located in zones near the squish gaps at the injector nozzle side of the domain, while fuel-rich regions are located at the opposite side. The allocation of turbulence kinetic energy is quite similar to the early injection case where increased values of u' are located in the centre of the domain. Similar results are achieved for computations with the RNG model.

6.2.3 Operating Point D3: $\lambda = 1.0$, $SOI = -25°$ CA

Volume shares of equivalence ratio and turbulent velocity fluctuations for the highly stratified mixture with $SOI = -25°$ CA are given in Figure 6.8 (a) for computations with the SST and RNG model. Similar results are obtained by the two models regarding values of the equivalence ratio, where-
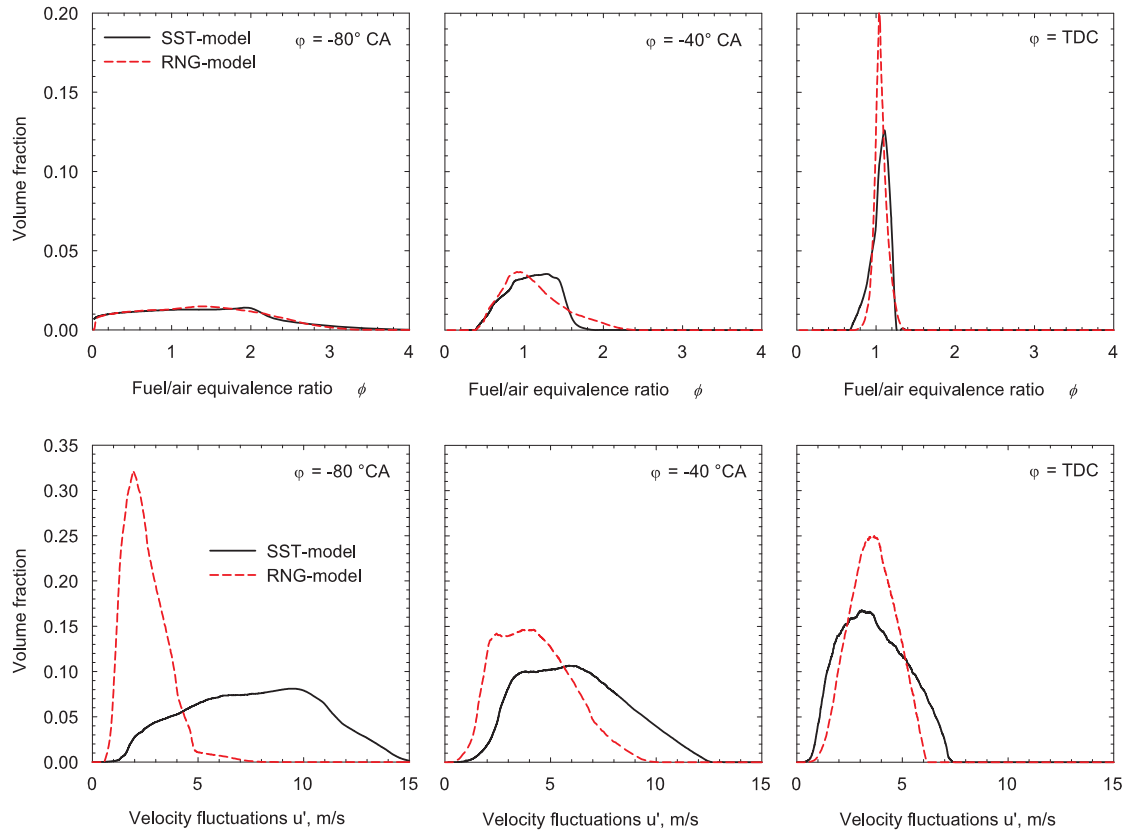
(a) **Operating point D1:** $SOI = -120°$ CA, $\lambda_{global} = 1.0$, $n = 2000$ rpm.
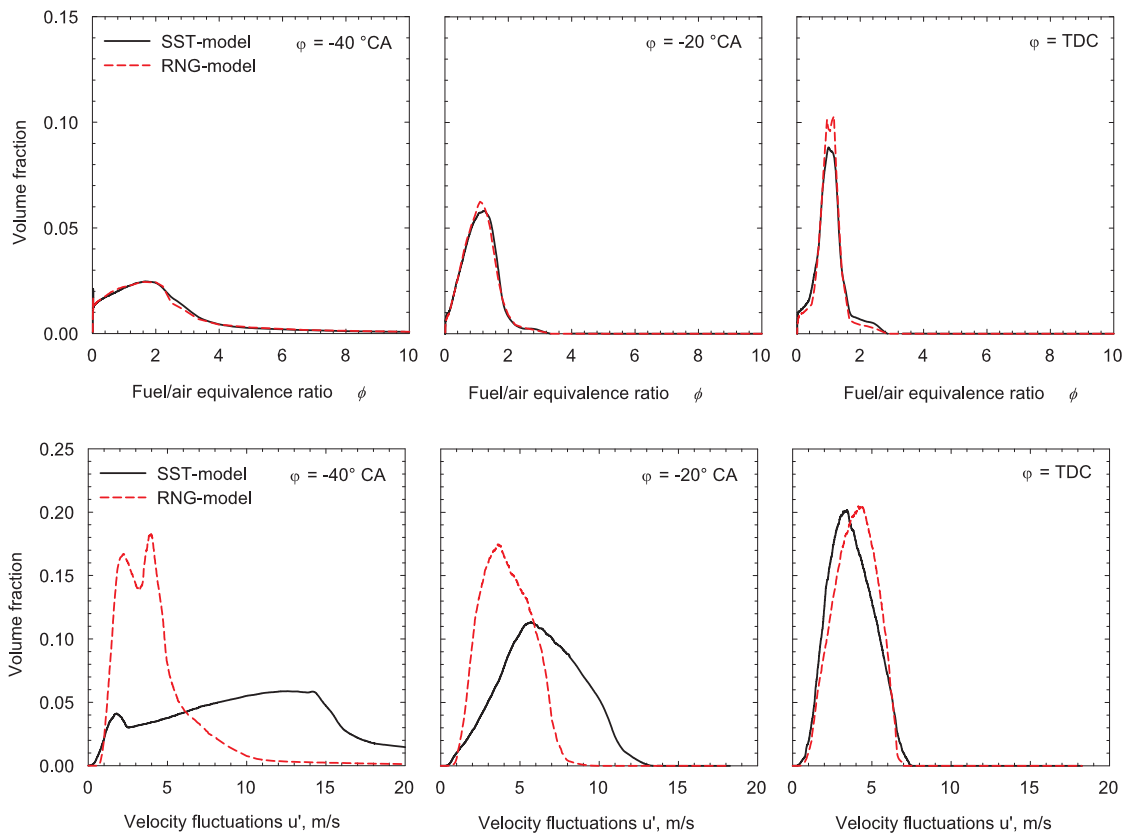
(b) **Operating point D2:** $SOI = -60°$ CA, $\lambda_{global} = 1.0$, $n = 2000$ rpm.

Figure 6.7: Volume shares of fuel/air equivalence ratio ϕ and turb. velocity fluctuations u'.
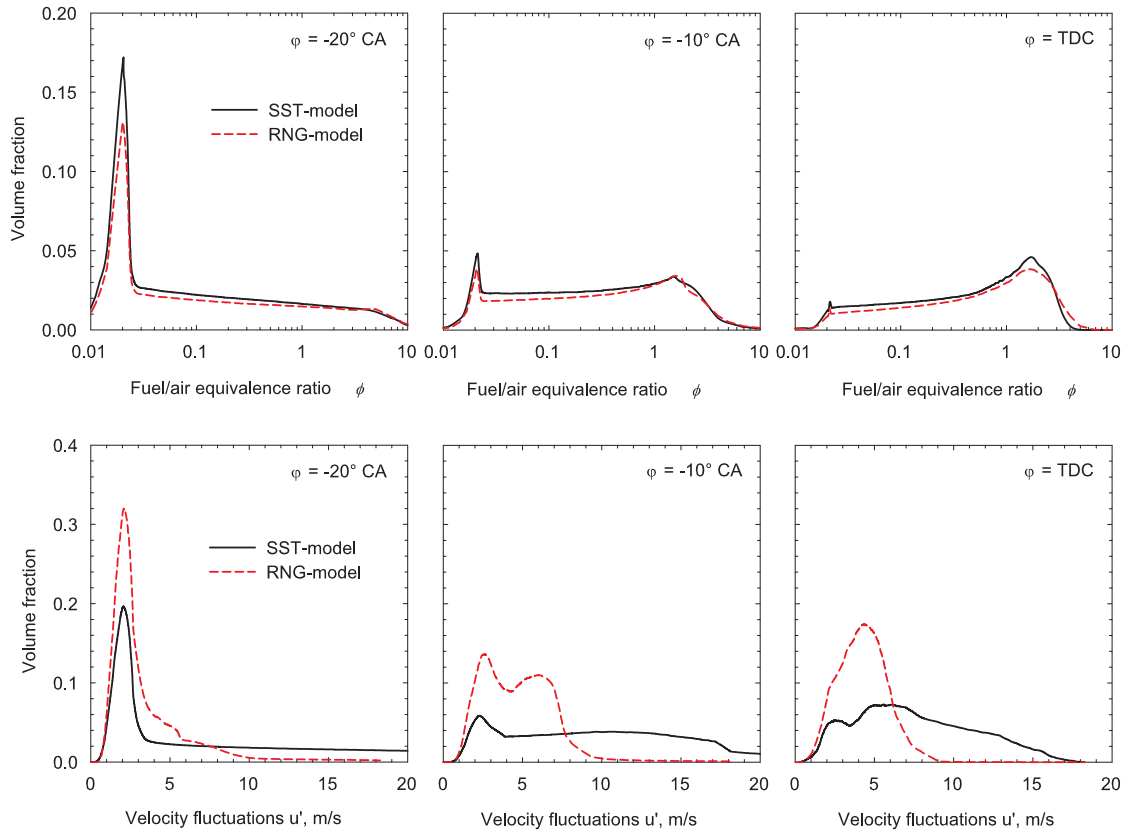
(a) **Operating point D3:** $SOI = -25°$ CA, $\lambda_{global} = 1.0$, $n = 2000$ rpm.
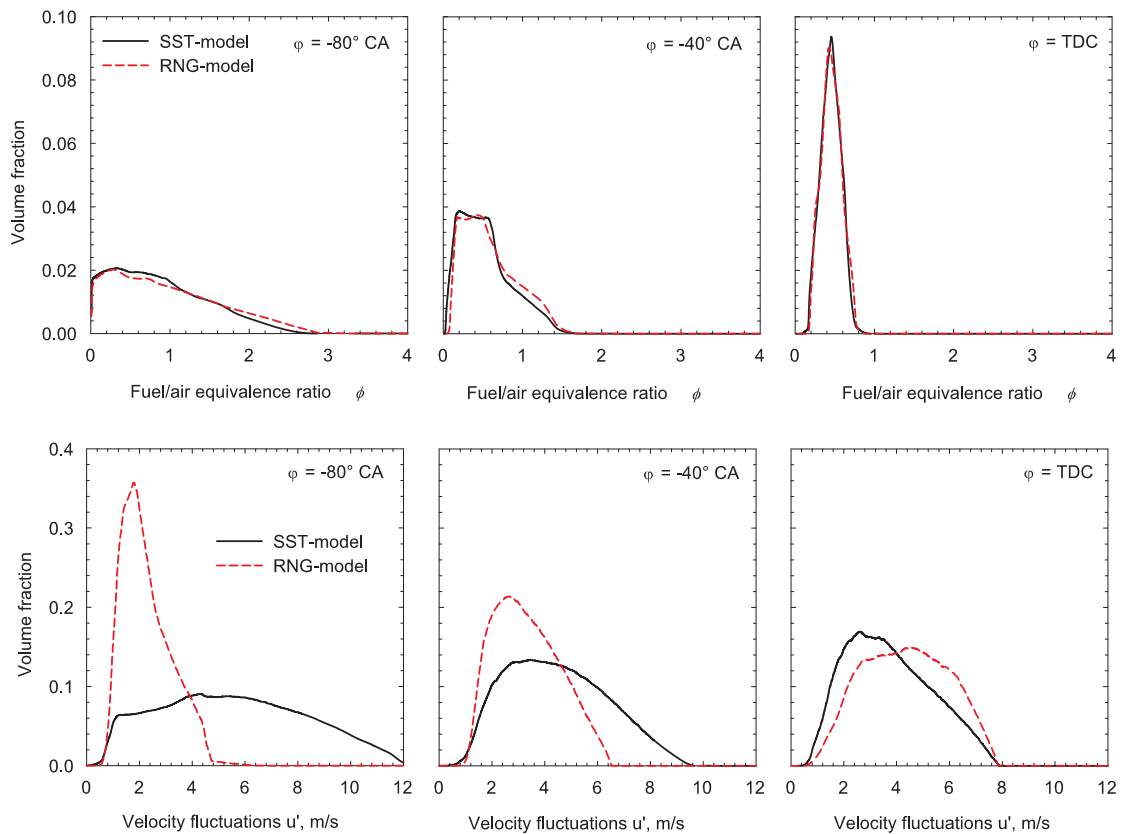
(b) **Operating point D4:** $SOI = -120°$ CA, $\lambda_{global} = 2.4$, $n = 2000$ rpm.

Figure 6.8: Volume shares of fuel/air equivalence ratio ϕ and turb. velocity fluctuations u'.

as the turbulent velocity fluctuations predicted by the approaches differ. Time scales between end of injection and ignition timing are too short to provide a sufficient mixture homogenisation. Consequently, relevant amounts of unmixed and fuel-rich zones are recognised at TDC by the computations, where fuel/air equivalence ratios are in the range from $\phi = 0.02$ to 4. Compared to results of the RNG approach, turbulent velocity fluctuations are increased for the SST model during injection. Again, time scales are too short for a dissipation of the high level of turbulent kinetic energy predicted by the SST model, so that at ignition timing the value of u' is significantly higher than that anticipated by the RNG approach.

Figure 6.9 (c) illustrates the flow fields of air/fuel equivalence ratio λ and turbulence velocity fluctuations u' obtained by the SST model at TDC in horizontal and vertical intersections. Results of computations with the RNG model, not depicted here, are almost identical with respect to λ-distribution. The field of u' is of similar shape compared to the SST results, however, differs remarkably in the magnitude of its absolute values.

6.2.4 Operating Point D4: $\lambda = 2.4$, $SOI = -120°$ CA

Computations of the lean operating point with early injection resemble the results of the stoichiometric case, described before. The volume shares of fuel/air equivalence ratio ϕ are similar for both turbulence models. At ignition timing, however, the local values range between $\phi = 0.2$ and 0.8, demonstrating an insufficient mixture homogenisation for this operating point (cf. Figure 6.8 b). The evolution of turbulent velocity fluctuations u' shows a dissipation of turbulent kinetic energy generated by injection. Consequently, almost equal levels of u' are obtained for both models, despite the initial turbulence level generated by hydrogen injection.

Figure 6.9 (d) demonstrates the flow fields of air/fuel equivalence ratio λ and turbulent velocity fluctuations u' for computations with the SST model. With respect to mixture formation, the expected homogeneity is not yet achieved. The turbulent velocity fluctuations show increased values in the centre of the domain on a level of $u' \approx 5$ m/s which are primarily caused by squish gaps during the compression phase. The intensity and
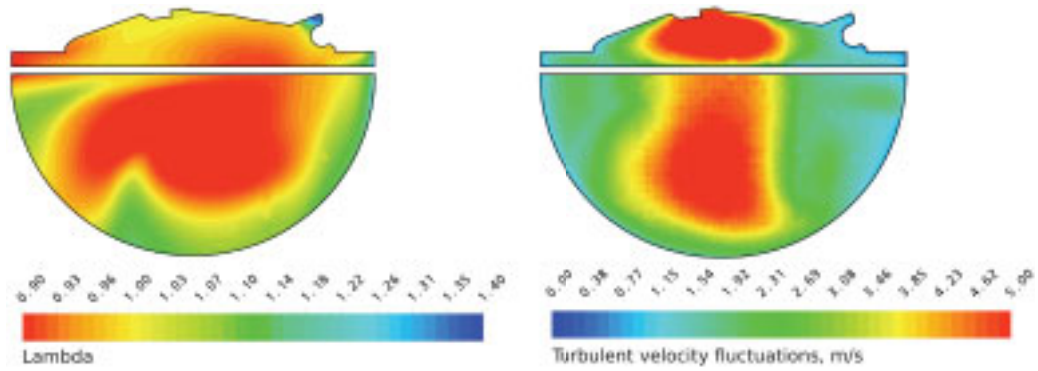
(a) **Operating point D1:** $\lambda = 1.0$, $SOI = -120°$ CA, $n = 2000$ rpm.
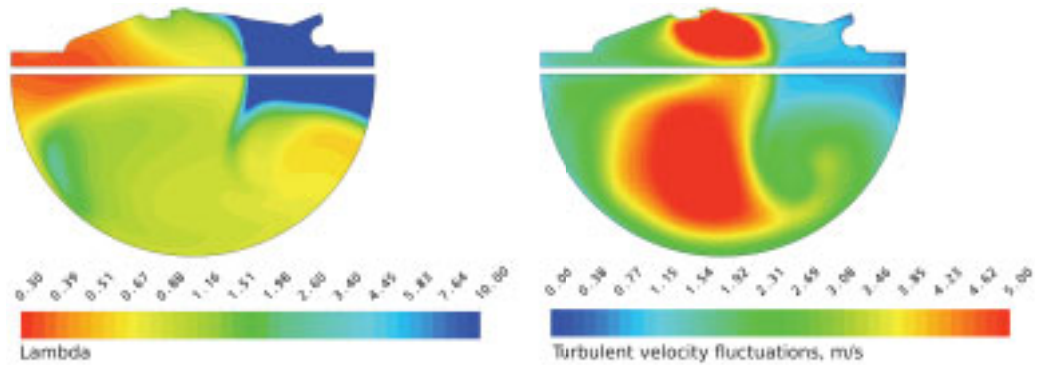
(b) **Operating point D2:** $\lambda = 1.0$, $SOI = -60°$ CA, $n = 2000$ rpm.
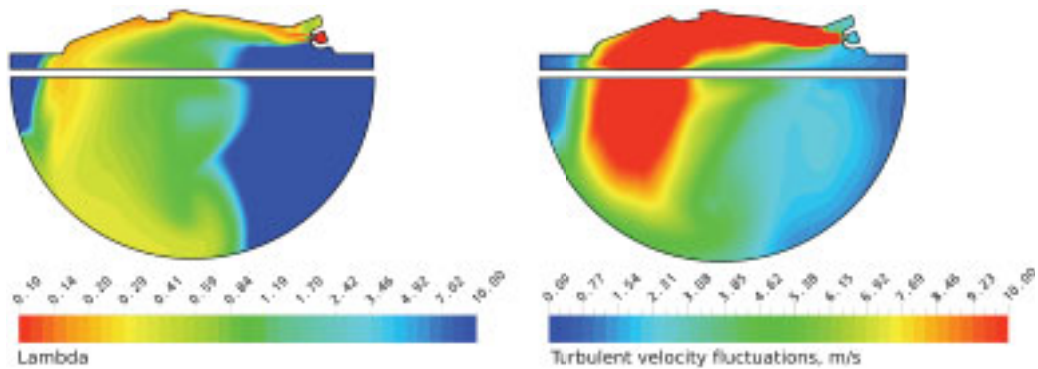
(c) **Operating point D3:** $\lambda = 1.0$, $SOI = -25°$ CA, $n = 2000$ rpm.
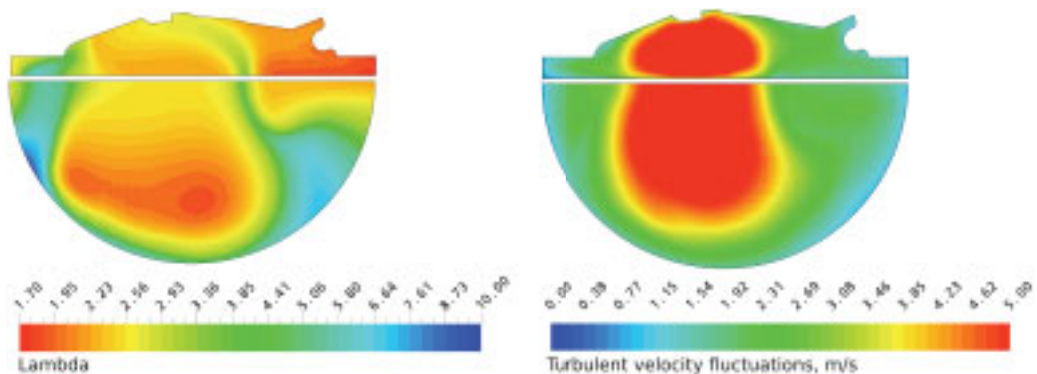
(d) **Operating point D4:** $\lambda = 2.4$, $SOI = -120°$ CA, $n = 2000$ rpm.

Figure 6.9: Comparison of local air/fuel equivalence ratios λ (left) and turbulent velocity fluctuations u' (right) **at ignition timing** computed with the SST turbulence model.

structure of turbulence is similar to results of early injection timings computed for the stoichiometric operating point (D1).

6.3   Summary of Results

Regarding the mixture distribution of operating points with early injection timing, for all investigated turbulence models only minor differences are noticeable. Computations with the RSM show the best agreement with LIF measurements. With respect to delayed injections, the discrepancy in mixture distribution between the investigated models vanishes almost completely, yielding to quite similar results.

Turbulence quantities, however, differ quite a lot among computations with the individual models. The RSM and the RNG model show a remarkable small production of turbulent kinetic energy during the injection phase, while the SST model predicts higher levels. Due to an increase in numerical effort by a factor of about 2 with the RSM model, only the RNG and SST approach is applied in further CFD simulations.

Despite the differences in production of turbulent kinetic energy due to hydrogen injection for the SST and RNG turbulence models, computations with the two approaches give comparable results for operating points when the time frames between end of injection and ignition timing are long enough for a dissipation of turbulent kinetic energy. In this case, the combustion-relevant turbulence is generated during compression, e.g. by the influence of squish gaps. This is not the case for delayed injection timings ($SOI = -25°$ CA) where the turbulence intensity is dominated by injection and different results are obtained by the SST and the RNG model. Consequently, with reference to combustion computations of stratified operating points, the predicted turbulent burning velocities strongly depend on the chosen turbulence modelling approach.

Regarding a statement which of the turbulence models is more credible, the conducted combustion simulations provide most accurate results with the SST model. However, for an detailed evaluation of the models, the computed flow field parameters have to be validated by experiments.

Chapter 7

Simulation of Heat Release

CFD combustion simulations are conducted employing the turbulent flame speed and the flame surface density models – Zimont, Bradley and ECFM – as specified in Sections 4.3 and 4.4. Laminar flame speed data, required as input for the combustion models, are provided by flame speed correlations defined in Section 5.5. Two distinct correlations are applied which are based on either a detailed chemical kinetic model (Reaction Mechanism Correlation) or on measurements (Extended Leeds Database), predicting burning velocities of stable and unstable laminar flames. Regarding modelling of turbulent quantities, the RNG and the SST turbulence model, as specified in Section 3.2, are used for the computations. The RSM model is not taken into consideration for combustion calculations, since the numerical effort is significantly increased in comparison to the two-equation models.

Operating points of the thermodynamic research engine in PFI and DI mode, defined in Section 2.1, are used for the validation of the computations in homogeneous, stratified and multi-injection operation. Corresponding mixture formation calculations are taken from the results presented in Chapter 6. The computations are validated by a comparison of cylinder pressure, heat release rate and heat transfer with experimental data and solutions obtained from zero-dimensional measurement analysis.

7.1 Sensitivity on Variable Enthalpy and Pressure

In the mixture fraction approach chemistry is decoupled from the flow computation and burned and unburned gas species are given by laminar flamelet libraries (cf. Section 4.2). With respect to IC engine applications, the unburned mixture is affected by a variation of temperature and pressure conditions during combustion. The standard flamelet library is only valid at a particular condition of unburned gas temperature and pressure. In order to include temperature and pressure dependency into the chemistry of the combustion model, several standard flamelet libraries are combined to an extended library which accounts for variable enthalpy and pressure. The number of standard flamelet libraries employed, is defined by pressure and temperature sampling points ($n_p \times n_T$) within a relevant range from $T = 600\,\text{K}$ to $3000\,\text{K}$ and $p = 20\,\text{bar}$ to $80\,\text{bar}$. At intermediate conditions, the solutions of the flamelet libraries are linearly interpolated.

A sensitivity study is conducted where the necessary number of sampling points is estimated to obtain an independent solution. Values for n_p and n_T are systematically increased, until the deviation of the computational results to the previous solution is minimised. Values for n_p range between 2 and 7; for n_T variations between 2 and 25 are investigated. The corresponding sampling points are proportioned equidistantly within the defined temperature and pressure range.

The influence of a variation of sampling points on pressure, temperature and species concentrations is demonstrated exemplarily for a port fuel injection operating point with stoichiometric equivalence ratio (operating point P1) in Figure 7.1. As combustion model, the Zimont approach is applied, using the Extended Leeds Database as an input for hydrogen laminar flame speed. The model constant $A = 0.84$ is calibrated to fit pressure measurements with the 7×25 flamelet library. Results of the variable flamelet library are compared to calculations employing standard flamelet libraries valid at a single combination of unburned temperature and pressure conditions ($T = 600\,\text{K}$ to $900\,\text{K}$, $p = 20\,\text{bar}$ to $60\,\text{bar}$). The results show that minor species concentrations are fundamentally affected by the type of flamelet library, while major species concentrations show
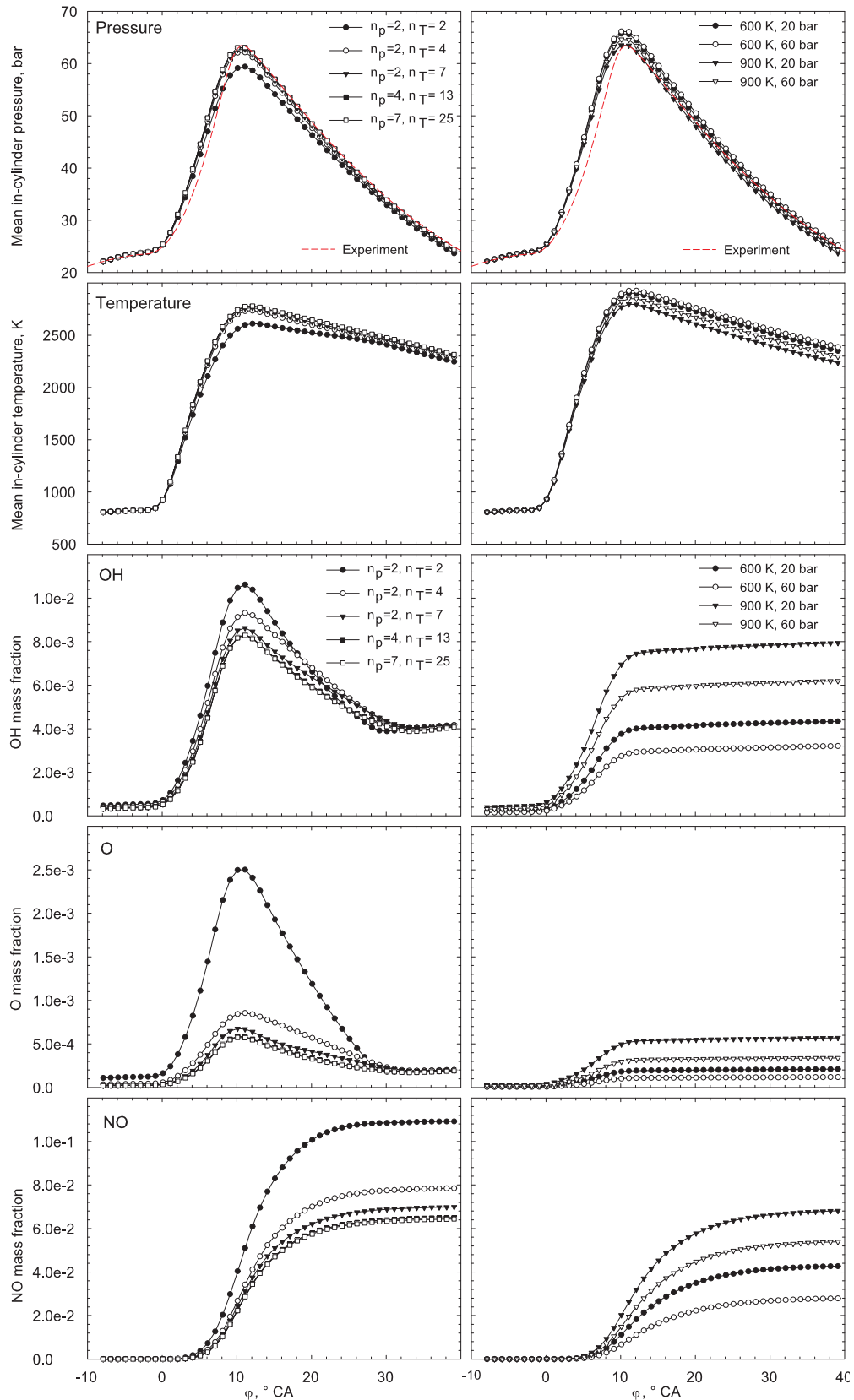
Figure 7.1: Sensitivity of flamelet libraries on pressure, temperature and species concentrations (PFI, $\lambda = 1$, $n = 2000$ rpm). Left: Extended flamelet library with n_p and n_T as pressure and temperature sampling points within the range from $T = 600$ K to 3000 K and $p = 20$ bar to 80 bar. Right: Standard flamelet library at given conditions. Nitrogen oxides concentrations are computed with the extended Zeldovich mechanism presented by [115].

only small dependency on the number of sampling points. Accordingly, with respect to the computation of nitric oxide emissions, the application of a variable flamelet library with a sufficient number of sampling points is required.

Regarding in-cylinder pressure, the application of the variable flamelet library shows that the maximum value and the descending slope are in good agreement with the experimental results even for a small number of sampling points. Contrary results are obtained from the standard flamelet library. Firstly, the maximum pressure depends on the chosen flamelet library; secondly, the descending pressure slope declines too fast and deviates from the experimental value during expansion. To avoid such inaccuracies, it is not recommended to use a standard flamelet library for IC engine applications, even if minor species concentrations and NO-formation are not taken into consideration. In the present example, an independent solution is found for a variable flamelet library with 7×25 sampling points which is employed in the subsequent computations.

7.2   Port Fuel Injection Operation

Regarding a first validation of the combustion models, the three port fuel injection operating points P1, P2 and P3 are employed. The objective is to verify the models with respect to premixed combustion modes, excluding the influence of direct-injection on mixture homogenisation and turbulence. The investigated engine speed is $n = 2000$ rpm, values of equivalence ratio include stoichiometric and lean mixtures ($\lambda = 1$, 1.2 and 1.8). Corresponding mixture formation results are obtained from calculations of an associated work, performed within the framework of *Hy-ICE* [32]. The SST approach is applied as turbulence model. As input for laminar flame speed, two cases are investigated using either the Extended Leeds Database or the Reaction Mechanism Correlation. The in-cylinder pressure is adjusted to match the value given by measurements at ignition timing. The model constants are calibrated using the stoichiometric operating point P1. Subsequently, calculations of operating points P2 and P3 are performed, using identical settings. In the following, results obtained by the Zimont model, the Bradley model and the ECFM model are presented.
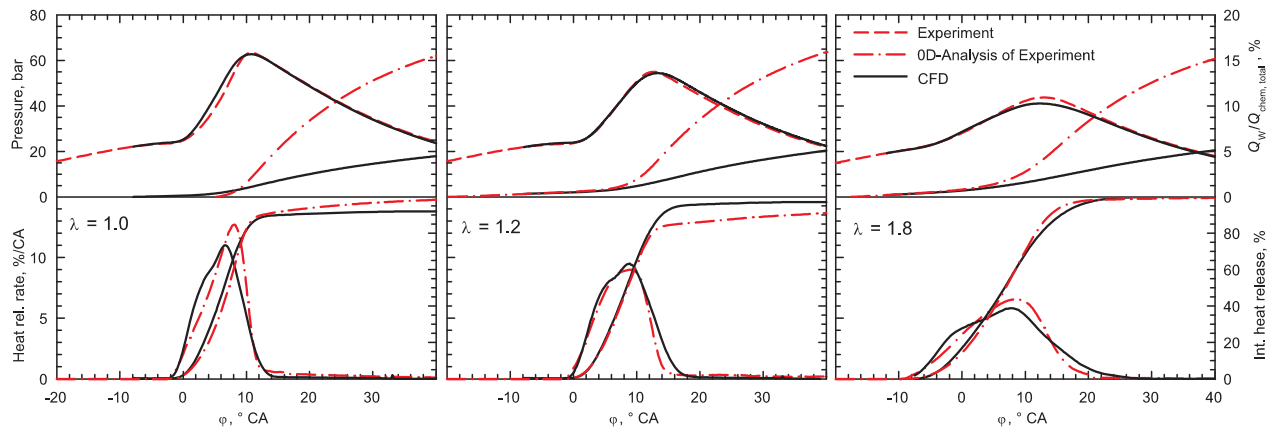
(a) Extended Leeds Database / Model coefficient $A = 0.84$.
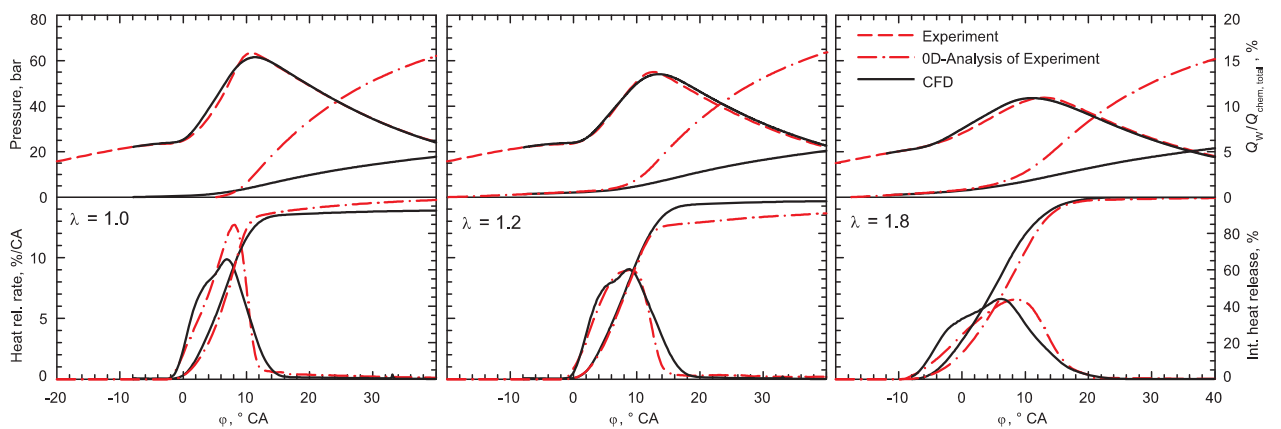
(b) Reaction Mechanism Correlation / Model coefficient $A = 0.84$.

Figure 7.2: Computations of PFI operating points P1-P3 ($n = 2000$ rpm) employing the **Zimont model** with the SST model for turbulence and different sets of laminar flame speed correlations. Results are depicted in terms of pressure traces, heat release and heat transfer. Measurements and data from zero-dimensional heat release analysis are given for comparison.

7.2.1 The Zimont Model

Calculations are performed with a dimensionless leading factor of $A = 0.84$ for both laminar flame speed correlations. As depicted in Figure 7.2, the calculated cylinder pressure and heat release displays an overall satisfying compliance with indicated pressure traces and heat release rates given by zero-dimensional analysis of experimental data. With respect to the location and magnitude of the maximum pressure, the results of the lean mixture ($\lambda = 1.8$) are slightly under-accentuated for computations with the Extended Leeds Database, while the Reaction Mechanism Correlation rather under-accentuates the $\lambda = 1$ operating point. It is re-

markable that, despite the fundamental differences of both laminar flame speed correlations, the models give quite similar results.

Regarding heat release rates, the CFD computations show a slight deceleration in fuel conversion prior to the maximum value of heat release rate, resulting in a bending of the curve. This effect is caused by a decrease of the flame surface due to wall interaction, which is not reproduced by zero-dimensional heat release analysis of experimental data.

The fluid to wall heat transfer is depicted in terms of the global integral heat transfer Q_W normalised by the total chemical heat of the fuel $Q_{chem,total}$. Heat flux measurements conducted in an associated work [73], employing surface temperature sensors, demonstrate that the results obtained with the approach of Woschni [119] give quite reasonable estimations of the heat transfer for homogeneous hydrogen combustion. Consequently, heat transfer rates predicted by zero-dimensional models using the approach of Woschni are taken as a reference. Wall heat fluxes in the CFD model are calculated with a logarithmic wall approach, where constant wall temperatures are specified as boundary conditions (cf. Section 3.3). In comparison to zero-dimensional models, the CFD-calculations predict equivalent levels of heat transfer during compression and for the first 50 % of heat release. Thereafter, the fluid to wall heat transfer is underestimated at least by a factor of 2 - 3. The reason for this discrepancy is caused by the temporal dynamics of pressure within IC engines which cannot be described with the chosen logarithmic wall model.

Figure 7.3 gives a comparison of the propagating flame front for the PFI operating points. An almost spherical shape of the expanding flame can be observed. The flame of the stoichiometric case consumes the mixture within $\Delta\varphi = 13°$ CA almost completely. Propagation speeds of considerable lean air/fuel equivalence ratios ($\lambda = 1.8$) are decelerated, resulting in a burning duration increased by a factor of 2.

To quantify the quality of the computational results, the deviation from experimental data is expressed by the mean indicated pressure p_{mi}, the magnitude and location of the maximum in-cylinder pressure p_{max} and $\varphi_{p_{max}}$, the position φ_{max} of the maximum value of heat release rate dQ/dt and the 50 % and 80 % point of the integral heat release, $\varphi_{50\%}$ and $\varphi_{80\%}$.
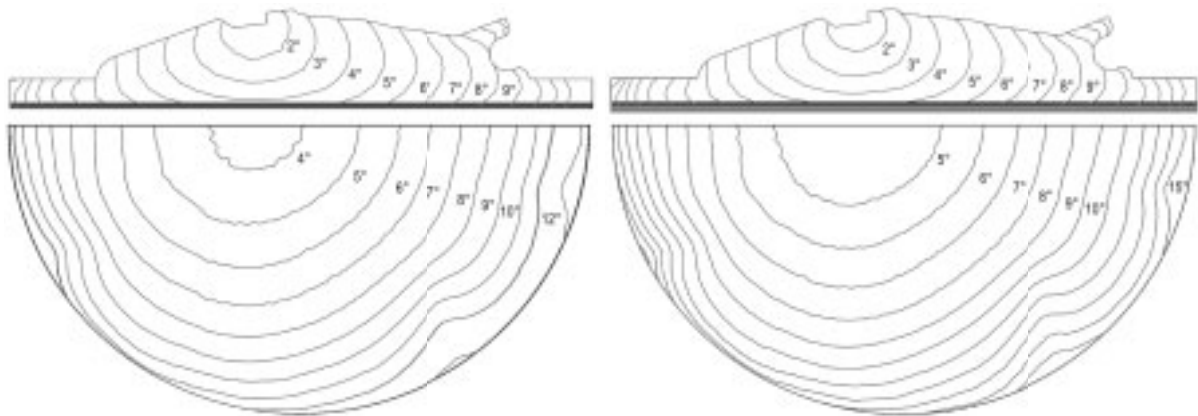
(a) Operating point P1: $\lambda = 1.0$, $n = 2000$ rpm.   (b) Operating point P2: $\lambda = 1.2$, $n = 2000$ rpm.
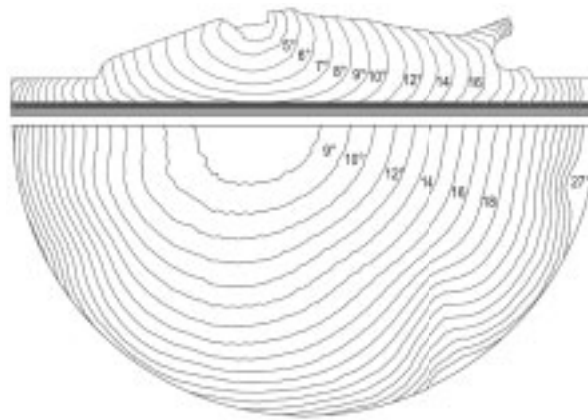
(c) Operating point P3: $\lambda = 1.8$, $n = 2000$ rpm.

Figure 7.3: Computed reaction progress for PFI operating points ($\tilde{c} = 0.5$) within a vertical and a horizontal sheet at $\Delta\varphi_{ign}$ given in CA after ignition timing. Results correspond to computations depicted in Figure 7.2 (a). The horizontal cross section is located 2 mm below the cylinder head gasket.

Corresponding values for PFI computations of the three investigated models are summarised in Figure 7.6. Results obtained by the Zimont model agree satisfyingly to experimental data. The value of p_{mi} is moderately underestimated. This is probably due to thermal drift of the pressure sensor during the expansion stroke where higher pressure levels are acquired by measurements. The maximum pressure levels range mostly within a deviation of $\Delta p = 2$ bar. The location of the maximum pressure is predicted within $\Delta\varphi = \pm 1°$ CA for nearly all operating points. With respect to the position of heat release points, the computations show satisfying compliance with heat release analysis up to at least 80 % of fuel conversion.

7.2.2   The Bradley Model

In contrast to the Zimont model, the Bradley model as another turbulent flame speed closure approach requires additional information on the Lewis number of the mixture (Le). Two different methods for a description of Le are investigated. Firstly, the Lewis number is defined by the deficient reactant of the mixture (Le_d), as originally proposed by Bradley et al. [22]. Secondly, the approach of Lipatnikov & Chomiak [68] is followed by specifying an effective Lewis number of the mixture (L_{eff}) in order to damp the Lewis number switch at stoichiometry. A comparison of both Le-approaches is conducted with the Extended Leeds Database as input for the laminar flame speed. As indicated in Figure 7.4 (a), results obtained by the Le_d-approach show increased heat release rates for lean operating points. The maximum levels of in-cylinder pressure are overrated by the computations for the $\lambda = 1.2$ and $\lambda = 1.8$ case. The described discrepancy is caused by the fact, that the Lewis number of the deficient reactant changes at $\lambda = 1$, being $Le_d = Le_{H_2} < 1$ for lean mixtures and $Le_d = Le_{O_2} > 1$ for rich mixtures. The results confirm that the simplistic approach of evaluating Le only by the deficient reactant, over-accentuates Lewis number effects between lean and rich mixtures, as also reported by Abdel-Gayed et al. [7]. Consequently, the value of turbulent flame speed is affected by this switch and the resulting flame speed is overestimated for computations of lean mixtures.

Employing an effective Lewis number of the mixture, as described in Equation 4.28, L_{eff} is a steady function within the entire range of equivalence ratio and has no instant increase at $\lambda = 1$. As presented in Figure 7.4 (b), heat release simulations show a better agreement between computational results and measurements for all the conducted operating points. The model constant is adjusted to the stoichiometric operating point resulting in $C = 2.5$. The value of this factor differs from that defined for the Le_d-approach due to the modified expression for the Lewis number which influences the effective burning velocity by $Le^{-0.3}$.

In Figure 7.4 (c) results are displayed using the L_{eff} approach and the Reaction Mechanism Correlation as laminar flame speed input. The computations show an overall good agreement with experimental results for a
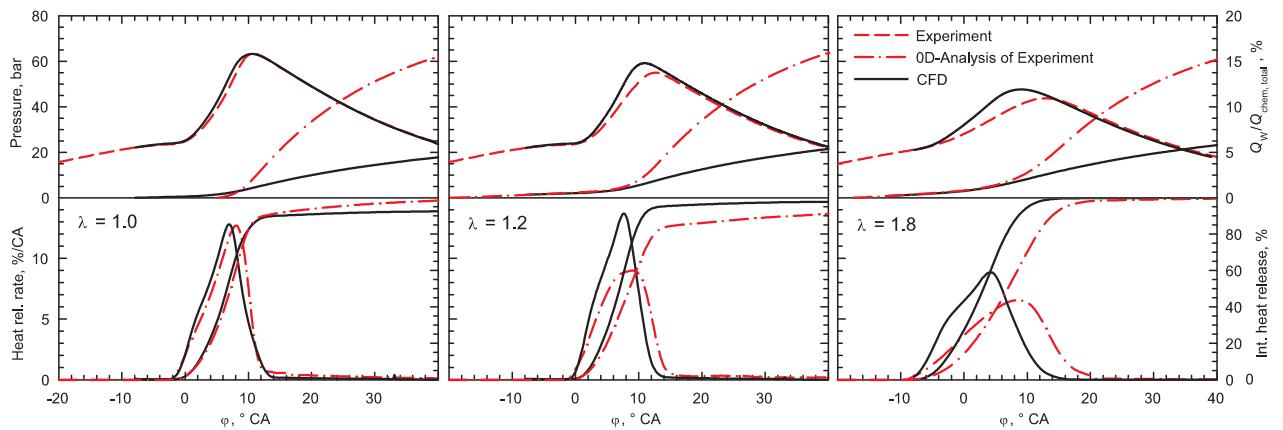
(a) Lewis number of deficient reactant Le_d / Extended Leeds Database / Model coefficient $C = 2.1$.
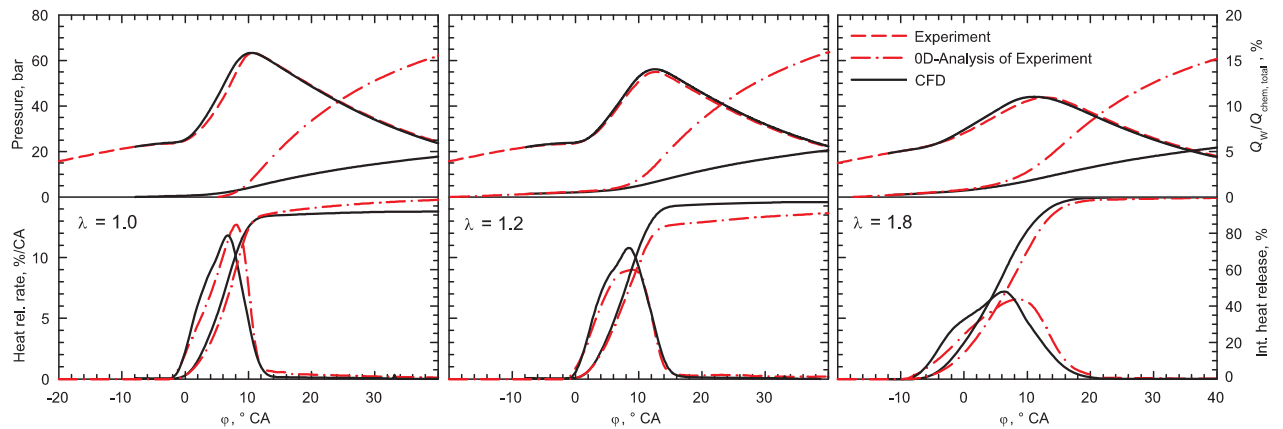
(b) Effective Lewis number of mixture Le_{eff} / Extended Leeds Database / Model coefficient $C = 2.5$.
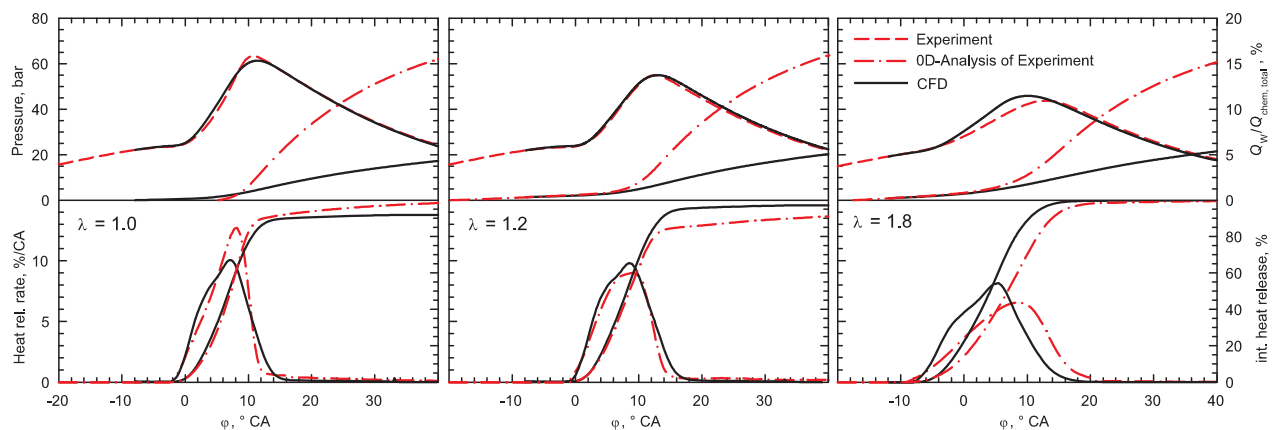
(c) Effective Lewis number of mixture Le_{eff} / Reaction Mechanism Correlation / Model coefficient $C = 2.5$.

Figure 7.4: Computations of PFI operating points P1-P3 ($n = 2000$ rpm) employing the **Bradley model** with the SST model for turbulence. A comparison of different Lewis number approaches is given in (a) and (b) using the Extended Leeds Database. Results of the Reaction Mechanism Correlation are depicted in (c).

model constant of $C = 2.5$. The heat release for the $\lambda = 1.8$ case is slightly shifted, resulting in an increased gradient of the rising pressure slope. The fluid to wall heat transfer is largely underestimated by the computations for levels of heat release above 50 %, as reported for the solutions obtained by the Zimont model.

The deviation of computational results from experimental data are depicted in Figure 7.6 in terms of p_{mi}, p_{max}, $\varphi_{p_{max}}$, φ_{max}, $\varphi_{50\%}$ and $\varphi_{80\%}$. The results of the Le_d-approach clearly show inconsistence for the lean operating points. The accuracy of computations with the Bradley model and the Le_{eff}-approach are approximately on the same level as computations with the Zimont model. With respect to results for $\lambda = 1.8$ obtained with the Reaction Mechanism Correlation, the Bradley model shows a larger discrepancy in the predicted heat release than the Zimont model as compared each time to experiments.

7.2.3   The Extended Coherent Flame Model

The ECFM model differs from the above presented turbulent flame speed closure approaches insofar as the increase in flame surface area is described by means of the surface density, obtained by solution of an additional transport equation. The Extended Leeds Database is applied as an input for the laminar flame speed.

To calibrate the combustion model, two main constants are provided: α and β which affect the flame surface production term $\mathcal{P}_1$ (Equation 4.32) and the destruction term $\mathcal{D}$ (Equation 4.36). Within the present computations, only the production term factor α is adjusted in order to match experimental data. The value of β is equal unity and is not changed. Computational results are compared to experimental data and heat release analysis in Figure 7.5.

The model shows best compliance to measured data of the stoichiometric operating point using a model factor of $\alpha = 0.14$. Calculations of lean operating points also demonstrate an acceptable agreement with experimental results. The computed heat release of the $\lambda = 1.8$ case is too fast and thus effects a slightly overrated gradient of the rising pressure slope.
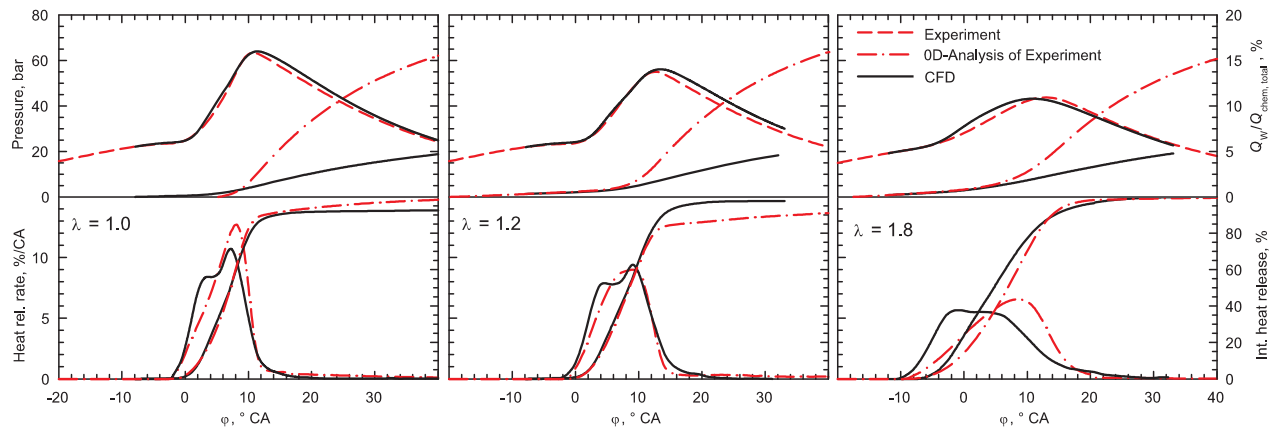
Figure 7.5: Computations of PFI operating points P1-P3 ($n = 2000$ rpm) employing the **ECFM model** with the SST model for turbulence and the **Extended Leeds Database** as input for laminar flame speed. Model coefficients: $\alpha = 0.14$, $\beta = 1.0$.

With respect to the $\lambda = 1.0$ and $\lambda = 1.2$ cases, a bending effect in the characteristics of heat release rate prior to its maximum value becomes apparent for the ECFM model due to reduction of flame front area caused by wall interaction of the flame. An effect which is also observed for calculations conducted with the turbulent flame speed models, however, in an insignificant amount.

The deviation of global quantities from experimental data is summarised in Figure 7.6. In comparison to the computations with the turbulent flame speed models, the ECFM approach shows a similar quality of results for the $\lambda = 1.0$ and $\lambda = 1.2$ cases. Regarding the $\lambda = 1.8$ operating point, remarkable deviations of $\Delta\varphi > 10°$ CA with respect to the location of the maximum heat release rate can be noted for results obtained by the ECFM model. Corresponding deviations of the Zimont and Bradley model are $\Delta\varphi < 1°$ CA and $\Delta\varphi < 2°$ CA, respectively. Despite these differences, the level of maximum in-cylinder pressure and the value of mean indicated pressure is adequately predicted by the ECFM model which is a combined effect of deviations in heat release rate dQ_B/dt and wall heat losses dQ_W/dt in opposite directions.

In general, the comparison with PFI operating points verifies the suitability of the three investigated combustion models with respect to homogeneous mixtures. It is remarkable that only minor differences between the results of the two investigated laminar flame speed correlations are observed. Simulations with the combustion models employing direct-injection mode are presented in the following section.
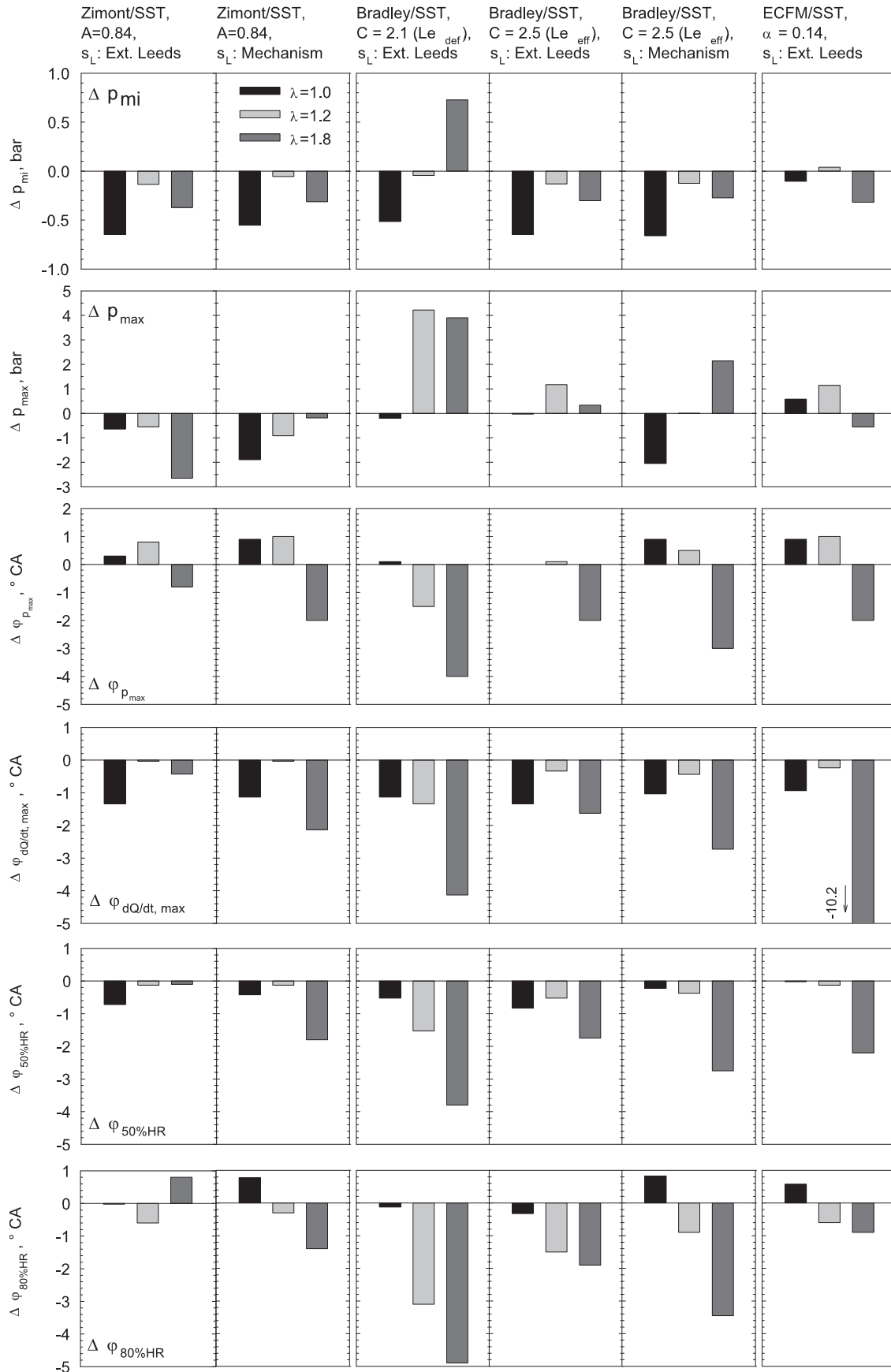
Figure 7.6: Deviation of computational results from experiments for **PFI operating points** (cf. Figures 7.2 to 7.5). Laminar flame speed s_L obtained by Extended Leeds Database and Reaction Mechanism Correlation.

7.3 Homogeneous and Stratified DI Operation

Regarding direct-injection operation points, the injection timing decisively influences the degree of mixture homogenisation and turbulence. Consequently, the accuracy of the entire CFD model with respect to partially premixed combustion not only depends on the combustion model itself, but is also influenced by the suitability of the non-reacting part of the model to predict local hydrogen concentration and turbulent velocity fluctuations. The mixing quality of the CFD results is verified by means of optical hydrogen concentration measurements out of which – in terms of RANS simulations – a satisfying agreement between computational and experimental results is observed, as discussed before in Chapter 6. Velocity measurements for the validation of computed turbulent quantities, however, are not available within the present work. Consequently, results obtained by different turbulence models have to be rated in combination with combustion models, using heat release curves and pressure traces.

Computations are conducted for the direct-injection operating points D1 to D4 using global values of air/fuel equivalence ratio of $\lambda = 1.0$ and $\lambda = 2.4$, cf. Section 2.1.1. The injection timing is varied in three steps with $SOI = -120°$ CA, $-60°$ CA and $-25°$ CA at a constant engine speed of $n = 2000$ rpm, covering homogeneous and stratified mixtures. Mixture formation results, as presented in Chapter 6, serve as initial conditions for the combustion calculations. Results obtained with the SST and RNG turbulence models are compared. Additionally, the influence of laminar flame speed on computational results is analysed.

It should be mentioned that the model coefficients $A = 0.84$, $C = 2.5$ and $\alpha = 0.14$ obtained from the PFI simulations may not be directly transferred to the DI model. The reason for the discrepancy between computations of PFI and DI cases is probably caused by a miscalculation of the absolute level of turbulent quantities. The source of turbulent velocity fluctuations which decisively affects the rate of heat release is of different nature for the two operation modes. Regarding PFI operation, the gas exchange process governs the allocation and level of velocity fluctuations, while the influence of the hydrogen injection is the determining

factor for DI operation. Accordingly, it is not surprising that in terms of two-equation turbulence models, only a relative prediction of turbulent quantities within the single operating modes is possible. Consequently, values for the model constants with respect to DI operation are estimated by adjustment of the simulations, using the homogeneous, stoichiometric operating point D1 ($SOI = -120°$ CA). Calculations of operating points D2 to D4 are performed using identical settings. In the following, results from the Zimont model, the Bradley model and the ECFM model are presented.

7.3.1 The Zimont Model

7.3.1.1 Pressure Traces and Heat Release Rate

Computations with the Zimont model are performed using the Extended Leeds Database as laminar flame speed input, representing unstable laminar flames. A comparison between computations conducted with the SST and the RNG turbulence model and measurements is given in Figure 7.7 for stoichiometric operating points with various injection timings and in Figure 7.8 for lean operation with early injection timing. With respect to stoichiometric operating points, $SOI = -120°$ CA is referred to as a homogeneous case, while $SOI = -60°$ CA and $-25°$ CA depict intermediate and highly stratified mixtures. Concerning a verification of the CFD results, additional information is given by zero-dimensional analysis of experimental data.

The SST and the RNG model are in good compliance with experiments for the homogeneous case ($\lambda = 1$) applying a model coefficient of $A = 0.6$. Pressure and heat release traces of the remaining investigated operating points are also well predicted by computations with the SST model using identical settings, thus approving a universal validity of the simulations.

In contrast, solutions predicted by the RNG model with $A = 0.6$ clearly deviate from the measurements for stratified operating points and lean mixtures. Employing the RNG approach as turbulence model, in order to achieve a satisfying compliance between numerical solutions and experiments, the model coefficient is adjusted to $A = 0.5$ for injection timings
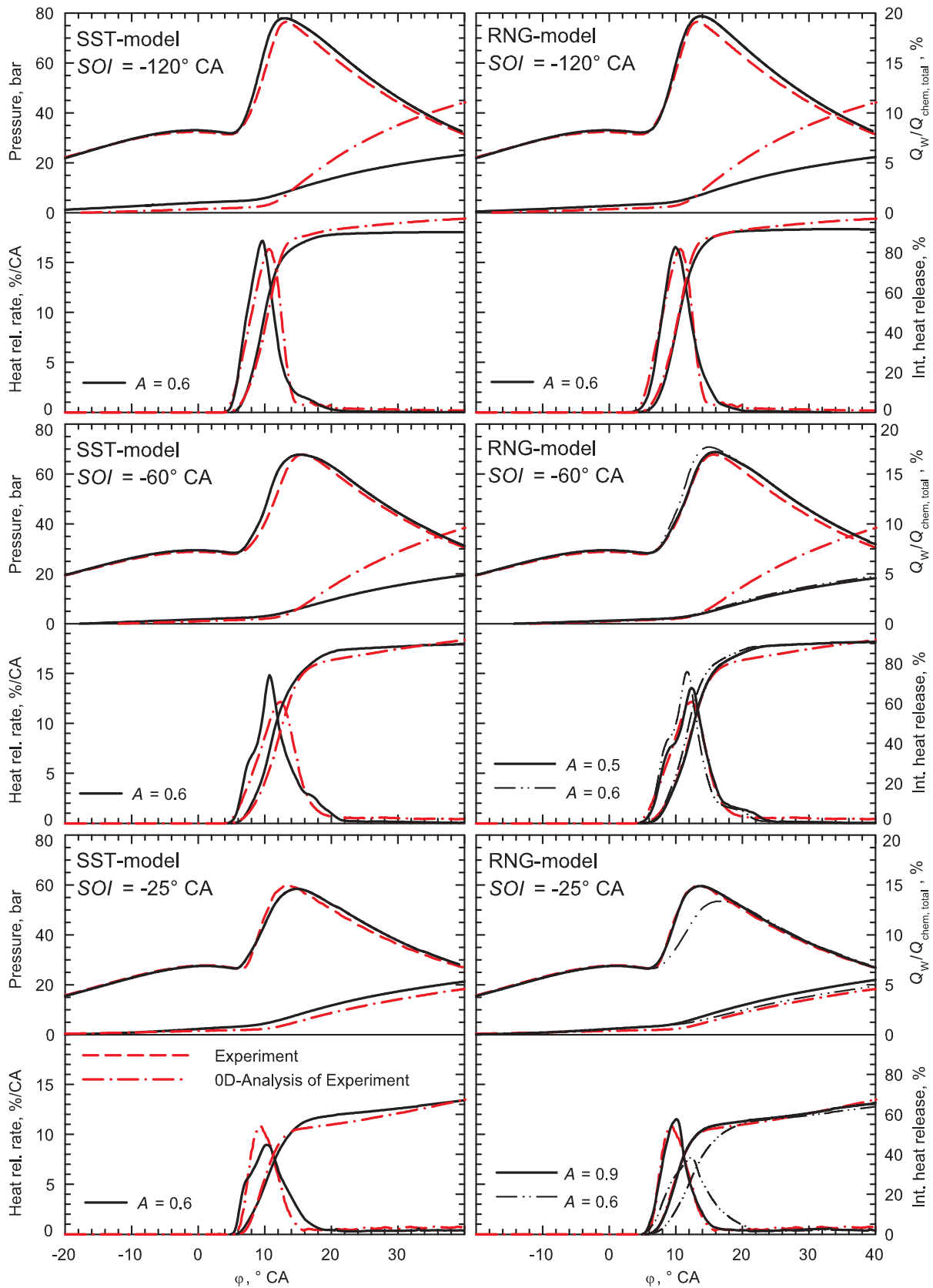
Figure 7.7: Computations of DI operating points employing the **Zimont model** and the **Extended Leeds Database** as laminar flame speed input ($\lambda = 1$, $n = 2000$ rpm). Injection timing variations are compared for the SST and RNG models. Data of heat release analysis are obtained from a zero-dimensional model using the Woschni approach [119] for a quantification of fluid to wall heat transfer.
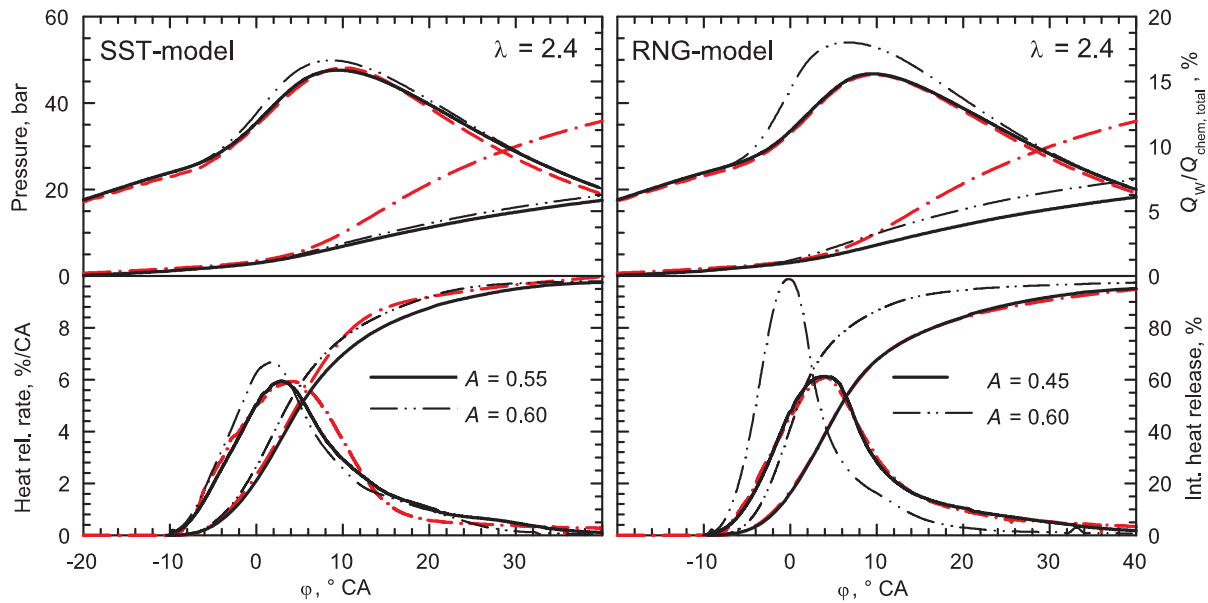
Figure 7.8: Results of lean operating point ($\lambda = 2.4$, $SOI = -120°$ CA, $n = 2000$ rpm) corresponding to computations shown in Figure 7.7.

of $SOI = -60°$ CA and to $A = 0.9$ for $SOI = -25°$ CA. Regarding the lean homogeneous case with $\lambda = 2.4$, the coefficient is set to $A = 0.45$ for computations with the RNG model. With respect to the quality of predicted pressure traces and heat release in comparison to experimental data, the RNG approach gives very accurate results after the adjustment of the model constant. These results are more precise than solutions obtained by the SST approach. The general quality of the models is evaluated by a comparison of global quantities, as listed in Figure 7.13 separately.

As already discussed for the PFI computations, in comparison to zero-dimensional analysis with the Woschni approach, the fluid to wall heat transfer is underrated by the CFD computations for integral heat release of $Q > 50$ %. Heat transfer results are very unreliable for highly stratified operating points. Incidentally, the discrepancy between CFD and Woschni vanishes at this condition. This effect is probably caused by miscalculation of the wall heat transfer by the zero-dimensional analysis, where stratification is not modelled. The results, however, may be taken as an example for the accurate compliance of heat release and pressure traces between CFD and zero-dimensional analysis in cases where equal wall heat transfer is assumed (c.f. Figure 7.7: $SOI = -25°$ CA, RNG-model, $A = 0.9$).

7.3.1.2 Characteristic Combustion Properties

Information on specific characteristics of the DI operating points is given in Figure 7.9 for simulations with the Zimont model in terms of mean values of air/fuel equivalence ratio at the flame front λ_{ff}, turbulent velocity fluctuations u', laminar and turbulent flame speed s_L and U_t, temperature T and area of the flame front A_F. Results are taken from the computations depicted in Figure 7.7 and 7.8. The temporal evolution of λ_{ff} emphasises the wide range of equivalence ratio for the stratified cases – operating points D2 and D3 – where fuel-rich conditions are present at start of combustion and extremely fuel-lean conditions are reached towards the end of combustion. The early injection cases – operating points D1 and D4 – are characterised by a homogeneous mixture where the local equivalence ratio slightly fluctuates around its global value. Simulations with the SST and the RNG model give almost identical results for values of λ_{ff}, but different levels for turbulent velocity fluctuations are predicted. Apparently, the highest turbulence intensity occurs for very late injection timings, e.g. $SOI = -25°$ CA. Here, turbulence is dominated by the propagation of the hydrogen jet. Corresponding mean values of turbulent velocity fluctuations at ignition timing are $\overline{u'} \approx 9$ m/s according to computations with the SST model and $\overline{u'} \approx 5$ m/s according to computations with the RNG model. In order to obtain approximately similar levels of turbulent burning velocities and thus similar combustion rates for both results, the model coefficient of the RNG computations has to be increased to $A = 0.90$. Concerning earlier injection timings the influence of the hydrogen jet on the global turbulence level is of lower impact and the discrepancies between turbulent velocity fluctuations predicted by the RNG and SST model diminish. Only small corrections of the leading model coefficient A are necessary.

According to the computations, mean turbulent burning velocities up to levels of $\overline{U_t} = 30$ m/s to 40 m/s are present during early stages of combustion. The effective value of U_t is reduced during expansion due to decreased turbulence levels and finally reaches the laminar value s_L. In comparison to hydrocarbon fuels where during the rapid burning phase the effective burning velocity is more than a magnitude larger than its laminar
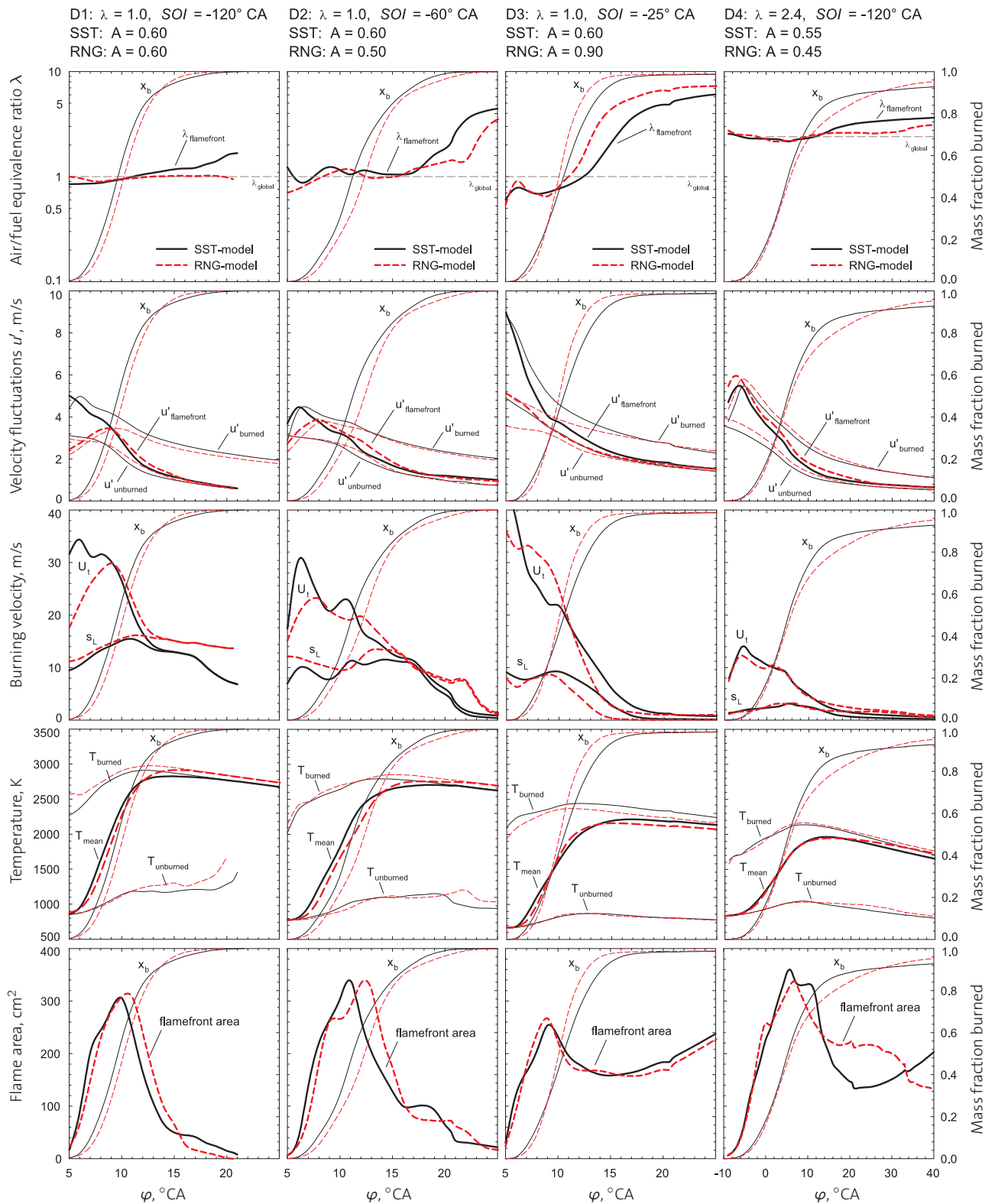
Figure 7.9: Temporal evolution of mean values of air/fuel equivalence ratio at the flame front λ_{ff}, turbulent velocity fluctuations u', laminar and turbulent flame speed s_L and U_t, temperature T and area of the flame front A_F predicted by the **Zimont model**. The burned zone mass fraction is given by x_b. Results are obtained from computations presented in Figures 7.7 and 7.8 for the **Extended Leeds Database**.

value, the ratio between effective and laminar values of burning velocities U_t/s_L for hydrogen engines is about a factor of 3 at stoichiometric conditions. This effect accentuates the relevance of high values of hydrogen laminar flame speed, which enables engine operation even at conditions of low turbulence kinetic energy.

Regarding combustion temperatures, a reduction of the burned zone temperature can be observed for stoichiometric operating points with delayed injection timing (D2 and D3) because of fuel-rich combustion and lowered compression end temperatures. Burned zone temperatures are remarkably lower for operating point D4 due to a reduction of the adiabatic flame temperature at lean conditions. The graph of the flame front area shows the standard characteristics of a spherical expanding flame for the homogeneous stoichiometric operating point D1, where the flame consumes the unburned zone entirely. With regard to the stratified case D3, however, the flame area furthermore increases after approximately $x_b = 50\ \%$ of mass fraction burned. This effect is caused by unmixed regions of pure air inside the combustion chamber and consequently leads to an increase of the flame area during the expansion phase. The lean operating point D4 shows a similar effect while the curve of the intermediate stratified operating point D2 is located somewhere between those of D3 and D1.

7.3.1.3 Propagation of Flame Front

The reaction progress of the burned gas zone is shown in Figure 7.10 for the investigated operating points by means of contour lines of the propagating flame front. Results are depicted in cross sectional views, specified by the vertical symmetry plane of the combustion chamber and by a horizontal cut located 2 mm below the cylinder head gasket. The flame front is defined by 50 % of the mean reaction progress ($\tilde{c} = 0.5$), describing the contour between the zones of the unburned and burned gas. The position is given as $\Delta\varphi_{ign}$ in CA after ignition timing.

With respect to early injection cases (Figure 7.10 a), an almost uniform expansion of the burned gas zone is observed for the stoichiometric operating point due to a sufficient homogenisation of the mixture prior to ignition. The flame front is only decelerated by the squish gap near the walls.
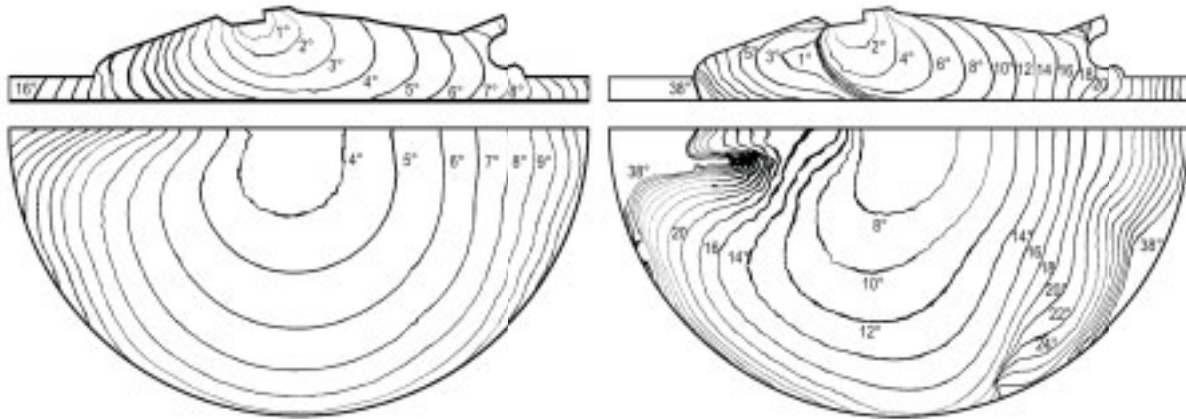
(a) Operating point D1: $\lambda = 1.0$, $SOI = -120°$ CA.   (b) Operating point D4: $\lambda = 2.4$, $SOI = -120°$ CA.
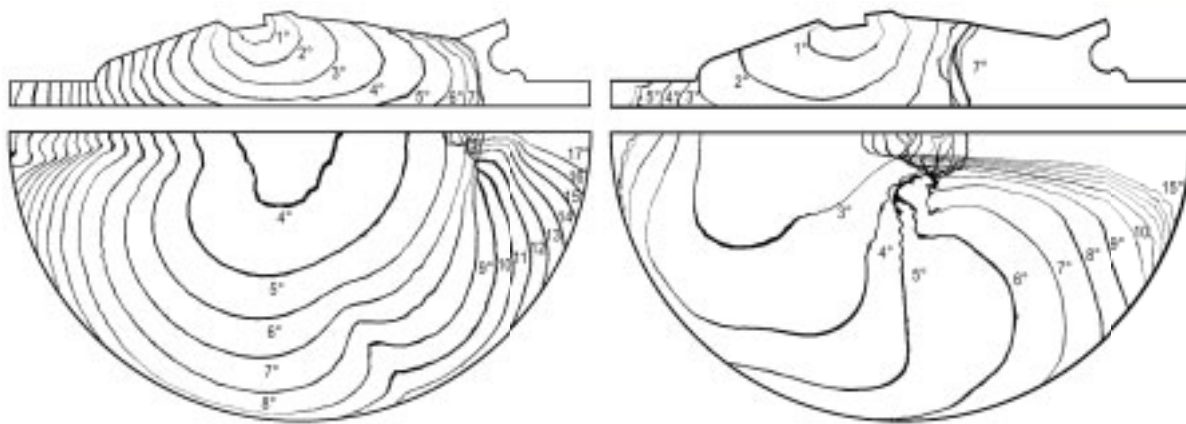
(c) Operating point D2: $\lambda = 1.0$, $SOI = -60°$ CA.   (d) Operating point D3: $\lambda = 1.0$, $SOI = -25°$ CA.

Figure 7.10: Computed reaction progress of the flame front ($\tilde{c} = 0.5$) within a vertical and a horizontal sheet at $\Delta\varphi_{ign}$ given in CA after ignition timing. Note the different scale in subfigure (b). Results correspond to computations depicted in Figure 7.9. The horizontal cross section is located 2 mm below the cylinder head gasket.

Stoichiometric operating points with delayed injection timings result in a more wrinkled and folded shape of flame front propagation caused by mixture stratification. The effect increases for SOI towards top dead centre. With regard to $SOI = -60°$ CA (Figure 7.10 c) – during the first $\Delta\varphi = 7°$ CA after spark ignition – the flame front expanses almost as uniformly as in the early injection case (a). The propagation speed, however, decelerates afterwards near the injector nozzle at very fuel-lean regions. The mixture is highly inhomogeneous for $SOI = -25°$ CA (Figure 7.10 d) and the characteristic of the reaction progress differs remarkably from the other cases. The flame front moves at fuel-rich zones with high flame speeds towards the domain opposite the injector, while the remaining zones re-

main primarily unaffected. Afterwards, the flame propagates along the cylinder wall in the direction of the centre of the domain while unmixed zones ($\lambda > 10$) around the injector nozzle stay unburned.

The flame propagation also deviates from the spherical shape for the lean operating point (Figure 7.10 b). This effect is caused by mixture inhomogeneities that are present despite early injection timings due to the low amount of fuel injected. In particular on the side of the domain opposite to the injector nozzle, extremely fuel-lean zones are found in the squish gap ($\lambda > 3$), and the speed of flame propagation is explicitly reduced, resulting in macroscopic folding of the flame front. Generally, an overall reduced effective burning velocity of the lean mixture compared to the stoichiometric case is observed.

7.3.1.4 Comparison with Reaction Mechanism Correlation

Regarding an evaluation of the impact of laminar flame speed on the combustion simulations, the DI operating points are computed using the Reaction Mechanism Correlation as model input for laminar flame speed. This correlation describes stable laminar flames where influences of flame front instabilities are neglected which results in lower burning velocities at corresponding conditions compared to flame speeds predicted by the Extended Leeds Database. Correspondingly, the value of the model constant is slightly increased for a calibration with experiments. Results of operating points D1, D2 and D3 are depicted in Figure 7.11. It is remarkable that the simulations give solutions similar to those obtained from computations with the Extended Leeds Database as laminar flame speed. Computations employing the SST turbulence approach are capable to show a satisfying prediction of burn rates and pressure traces for all investigated operating points using a model coefficient of $A = 0.7$.

The Zimont model shows reasonable results for operating point D1 in conjunction with the RNG turbulence approach using a model coefficient of $A = 0.7$. Computations of stratified cases (operating points D2, D3), however, are failing to provide satisfactory agreement to experimental data with this model coefficient, since the computed heat release is too early
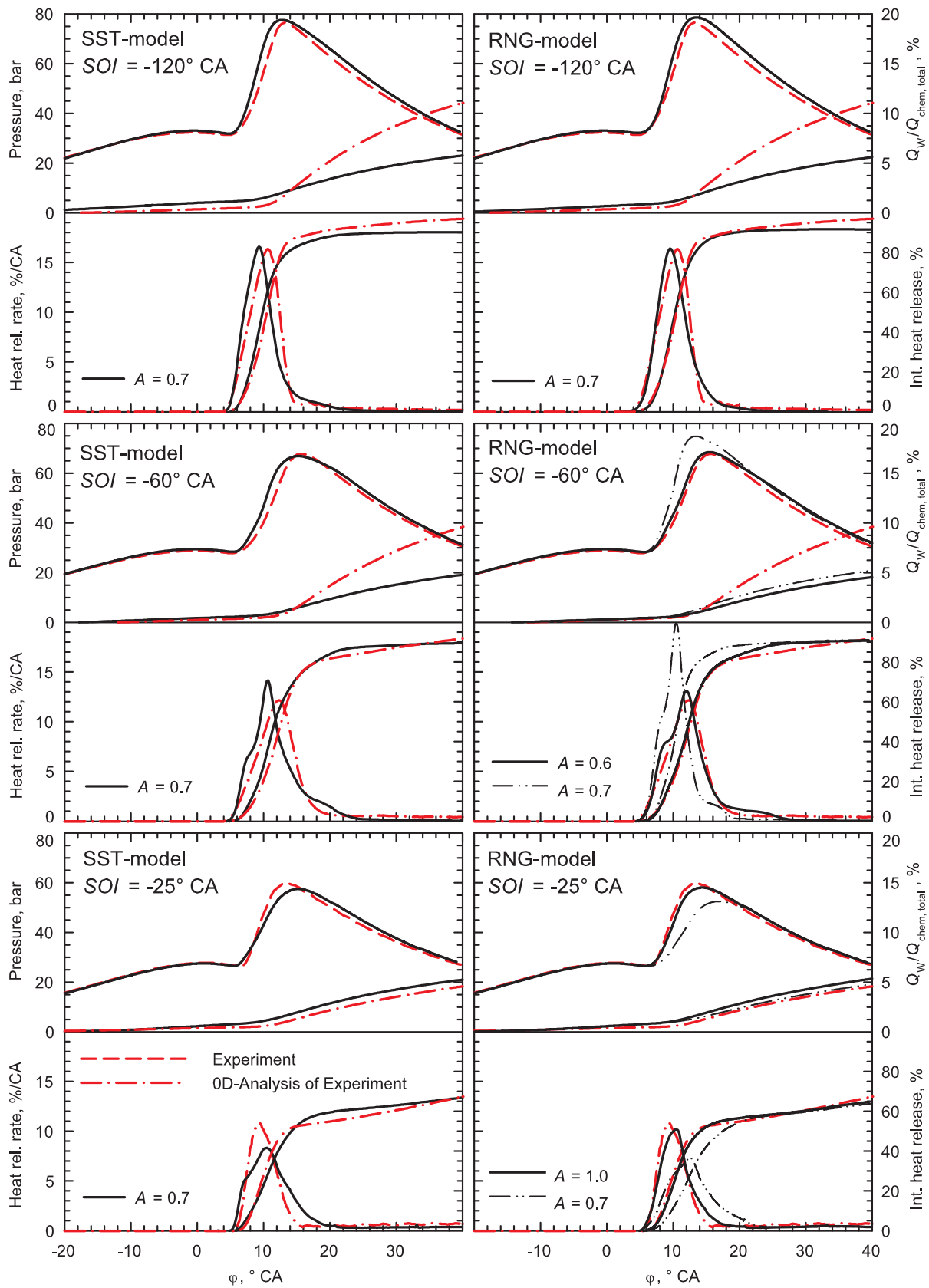
Figure 7.11: Complementary results to Figure 7.7 using the **Reaction Mechanism Correlation** as laminar flame speed input of the **Zimont model**.

for $SOI = -60°$ CA and too late for $SOI = -25°$ CA. The inconsistency is due to the interaction of turbulence generated by the gas exchange motion with the relatively low level of turbulence predicted by the RNG model for hydrogen injection (cf. Figure 6.6). This effect is not observed with the SST turbulence model, where the turbulence kinetic energy generated by the injection event overrides the turbulence produced by the gas exchange motion. Consequently, using the RNG turbulence model the prefactor is adjusted to $A = 0.6$ for computations with $SOI = -60°$ CA and to $A = 1.0$ for computations with $SOI = -25°$ CA.

7.3.1.5 Comparison with ETH-LAV Experimental Correlation

The validity of the ETH-LAV Experimental Correlation, which is based on measurements of hydrogen laminar burning velocities presented in Chapter 5, is analysed by comparison with results of the Extended Leeds Database and the Reaction Mechanism Correlation.

CFD computations of the engine have not been performed with the ETH-LAV Experimental Correlation. Therefore, flame speed values are differentiated by means of a post-processing approach. In-cylinder traces of the unburned gas temperature T_u, the pressure p and the mean air/fuel equivalence ratio at the flame front λ_{ff} are taken from CFD results presented in Figure 7.9. Laminar burning velocities are computed with the results of these quantities for each investigated flame speed correlation.

Corresponding results are depicted in Figure 7.12 for operating points D1-D4. Theoretical values of mean laminar burning velocities at the flame front, predicted by the different correlations, are displayed as a function of crank angle. The Reaction Mechanism Correlation generally gives the lowest flame speed values; results of the Extended Leeds Database are slightly located above; the ETH-LAV Experimental Correlation shows the highest values of all three correlations. Additionally, laminar burning velocities of the ETH-LAV Experimental Correlation are adjusted by multiplication with a constant factor of $a = 0.65$ in order to correspond to the level predicted by the other correlations for operating point O1. The modified curve shows a satisfying agreement with the other correlations for
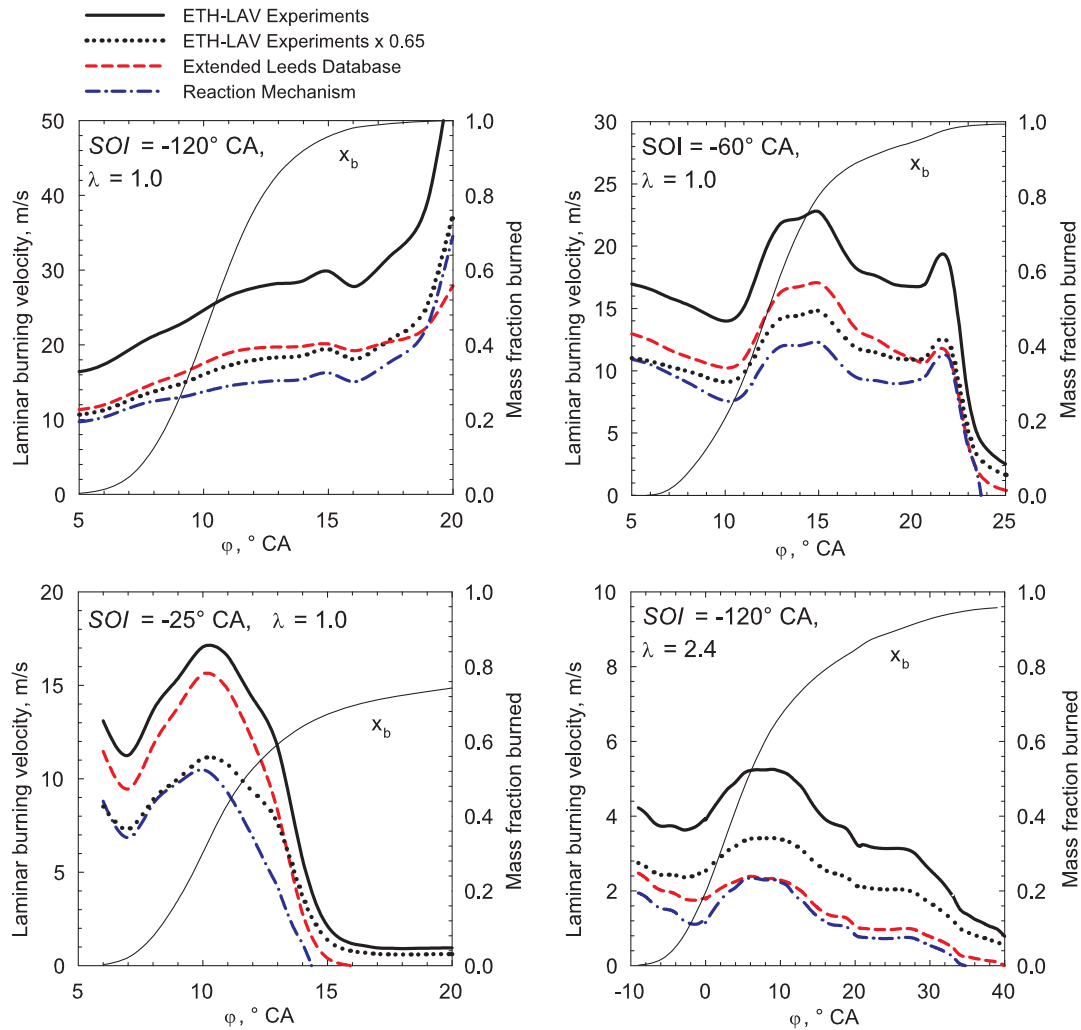
Figure 7.12: Comparison of theoretical mean laminar burning velocities at the flame front for operating points D1-D4 ($n = 2000$ rpm). Values are calculated with the correlations proposed in Section 5.5 using in-cylinder traces of λ_{ff}, T_u and p of CFD calculations displayed in Figure 7.9.

the operating point O2 ($\lambda = 1.0$, $SOI = -60°$ CA). With respect to highly stratified mixtures ($\lambda = 1.0$, $SOI = -25°$ CA), the laminar burning velocities are on the level of the results predicted by the Reaction Mechanism Correlation. Despite the adjustment, the flame speed of the lean mixture ($\lambda = 2.4$, $SOI = -120°$ CA) is slightly increased in a qualitative sense compared to the other results. Overall, the different correlations show quite comparable predictions regarding the sensitivity of laminar burning velocities for all investigated operating points.

Employing the ETH-LAV Experimental Correlation in future engine CFD computations, the required model settings may be estimated by the comparison given above. A modification of the laminar burning velocity by

a constant factor a is equivalent to a multiplication of the global model coefficient A of the Zimont approach by $\sqrt{a}$. Referring to the SST turbulence approach, the model coefficient employed with the Extended Leeds Database and the Reaction Mechanism Correlation ranges between $A = 0.6$ and 0.7. Assuming identical turbulence and fuel distribution, the factor $a = 0.65$ may be rewritten to a corresponding model coefficient of $A = 0.48$ to 0.56 for computations using the ETH-LAV Experimental Correlation.

Zimont & Lipatnikov [126] determined the model coefficient A by stirred bomb experiments for a wide range of fuels and operating conditions. The best accuracy for a reproduction of experimental data is reported for a value of $A = 0.52$. The value of A proposed for the ETH-LAV Experimental Correlation is close to these suggestions and consequently supports the use of this correlation.

7.3.1.6 Global Quantities

Figure 7.13 summarises the results obtained by the Zimont model for DI operation. A comparison of global quantities for all model combinations, the SST and RNG turbulence model and different laminar flame speed types is given. Again, the deviation of computational results from measurements and heat release analysis is expressed in terms of p_{mi}, p_{max}, $\varphi_{p_{max}}$, φ_{max}, $\varphi_{50\%}$ and $\varphi_{80\%}$. The model shows the best results for computations with the SST turbulence model and the Extended Leeds Database as laminar flame speed input using a model constant of $A = 0.60$. Corresponding values of indicated mean effective pressure are predicted with an accuracy of $\Delta p_{mi} = 0.5$ bar. The deviation of the calculated maximum in-cylinder pressure is within $\Delta p_{max} = \pm 2$ bar. The points of 50 % heat release, maximum value of heat release rate and the location of the maximum pressure level are within a tolerance of $\Delta\varphi = \pm 2°$ CA. Computations with the SST model using the Reaction Mechanism Correlation are also of satisfying quality. The results of this correlation for the highly stratified operating point D3 and the lean operating point D4, however, are of less accuracy.

Figure 7.13: Deviation of computational results with **Zimont model** from experiments (cf. Figures 7.7 and 7.11). Laminar flame speed s_L obtained by Extended Leeds Database and Reaction Mechanism Correlation.

The quality of simulations with the RNG model is limited for the stratified cases using a constant value of $A = 0.70$. Adequate results are only obtained if the model coefficient is adapted. For an analysis of experimental data a corresponding calibration of the model by measurements is justified. With regard to predictive computations of new engine designs, the Zimont model in combination with the SST turbulence approach seems to be more convenient, since a re-calibration of the model coefficient is not required. Nevertheless, even if an adjustment of a single constant A is necessary for the computations to agree with experimental results, the Zimont model is qualified to calculate premixed and partially premixed combustion quite well. Because the combustion model depends on uncertain input data, such as the laminar flame speed or the absolute level of turbulent quantities, the factor A may be considered as a corrective multiplier.

7.3.2 The Bradley Model

Considering the PFI results discussed in Section 7.2.2, direct-injection combustion calculations with the Bradley model are conducted, using the effective Lewis number Le_{eff} of the mixture instead of the original Lewis number description, employing the deficient reactant.

7.3.2.1 Pressure Traces and Heat Release Rate

Computations for both turbulent models, the SST and the RNG approach, are presented in Figures 7.14 and 7.15 using the Extended Leeds Database and the Reaction Mechanism Correlation as laminar flame speed input. The investigated operating points are identical to computations with the Zimont model. Again, the results are compared to experimental pressure traces and heat release analysis of a zero-dimensional model.

The outcome of the simulations is quite similar to that achieved by computations with the Zimont model. For both types of the chosen laminar flame speed correlation, the SST model leads to more convenient solutions than the RNG approach, using a constant model coefficient of $C = 2.0$ for

Figure 7.14: Computations of DI operating points employing the **Bradley model** and the **Extended Leeds Database** as laminar flame speed input ($\lambda = 1$, $n = 2000$ rpm). Injection timing variations are compared for the SST and RNG models. Data of heat release analysis are obtained from a zero-dimensional model using the Woschni approach [119] for a quantification of fluid to wall heat transfer.
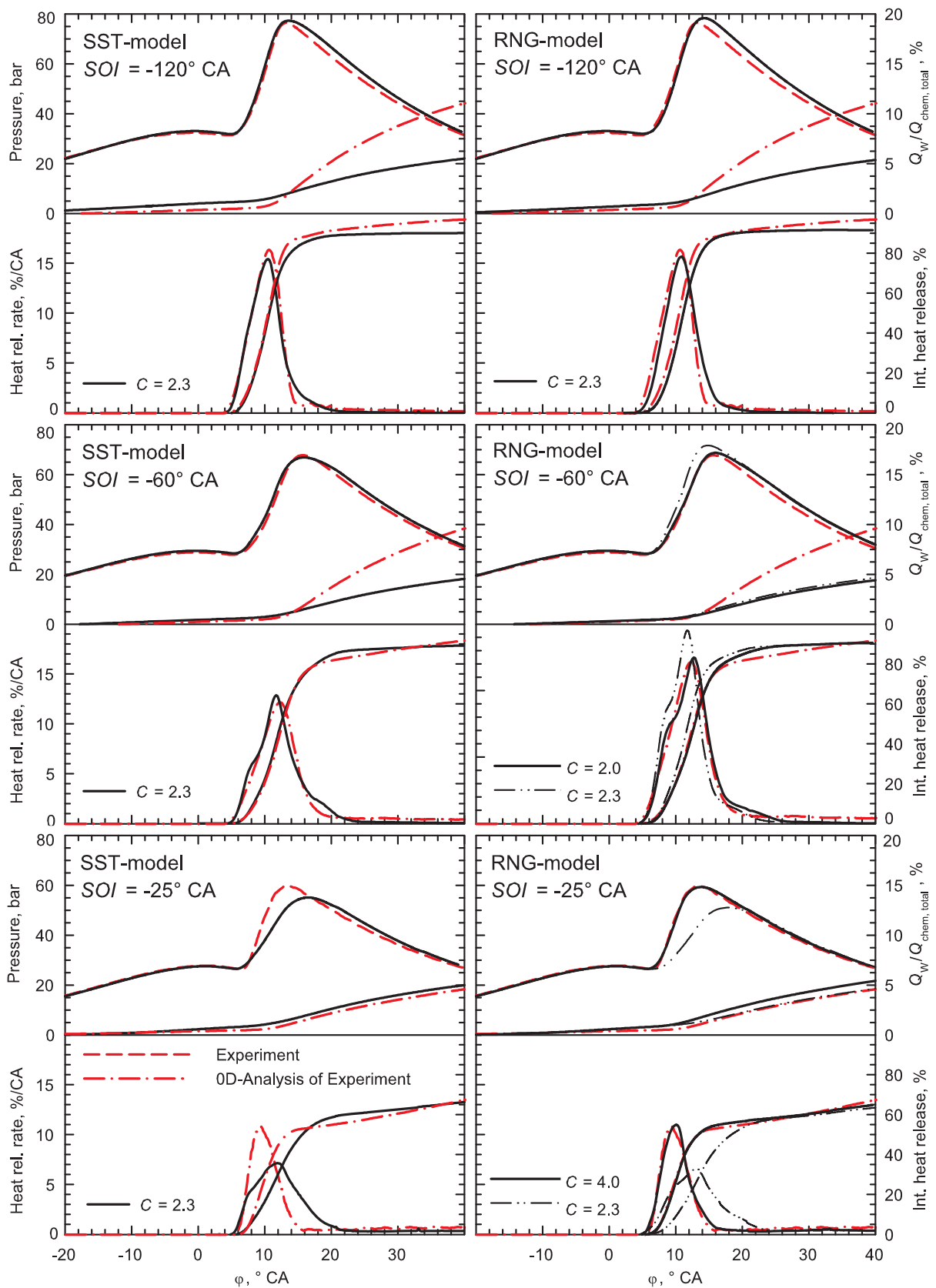
Figure 7.15: Complementary results to Figure 7.14 using the **Reaction Mechanism Correlation** as laminar flame speed input of the **Bradley model**.

the Extended Leeds Database and $C = 2.3$ for the Reaction Mechanism Correlation. With respect to stoichiometric operation, the homogeneous and moderately stratified operating points D1 and D2 are appropriately reproduced by the Bradley model if the SST turbulence approach is applied. Computations of the highly stratified operating point D3, however, underestimate the level of maximum in-cylinder pressure in a larger extent than observed for the Zimont model.

Results obtained by the Bradley model using the RNG turbulence approach show satisfying compliance with experimental results for stoichiometric homogeneous operation where $SOI = -120°$ CA (D1). Regarding stratified operation, the calculations slightly deviate for the $SOI = -60°$ CA case (D2) and show poor compliance with experimental data for $SOI = -25°$ CA (D3). Consequently, the model coefficient is adjusted in order to receive the best agreement between simulated and measured data. Employing the Extended Leeds Database as laminar flame speed, the coefficients for operating points D2 and D3 result in $C = 1.7$ and $C = 3.2$, respectively. With the Reaction Mechanism Correlation, the model coefficients of the same operating points become $C = 2.0$ and $C = 4.0$.

7.3.2.2   Global Quantities

Figure 7.16 gives an overview on the quality of global quantities of all operating points computed with the Bradley model in terms of deviation from experimental results. With respect to a constant model coefficient, the Bradley model shows the best accuracy employing the SST turbulence approach and the Extended Leeds Database as laminar flame speed. The accuracy of the characteristic quantities for operating points D1 and D2 is within an acceptable tolerance where deviations of $\Delta p_{mi} \leq 0.5$ bar, $\Delta p_{max} \leq 2.0$ bar, $\Delta \varphi_{p_{max}} \leq 0.5°$ CA, $\Delta \varphi_{dQ/dt,max} \leq 1.0°$ CA and $\Delta \varphi_{50\%} \leq 1.0°$ CA are achieved. The quality of results is comparable to solutions of the Zimont model as depicted in Figure 7.13. The discrepancy of results of the highly stratified operating point (D3) and lean homogeneous combustion (D4), however, is located above these limits and does not reach the quality obtained by the Zimont model. Regarding computations employ-
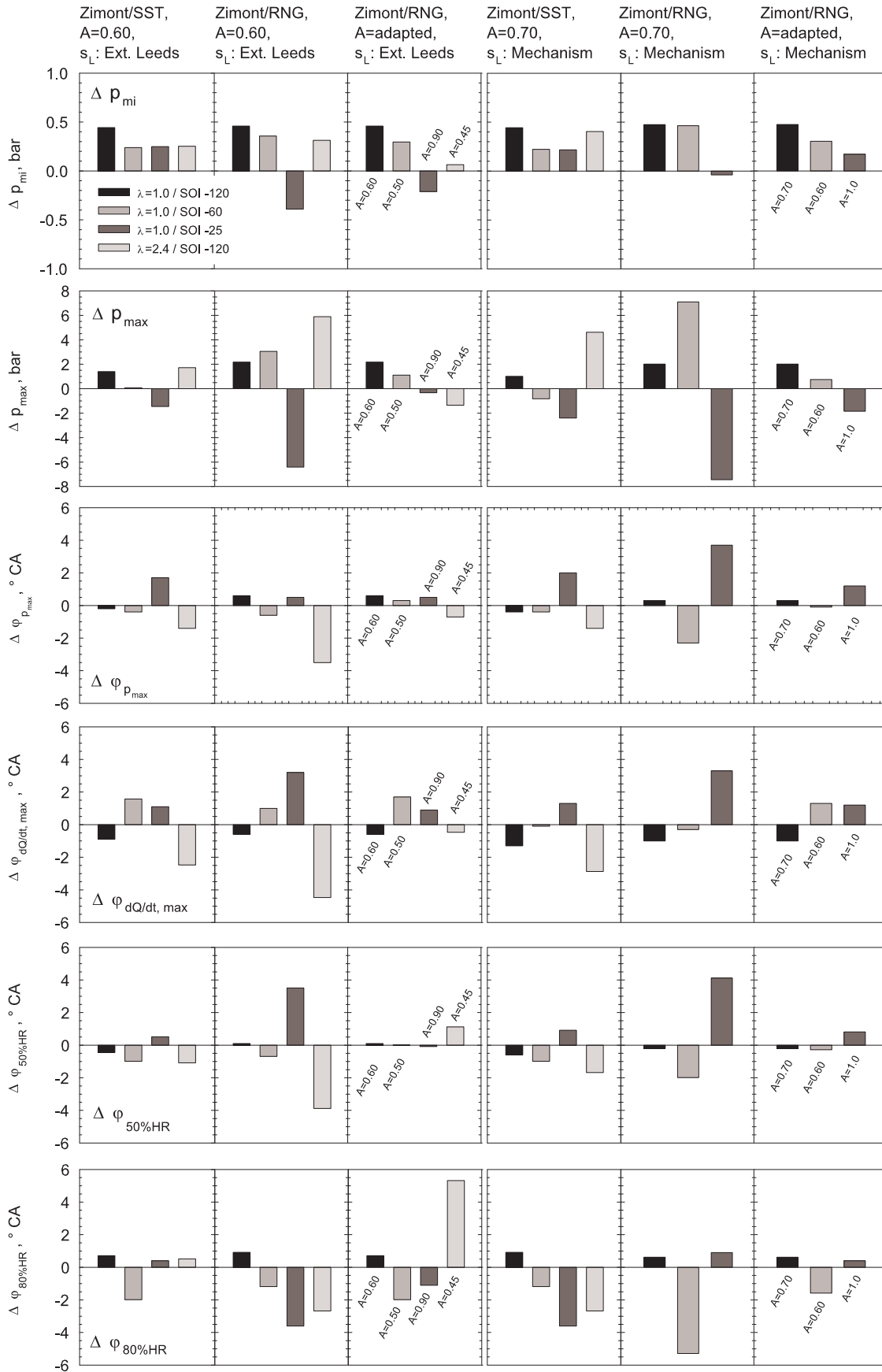
Figure 7.16: Deviation of computational results with **Bradley model** from experiments (cf. Figures 7.14 and 7.15). Laminar flame speed s_L obtained by Extended Leeds Database and Reaction Mechanism Correlation.

ing the Reaction Mechanism Correlation and the SST turbulence model, the same conclusion is valid.

In case the model coefficient is kept constant, combustion simulations conducted with the RNG approach as turbulence model show inadequate deviations in the characteristic quantities for most of the operating points. After adjustment of the coefficient a satisfying agreement of computational and experimental results is achieved for simulations with both laminar flame speed correlations.

7.3.3 The Extended Coherent Flame Model

7.3.3.1 Pressure Traces and Heat Release Rate

Simulations of operating points D1, D2, and D3 are conducted with the ECFM model, using the Extended Leeds Database as laminar flame speed and either the SST or RNG turbulence approach. Corresponding results are depicted in Figure 7.17.

In comparison to PFI results presented in Section 7.2, the ECFM model requires a fundamental change of the model coefficient for DI mode. In order to calibrate the computational results to experimental data of the homogeneous stoichiometric DI operating point D1, α is adjusted to a value of 0.50. This corresponds to an increase of the coefficient by more than a factor of 2.5 compared to the homogeneous stoichiometric PFI case. Contrarily, the model coefficients of the turbulent flame speed closure combustion models, A (Zimont) and C (Bradley), differ by only $15-20\%$ among corresponding PFI and DI computations.

The characteristics of pressure traces and heat release computed with the ECFM model and a coefficient of $\alpha = 0.50$ are of less good agreement with experiments than the results obtained by the turbulent flame speed models. A too fast heat release rate is predicted for the homogeneous operating point D1 when the SST turbulence approach is applied. The results show an increased level of pressure rise and a slightly overestimated maximum in-cylinder pressure. The simulations with the RNG turbulence approach give results that are closer to experimental data for this operating
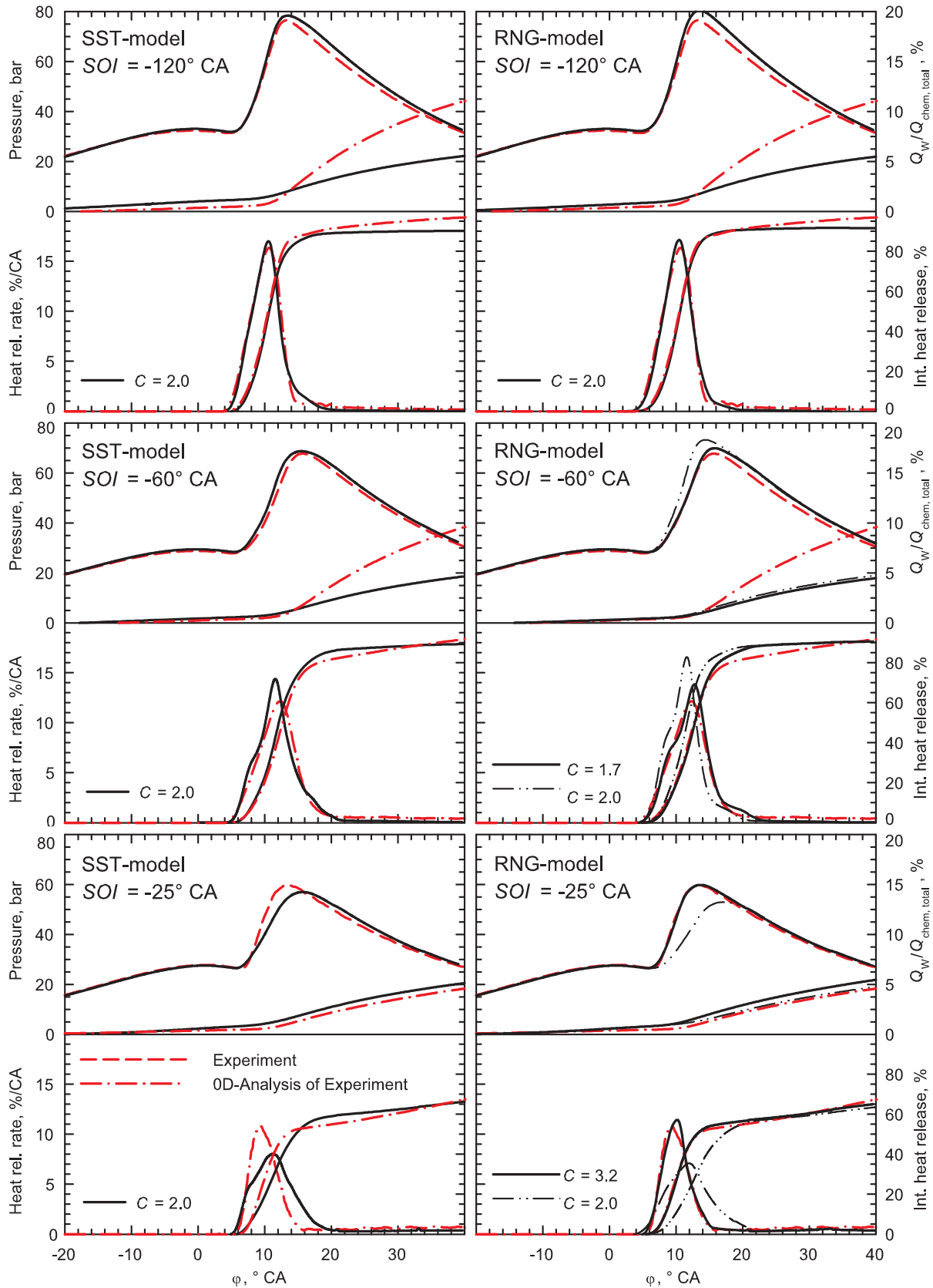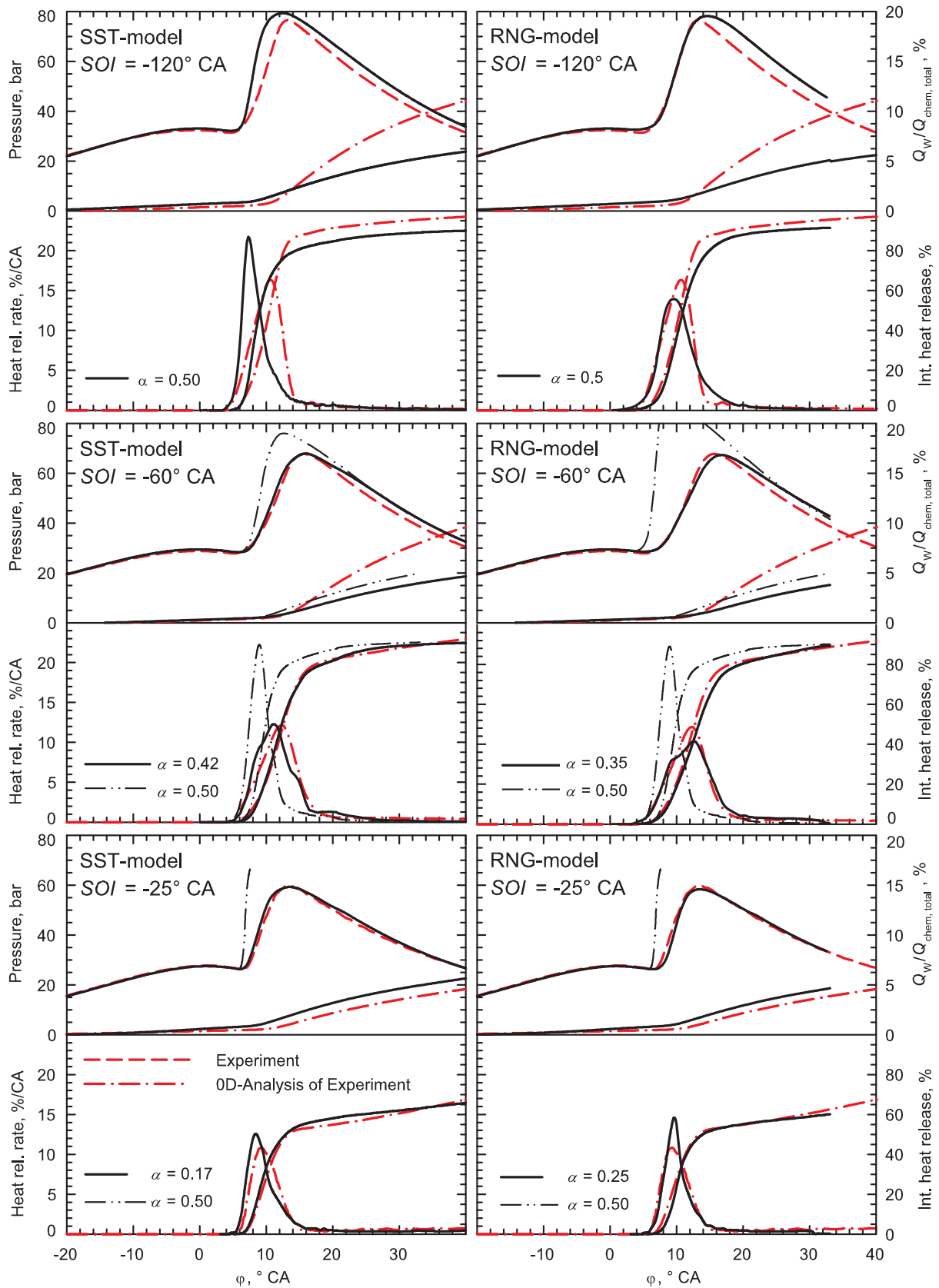
Figure 7.17: Computations of DI operating points employing the **ECFM model** and the **Extended Leeds Database** as laminar flame speed input ($\lambda = 1$, $n = 2000$ rpm). Injection timing variations are compared for the SST and RNG models. Data of heat release analysis are obtained from a zero-dimensional model using the Woschni approach [119] for a quantification of fluid to wall heat transfer.

point. During the expansion stroke the declining pressure traces of both computations are above the experimental value. These discrepancies are higher than that obtained from computations with the turbulent flame speed models and may not only be explained by miscalculation of fluid to wall heat transfer losses.

While for PFI operation, as discussed before, the ECFM model shows good transferability between different operating points without adjustment of the coefficient, stratified operating points in DI mode require a modification of the model coefficient. Computations with an unchanged value of $\alpha = 0.50$ result in considerably overrated levels of heat release rate and in-cylinder pressures for the intermediate stratified case D2, using either the SST or RNG turbulence approach. Corresponding results for the highly stratified case D3 with $\alpha = 0.50$ show an unphysical rapid heat release within $\Delta\varphi = 2°$ CA. Appropriate results are achieved when the model coefficient is adjusted to explicitly lower values of α. Computations of the lean operating point D4 have not been conducted with the ECFM model.

7.3.3.2   Global Quantities

Concerning a quantification of the ECFM results, the deviation of computed global quantities from experimental data is listed in Figure 7.18. The results show that most characteristic quantities are far beyond an acceptable tolerance without adaptation of the model coefficient or provide even unphysical solutions. After re-calibration of the model coefficient for each operating point, the quality of the results is satisfactory, however, still below the accuracy presented for the results of the Zimont model and the Bradley model.

The reason for the poor performance of the ECFM simulations with respect to DI operating points may be explained by the complexity of the model, which causes a strong sensibility to various influence variables. As explained in Section 4.4 in detail, a transport equation for the flame surface density is solved in the ECFM model, which includes various production terms, accounting for flame surface production due to turbulent stretch, strain rate and thermal expansion. The growth of surface produc-
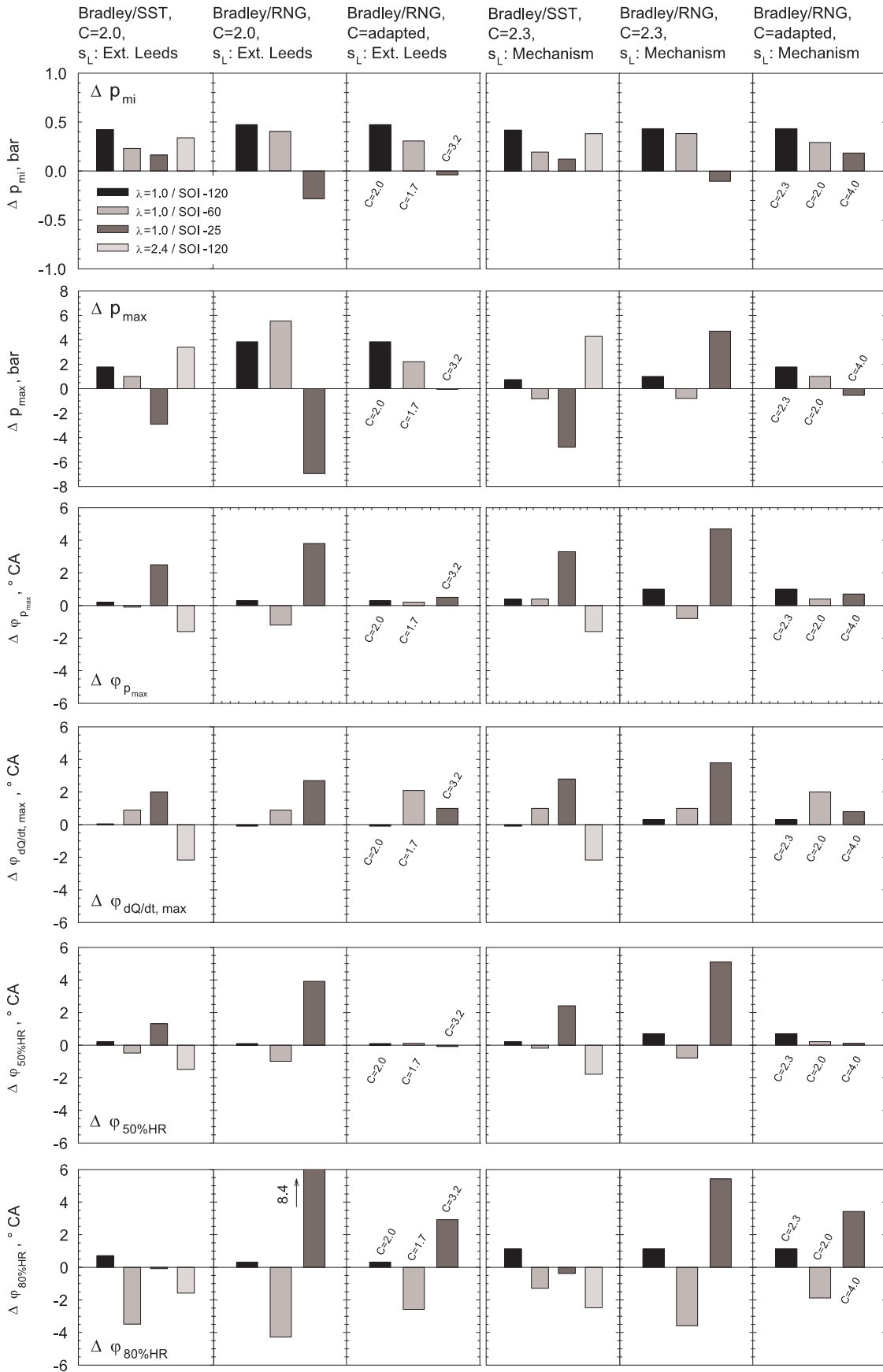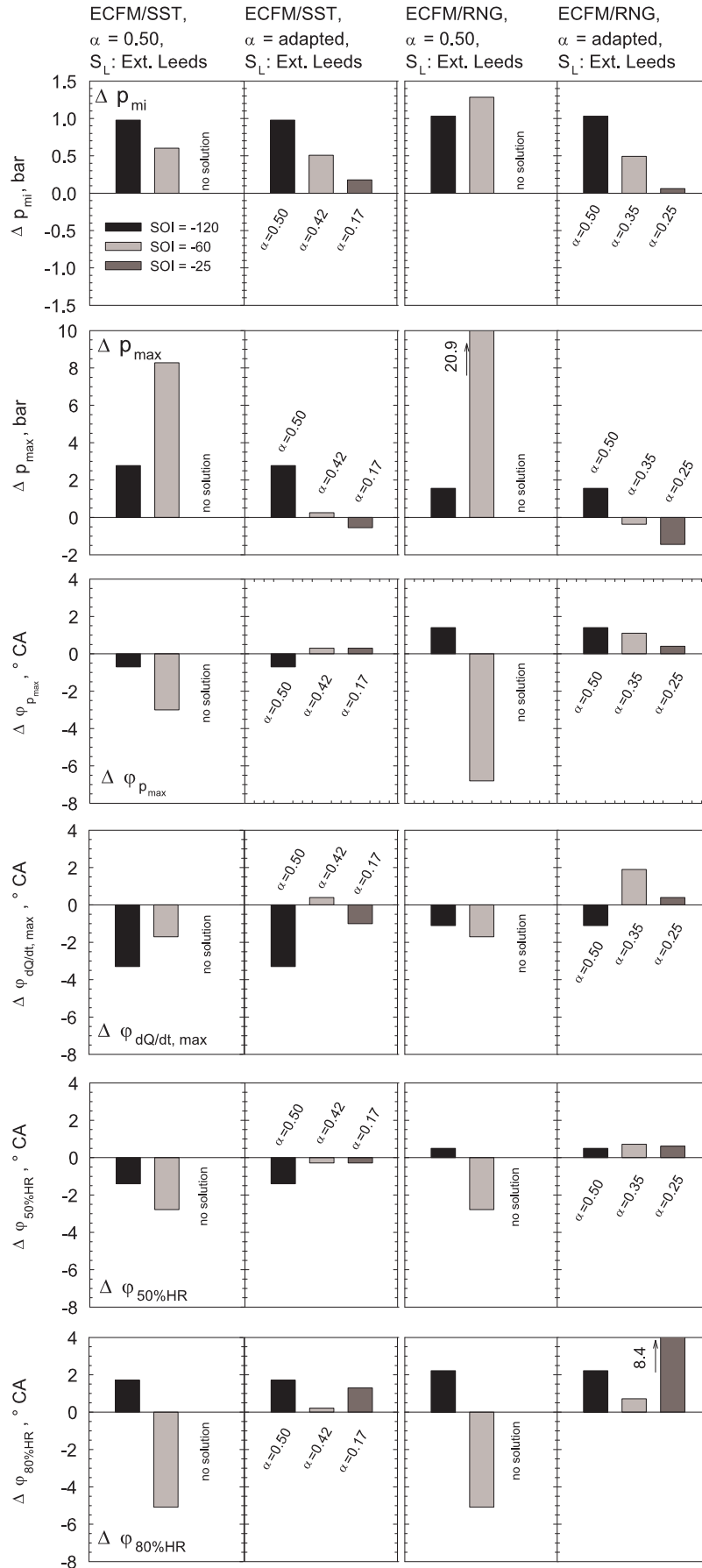
Figure 7.18: Deviation of computational results with **ECFM model** from experiments (cf. Figure 7.17). Laminar flame speed s_L obtained by Extended Leeds Database.

tion is limited by a single destruction term. A balance has to be found between production and consumption of flame surface density, in order to predict the main reaction rate of the progress variable transport equation. Beside the laminar flame speed correlation, additional submodels for the turbulent strain rate (Equation 4.38) and the laminar flame thickness (Equation 4.39) are required for the ECFM model, increasing the sensitivity of the entire model. Consequently, the ECFM model fundamentally differs from the less complex turbulent flame speed closure approach of the Zimont model and the Bradley model where the value of laminar flame speed is directly augmented by turbulent quantities.

Computations with the ECFM model may be affected by deficiencies of the submodels, the ITNFS or the Blint correlation. It may be the case that the simulations require additional tuning of the destruction term coefficient β which is kept equal unity for the existing results.

Numerical effects have to be also taken into consideration as a reason for possible miscalculations of the operating points. As already mentioned in Section 4.4, unphysical production of flame surface density may develop in regions, where the laminar flame speed is zero, due to the formulation of terms $\mathcal{P}_1$, $\mathcal{P}_2$ and $\mathcal{D}$ (Equations 4.32, 4.33 and 4.36). Although modifications are arranged to suppress numerical difficulties, it cannot be excluded that the flame surface production rate is completely unaffected for highly stratified operating points where the laminar flame speed is locally zero.

In view of the enormous uncertainties that emerge from turbulent combustion, simpler combustion models (e.g. the TFC approach) are recommended with which sensitivities can be managed and calibration can be accomplished easier.

7.4　Multi-Injection Operation

The validation of the turbulent flame speed closure model for premixed and partially premixed propagation flame combustion has been successfully demonstrated, using PFI and DI operating points. Since the combustion model is coupled with a laminar flamelet approach in the CFD code,

also non-premixed flames may be computed. Consequently, the Zimont model, which revealed best results of all the above investigated combustion models, is additionally employed for simulations of multi-injection engine operation. The intention is to evaluate the suitability of this approach for highly turbulent partially premixed flames. The computations are conducted with settings taken from single injection DI calibration where the model coefficient A is adjusted to 0.60 using the SST turbulence approach and the Extended Leeds Database as laminar flame speed.

The multi-injection is organised as follows: A premixed lean mixture is established by means of an early injection of a first portion of the fuel with $SOI_1 = -120°$ CA and $\phi_1 = 0.4$ ($\lambda_1 \approx 2.4$). The mixture is ignited by the spark at $\varphi = 13°$ CA BTDC and a second portion of fuel is injected into the propagating flame front ($SOI_2 = -5°$ CA, $\phi_2 = 0.6$), resulting in an overall stoichiometric value of equivalence ratio ($\phi = \phi_1 + \phi_2 = 1$).

7.4.1 Pressure Traces and Heat Release Rate

A comparison of pressure traces and heat release rate between computational and experimental results is given in Figure 7.19. Up to the start of the second injection at $SOI_2 = -5°$ CA, the pressure and the heat release rate is accurately predicted by the simulation. Thereafter, the values of these quantities are overestimated by the computational results. In particular the value of integral heat release at $\varphi = 50°$ CA ATDC, specified by the model ($Q = 95$ %), is considerably located above the value given by heat release analysis ($Q = 80$ %). The deviation in heat release rate between computational results and experiments after SOI_2 clearly indicates that the CFD model involves some uncertainties regarding the simulation of non-premixed combustion.

The level and points of maximum in-cylinder pressure and maximum heat release rate, however, are predicted more accurately. Corresponding deviations of the computational results from experimental values are $\Delta p_{max} = +2.5$ bar, $\Delta\varphi_{p_{max}} = +1.1°$ CA and $\Delta\varphi_{dQ/dt,max} = -0.13°$ CA. The discrepancy for the 50 % heat release point is $\Delta\varphi_{50\%} = -2.18°$ CA. The indicated mean effective pressure is calculated with an accuracy of $\Delta p_{mi} = -0.5$ bar at an IMEP of $p_{mi} = 10$ bar . Altogether, it is found that the results ob-
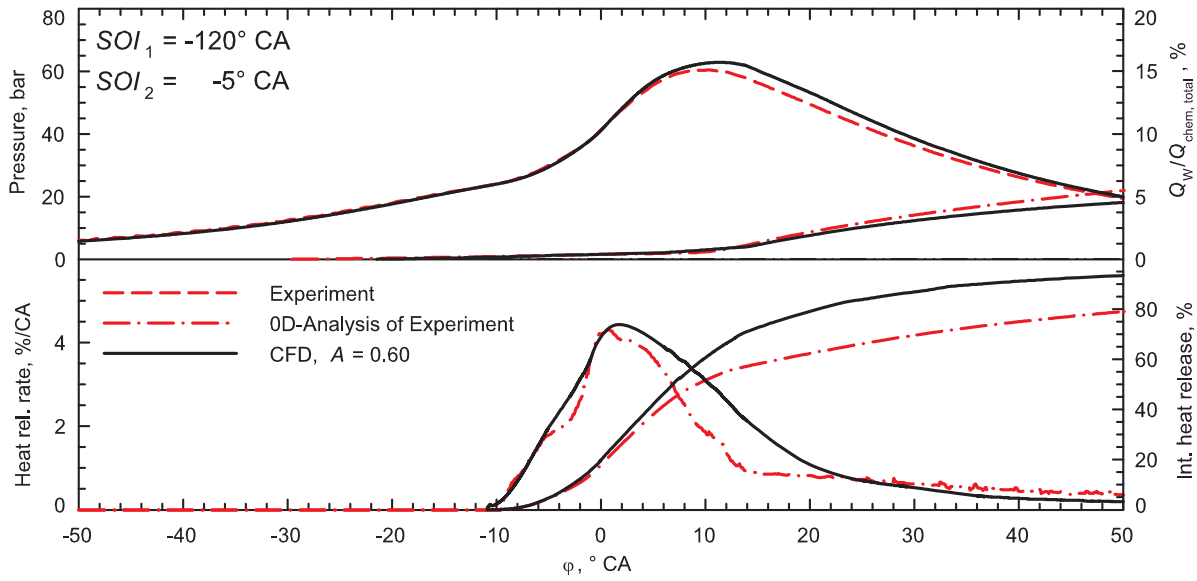
Figure 7.19: Multi-injection operating point D5 ($\lambda = 1$, $n = 2000$ rpm) computed with the **Zimont model** and the SST turbulence approach using the **Extended Leeds Database**.
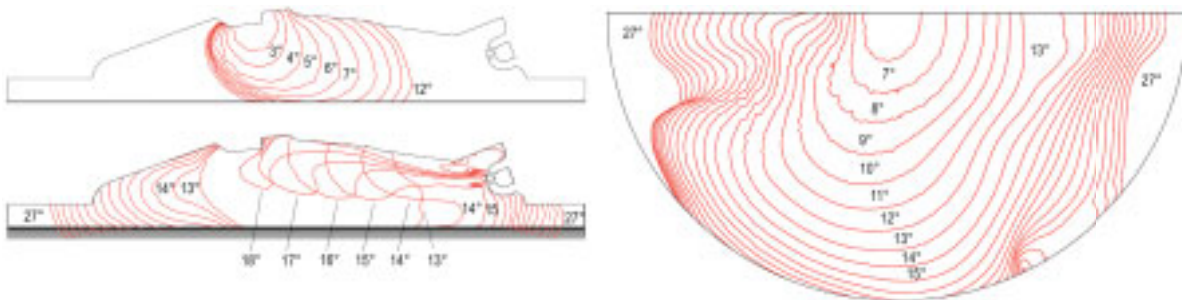
(a) Isolines of the flame front ($\tilde{c} = 0.5$) at $\Delta\varphi$ given in CA after ignition timing.
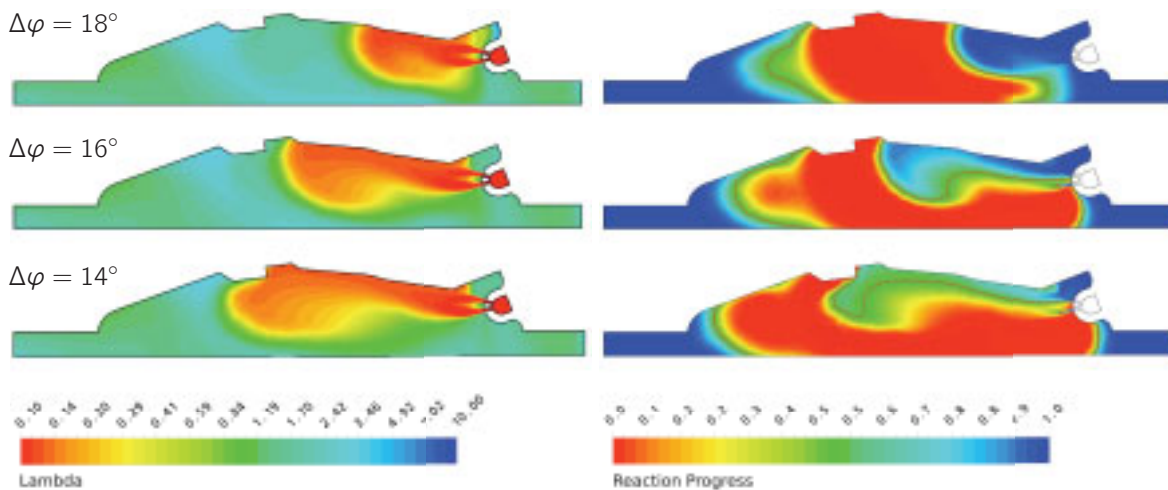
(b) Air/fuel equivalence ratio λ during second injection ($\Delta\varphi$ in CA after ignition).

(c) Local extinction of reaction progress during second injection corresponding to (b).

Figure 7.20: Reaction progress and air/fuel equivalence ratio λ of multi-injection operating point shown in Figure 7.19 ($\lambda = 1$, $n = 2000$ rpm). The horizontal cross section is located 2 mm below the cylinder head gasket.

tained by the computations for the multi-injection operating points are of less predictive quality than the results acquired for homogeneous and stratified DI operation.

7.4.2 Propagation of Flame Front

The reaction progress and the local distribution of air/fuel equivalence ratio λ during the second injection period are illustrated in Figure 7.20. Isolines at $\tilde{c} = 0.5$ depict the limit between unburned and burned gas zones. The front of the premixed flame propagates almost spherically during the first $\Delta\varphi = 12°$ CA after ignition timing. Afterwards, fresh fuel of the second hydrogen injection locally extinguishes the flame front. Fuel-rich zones are formed which are gradually consumed by the flame. As a consequence, the heat release is delayed in comparison to premixed operating points. The flame propagation proceeds in the lean premixed zones which are not directly affected by the second injection.

Multi-injection operation results in lower in-cylinder peak pressures. Consequently, the technique may be employed for high engine loads in conjunction with increased compression ratios. Additionally, the level of nitric oxides emissions is remarkably reduced as demonstrated in experiments (cf. Section 2.2).

7.5 Summary of Results

The sensitivity of the combustion model regarding variable pressure and enthalpy is investigated. With respect to IC engine applications, the necessity of an extended flamelet library, accounting for changing pressure and temperature conditions, is demonstrated. A comparison of major and minor species concentrations confirms inadequate results for standard (i.e. not variable in p and T) flamelet libraries.

Computations with the employed combustion models (Zimont, Bradley and ECFM) show good results for PFI operating points in a wide range of equivalence ratio. Only minor differences between the two investigated

laminar flame speed correlations are reported, indicating a slightly improved compliance with experimental data for heat release predicted by the Extended Leeds Database. An estimation of the Zimont model coefficient for computations with the ETH-LAV Experimental Correlation is given which is remarkably close to recommendations of Zimont & Lipatnikov.

An improvement of the Bradley model is presented, expressing Le as the effective Lewis number of the mixture instead of evaluating Le by the deficient reactant. Applying the modifications, the model gives reasonable results also for mixtures close to $\lambda = 1.0$ where the Lewis number of the deficient reactant changes discontinuously.

Regarding the computation of direct-injection operating points, the impact of the turbulence modelling approach is significant. The Zimont model shows a satisfying agreement with experimental data for a wide range of injection timings, provided that simulations are based on the SST approach. The Bradley model produces comparable results. Calculations with the RNG approach generally underestimate heat release rates for highly stratified mixtures, due to reduced production of turbulent kinetic energy during injection. In contrast to the TFC combustion models, adequate results for the ECFM model can only be achieved by adjustment of model coefficients for every operating point.

It is recommended to apply the Zimont combustion model in conjunction with the SST turbulence model in future CFD investigations. In the present work, employing the Extended Leeds Database, most suitable model coefficients result in $A = 0.84$ for PFI operating points and $A = 0.6$ for DI operation points. Applying the recently derived ETH-LAV Experimental Correlation a coefficient of $A = 0.48$ to 0.56 for the Zimont model is proposed. The employed coefficients of all combustion models are summarised in App. A.2.

A comparison of numerical results with wall heat calculations using the Woschni approach shows that the CFD computations underestimate the fluid to wall heat transfer at least by a factor of 2 for heat release at 50 % and by a factor of 3 at the end of combustion. The computed heat transfer is almost independent from the chosen turbulence model and from the numerical grid using the logarithmic wall approach.

The simulation of a multi injection operating point demonstrates that the combustion model is applicable only qualitatively for the prediction of partially premixed and non-premixed combustion. Although the computational results agree well with the experimental pressure traces (also due to an artefact of wall heat transfer), the comparison to heat release analysis reveals the limitations of the CFD model for these combustion modes. Additional uncertainties evolve from the zero-dimensional model which does not incorporate inhomogeneous combustion for the determination of heat release rate from in-cylinder pressure analysis. Future investigations should address an improvement of the modelling approach for partially premixed and non-premixed combustion modes.

Chapter 8

Conclusions and Outlook

The mixture formation and combustion in hydrogen internal combustion engines is successfully computed for PFI and DI operating points, employing a modified version of the 3-D CFD code ANSYS CFX. Different types of combustion models which are capable to predict combustion modes of simultaneously premixed and non-premixed flames are investigated. Hydrogen concentration PLIF measurements are used for validation of mixture formation simulations; heat release simulations are compared to zero-dimensional analysis of pressure traces from a single cylinder research engine. A fundamental contribution to the definition of hydrogen laminar burning velocities at engine-relevant conditions is provided by flame speed measurements in a single-cylinder compression machine. A refinement of operation strategy and engine design may be deduced from the computational results, allowing detailed insight into the mixture preparation and fuel conversion of the engine.

8.1   Computational Model

Different turbulence models, a Shear Stress Transport (SST) model, a k-ε model based on Renormalisation Group theory (RNG) and a Reynolds Stress Model (RSM) are discussed. Regarding hydrogen injection simulations, it is demonstrated that the main influence on the numerical results occurs from the applied turbulence modelling approach with respect to turbulence parameters. The hydrogen concentration is less influenced by the different types of turbulence models. The process of mixture forma-

tion is successfully validated for each of the models with respect to local hydrogen concentrations through PLIF measurements. During the hydrogen injection phase, however, the RSM model and the RNG k-ε model ($u' \approx 3.5$ m/s) show considerably lower mean levels of turbulence kinetic energy than the SST model ($u' \approx 15$ m/s). The largest discrepancy between the models is observed for late injection timings. Regarding heat release calculations, computations with the SST model provide appropriate results, whereas computations of highly stratified engine operation with the RNG model show reduced heat release rates. It may be the case that the RNG model underestimates the level of turbulence induced by the hydrogen jet.

Computed flow field parameters (e.g. turbulent velocity fluctuations) have not yet been validated by experiments. It is proposed to conduct experiments of segregated hydrogen injections in a high-pressure vessel and to use corresponding results for a validation of CFD simulations. An adequate measurement technique has to be defined in order to carry out gas-phase velocity field measurements (e.g. Particle Image Velocimetry, Flow Tagging Technique [65]). Measurements of turbulent velocity fluctuations could provide essential information on the calibration of the turbulence model constants which would further improve the predictability of the combustion simulations of highly stratified mixtures.

Amongst the investigated combustion models, the different Turbulent Flame Speed Closure (TFC) approaches proposed by Zimont and Bradley provide satisfying results for PFI and DI operating points. An acceptable agreement of specific characteristics, such as level and crank angle position of the mean and maximum cylinder pressure and 50 % fuel conversion point, is achieved in comparison to experimental data ($\Delta p_{mi} < \pm 0.5$ bar, $\Delta p_{max} < \pm 2$ bar, $\Delta \varphi_{p_{max}} < \pm 2°$ CA, $\Delta \varphi_{50\% HR} < \pm 1°$ CA). Regarding computations of a multi-injection operating point the coupled flamelet model, designed for partially premixed and non-premixed combustion, demonstrated satisfying results in a qualitative sense, only. The issue of multiple-injections combustion must be investigated in detail in the future. The Lewis number description involved in the Bradley model is redefined, expressing the effective Lewis number of the mixture. Due to

a discontinuity at $\lambda = 1$, computations with the original assumption, using the Lewis number of the deficient reactant, showed inaccurate results. The new specification is a remarkable improvement of the predictability for stratified DI operation where lean and rich values of equivalence ratio are present.

The Extended Coherent Flame Model (ECFM) shows satisfying results for premixed operating points. With regard to stratified DI mode, adequate results are only obtained when the model coefficient is adjusted for each operating point. The numerical stability of this model is also less satisfactory than the simplistic approach of the TFC models. Inconsistencies are observed in computations of stratified DI operating points with this model and it remains to be investigated where these derive from. In order to improve the accuracy of the numerical results, the applied submodel for the computation of the turbulent strain rate κ_t (Equation 4.38) and the description of the laminar flame thickness (Equation 4.39) have to be eventually revised.

The ignition model of the partially premixed combustion approach presently employed does not consider auto ignition effects. Regarding the computation of self-ignition engine operation and abnormal combustion, such as knock, the development of a more sophisticated ignition model is recommended.

8.2 Hydrogen Burning Velocities

Hydrogen laminar burning velocities are a crucial input parameter for the employed combustion models. Accurate values of laminar flame speed between the lean and rich extinction limits of hydrogen/air mixtures are required for the computation of DI operating points. Due to the insufficient amount of existing data on laminar burning velocities at engine-relevant conditions, investigations on a single-cylinder compression machine have been conducted in this work in order to determine laminar propagation speeds of high-pressure, high-temperature hydrogen flames. Correlations for laminar flame speed have then been derived from the compression

machine measurements and corresponding results have been compared to data obtained from reaction mechanism computations.

Caused by an acceleration of the flame front due to hydrodynamic and thermo-diffusive instabilities, a disagreement between the magnitude of measured and computed results is observed finally. The instabilities emerge at elevated pressure levels and influence the propagation speed of the flame. Computations with a kinetic scheme are not able to reproduce these effects, yielding lower values of laminar flame speed than the experiments. As comparison, the linear stability analysis proposed by Bradley et al. [23] is applied to exclude instability effects from the measured data providing laminar burning velocities of stable flames. The derived theoretical values are on a level comparable to results predicted by the kinetic model. The estimated increase of flame speed due to instabilities is a factor of about 2 for stoichiometric mixtures and increases even more for lean air/fuel equivalence ratios λ. The question is addressed whether the assumption of stable laminar flames (e.g. provided by reaction mechanism computations) is justified as input for the combustion models with respect to IC engine conditions. At high-pressure conditions ($p \geq 20$ bar), the combustion simulations show improved results for alternative flame speed correlations provided by measurements accounting for flame front instability effects. The recent measurements on hydrogen laminar burning velocities provide flame speed data for a wide range of equivalence ratio, temperature and pressure ($\lambda = 0.4 \ldots 2.8$, $T = 350 \ldots 700$ K, $p = 5 \ldots 45$ bar) and represent an essential amelioration of the existing literature on hydrogen laminar flame speed. In the present work, instability effects of the fully unstable flame at large flame radii are considered. Future examinations may also focus on the development of instabilities accounting for the history of the flame.

Moreover, the superimposition of instability effects and turbulent velocity fluctuations on the flame propagation has to be closely examined in further investigations. It is suggested to compare burning velocities of premixed laminar unstable flames with those of corresponding turbulent flames while the level of turbulent quantities is gradually increased. The question whether instability effects are suppressed by turbulent stretch may then be answered.

8.3 Consequences for Engine Combustion Design

The presented simulation models have been validated for a wide range of operating points using the present engine geometry and may be consequently employed for a further improvement of the engine design.

Regarding an assessment of the present engine configuration, the conducted simulations depict an insufficient mixture preparation for some of the operating points. Stoichiometric operation with early injection timing results in an overall good mixture homogenisation. Delayed injection timings, however, show fuel-rich zones in the squish gaps which cause a deceleration of the heat release rate. Concerning fuel-lean operating points with $\lambda = 2.4$, it is noticed that a reduction in the amount of injected fuel – in comparison to stoichiometric operation – considerably increases the mixture inhomogeneity despite early injection timings ($SOI = -120°\,CA$). With respect to the formation of nitric oxides, an improvement of the mixture homogenisation would remarkably reduce the emission level of corresponding operating points.

A refinement of the injection design – not published within the present work – has been investigated by means of 3-D CFD simulations and proved to be a remarkable enhancement of the mixture formation and combustion process. Components of corresponding injectors have already been manufactured and are currently examined in engine test bench experiments, providing promising results [41].

Combustion simulations of the present engine geometry show that the propagating flame is decelerated in the squish gaps due to the uneven cylinder head geometry. Although squish gaps are necessary for premixed engine operation in order to increase the turbulence level in the combustion chamber, a simplification of the squish gaps and the cylinder head geometry should be examined with focus on increased laminar burning velocities of hydrogen flames. The proposed simulation models provide an approved method in order to predict mixture formation and heat release of virtual engine designs and may remarkably enhance the development processes of forthcoming engine types.

Regarding future engine strategies, the significance of multi-injection, partially diffusion-flame operation has to be considered. Present results show a slight decrease of the engine efficiency in this operation mode, however, peak in-cylinder pressures and combustion anomalies are remarkably reduced. It is possible that this type of combustion may be adequate in conjunction with a highly compressed supercharged engine in order to control full load operation. Currently, corresponding investigations are undertaken within an Austrian national research project [5] and in an associated research work [102]. The combustion models presented above may be regarded as a contribution to further optimisation of the engine design.

Appendix A

Model Coefficients

A.1 Turbulence Models

A.1.1 The Standard k-ε Model

The model coefficients[1] in the Equations (3.17) to (3.19) for the standard k-ε model are defined as

$$C_{\varepsilon 1} = 1.44, \quad C_{\varepsilon 2} = 1.92, \quad C_\mu = 0.09$$

and

$$\sigma_k = 1.0, \quad \sigma_\varepsilon = 1.3 \, .$$

A.1.2 The RNG k-ε Model

In contrast to the standard k-ε approach, the model coefficients in Equations (3.17) to (3.19) are replaced by

$$C_{\varepsilon 1} = 1.42 - \frac{a(1 - \frac{a}{b})}{1 + ca^3}, \quad C_{\varepsilon 2} = 1.68, \quad C_\mu = 0.085$$

and

$$\sigma_k = 0.7179, \quad \sigma_\varepsilon = 0.7179,$$

---

[1]The turbulence model coefficients applied here are taken from [78].

where the absolute terms *a*, *b* and *c* as part of the analytic function for the definition of constant $C_{\varepsilon 1}$ are specified as

$$a = \sqrt{\frac{P_k}{(\rho C_\mu \varepsilon)}}, \quad b = 4.38, \quad c = 0.012 \,.$$

A.1.3   The Shear Stress Transport Model

The coefficients in Equations (3.21) and (3.22) result from linear blending of the model constants of the underlying *k-ω* and *k-ε* approach:

$$C_k = 0.09, \quad \sigma_k = F_1 + 1, \quad \sigma_{\omega_1} = 2F_1 + \frac{1-F_1}{0.856}, \quad \sigma_{\omega_2} = 1/0.856,$$
$$C_{\omega 1} = 5/9 F_1 + 0.44(1 - F_1) \quad \text{and} \quad C_{\omega 2} = 0.075 F_1 + 0.0828(1 - F_1).$$

$F_1 = \tanh(arg)^4$ is a hyperbolic tangent blending function specified in [78].

A.1.4   The Reynolds Stress Turbulence Model

The model coefficients in Equations (3.19) and (3.23) are defined as

$$C_\mu = 0.1, \quad C_s = 0.22, \quad \sigma_\varepsilon = 1.36, \quad C_{\varepsilon 1} = 1.45, \quad \text{and} \quad C_{\varepsilon 2} = 1.83 \,.$$

A quadratic approach for the pressure strain-correlation Φ_{ij}, specified in [78], is employed. Appropriate model constants are defined as

$$C_{s1} = 1.7, \quad C_{s2} = -1.05,$$
$$C_{r1} = 0.9, \quad C_{r2} = 0.8, \quad C_{r3} = 0.65, \quad C_{r4} = 0.625, \quad \text{and} \quad C_{r5} = 0.2.$$

A.2   Combustion Models

A.2.1   The Zimont Model

Values employed for the model coefficient A of Equation (4.17) in dependence of the applied laminar flame speed correlation and turbulence modelling approach:

Zimont model coefficients	Port Fuel Injection		Direct Injection	
	SST	RNG	SST	RNG
Reaction Mechanism Correlation	$A = 0.84$	-	$A = 0.7$	$A = 0.6$ to 1.0
Extended Leeds Database	$A = 0.84$	-	$A = 0.55$ to 0.6	$A = 0.45$ to 0.9

A.2.2   The Bradley Model

Values employed for the model coefficient C of Equation (4.25) in dependence of the applied laminar flame speed correlation and turbulence modelling approach:

Bradley model coefficients	Port Fuel Injection		Direct Injection	
	SST	RNG	SST	RNG
Reaction Mechanism Correlation	$C = 2.5$	-	$C = 2.3$	$C = 2.0$ to 4.0
Extended Leeds Database	$C = 2.5$	-	$C = 2.0$	$C = 1.7$ to 3.2

A.2.3   The Extended Coherent Flame Model

Values employed for the model coefficients α and β in Equations (4.32) to (4.36).

ECFM model coefficients	Port Fuel Injection		Direct Injection	
	SST	RNG	SST	RNG
Extended Leeds Database	$\alpha = 0.14$	-	$\alpha = 0.17$ to 0.5	$\alpha = 0.25$ to 0.5
	$\beta = 1$		$\beta = 1$	$\beta = 1$

Equation 4.39 is closed by the following expression for the coefficient κ according to Benkenida et al. [15]:

$$\kappa = \alpha_0 f(\phi)g(T_u)h(p) \,, \tag{A.1}$$

$$\alpha_0 = 3.37 \tag{A.2}$$

For $0.8 \leq \phi \leq 1.2$

$$f(\phi) = -6.992 \cdot 10^{-1} + 2.853\phi - 1.154\phi^2 \tag{A.3}$$

For $1.2 < \phi \leq 2.0$

$$f(\phi) = f(\phi = 1.2) \tag{A.4}$$

$$g(T_u) = 4.329 \cdot 10^{-1} + 7.496 \cdot 10^{-5}T_u + 1.450 \cdot 10^{-6}T_u^2 \tag{A.5}$$

$$h(p) = 1.455 - 1.821 \cdot 10^{-2}\left(\frac{p}{p_0}\right) + 1.062 \cdot 10^{-4}\left(\frac{p}{p_0}\right)^2 \tag{A.6}$$

with $p_0 = 1.013$ bar.

Appendix B

Hydrogen laminar flame speed correlations

B.1 ETH-LAV Experimental Correlation (2007)

Results of flame speed measurements, obtained from thermodynamic analysis of pressure traces, are incorporated into a correlation for unstable laminar flames, cf. Section B.1. The correlation is based on the expression specified in Equation 5.7. The basic conditions are $p_0 = 20$ bar and $T_0 = 600$ K indicating engine-relevant conditions. The basic laminar flame speed s_{L0} is defined as

$$
s_{L0} = \begin{cases} a_6\phi^6 + a_5\phi^5 + a_4\phi^4 + a_3\phi^3 + a_2\phi^2 + a_1\phi - a_0 & 0.4 \leq \phi \leq 2.5 \\ s_{L0}(\phi = 2.5) + [7.23 - s_{L0}(\phi = 2.5)]\frac{\phi - 2.5}{5 - 2.5} & \phi > 2.5 \end{cases}
$$

where the pre-factors a_0 to a_6 are defined as

$$
\begin{aligned}
&a_0 = 1.2994, \quad a_1 = -13.976, \quad a_2 = 52.317, \quad a_3 = -46.525, \\
&a_4 = 18.498, \quad a_5 = -3.4774, \quad a_6 = 0.25.
\end{aligned}
$$

The expression exponents α and β are linear functions of $\lambda = 1/\phi$

$$
\begin{aligned}
\alpha &= 0.0163(1/\phi) + 2.2937, \\
\beta &= 0.2037(1/\phi) - 0.575.
\end{aligned}
$$

The correlation is validated by experiments within $0.4 \leq \phi \leq 2.5$. Outside this range, the flame speed correlation yields reasonable values. In order to express the influence of exhaust gas,

$$\gamma = 2.715 - 0.5\phi \tag{B.1}$$

is adopted from the correlation proposed by Verhelst [111]. The validity domain of the correlation, based on experimental results of the present work is $0.4 \leq \phi \leq 2.5$, $10 \leq p \leq 45$ bar and $350 \leq T_u \leq 700$ K.

B.2   Reaction Mechanism Correlation

Laminar flame speed computations conducted with a kinetic scheme are summarised in a correlation, as presented in Section 5.3. The fundamental flame speed s_{L0} in Equation 5.7 is defined as

$$s_{L0} = \begin{cases} a_6\phi^6 + a_5\phi^5 + a_4\phi^4 + a_3\phi^3 + a_2\phi^2 + a_1\phi - a_0 & \phi \leq 2 \\ 0.172\phi^3 - 1.603\phi^2 + 3.593\phi + 2.940 & \phi > 2 \end{cases}$$

where the pre-factors a_0 to a_6 are defined as

$$\begin{array}{llll} a_0 = -2.813, & a_1 = 20.818, & a_2 = -65998, & a_3 = 108.95 \\ a_4 = -84.173, & a_5 = 30.521, & a_6 = -4.239. \end{array}$$

The expression exponents α and β are

$$\alpha = \begin{cases} -54.278\phi^3 + 116.3\phi^2 - 85.633\phi + 24.877 & \phi \leq 0.5 \\ -0.0685\phi^5 + 0.9066\phi^4 - 4.7032\phi^3 & \phi > 0.5 \\ +12.019\phi^2 - 14.929\phi + 9.37, \end{cases}$$

$$\beta = \begin{cases} -0.2426\phi^2 + 0.8\phi - 1.1522 & \phi \leq 1.75 \\ 0.0075\phi^3 - 0.0994\phi^2 + 0.243\phi - 0.6638 & \phi > 1.75, \end{cases}$$

$$\gamma = 2.715 - 0.5\phi$$

where the factor γ, considering effects of residual gases, is adopted from the correlation of Verhelst [111]. The basic conditions, representing the fun-

damental flame speed s_{L0}, are $p_0 = 20$ bar and $T_0 = 500$ K. The validity domain of the correlation based on reaction mechanism computations is $0.4 \leq \phi \leq 3.75, 1 \leq p \leq 80$ bar and $300 \leq T_u \leq 900$ K.

B.3 Extended Leeds Database

For an extension to the rich regime, the correlation of Verhelst [111] is enhanced with data provided by reaction mechanism calculations, cf. Section 5.5. The resulting expression for s_{L0} reads as

$$
s_{L0} = \begin{cases} a_6\phi^6 + a_5\phi^5 + a_4\phi^4 + a_3\phi^3 + a_2\phi^2 + a_1\phi - a_0 & 0.3 \leq \phi \leq 2.5 \\ s_{L0}(\phi = 2.5) + [1.9596 - s_{L0}(\phi = 2.5)]\frac{\phi - 2.5}{5 - 2.5} & \phi > 2.5 \end{cases}
$$

where the pre-factors a_0 to a_6 are defined as

$$
\begin{aligned}
a_0 &= -0.3364, & a_1 &= -0.7086, & a_2 &= 11.392, & a_3 &= -10.389, \\
a_4 &= 3.9056, & a_5 &= -0.6791, & a_6 &= 0.0449.
\end{aligned}
$$

The expression exponents α and β and the factor γ are adopted from the original correlation according to

$$
\begin{aligned}
\alpha &= 1.232, \\
\beta &= \begin{cases} 2.9025\phi^3 - 6.6943\phi^2 + 5.0596\phi - 1.1599 & \phi < 0.6 \\ 0.0246\phi + 0.078082 & \phi \geq 0.6, \end{cases} \\
\gamma &= 2.715 - 0.5\phi.
\end{aligned}
$$

The basic conditions, representing the fundamental flame speed s_{L0}, are $p_0 = 5$ bar and $T_0 = 365$ K. The validity domain of the correlation based on experiments is $0.3 \leq \phi \leq 1.0, 1 \leq p \leq 10$ bar, $300 \leq T_u \leq 430$ K and $0 \leq X_{EGR} \leq 0.3$. For values of $1 < \phi \leq 3.75$, the correlation is based on results of kinetic computations.

Appendix C

Computational Mesh
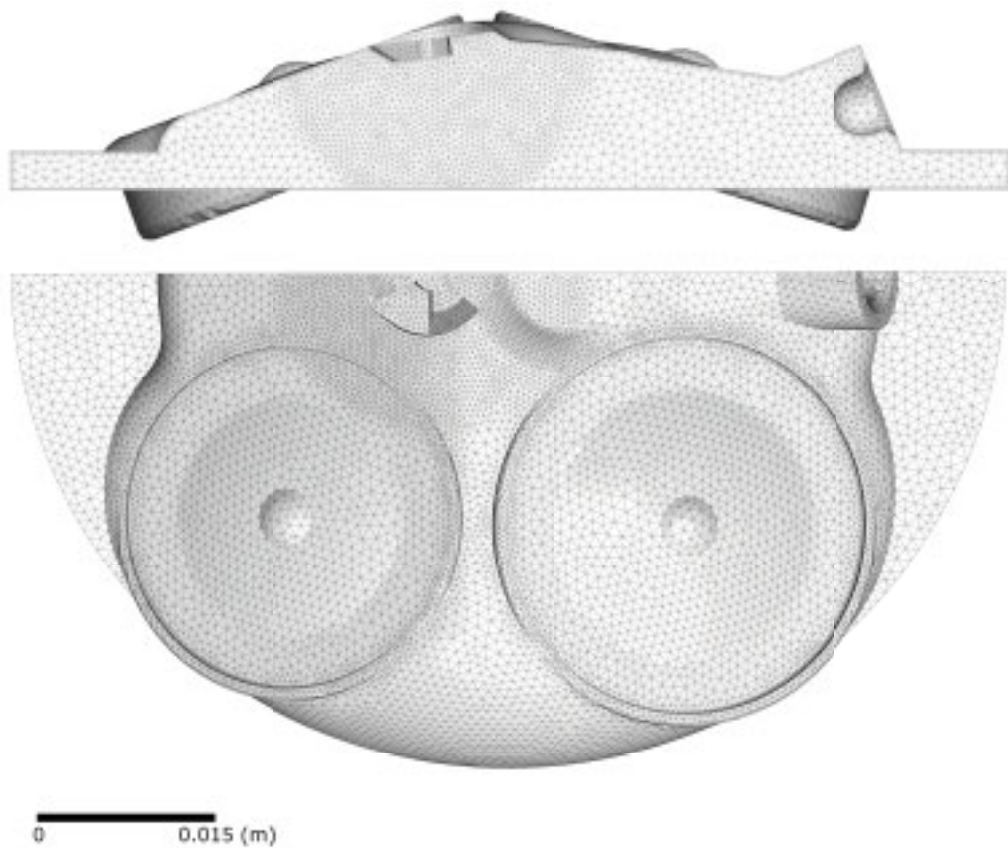
Figure C.1: Top and front view of the computational domain at TDC employed for combustion calculations. The maximum size of tetrahedral elements in the combustion chamber is $h = 3$ mm. The grid is refined to $h = 1$ mm in the region of the spark. The overall number of cells is approx. 0.5 million elements.
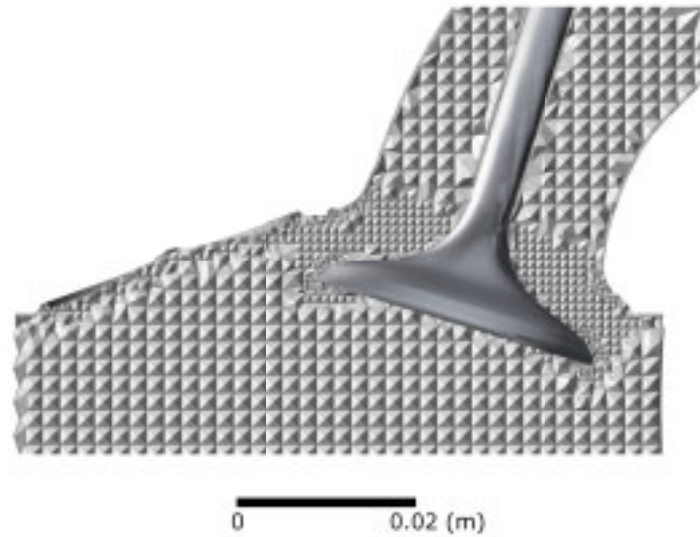
(a) Grid resolution during intake phase.
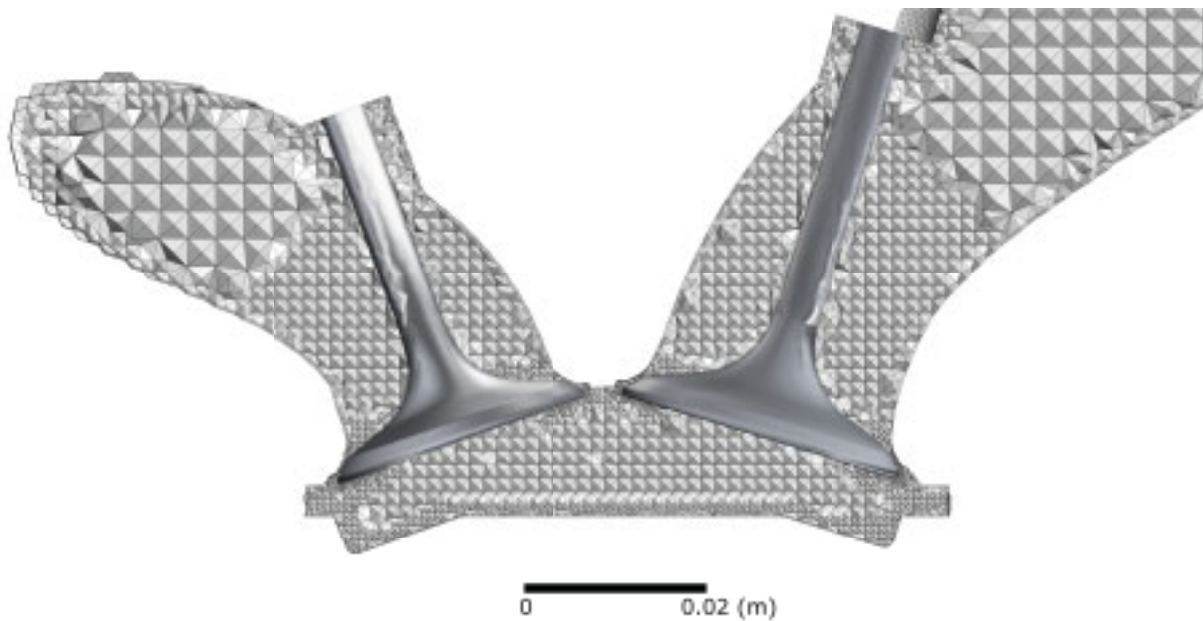
(b) Grid resolution of exhaust valve (left) and intake valve (right) during overlap phase.

Figure C.2: Cross-sectional view through the computational domain employed for gas exchange simulations. The duct is modelled with tetrahedral elements of $h = 5$ mm size. The grid is refined near the valves to $h = 2$ mm and near the valve seats to $h = 0.1$ mm. The overall size of the computational mesh is between 2 and 3 million elements.

Appendix D

Hydrogen/Oxygen Reaction Mechanism

In order to calculate hydrogen laminar burning velocities, reaction rate co-efficients k are determined by

$$k = AT^n \exp(-E_a/RT) \tag{D.1}$$

using values for the constant A, the exponent n and the activation energy E_a as listed in the following.

	H_2/O_2 chain reactions	A	n	E_a
1	$H+O_2=O+OH$	$1.92E+14$	0	$1.64E+04$
rev		$5.48E+11$	0.39	$-2.93E+02$
2	$O+H_2=H+OH$	$5.08E+04$	2.67	$6.29E+03$
rev		$2.67E+04$	2.65	$4.88E+03$
3	$OH+H_2=H+H_2O$	$2.16E+08$	1.51	$3.43E+03$
rev		$2.30E+09$	1.4	$1.83E+04$
4	$O+H_2O=OH+OH$	$2.97E+06$	2.02	$1.34E+04$
rev		$1.47E+05$	2.11	$-2.90E+03$

Table D.1: H_2/O_2 reaction mechanism proposed by Conaire et al. [86], pto. (units: A (cm, mol, s), E_a (cal/mol).

	H_2/O_2 dissociation/recombination reactions	A	n	E_a
5	$H_2+M=H+H+M$	$4.58E+19$	-1.4	$1.04E+05$
rev		$1.15E+20$	-1.68	$8.20E+02$
6	$O_2+M=O+O+M$	$4.52E+17$	-0.64	$1.19E+05$
rev		$6.17E+15$	-0.5	$0.00E+00$
7	$OH+M=O+H+M$	$9.88E+17$	-0.74	$1.02E+05$
rev		$4.71E+18$	-1	$0.00E+00$
8	$H_2O+M=H+OH+M$	$1.91E+23$	-1.83	$1.19E+05$
rev		$4.50E+22$	-2	$0.00E+00$

	Formation and consumption of HO_2	A	n	E_a
9	$H+O_2+M=HO_2+M$	$1.48E+12$	0.6	$0.00E+00$
rev		$3.09E+12$	0.53	$4.89E+04$
10	$HO_2+H=H_2+O_2$	$1.66E+13$	0	$8.23E+02$
rev		$3.16E+12$	0.35	$5.55E+04$
11	$HO_2+H=OH+OH$	$7.08E+13$	0	$2.95E+02$
rev		$2.03E+10$	0.72	$3.68E+04$
12	$HO_2+O=OH+O_2$	$3.25E+13$	0	$0.00E+00$
rev		$3.25E+12$	0.33	$5.33E+04$
13	$HO_2+OH=H_2O+O_2$	$2.89E+13$	0	$-4.97E+02$
rev		$5.86E+13$	0.24	$6.91E+04$

	Formation and consumption of H_2O_2	A	n	E_a
14	$H_2O_2+O_2=HO_2+HO_2$	$4.63E+16$	-0.35	$5.07E+04$
rev		$4.20E+14$	0	$1.20E+04$
14*	$H_2O_2+O_2=HO_2+HO_2$	$1.43E+13$	-0.35	$3.71E+04$
rev		$1.30E+11$	0	$-1.63E+03$
15	$H_2O_2+M=OH+OH+M$	$2.95E+14$	0	$4.84E+04$
rev		$3.66E+08$	1.14	$-2.58E+03$
16	$H_2O_2+H=H_2O+OH$	$2.41E+13$	0	$3.97E+03$
rev		$1.27E+08$	1.31	$7.14E+04$
17	$H_2O_2+H=H_2+HO_2$	$6.03E+13$	0	$7.95E+03$
rev		$1.04E+11$	0.7	$2.40E+04$
18	$H_2O_2+O=OH+HO_2$	$9.55E+06$	2	$3.97E+03$
rev		$8.66E+03$	2.68	$1.86E+04$
19	$H_2O_2+OH=H_2O+HO_2$	$1.00E+12$	0	$0.00E+00$
rev		$1.84E+10$	0.59	$3.09E+04$
19*	$H_2O_2+OH=H_2O+HO_2$	$5.80E+14$	0	$9.56E+03$
rev		$1.07E+13$	0.59	$4.05E+04$

Table D.1 continued.

Bibliography

[1]   http://ec.europa.eu/research/transport/news/article_
       2796_en.html

[2]   http://irh.uqtr.ca

[3]   http://www.gtisoft.com/broch_gtpower.html

[4]   http://www.ansys.com/products/icemcfd.asp

[5]   http://www.bmvit.gv.at/innovation/verkehrstechnologie/
       downloads/a34projekte.pdf

[6]   ABDEL-GAYED, R. G. ; AL-KHISHALI, K. J. ; BRADLEY, D. : Turbulent burn-
       ing velocities and flame straining in explosions. In: *Proc. R. Soc. Lond.
       A* 391 (1984), p. 393–414

[7]   ABDEL-GAYED, R. G. ; BRADLEY, D. ; HAMID, M. N. ; LAWES, M. : Lewis
       number effects on turbulent burning velocity. In: *20th Symp. (Int.)
       on Combustion*. Pittsburgh : The Combustion Institute, 1984, p.
       505–512

[8]   ADDABBO, R. ; BECHTOLD, J. K. ; MATALON, M. : Wrinkling of spherically
       expanding flames. In: *Proc. Combust. Inst.* 29 (2002), p. 1527–35

[9]   AL-SHAHRANY, A. S. ; BRADLEY, D. ; LAWES, M. ; WOOLLEY, R. : Mea-
       surement of unstable burning velocities of iso-octane-air mixtures
       at high pressure and the derivation of laminar burning velocities. In:
       30th Sym. (Int.) on Combustion (2005), p. 225–232

[10]   AMSDEN, A. A. ; O'ROURKE, P. J. ; BUTLER, T. D.: KIVA-II: A Computer
       Program for Chemically Reactive Flows with Sprays. In: *Los Alamos
       National Laboratory Report LA-11560-MS* (1989)

[11] AUNG, K. ; HASSAN, M. ; FAETH, G. : Flame stretch interactions of laminar premixed hydrogen/air flames at normal temperature and pressure. In: *Combust. Flame* 109 (1997), p. 1–24

[12] BARTUNEK, B. ; TOUCHETTE, A. ; MUMFORD, D. ; WING, R. ; HEBBES, M.; LOO, C. ; CLAPA, D. ; WELCH, A. : Development of H_2 Direct Injection Technology for High Efficiency / High BMEP Engines. In: 1*st Int. Sym. on Hydrogen Internal Combustion Engines* Graz University of Technology, Austria, 2006

[13] BECHTOLD, J. K. ; MATALON, M. : Hydrodynamic and Diffusion Effects on the Stability of Spherically Expanding Flames. In: *Combust. Flame* 67 (1987), p. 77–90

[14] BENDER, R. : ANSYS CFX 10 Flow Solver with Extended Coherent Flame Model. In: *Internal Report, D3.2.J, EU integrated project Hy-ICE, No.* 506604 (2007)

[15] BENKENIDA, A. ; COLIN, O. ; KNOP, V. : Adaptation of the ECFM Combustion Model to Hydrogen Internal Combustion Engines. In: 1*st Int. Sym. on Hydrogen Internal Combustion Engines* Graz University of Technology, Austria, 2006

[16] BERCKMÜLLER, M. ; ROTTENGRUBER, H. ; EDER, A. ; BREHM, N. ; ELSÄSSER, G. ; MÜLLER-ALANDER, G. ; SCHWARZ, G. : Potentials of a Charged SI-Hydrogen Engine. In: *SAE Paper no.* 2003-01-3210 (2003)

[17] BLOTEVOGEL, J. ; EGERMANN, T. ; GOLDLÜCKE, J. ; LEIPERTZ, A. ; HARTMANN, M. ; SCHENK, M. ; BERCKMÜLLER, M. : Untersuchungen zur Gemischbildung in Wasserstoffmotoren. In: 6*th Congress Engine Combustion Processes, Munich* (2003), p. 77–88

[18] BLOTEVOGEL, T. : *Untersuchung der Gemischbildung und Verbrennung bei Wasserstoffmotoren mit Hilfe optischer Meßtechniken*, University of Erlangen-Nürnberg, PhD thesis, 2007

[19] BORGHI, R. : Turbulent combustion modelling. In: *Prog. Energy Combust. Sci.* 14 (1988), p. 245–292

[20] BOUDIER, P. ; HENRIOT, S. ; POINSOT, T. ; BARITAUD, T. : A model for turbulent flame ignition and propagation in spark ignition engines. In: 24*th Symp. (Int.) on Combustion, The Combustion Institute* (1992), p. 503

[21] BRADLEY, D. : Instabilities and flame speeds in large-scale pre-mixed gaseous explosions. In: *Phil. Trans. R. Soc. Lond. A* 357 (1999), p. 3567–3581

[22] BRADLEY, D. ; LAU, A. K. C. ; LAWES, M. : Flame stretch rate as a determinant of turbulent burning velocity. In: *Phil. Trans. R. Soc. Lond. A* 338 (1992), p. 359–387

[23] BRADLEY, D. ; LAWES, M. ; LIU, K. ; VERHELST, S. ; WOOLLEY, R. : Laminar burning velocities of lean hydrogen-air mixtures at pressures up to 1.0 MPa. In: *Combust. Flame* 149 (2007), p. 162–172

[24] BRIEM, M. : *Untersuchungen zur inneren Gemischbildung an einem Wasserstoff-Forschungsmotor*, University of Stuttgart, PhD thesis, 1998

[25] COLIN, O. : Hydrogen turbulent mixing modeling. In: *Internal Report, D3.2.C, EU integrated project HyICE, No.* 506604

[26] COLIN, O. ; BENKENIDA, A. ; ANGELBERGER, C. : 3D Modeling of Mixing, Ignition and Combustion Phenomena in Highly Stratified Gasoline Engines. In: *Oil & Gas Science and Technology - Rev. IFP* 58 (2003), Vol. 1, p. 47–62

[27] CONTE, E. : *Combustion of reformer gas/gasoline mixtures in spark ignition engines: A concept for near-zero emission transportation*, Swiss Federal Institute of Technology Zurich, PhD thesis, 2006

[28] DAS, L. : Hydrogen engines: a view of the past and a look into the future. In: *Int. J. Hydrogen Energy* 15 (1990), p. 425–43

[29] DORER, F. : *Kompressionsmaschine zur Simulation von Brennraum-vorgängen in Wasserstoff-Großdieselmotoren*, Technical University Munich, PhD thesis, 2000

[30] EDER, A. : *Brennverhalten schallnaher und überschall-schneller Wasserstoff-Luft Flammen*, Technical University Munich, PhD thesis, 2001

[31] EISEN, S. M. ; OFNER, B. ; MAYINGER, F. : Schnelle Kompressions-maschine - Eine Alternative zum Transparentmotor? In: *MTZ* 62 (2001), 9, p. 680–685

[32] ELLGAS, S. : *Simulation of a Hydrogen Internal Combustion Engine with Cryogenic Mixture Formation*, University of Armed Forces, Munich, PhD thesis, 2007

[33] ERREN, R. ; CAMPBELL, W. : Hydrogen: A Commercial Fuel for Internal Combustion Engines and Other Purposes. In: *The Institute of Fuel* 29 (1933), p. 277–290

[34] ERRICO, G. D. ; ONORATI, A. ; ELLGAS, S. ; OBIEGLO, A. : Thermo-Fluid Dynamic Simulation of a S.I. Single-Cylinder H_2 Engine and Comparison with Experimental Data. In: *Proceedings of ICES*2006 *ASME Internal Combustion Engine Division, Spring Technical Conference* (2006), May 8-10

[35] ESCHER, W. J. D.: Hydrogen-fueled internal combustion engine, a technical survey of contemporary U.S. projects / U.S. Energy Research and Development Administration, Report TEC-75/005. 1975. – Report

[36] FERREIRA, J. ; BENDER, R. ; FORKEL, H. : Flamelet Modelling of Partially Premixed Hydrogen Combustion in a Direct Fuel Injection Engine. In: 1*st Int. Sym. on Hydrogen Internal Combustion Engines* Graz University of Technology, Austria, 2006

[37] FURUHAMA, S. : Hydrogen engine systems for land vehicles. In: *Int. J. Hydrogen Energy* 14 (1989), Vol. 12, p. 907–913

[38] GERBIG, F. ; STROBL, W. ; EICHLSEDER, H. ; WIMMER, A. : Potentials of the Hydrogen Combustion Engine with innovative Hydrogen specific Combustion Processes. In: *FISITA World Automotive Congress*. Barcelona, 2004

[39] GERKE, U. ; BOULOUCHOS, K. ; WIMMER, A. : Numerical Analysis of the Mixture Formation and Combustion Process in a Direct Injected Hydrogen Internal Combustion Engine. In: 1*st International Symposium on Hydrogen Internal Combustion Engines, Graz*, 2006

[40] GERKE, U. ; BOULOUCHOS, K. ; WIMMER, A. ; KIRCHWEGER, W. : Analysis of Hydrogen Direct-Injection Internal Combustion Engines with Methods of Computational Fluid Dynamics. In: *Diesel- und Benzindirekteinspritzung, IV* Bd. 77. Haus der Technik, Berlin, 2006

[41] GOLLING, M. : *in preparation*, BMW Group, Munich, Master thesis, 2007

[42] GÖSCHEL, B. : Der Wasserstoff-Verbrennungsmotor als Antrieb für den BMW der Zukunft! In: *Proc.* 24. *Internationales Wiener Motorensymposium*, 2003

[43] GRABNER, P. : *in preparation*, Technical University of Graz, PhD thesis, 2007

[44] GRABNER, P. ; EICHLSEDER, H. ; GERBIG, F. ; GERKE, U. : Optimisation of a Hydrogen Internal Combustion Engine with Inner Mixture Formation. In: 1*st Int. Sym. on Hydrogen Internal Combustion Engines* Graz University of Technology, Austria, 2006

[45] HALLMANNSEGGER, M. : *Potenziale des 4-Takt-Ottomotors mit Saugrohreinblasung von kryogenem Wasserstoff*, Technical University of Graz, PhD thesis, 2005

[46] HAN, Z. ; REITZ, R. : Turbulence modeling of internal combustion engines using RNG k-ϵ models. In: *Combust. Sci. and Tech.* 106 (1995), p. 267–295

[47] HASSE, C. : *A Two-Dimensional Flamelet Model for Multiple Injections in Diesel Engines*, RWTH Aachen, PhD thesis, 2004

[48] HEFFEL, J. W.: NO_x emission reduction in a hydrogen fueled internal combustion engine at 3000 rpm using exhaust gas recirculation. In: *Int. J. Hydrogen Energy* 28 (2003), p. 1285–1292

[49] HELLER, K. ; ELLGAS, S. : Optimisation of a Hydrogen Internal Combustion Engine with Cryogenic Mixture Formation. In: 1*st Int. Sym. on Hydrogen Internal Combustion Engines* Graz University of Technology, Austria, 2006

[50] HEYWOOD, J. B.: *Internal Combustion Engine Fundamentals*. McGraw-Hill, 1988 (Automotive Technology Series)

[51] HIRSCHFELDER, J. O. ; CURTISS, C. F. ; BIRD, R. B.: *Molecular Theory of Gases and Liquids*. John Wiley & Sons, 1966

[52] HOMAN, H. S. ; DE BOER, P. C. T. ; MCLEAN, W. J.: The effect of fuel injection on NO_x emissions and undesirable combustion for hydrogen-fuelled piston engines. In: *Int. J. Hydrogen Energy* 8 (1983), Vol. 2, p. 131–146

[53]	IIJIMA, T. ; TAKENO, T. : Effects of Temperature and Pressure on Burning Velocity. In: *Combust. Flame* 65 (1986), p. 35–43

[54]	JOHNSON, N. L. ; AMSDEN, A. A. ; BUTLER, T. D.: Hydrogen Program Combustion Research: Three Dimensional Computational Modeling. In: *Proc. of the* 1995 *DOE/NREL Hydrogen Program Review, NREL/CP*-430-20036 2 (1995), p. 285–304

[55]	JORACH, R. W.: *Brennverfahren für einen Wasserstoff-Omnibusmotor mit niedriger Stickoxidemission*, University of Stuttgart, PhD thesis, 1996

[56]	KAMIMOTO, T. : Summary of JHFC Activities / Report on 4th Seminar, Joint Hydrogen and Fuel Cell Demonstration Project, Japan. 2006. – Report

[57]	KARPOV, V. ; LIPATNIKOV, A. N. ; ZIMONT, V. L.: A test of an engineering model of premixed turbulent combustion. In: *26th Symp. (Int.) on Combustion*, The Combustion Institute, 1996, p. 249–257

[58]	KEE, R. J.: *CHEMKIN Release* 4.0.2. Reaction Design, San Diego, CA, 2005

[59]	KIRCHWEGER, W. : *Laseroptische Messmethoden zur Optimierung von Wasserstoff DI-Brennverfahren*, Technical University of Graz, PhD thesis, 2007

[60]	KIRCHWEGER, W. ; HASLACHER, R. ; HALLMANNSEGGER, M. ; GERKE, U.: Applications of the LIF-method for the diagnostics of the combustion process of gas-IC-engines. In: *13th Int. Symp. On Applications of Laser Techniques to Fluid Mechanics, Lisbon Portugal also Exp. Fluid, Springer* 03/2007, 2006

[61]	KOCH, A. ; LUGERT, G. ; MAGORI, E. ; BACHMAIER, G. ; EISEN, S. : Key Components for Gaseous Fuels: Actual Demands and Future Components. In: *1st Int. Sym. on Hydrogen Internal Combustion Engines* Graz University of Technology, Austria, 2006

[62]	KOOP, O. N.: *Experimentelle Untersuchung der Gemischbildung und Verbrennung turbulenter Wasserstoffstrahlen in Querströmungen*, Technical University of Munich, PhD thesis, 1996

[63]	KOVAC, K. : *Optimierung der Gemischbildung an einen DI-Wasserstoffmotor*, Technical University of Graz, PhD thesis, 2005

[64] Kremer, H. ; Lutz, M. ; Koch, P. ; Blotevogel, T. ; Leipertz, A. ; Hartmann, M. : Optical Measurement Techniques for the Investigation of Mixture Formation and Combustion in Hydrogen Internal Combustion Engines. In: *1st Int. Sym. on Hydrogen Internal Combustion Engines* Graz University of Technology, Austria, 2006

[65] Krüger, S. ; Grünefeld, G. : Gas-phase velocity field measurements in dense sprays by laser-based flow tagging. In: *Applied Physics B: Lasers and Optics* 70 (2000), Vol. 3

[66] Law, C. K.: Propagation, Structure, and Limit Phenomena of Laminar Flames at Elevated Pressures. In: *Combust. Sci. and Tech.* 178 (2006), p. 335–360

[67] Law, C. K. ; Jomaas, G. ; Bechtold, J. K.: Cellular instabilities of expanding hydrogen/propane spherical flames at elevated pressures: Theory and experiment. In: *Proc. Combust. Inst.* 30 (2005), p. 159–167

[68] Lipatnikov, A. N. ; Chomiak, J. : Molecular transport effects on turbulent flame propagation and structure. In: *Prog. Energy Combust. Sci.* 31 (2005), p. 1–73

[69] Liu, F. : *CFD Study on Hydrogen Engine Mixture Formation and Combustion*, Technical University of Cottbus, PhD thesis, 2004

[70] Magnussen, B. ; Hjertager, B. : On Mathematical Modeling of Turbulent Combustion with Special Emphasis on Soot Formation and Combustion. In: *Proc. Combust. Inst.* 16 (1977), p. 719–729

[71] Meneveau, C. ; Poinsot, T. : Stretching and quenching of flamelets in premixed turbulent combustion. In: *Combust. Flame* 86 (1991), p. 311

[72] Menter, F. : Zonal Two Equation-Turbulence Models for Aerodynamic Flows. In: *AIAA Paper* 93-2906 (1993)

[73] Messner, D. : *Wirkungsgradoptimierung von H_2-Verbrennungsmotoren mit innerer Gemischbildung*, Technical University of Graz, PhD thesis, 2007

[74] Messner, D. ; Wimmer, A. ; Gerke, U. ; Gerbig, F. : Application and Validation of the 3D CFD method for a Hydrogen Fueled IC En-

gine with Internal Mixture Formation. In: *SAE World Congress, Detroit/MI, USA*, 2006

[75] MILTON, B. E. ; KECK, J. C.: Laminar Burning Velocities in Stoichiometric Hydrogen and Hydrogen-Hydrocarbon Gas Mixtures. In: *Combust. Flame* 58 (1984), p. 13–22

[76] MUNSON, B. R. ; YOUNG, D. F. ; OKIISHI, T. H.: *Fundamentals of Fluid Mechanics, 5th Edition*. John Wiley & Sons

[77] N.N.: *ANSYS CFX computational fluid dynamics (CFD) software.* `http://www.ansys.com/products/cfx.asp`

[78] N.N.: *CFX Solver Theory*. ANSYS CFX

[79] N.N.: *Representative Interactive Flamelets: CFX-RIF*. ANSYS CFX

[80] N.N.: Hydrogen Energy and Fuel Cells - A vision of our future / European Commission. Version: 2003. `http://europa.eu.int/comm/research/energy/pdf/hlg_vision_report_en.pdf` (EUR 20719 EN). – Report

[81] N.N.: European Hydrogen and Fuel Cell Technology Platform / www.HFPeurope.org. 2005. – Report

[82] N.N.: Hydrogen Storage Systems for Automotive Application, Periodic Activity Report / EU integrated project StorHy. 2006 (502667). – Report

[83] N.N.: LES (Large Eddy Simulation) techniques to Simulate and Control by design Cyclic variability in Otto cycle engines / EC funded research project, http://project.ifp.fr/lessco2. 2006. – Report

[84] N.N.: Well-to-Wheels analysis of future automotive fuels and powertrains in the European context / European Commission, Joint Research Center. Version: 2007. `http://ies.jrc.ec.europa.eu/WTW`. – Report

[85] N.N.: Hydrogen Posture Plan / U.S. Department of Energy, U.S. Department of Transportation. December 2006. – Report

[86] Ó CONAIRE, M. ; CURRAN, H. ; SIMMIE, J. ; PITZ, W. ; WESTBROOK, C. : A Comprehensive Modeling Study of Hydrogen Oxidation. In: *Int. J. Chem. Kinetics* 36 (2004), p. 603–622

[87] OBRECHT, P. : *WEG: Benutzerhandbuch und Programmdokumentation*. ETH Zurich, Aerothermochemistry and Combustion Systems Laboratory

[88] OEFELEIN, J. C.: LES of mixing and combustion for direct-injection operation. In: *HyICE European Commission co-funded project no. 506604, internal review D4.3.G.* (2007)

[89] OEHMICHEN, M. : Wasserstoff als Motortreibmittel. In: *Deutsche Kraftfahrtforschung* 68 (1942), p. 1–30

[90] PESCHKA, W. : Die Entwicklung des Wasserstoffantriebs zur Serienreife, Teil 1. In: *ATZ* 6 (2004), p. 554–561

[91] PETERS, H. ; WORRET, R. ; SPICHER, U. : Numerical Analysis of the Combustion Process in a Spark-Ignition Engine. In: *The Fifth Symposium on Diagnostics and Modeling of Combustion in Internal Combustion Engines (COMODIA 2001), Nagoya* (2001), p. 2–20

[92] PETERS, N. : Laminar Diffusion Flamelet Model in Non-Premixed Turbulent Combustion. In: *Prog. Energy Combust. Sci.* 10 (1984), p. 319–339

[93] POINSOT, S. C. T.: Flame Stretch and the Balance Equation for the Flame Area. In: *Combustion Science and Technology* (1990), Vol. 70, p. 1–15

[94] POINSOT, T. ; VEYNANTE, D. : *Theoretical and Numerical Combustion, 2nd Edition*. Edwards, Philadelphia

[95] POPE, S. B.: *Turbulent Flows*. Cambridge University Press

[96] PORUBA, C. : *Turbulente Flammausbreitung in Wasserstoff-Luft-Gemischen*, Technical University of Munich, PhD thesis, 2003

[97] PRECHTL, P. : *Analyse und Optimierung der innermotorischen Prozesse in einem Wasserstoff-Dieselmotor*, Technical University of Munich, PhD thesis, 2000

[98] PRÜMM, W. : Wasserstoffmotor mit äusserer Gemischbildung für Nutzfahrzeuge. In: *Motorische Verbrennung, Aktuelle Probleme und moderne Lösungsansätze*, 1999

[99]   PRÜMM, W. :   Hydrogen Engines for City Busses - the MAN Engines
       H2866 / H2876. In: *1st Int. Sym. on Hydrogen Internal Combustion
       Engines* Graz University of Technology, Austria, 2006

[100] REBECCHI, P. : *Optical Measurements of Flame Velocity on Hydrogen-
       Air Mixtures as a Function of Pressure, Temperature and Equivalence
       Ratio*, ETH Zurich, Aerothermochemistry and Combustion Systems
       Laboratory, Master thesis, 2007

[101] RICARDO, H. R.:   Further Notes on Fuel Research. In: *International
       Automobile Engineers* (1924), Vol. 18, p. 327–341

[102] RINGLER, J. : *in preparation*, Graz University of Technology, Austria,
       PhD thesis, 2007

[103] ROTTENGRUBER, H. :   *Untersuchung der Stickoxidbildung an einem
       Wasserstoff-Dieselmotor*, Technical University Munich, PhD thesis,
       1999

[104] SCHULTZ, M. ; DIEHL, T. ; BRASSEUR, G. ; ZITTEL, W. : Air Pollution and
       Climate-Forcing Impacts of a Global Hydrogen Economy. In: *Science
       Magazine* 302 (2003), Vol. 5645, p. 624–627

[105] SPEZIALE, C. ; SARKAR, S. ; GATSKI, T. :   Modelling the pressure-
       strain correlation of turbulence: an invariant dynamical systems ap-
       proach. In: *J. Fluid Mechanics* 277 (1991), p. 245–272

[106] STEURS, K. :   *Development of flame speed correlations of hy-
       drogen/air mixtures for different thermochemical parameters*, ETH
       Zurich, Aerothermochemistry and Combustion Systems Laboratory,
       Master thesis, 2007

[107] TANG, X. ; KABAT, D. ; NATKIN, R. J. ; STOCKHAUSEN, W. F. ; HEFFEL, J. :
       Ford P2000 Hydrogen Engine Dynamometer Development. In: *SAE
       Paper no.* 2002.01.0242 (2002)

[108] TAYLOR, S. : *Burning Velocities and the Influence of Flame Stretch*,
       University of Leeds, U.K., PhD thesis, 1991

[109] TROMP, T. ; SHIA, R. ; ALLEN, M. ; EILER, J. ; YUNG, Y. : Potential Envi-
       ronmental Impact of a Hydrogen Economy on the Stratosphere. In:
       Science Magazine 300 (2003), Vol. 5626, p. 1740–1742

[110] Tse, S. D. ; Zhu, D. L. ; Law, C. K.: Morphology and burning rates of expanding spherical flames in H_2/O_2/inert mixtures up to 60 atmospheres. In: *Proc. Combust. Inst.* 28 (2000), p. 1793–1800

[111] Verhelst, S. : *A Study of the Combustion in Hydrogen-Fuelled Internal Combustion Engines*, Ghent University, Belgium, PhD thesis, 2005

[112] Vogl, P. ; Heckelmann, I. ; Pfitzner, M. : Modelling of Hydrogen Injection and Combustion in Internal Combustion Engines. In: 1*st Int. Sym. on Hydrogen Internal Combustion Engines* Graz University of Technology, Austria, 2006

[113] Wallner, T. : *Entwicklung von Brennverfahrenskonzepten für einen PKW-Motor mit Wasserstoffbetrieb.*, Graz University of Technology, Austria, PhD thesis, 2004

[114] Wallner, T. ; Ciatti, S. ; Stockhausen, W. ; Boyer, B. : Endoscopic Investigations in a Hydrogen Internal Combustion Engine. In: 1*st Int. Sym. on Hydrogen Internal Combustion Engines* Graz University of Technology, Austria, 2006

[115] Warnatz, J. ; Maas, U. ; Dibble, R. W.: *Verbrennung*. Springer Verlag, Berlin

[116] White, C. ; Steeper, R. ; Lutz, A. : The hydrogen-fuelled internal combustion engine: a technical review. In: *Int. J. Hydrogen Energy* 10 (2006), p. 1292–1305

[117] Wiebicke, U. : *Untersuchung zum Betriebsverhalten eines mittelschnellaufenden Wasserstoff-Dieselmotors*, Technical University of Munich, PhD thesis, 1998

[118] Wimmer, A. ; Chmela, F. ; Dimitrov, D. ; Eichlseder, H. ; Messner, D. : Prediction of Heat Release for Hydrogen IC Engines with Port Injection. In: 1*st Int. Sym. on Hydrogen Internal Combustion Engines* Graz University of Technology, Austria, 2006

[119] Woschni, G. : A Universally Applicable Equation for the Instantaneous Heat Transfer Coefficient in the Internal Combustion Engine. In: *SAE Transactions* 76 (1967), p. 3065–3083

[120] WRIGHT, Y. M.: *Numerical Investigation of turbulent spray combustion with Conditional Moment Closure*, Swiss Federal Institute of Technology Zurich, PhD thesis, 2005

[121] YAKHOT, V. ; ORSZAG, S. : Renormalization group analysis of turbulence. In: *J.Sci.Comput.* 1 (1986), p. 3

[122] ZANARDELLI, V. : The Design, Development, Validation and Delivery of the Ford H_2 ICE E450 Shuttle Bus Product. In: 1*st Int. Sym. on Hydrogen Internal Combustion Engines* Graz University of Technology, Austria, 2006

[123] ZIEGER, J. ; KRÄMER, M. : Wasserstoff-Projekt HYPASSE. In: *Stuttgarter Symposium Kraftfahrwesen und Verbrennungsmotoren* (1995), 20-22 Feb.

[124] ZIMONT, V. : Gas Premixed Combustion at High Turbulence. Turbulent Flame Closure Combustion Model. In: *Proc. of the Mediterranean Combustion Sym., Antalya, Turkey* (1999)

[125] ZIMONT, V. ; BIAGIOLI, F. ; SYED, K. : Modeling turbulent premixed combustion in the intermediate steady propagation regime. In: *Progress in Comp. Fluid Dyn.* (2001), Vol. 1, p. 14

[126] ZIMONT, V. ; LIPATNIKOV, A. : A numerical model of premixed turbulent combustion of gases. In: *Chem. Phys. Report* (1995), Vol. 14, p. 993–1025

[127] ZIMONT, V. ; POLIFKE, W. ; BETTELINI, M. ; WEISENSTEIN, W. : An efficient computational model for premixed turbulent combustion at high Reynolds numbers based on a turbulent flame speed closure. In: *ASME Int. Gas turbine & Aeroengine Congress & Exhibition; Orlando, Florida* (1997)

Curriculum Vitae

Udo Gerke   Born February 26th, 1978 in Stuttgart, Germany

Education

05/2004 – 12/2007	**ETH-Zürich,** **Swiss Federal Institute of Technology (CH)** Aerothermochemistry and Combustion Systems Laboratory, PhD
10/1998 – 11/2003	**University of Stuttgart (D)** Diplom-Ingenieur in Mechanical Engineering (with distinction)
08/1988 – 06/1997	**Burg-Gymnasium, Schorndorf (D)** Abitur

Work experience

05/2004 – present	**BMW Group Research and Technology,** **Munich (D)** Combustion process development for IC engines
05/2003 – 11/2003	**German Aerospace Center DLR, Stuttgart (D)** Institute of Technical Thermodynamics, Thesis research on alkaline fuel cell technology
09/2002 – 02/2003	**University of California, Santa Barbara (USA)** Department of Mechanical and Environmental Engineering, Thesis research on computational fluid dynamics and linear stability theory
04/2002 – 07/2002	**DaimlerChrysler AG, Stuttgart (D)** Internship, Development of hybrid power train systems
10/2001 – 03/2002	**CTS Car Top Systems, Korntal-Münchingen (D)** Internship, Development of retractable hardtop systems for passanger cars
07/1997 – 07/1998	**Alternative Civilian Service** Sozialstation, Schorndorf (D)

Contact

Email: udo.gerke@bmw.de
Telephone: +49 (0) 89 / 382 66575

Publications and Presentations

in preparation	Gerke, U.; Boulouchos, K. Turbulent flame speed closure models for the computation of hydrogen internal combustion engines. **Combustion Science and Technology**
submitted	Haslacher, R.; Eichlseder, H.; Hallmannsegger, M.; Gerke, U. Application of Optical Instrumentation for the Diagnostics of Innovative Hydrogen Combustion Processes. **14th Int. Symp. on Applications of Laser Techniques to Fluid Mechanics, Lissabon**
12/2006	Gerke, U.; Boulouchos, K.; Wimmer, A.; Kirchweger, W. Analysis of Hydrogen Direct-Injection Internal Combustion Engines with Methods of Computational Fluid Dynamics. **Diesel- und Benzindirekteinspritzung, IV Bd. 77, Haus der Technik, Berlin**
10/2006	Kirchweger, W.; Haslacher, R.; Hallmannsegger, M.; Gerke, U. Applications of the LIF-method for the diagnostics of the combustion process of gas-IC-engines. **Experiments in Fluids, Springer-Verlag 03/2007**
09/2006	Gerke, U.; Boulouchos, K.; Wimmer, A. Numerical Analysis of the Mixture Formation and Combustion Process in a Direct Injected Hydrogen Internal Combustion Engine. **1st Int. Symp. on Hydrogen Internal Combustion Engines, Graz**
09/2006	Grabner, P.; Eichlseder, H.; Gerbig F.; Gerke, U. Optimisation of a Hydrogen Internal Combustion Engine with Inner Mixture Formation. **1st Int. Symp. on Hydrogen Internal Combustion Engines, Graz**
06/2006	Kirchweger, W.; Haslacher, R.; Hallmannsegger, M.; Gerke, U. Applications of the LIF-method for the diagnostics of the combustion process of gas-IC-engines. **13th Int. Symp. on Applications of Laser Techniques to Fluid Mechanics, Lissabon**
05/2006	Kirchweger, W.; Eichlseder, H.; Gerbig F.; Gerke, U. Optische Messmethoden zur Optimierung von Wasserstoff-DI-Brennverfahren. **7. Internationales Symposium für Verbrennungsdiagnostik, Baden-Baden**
04/2006	Messner, D.; Wimmer, A.; Gerke, U.; Gerbig F. Application and Validation of the 3D CFD method for a Hydrogen Fueled IC Engine with Internal Mixture Formation. **2006 SAE World Congress, Detroit**
02/2006	Gülzow, E.; Schulze, M.; Gerke, U. Bipolar concept for alkaline fuel cells. **Journal of Power Sources, 156 (2006) 1-7, Elsevier Science Direct**
11/2005	Gerke, U.; Ellgas, S. Der virtuelle Wasserstoffmotor – Fortschrittliche Methoden in der Berechnung und im Experiment. **Lecture: ZT Forschungskolloquium BMW Group, Munich**
09/2005	Kirchweger, W.; Eichlseder, H.; Gerbig F.; Gerke, U. Analysis of the Hydrogen-DI-Combustion Process with special Measuring Techniques **10. Tagung Der Arbeitsprozess des Verbrennungsmotors, Graz**